

Award Number:
W81XWH-07-1-0708

TITLE :
Design, Fabrication, Characterization and Modeling of Integrated Functional Materials

PRINCIPAL INVESTIGATOR :
PI: Pritish Mukherjee, Ph. D.

CONTRACTING ORGANIZATION :
University of South Florida

Tampa, FL 33620, USA

REPORT DATE :
October 2013

TYPE OF REPORT :
Final Report

PREPARED FOR : U.S. Army Medical Research and Materiel Command
Fort Detrick, Maryland 21702-5012

DISTRIBUTION STATEMENT :

X Approved for public release; distribution unlimited

The views, opinions and/or findings contained in this report are those of the author(s) and should not be construed as an official Department of the Army position, policy or decision unless so designated by other documentation.

REPORT DOCUMENTATION PAGE				Form Approved OMB No. 0704-0188	
Public reporting burden for this collection of information is estimated to average 1 hour per response, including the time for reviewing instructions, searching existing data sources, gathering and maintaining the data needed, and completing and reviewing this collection of information. Send comments regarding this burden estimate or any other aspect of this collection of information, including suggestions for reducing this burden to Department of Defense, Washington Headquarters Services, Directorate for Information Operations and Reports (0704-0188), 1215 Jefferson Davis Highway, Suite 1204, Arlington, VA 22202-4302. Respondents should be aware that notwithstanding any other provision of law, no person shall be subject to any penalty for failing to comply with a collection of information if it does not display a currently valid OMB control number. PLEASE DO NOT RETURN YOUR FORM TO THE ABOVE ADDRESS.					
1. REPORT DATE October 2013		2. REPORT TYPE Final		3. DATES COVERED 20 September 2007- 19 September 2013)	
4. TITLE AND SUBTITLE Design, Fabrication, Characterization and Modeling of Integrated Functional Materials				5a. CONTRACT NUMBER W81XWH-07-1-0708	
				5b. GRANT NUMBER W81XWH-07-1-0708	
				5c. PROGRAM ELEMENT NUMBER	
6. AUTHOR(S) PI: Pritish Mukherjee, Ph. D. co-PIs: Hariharan Srikanth, Ph.D.; Sarath Witanachchi, Ph. D.; George Nolas, Ph. D.				5d. PROJECT NUMBER	
				5e. TASK NUMBER	
				5f. WORK UNIT NUMBER	
7. PERFORMING ORGANIZATION NAME(S) AND ADDRESS(ES) University of South Florida 4202 East Fowle Avenue Tampa, FL 33620, USA				8. PERFORMING ORGANIZATION REPORT NUMBER	
9. SPONSORING / MONITORING AGENCY NAME(S) AND ADDRESS(ES) U.S. Army Medical Research and Materiel Command Fort Detrick, Maryland 21702-5012				10. SPONSOR/MONITOR'S ACRONYM(S)	
				11. SPONSOR/MONITOR'S REPORT NUMBER(S)	
12. DISTRIBUTION / AVAILABILITY STATEMENT Approved for public release; distribution unlimited					
13. SUPPLEMENTARY NOTES					
14. ABSTRACT The dynamically evolving needs of the U.S. soldier in the battlefield in response to changes in the technology of warfare and associated threats require advances in multiple areas including biomedical diagnostics, chemical sensing, communication technology, efficient power generation without increased payload, and mobile refrigeration. These technological advances are critically dependent on the development of new and currently non-existing materials. This research addresses the directed development of novel materials towards long-term needs of the United States Army. In order to address specific areas of integrated functional materials targeted towards the needs of the U.S. soldier in the field we have initiated research efforts in three main areas which are diagnostics and sensing, communication and energy, and power generation and refrigeration. The specific three independent "Tasks" that have been undertaken are: Task I: Nanostructured materials for biomedical diagnostics and chemical sensing Task II: Multifunctional composites for communication and energy applications Task III: Solid-state materials for power generation and refrigeration The specific outcome of the research activities is expected to lead to new devices/systems/composite materials useful for the USAMRMC.					
15. SUBJECT TERMS Functional materials, integrated fabrication, nanobiotechnology, multifunctional, dimensional integration, nanocomposites, sensor technology, thermoelectrics, solar cells, photovoltaics, polypeptide multilayer films, multiferroics, biomaterials, biodetection					
16. SECURITY CLASSIFICATION OF:			17. LIMITATION OF ABSTRACT UU	18. NUMBER OF PAGES 202	19a. NAME OF RESPONSIBLE PERSON USAMRMC
a. REPORT U	b. ABSTRACT U	c. THIS PAGE U			19b. TELEPHONE NUMBER (include area code)

Design, Fabrication, Characterization and Modeling of Integrated Functional Materials
(Program Director and PI: Prof. Pritish Mukherjee, Department of Physics, USF, Tampa, FL)
(co-PIs: Profs. Hariharan Srikanth, Sarath Witanachchi and George Nolas)

Table of Contents

	<u>Page</u>
I. Introduction.....	4
II. Technical Description of Research	6
III. Key Research Accomplishments.....	158
IV. Reportable Outcomes.....	165
V. Conclusion.....	188
VI. References.....	192

Design, Fabrication, Characterization and Modeling of Integrated Functional Materials

(Program Director and PI: Prof. Pritish Mukherjee, Department of Physics, USF, Tampa, FL)

(co-PIs: Profs. Hariharan Srikanth, Sarath Witanachchi and George Nolas)

I. Introduction

The dynamically evolving needs of the U.S. soldier in the battlefield in response to changes in the technology of warfare and associated threats require advances in multiple areas including biomedical diagnostics, chemical sensing, communication technology, efficient power generation without increased payload, and mobile refrigeration. These technological advances are critically dependent on the development of new and currently non-existing materials. This research addressed the directed development of novel materials towards long-term needs of the United States Army.

Objective:

In addition to the integration of multiple functionalities with desirable properties (thermal, electrical, magnetic, mechanical, optical, etc.), the connection to real-world applications and devices also requires the seamless integration of dimensions (nano, micro, meso, macro) leading to integrated functional materials. We have initiated this Integrated Functional Materials Project at the Physics Department at the University of South Florida (USF) geared towards precisely addressing this grand challenge of dual integration. A series of targeted projects specifically addressed a spectrum of issues relevant to the needs of the U.S. soldier.

Specific Aims:

The Physics Department at the University of South Florida is home to a unique doctoral program in Applied Physics with an affiliated industrial practicum and nationally recognized research programs in physical and chemical materials synthesis and characterization of bulk materials, thin films and nanomaterials; crystal fiber growth; fundamentals of materials manufacturing processes and computational theoretical materials physics. This research synergistically coalesced existing expertise and leverages research infrastructure at USF in novel bulk materials synthesis, thin film growth, and nanotechnology. These goals were further addressed through multidisciplinary research and new infrastructure development. The basic purpose of this project was to develop the novel science base both in the areas of multi-scale dimensional integration as well as multiple functional integration leading to previously unattained integrated functional materials.

Study Design:

In order to address specific areas of integrated functional materials targeted towards the needs of the U.S. soldier in the field we directed the research efforts in three main areas which are diagnostics and sensing, communication and energy, and power generation and refrigeration. The specific three independent “Tasks”, further subdivided into seven “Projects” were:

Task I: Nanostructured materials for biomedical diagnostics and chemical sensing

(Technical Directors.: Drs. H. Srikanth and P. Mukherjee)

- Project 1* Functional magnetic fluids for biomedical applications
- Project 2* Nanoporous/nano-wire structures and polymer nanotemplates for sensing and molecular manipulation
- Project 3* Carbon-nanotube based sensors
- Project 4* Functional materials for affecting cell proliferation and locomotion

Task II: Multifunctional composites for communication and energy applications

(Technical Director: Dr. S. Witanachchi)

- Project 5* Tunable multifunctional nano- and heterostructures for RF and microwave applications
- Project 6* Flexible photonic materials for solar-based energy sources

Task III: Solid-state materials for power generation and refrigeration

(Technical Director: Dr. G. S. Nolas)

- Project 7* High-performance nanofabricated thermoelectric materials for power generation and refrigeration

II. Technical Description of Research

Technical progress on the conducted research was provided throughout the duration of the grant through quarterly reports, annual reports and two product-line reviews.

Throughout the six-year period of the grant, the following faculty members at the University of South Florida (USF), all Ph.D.s with current ranks noted parenthetically, received partial pay from the research effort: Donald Haynie (Associate Professor), Xiaomei Jiang (Associate Professor), Chun-Min Lo (previously Assistant Professor at USF Physics), George Nolas (Professor), Ivan Oleynik (Professor), Hari Srikanth (Professor), Sarath Witanachchi (Professor) and Lilia Woods (Associate Professor).

The nine postdoctoral scientists supported by the grant include: Drs. Anis Biswas, Eunhee Cho, Anuja Datta, Tara Dhakal, Hafsa Khurshid, Xiunu Lin, Devajyoti Mukherjee, Susmita Pal and Manh-Huong Phan.

The following graduate students received support from the grant: Sayan Chandra, Anurag Chaturvedi, Gayan Dedigamuwa, Daniel Denmark, Jagannath Devakota, Dino Ferizovic, Chaminda Hettiarachchi, Mahesh Hordagoda, Robert Hyde, Vuaysankar Kalappattil, Hillary Kirby, Joshua Martin, Marek Merlak, Marienette Morales, Zohreh Nemati Porshokouh, Jason Rejman and Kristen Stojak. Undergraduate research students supported by the grant include: Spandan Bandyopadhyay, Shaun Desouza, Daniel Hromalik, Amir Allah Mansour, Chadwick Myers, Diana Nesbitt and Chandler Schlupf.

The following discussion provides salient technical details of research performed on each of the Tasks during the six-year course of research. The technical discussion of research associated with each of the three Tasks described in the Introduction is divided into descriptions for each of the seven constituent Projects, further sub-divided into specific sub-headings for each Project. Supplemental funding was provided for some of the Tasks through Grant No. W81XWH-1020101/3349 since September 2010. This three-year grant also concluded on September 19, 2013 and a 24-month no-cost extension to complete parts of the work by September 19, 2015 has been approved. The status of the milestones for the project and the resultant scope of future continuing work are detailed in the Conclusion (Section V).

Task I: Nanostructured materials for biomedical diagnostics and chemical sensing

Project 1: Functional magnetic nanoparticles and their ferrofluids for biomedical applications:

The goal of this project was to synthesize and characterize functional magnetic nanoparticles and their ferrofluids for a wide range of biomedical applications. During this project duration, we have successfully fabricated a wide range of ferrite nanoparticles with controlled size and shape, biofunctional metal-oxide coupled and core-shell nanostructures, and ferrofluids containing these nanoparticles. We highlight below some of the main results featuring these achievements.

1.1. Synthesis and characterization of functional ferrite nanoparticles with controlled size and shape:

Control over the size and shape of nanomaterials is a vital and challenging task in exploring the novelty and uniqueness of material properties for practical applications [1]. In this project, we have successfully synthesized and characterized ferrite nanoparticles of Fe_3O_4 , CoFe_2O_4 , NiFe_2O_4 , and MnFe_2O_4 with controlled size and shape. The size of particles can be tuned from 5 nm to 20 nm, while the shape of nanoparticles can be altered from spherical to cubic and octopod. While previous efforts were not successful in making shape-variant ferrite nanoparticles with a small size distribution [1,2], we have advanced our chemical technique that allows for fabrication of monodisperse and uniform nanoparticles. We present here selected results on spherical and cubic nanoparticle systems of CoFe_2O_4 , demonstrating the important impact of particle shape on the magnetic properties of the material. Figure 1 shows TEM images of spherical and cubic monodisperse CoFe_2O_4 nanocrystals with diameter of $8 \text{ nm} \pm 1 \text{ nm}$.

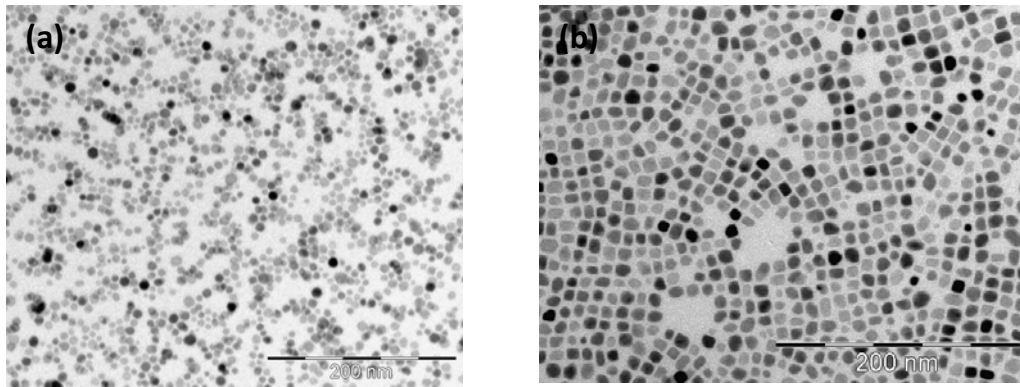


Figure 1: TEM images of (a) spherical (b) cubic CoFe_2O_4 nanoparticles

The temperature and magnetic field variation magnetic properties of the nanocrystals were studied using a physical property measurement system (PPMS) in our laboratory. Figure 2a shows the zero-field-cooled (ZFC) and field-cooled (FC) M-T curves, as well as the M-H loops at 300 K for spherical and cubic nanocrystals. The blocking temperature (T_B) of spherical CoFe_2O_4 (CFO-s) is 104 K, while it is 294 K for cubic CoFe_2O_4 (CFO-c). At 10 K the saturation magnetization (M_s) and coercivity (H_c) values of the nanocubes are significantly higher than the spherical nanocrystals. The M_s and H_c values for CFO-c is 41 emu/g and 24 kOe whereas the M_s and H_c of CFO-s are 29 emu/g and 10.5 kOe. The significant increase in T_B , H_c and M_s in cubic particles is due to the enhancement of magnetic

anisotropy compared to spherical particles. The room temperature M-H data for CFO-c and CFO-s do not show any coercivity, which indicate that both the systems are superparamagnetic in nature (Figure 2b).

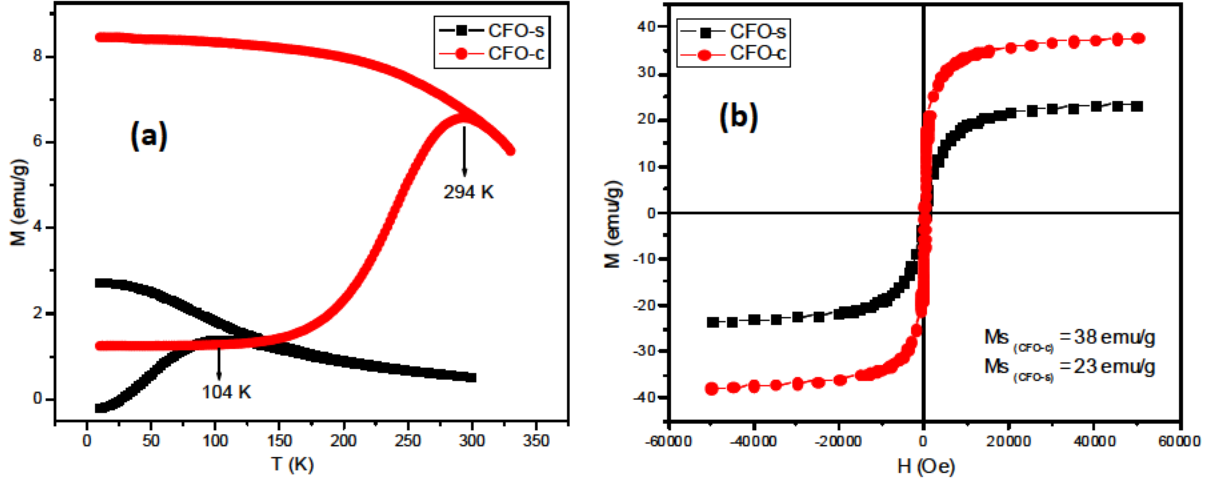


Figure 2: Comparison of (a) M-T and (b) M-H data for spherical and cubic CoFe_2O_4 nanocrystals.

These results indicate that the synthesized nanoparticles are very promising for biomedical applications. In particular, these particles can provide more magnetic labeling options that are currently restricted to spherical magnetic nanoparticles below 15 nm in size [3]. Once shape-variant magnetic nanoparticles are used, different biological molecules (e.g., proteins and lipids) can be labeled to simultaneously target different sites within a single sample, giving a direct comparison of signaling networks or multisubunit molecular machines [4]. As we show in Section 1.6, the shape of ferrite nanoparticles plays an important role in determining the MRI contrast and the inductive heating capacity of ferrofluids in hyperthermia applications.

1.2. Synthesis and characterization of metal-oxide coupled nanostructures:

Functional core-shell Fe_3O_4 -Au nanoparticles for biomedical applications: It has been reported that using gold (Au) coating, the magnetic nanoparticles, such as Fe_3O_4 nanoparticles, can be stabilized more efficiently and readily functionalized through the well developed Au-S chemistry in thiol capped gold nanoparticle [5]. The coating also renders the magnetic nanoparticles with plasmonic properties. This makes the core/shell composite nanoparticles extremely interesting for magnetic, optical, and biomedical applications. However, it has remained challenging to control the uniform thickness of the Au coating layer.

In this project, we have successfully developed a chemical method for the synthesis of Au-coated Fe_3O_4 nanoparticles with controlled particle size [6]. Figure 3 shows a representative set of TEM images of Fe_3O_4 nanoparticles before (a) and after the formation of a gold shell (b). The well-isolated particles show non spherical shape in Fe_3O_4 , whereas the shape is nearly spherical shape in Au-coated Fe_3O_4 . The two major findings from the morphological comparison are: (i) the Fe_3O_4 particles after coating with Au appear much darker than before coating with Au, (ii) the average particle sizes changed from $5.9 \pm 0.5 \text{ nm}$ for particles before coatings (Figure 3a) to $6.9 \pm 0.5 \text{ nm}$ for the particles after coating

(Figure 3b) with Au. We have studied the magnetic properties including M-T, M-H, AC and radio-frequency (RF) transverse susceptibility using the PPMS. The M-T data measured at a field of 200 Oe in ZFC-FC regimes for the Fe_3O_4 and $\text{Fe}_3\text{O}_4@\text{Au}$ nanoparticles show a superparamagnetic response at 300 K, with T_B of ~ 35 K and ~ 40 K, respectively (Figure 3c,d). The slight increase in blocking temperature for Au-coated particles could be due to the overall increase in particle size as observed from TEM.

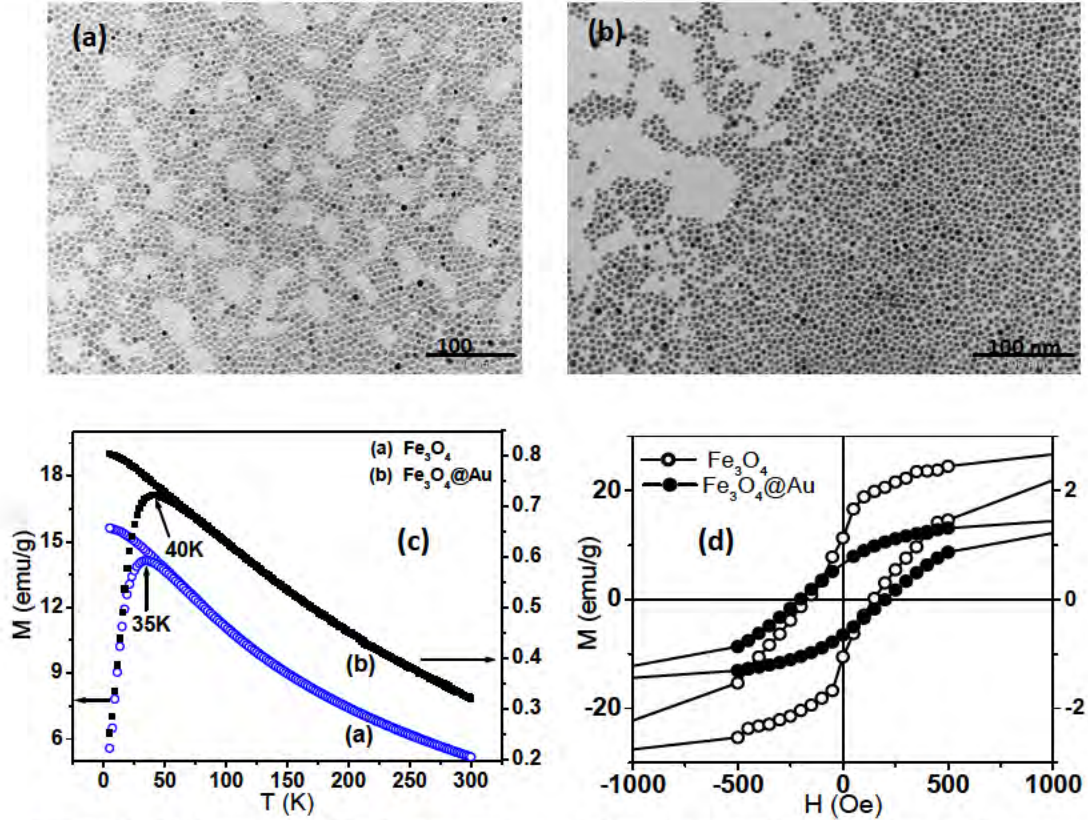


Figure 3: TEM images of Fe_3O_4 nanoparticles before (a) and after (b) coating with Au shell; (c) ZFC and FC M-T data for bare Fe_3O_4 and core-shell $\text{Fe}_3\text{O}_4@\text{Au}$ nanoparticles; (d) The M-H loops taken at 5 K after 5 T field cooling.

The M-H curves were recorded at 5 K under ZFC-FC modes. The M_s values of Fe_3O_4 NPs and $\text{Fe}_3\text{O}_4@\text{Au}$ are 33 emu/g and 1.8 emu/g respectively. This reduction is expected in nanoparticles as the surface magnetic order can be affected by structural distortions that cause spin canting. The M-H loops taken after a 5 T field cooling were not shifted, indicating no exchange bias (or the interfacial coupling between the core and shell) in these systems. The synthesized $\text{Fe}_3\text{O}_4@\text{Au}$ nanoparticles are therefore desirable for biomedical applications. As we report in Section 3.3, such nanoparticles are interesting for biodetection of kidney cells. The main results featuring the importance of $\text{Fe}_3\text{O}_4@\text{Au}$ nanoparticles for biomedical applications have been published in *Journal of Applied Physics* 2009 and *Sensors* 2013.

Novel hybrid $\text{Pt-}\gamma\text{Fe}_2\text{O}_3$ nanoparticles for biomedical applications: According to a recent report, Pt nanoparticles strongly enhance the biological efficiency of radiations, which makes them a very good candidate for radiation therapy and other biological applications [7]. When compared with conventional single-component nanoparticles, a hybrid nanostructure of Pt and iron-oxide could provide multifunctional hybrid probes, where (1) the presence of Pt and iron-oxide surfaces facilitates the

stepwise attachment of antigens and biomolecules, and (2) the structure can serve as both magnetic and optical probes for radiation therapy and diagnosis. In order to gain better control over their properties, it is very important to understand the chemical reaction conditions of controlling monodispersity, size and shape of these hybrid nanostructures.

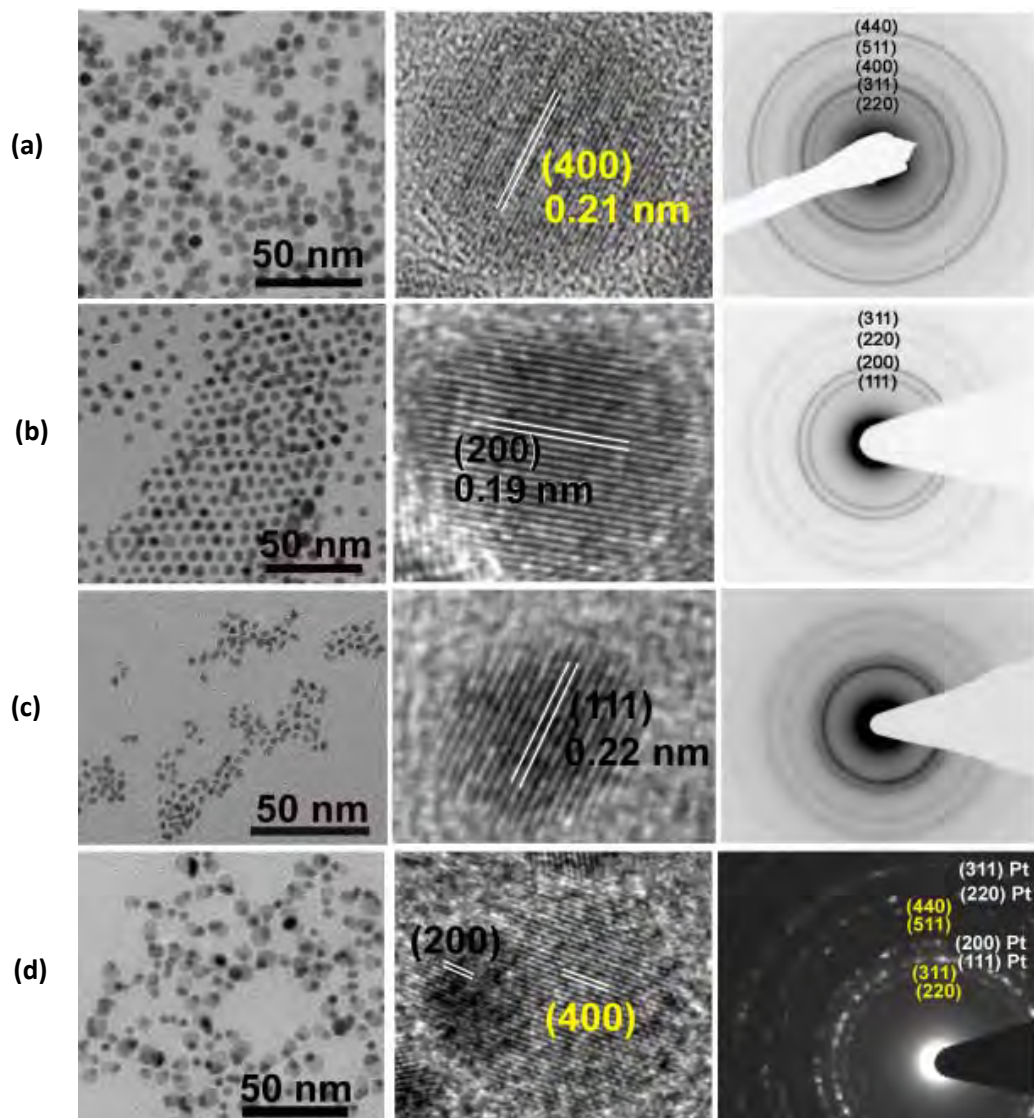


Figure 4: TEM images, HRTEM and SAED patterns of $\gamma\text{Fe}_2\text{O}_3$ nanoparticles (row a), FePt nanoparticles (row b), Pt seeds (row c) and dumbbell-shaped Pt- $\gamma\text{Fe}_2\text{O}_3$ nanoparticles (row d).

To address this outstanding issue, in this project we have focused on the synthesis and characterization of hybrid nanoparticles consisting of Pt and iron-oxide (Pt- $\gamma\text{Fe}_2\text{O}_3$) nanoparticles and their magnetic properties in the dumbbell morphology, with particular emphasis on size and shape control [8]. Our results indicate that in order to synthesize Pt-based magnetic hybrid nanostructures, there exists a size limit for Pt seeds. The dumbbell-like morphology of Pt and $\gamma\text{Fe}_2\text{O}_3$ can be used as an extra degree of freedom to control the magnetic properties for potential applications in biomedicine and cancer therapy.

Figure 4 shows TEM images (1st column), HRTEM images (2nd column) and SAED patterns (3rd column) of $\gamma\text{Fe}_2\text{O}_3$ (Figure 4a), FePt (Figure 4b), Pt (Figure 4c) and dumbbell-shaped Pt- $\gamma\text{Fe}_2\text{O}_3$ nanoparticles (Figure 4d). In the case of dumbbell-shaped Pt- $\gamma\text{Fe}_2\text{O}_3$, the Pt domain appears darker because of its high electronic density. The HRTEM image of $\gamma\text{Fe}_2\text{O}_3$ nanoparticles reveals their high crystallinity. The measured lattice fringes correspond to the inter-planar distance of (400) planes of $\gamma\text{Fe}_2\text{O}_3$. SAED also matches well with the characteristic reflections of $\gamma\text{Fe}_2\text{O}_3$, which is consistent with the results obtained from XRD. The decomposition of iron-carbonyl produces metallic iron nanoparticles, which, when combined with traces of oxygen dissolved in the solvent, oxidizes them to produce iron-oxide nanoparticles. When $\text{Fe}(\text{CO})_5$ was decomposed along with $\text{Pt}(\text{acac})_2$, highly crystalline fcc structure FePt nanoparticles were obtained. The lattice spacing measured from the fringes is found to be 0.198 nm, which corresponds to the (200) inter-planar spacing of the fcc structure of FePt. Figure 4c shows the TEM image of Pt nanoparticles that were obtained after refluxing the reaction mixture at 150°C for two hours. The SAED matches well to the characteristic reflections of Pt, as obtained from XRD. The average particle size is found to be 3.2 ± 1.5 nm, which is very close to the size calculated from XRD using the Sherrer's formula. Figure 4d shows the TEM image of hybrid nanostructures of $\gamma\text{Fe}_2\text{O}_3$ and Pt. The particles appeared to be 'dumbbell-like,' where each Pt nanoparticle is sticking to an iron-oxide nanoparticle or vice versa. High-resolution TEM (HRTEM) images of individual dumbbell particles reveal the high crystallinity of the Pt and $\gamma\text{Fe}_2\text{O}_3$ and show a clear interface between $\gamma\text{Fe}_2\text{O}_3$ and Pt. The adjacent lattice fringes of the Pt domain are measured to be 0.194 nm, which matches well with the (200) inter-planar distance of Pt. The measured distance between lattice fringes of a $\gamma\text{Fe}_2\text{O}_3$ nanoparticle (0.21 nm) corresponds to the (400) inter-planar distance of fcc (spinel structure) $\gamma\text{Fe}_2\text{O}_3$. Such a structure would form because of the epitaxial growth of one domain over the other. It is noteworthy that the dumbbell morphology was not seen when Fe and Pt precursors were decomposed simultaneously, instead spherical FePt nanoparticles were obtained.

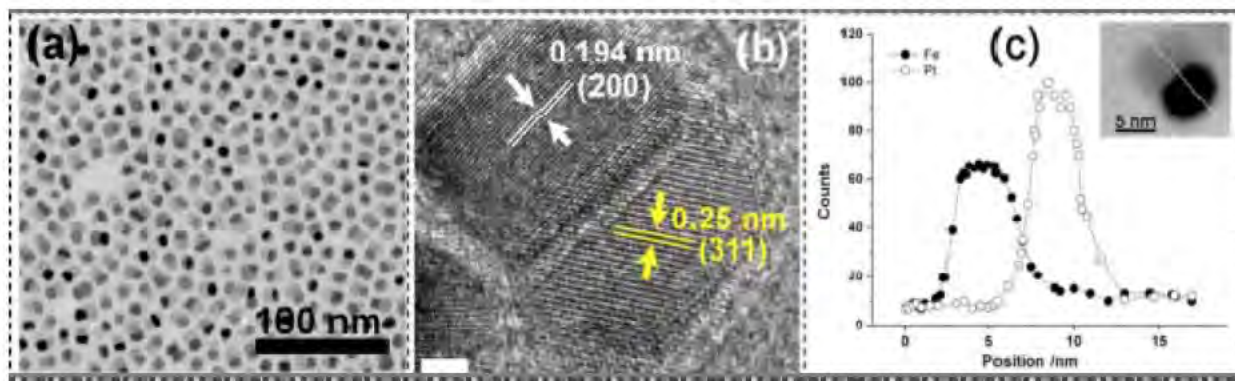


Figure 5: TEM image of (a) Pt- Fe_2O_3 hybrid nanoparticles in cubic morphology, (b) HRTEM of one of the particles in 'a' and (c).

A typical reaction mechanism for FePt formation involves the formation of a Pt rich seed cluster, on which Fe atoms nucleate and then diffuse into the cluster [9]. However, when the Fe precursor was decomposed in a reaction, the mixture populated with Pt nanoparticles, and the Fe atoms would nucleate at Pt sites and grow independently. By varying molar ratios of OY to OA during reaction, Pt- $\gamma\text{Fe}_2\text{O}_3$ particles were synthesized with a cubic morphology. When the OA concentration was reduced during the reaction, cubic Pt nanoparticles were obtained, as shown in Figure 5a. OY is known to bind more strongly onto the {100} facets of fcc metals [10], which resulted in faster growth in the $\langle 111 \rangle$ direction,

reducing the {111} facet areas, and hence leaving a cubic particle. When $\text{Fe}(\text{CO})_5$ was decomposed in the presence of cubic Pt nanoparticles, dumbbell-shaped $\text{Pt-}\gamma\text{Fe}_2\text{O}_3$ nanoparticles of cubic morphology were obtained (see Figure 5a). A flat interface between Pt and $\gamma\text{Fe}_2\text{O}_3$ indicates epitaxial growth of $\gamma\text{Fe}_2\text{O}_3$ over Pt cube [11]. In the case of epitaxial growth, the interface should be flat (as seen in Figure 5b), however, the other directions are not restrained.

The effect of the dumbbell-like $\text{Pt-}\gamma\text{Fe}_2\text{O}_3$ morphology on the magnetic properties of $\gamma\text{Fe}_2\text{O}_3$ was studied by conducting systematic magnetometry on the dumbbell and Pt-etched $\gamma\text{Fe}_2\text{O}_3$ nanoparticles. By chemically etching away Pt, we managed to obtain a sample composed solely of $\gamma\text{Fe}_2\text{O}_3$. Figure 6 shows the ZFC-FC M-T curves under an applied field of 100 Oe for the $\text{Pt-}\gamma\text{Fe}_2\text{O}_3$ nanoparticles (Fig. 6a) and Pt-etched $\gamma\text{Fe}_2\text{O}_3$ nanoparticles (Fig. 6b). The T_B is identified as the peak temperature of a ZFC M-T curve. For the $\text{Pt-}\gamma\text{Fe}_2\text{O}_3$ nanoparticles, the T_B is about 85 K and is shifted to a significantly lower value of 44 K for the Pt-etched particles. This experimental observation indicates that either (i) interactions among Pt and $\gamma\text{Fe}_2\text{O}_3$ domains within each $\text{Pt-}\gamma\text{Fe}_2\text{O}_3$ particle yield magnetic frustration, which increases the effective blocking temperature of $\gamma\text{Fe}_2\text{O}_3$ in the dumbbell morphology, or (ii) there is an enhanced value of the anisotropy energy per unit volume of $\gamma\text{Fe}_2\text{O}_3$ in the dumbbell morphology ($\text{Pt-}\gamma\text{Fe}_2\text{O}_3$) with respect to that of the Pt-etched $\gamma\text{Fe}_2\text{O}_3$ nanoparticles with the same magnetic volumes [12].

To quantify the interactions among $\gamma\text{Fe}_2\text{O}_3$ nanoparticles in the two different morphologies, we have carried out ac susceptibility measurements at various frequencies under 10 Oe applied magnetic field. Figures 7(a) and 7(b) show the real part of ac susceptibility (χ') as a function of temperature for the $\text{Pt-}\gamma\text{Fe}_2\text{O}_3$ and Pt-etched $\gamma\text{Fe}_2\text{O}_3$ nanoparticles. For both systems, it can be seen that the peak associated with the blocking transition increases in temperature with an increase in frequency, which is consistent with typical nanoparticle behavior [10]. In order to probe the spin dynamic behavior, we have fitted the T_{max} of the $\chi'(T)$ to the Néel-Arrhenius (NA) and Vogel-Fulcher (VF) models of relaxation. According to the Néel theory of superparamagnetism, the magnetic moments of non-interacting particles thermally fluctuate between two energy minima and the anisotropy energy creates two potential wells separated by the energy barrier [13]. The relaxation time (τ) for the over-barrier rotation can be written as

$$\tau = \tau_0 \exp \frac{E_a}{k_B T_B}, \quad (1-1)$$

where E_a is the anisotropy barrier energy needed to overcome the moment rotation, T_B is the blocking temperature and τ_0 is the relaxation time 10^{-9} - 10^{-12} s. Fitting Eq. (1) to χ' yielded an unphysical value of

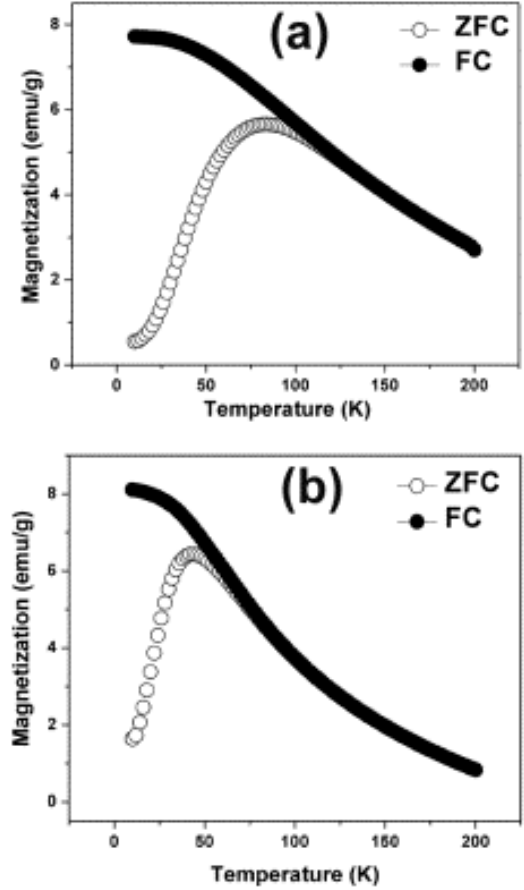


Figure 6: Magnetization dependence upon temperature in ZFC and FC protocol for dumbbell (a) and etched (b) nanoparticles.

τ_o , indicating that particles' dynamics cannot be explained by the non-interacting model. Thus, particles' interactions were further probed by the VF model for weakly interacting particles, described as Eq. (1-2)

$$\tau = \tau_o \exp\left[\frac{E_a}{k_B (T - T_o)}\right] \quad (1-2)$$

where T_o is the characteristic temperature, which gives a qualitative measure of the inter-particle interaction energy.

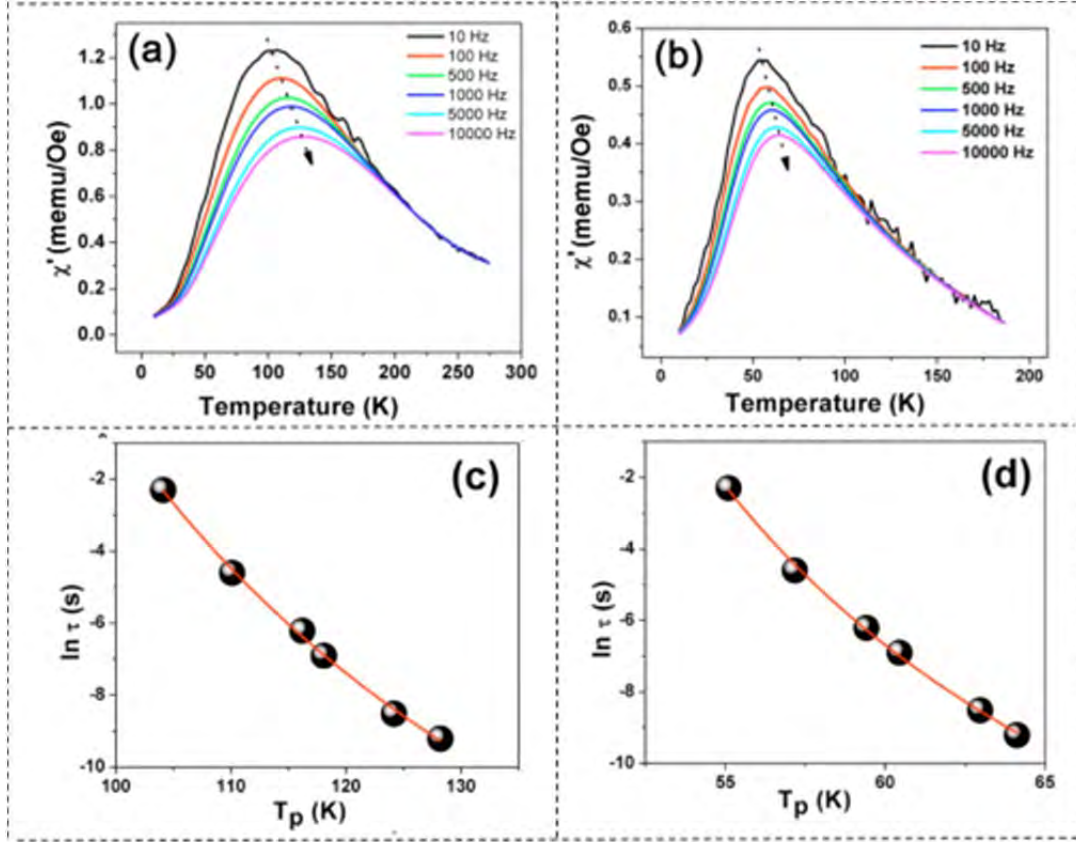


Figure 7: Real part of ac susceptibility data for dumbbell (a) and Pt-etched (b) nanoparticles. The lower panel shows Vogel-Fulcher fitting to T_m of χ' for dumbbell (c) and etched (d) nanoparticles.

The VF model fitted well to the χ' data of both dumbbell (Pt- $\gamma\text{Fe}_2\text{O}_3$) and Pt-etched $\gamma\text{Fe}_2\text{O}_3$ particles indicates the presence of weak inter-particle interactions. The best fit values of the relaxation time, (τ_o) for dumbbell and etched particles are 1.6×10^{-12} s and 8.4×10^{-11} s, respectively. The parameter associated with magnetic anisotropy energy, E_a/k_B , was used to estimate the effective anisotropy constant K_{eff} ($E_a = K_{eff}V$). The calculated value for the dumbbell particles was found to be 3.2×10^6 erg/cm³, which is shifted to 5.2×10^5 erg/cm³ after etching of Pt. This experimental observation indicates that there is an enhancement of effective anisotropy for our nanoparticles in the dumbbell morphology, and such a significant increase in the K_{eff} would have caused the enhancement of T_B as well. Based on these results, it is concluded that Pt plays an essential role in the enhancement of the effective anisotropy of Pt- $\gamma\text{Fe}_2\text{O}_3$ dumbbell nanoparticles. Orbital hybridization, strain due to lattice mismatch, and inverse magneto-restriction effects may also induce interfacial anisotropy in multilayered hybrid structures, and hence,

enhance the effective anisotropy of the system [14]. In a multilayer system of Ni and Pt, X-ray magnetic circular dichroism (XMCD) studies have shown that at the Ni/Pt interface, Pt acquires a large induced magnetic moment ($\sim 0.29 \mu_B/\text{atom}$) that decays sharply from the interface on the Pt-side.

In conclusion, we have found out the mechanism for growth of dumbbell-like Pt- $\gamma\text{Fe}_2\text{O}_3$ nanoparticles with controlled size and shape. The hybrid nanostructures of Pt and $\gamma\text{Fe}_2\text{O}_3$ can be used as an extra degree of freedom to control magnetic properties for potential applications in memory storage devices and biomedicine, and their unique morphology can serve as both magnetic and optical probes for radiation therapy and diagnosis. The results featuring these important findings have been reported in *Journal of Materials Chemistry C* 2013.

1.3. Synthesis and characterization of magnetic core-shell nanostructures:

Controlled growth of shape and size variant core-shell FeO/Fe₃O₄ nanoparticles: Over the past few decades, iron oxide nanoparticles have been widely explored because of their potential applications in various fields, including storage media, environmental remediation, and as multifunctional clinical tools. However, recently much attention has been paid to wüstite (FeO) nanoparticles because of their interesting defect-related magnetic properties and their ability to transform to different phases of nanostructures when processed chemically or thermally [15]. At room temperature, the formation of FeO is only possible at the nanoscale due to the large contribution of surface energy in nanoscale materials. In order to attain stability of FeO nanoparticles, one possible approach is to manipulate surface energy contribution by varying the size and shape of the nanoparticles. It is well-known that different shapes of nanoparticles can introduce electronic and optical properties that are different from those observed in their spherical counterparts. Furthermore, nanoparticle's shape plays an important role in determining magnetic properties. Because of higher symmetry of the fcc crystal structure for iron oxide crystals, isotropic morphologies (spheres, octahedrons, cuboctahedrons) are much easier to synthesize. In order to synthesize anisotropic morphologies (eg. octopods and rods), the seed structure must be manipulated by varying the free energy of the crystal lattice.

In this project, we have performed a systematic study of the shape and size control of FeO nanoparticles by varying parameters in the chemical reaction [16]. Furthermore, we have investigated the exchange coupling phenomena in core/shell structured FeO/Fe₃O₄ nanoparticles. Our findings give direct evidence that during the initial stage of FeO nanoparticle formation, the seeds adopt a cuboctahedral morphology (wolf theorem). In the growth step, competitive growth rates of {111} and {100} facets can be used to tune the final shape of these nanoparticles. This is of practical importance, as such nanostructures can be ideal for use in applications where their anisotropic magnetic properties can be controlled using an “exchange bias” mechanism.

Figure 8 shows TEM images of all the shapes obtained in this work along with selected area diffraction pattern from area shown in Figure 8(a) with different reaction conditions used for synthesis of nanoparticles with different shapes. Depending upon the reaction conditions, particles adopt a cubic, spherical, octopodal, triangular, rod or cuboctahedral shape. When the OA/OY ratio decreases from 1 (so that there is more OY than OA in the system), particles' shape varies from cubic to spherical. Additionally, when 1,2-hexadecanediol was added to the reaction mixture with a concentration of 15 mmol, while keeping the OA/OY ratio to 1, cuboctahedral shaped particles were observed. The use of surfactants as a reaction solvent together with changing the OY/OA molar ratio were found to be another way to control particles' shape. With an OA/OY ratio of 0.4, particles have spherical shape. When this

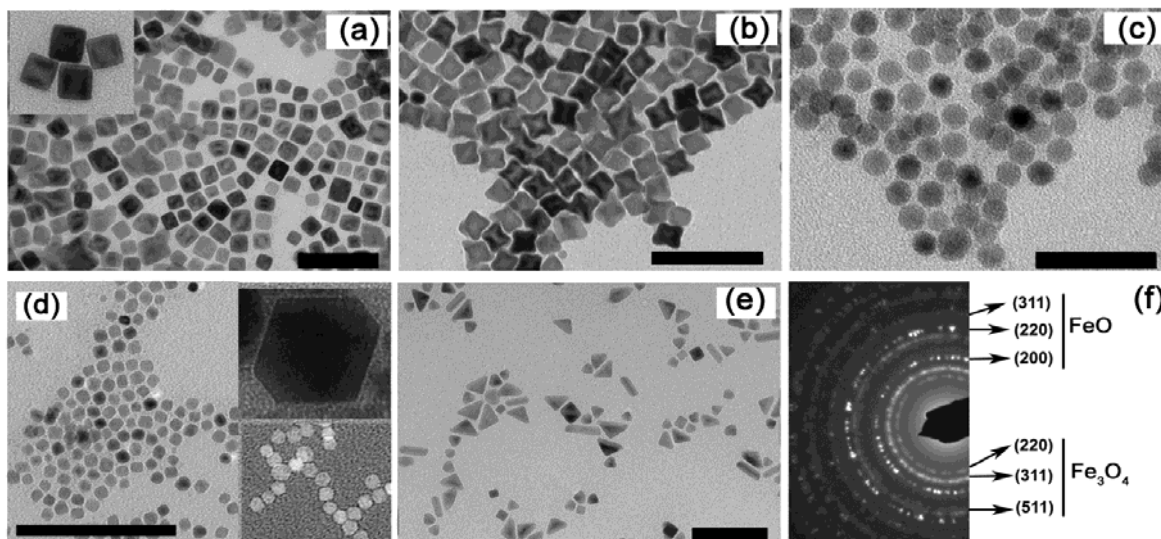


Figure 8: Formation of cubical (a), octopod-cubic (b), spherical (c), octahedral/cuboctahedral (d), triangular/hexagonal nanoplates and faceted rods/beams shape nanoparticles (e) and the selected diffraction from cubic particles (f). The inset of (a) and (d) shows zoom-in view of cubes and octahedrons. The scale bar is 100 nm.

ratio was increased to 1, while fixing all the other parameters, the resulting particles had an octopodal shape. Furthermore, the formation of octopods was also observed when the solvent concentration was reduced to half, and also when the precursor and surfactant concentration was doubled. Another reaction parameter that was studied was the precursor decomposition time, which was varied from 10°C/min to 2°C/min in order to control the reaction kinetically instead of thermodynamically. A slower reaction rate appeared to favor the formation of rods and triangular particles.

The composition and crystallographic phase of nanoparticles was studied from their XRD and selected area diffraction (SAD) analysis. Figure 9a shows the XRD plot of cubic nanoparticles. It can be seen that all peaks correspond to the characteristic reflections of the wustite phase of iron oxide (FeO JCPDF #46-1312), FeO, with the same intensity ratios as its bulk powder counterpart. The XRD micrographs for octopods and spheres also showed a similar crystallographic structure, with the exception of estimated grain size. The grain sizes were calculated from XRD using Scherrer's formula for cubes (20

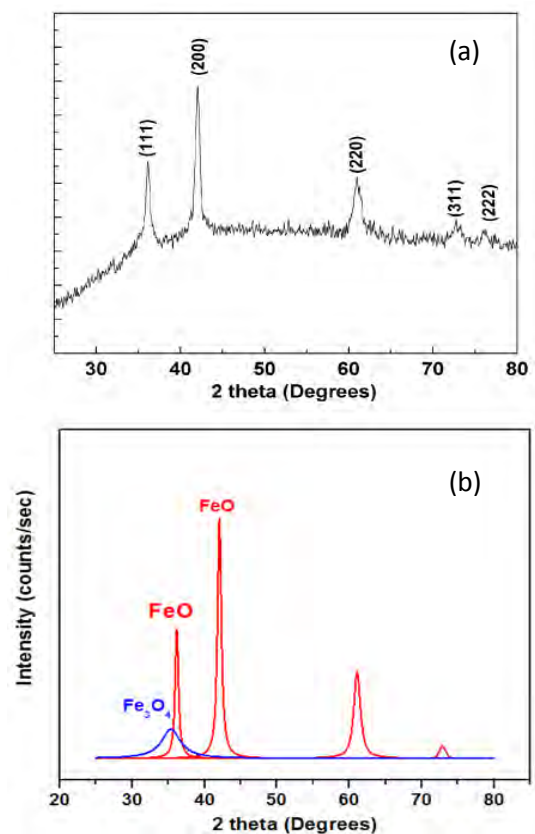


Figure 9: (a) XRD micrograph of FeO nanoparticles and (b) deconvoluted parts of the fitted curve.

nm), octopods (25 nm) and spheres (16 nm) and match well to the sizes obtained from TEM, indicating that each particle is single crystalline in nature. When the XRD data of the various nanoparticle samples were analyzed, it was deconvoluted into its constituents using an X-Fit program (a graphical X-ray line profile fitting program XFIT that integrates the familiar Pseudo Voigt and Split Pearson functions). It is observed that all prominent x-ray peaks are the peaks from FeO (Figure 9b). However, there is a broad peak at 2-theta $\sim 35.5^\circ$ that appears as a shoulder, superimposed on the sharp crystalline FeO (111) peak; this indicates the presence of Fe₃O₄. It is most likely that the particle's surface started oxidizing to Fe₃O₄ giving rise to a core/shell type morphology, due to the metastability of FeO at room temperature.

We have also carried out HRTEM studies on different shapes of FeO nanoparticles to determine the crystallinity, homogeneity and facet orientations. The HRTEM studies of the cubic nanoparticles revealed their single crystalline nature as the lattice fringes continued uninterrupted throughout the nanoparticle. Additional information about the structure and composition of the nanocubes can be obtained through detailed analysis of HRTEM images. HRTEM image (Figure 10) of a nanocube along [001] zone axis along with corresponding fast Fourier transform (FFT) shows that cubic particles are bounded by {100} facets with some {110} truncation at the corners. The distance between lattice fringes is measured to be 0.208 nm which corresponds to (200) FeO. It is worth mentioning that this distance (0.208 nm) is close to the (400) lattice planes of Fe₃O₄. The main direction $\langle 100 \rangle$ is indicated on the image (Figure 10), as well as the measured inter planar distance of 2.98 Å, which is identified as the separation between (220) planes in magnetite. The particles exhibit core/shell-type morphology with FeO as the core and Fe₃O₄ as the shell, according to XRD data. In the case of spherical particles with a core/shell-type morphology, the inner contrast variation is more pronounced. The selected area diffraction (SAD) pattern from these spherical particles indicates that all diffraction rings correspond to the characteristic reflection from FeO and Fe₃O₄ reflection. It is very clear that the diffraction rings from Fe₃O₄ are broad and uniform whereas diffraction rings from FeO are bright and sharp. This is due to the difference in grain size of the two phases. Since we did not see indication of bimodal size distribution, the broader reflections from Fe₃O₄ must be from the shell of the nanoparticles. It should be noted that HRTEM imaging does not allow us to distinguish between the core and the shell in this system, because the shell grows epitaxially over the core, and the crystal structure of FeO and Fe₃O₄ are similar.

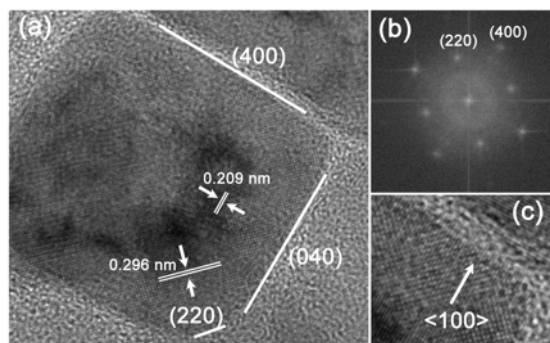


Figure 10: HRTEM of cubic nanoparticles (a) and the corresponding FFT (b). The arrow indicates the $\langle 100 \rangle$ direction in (c).

An octopod can be imagined as a truncated cube with eight tetrahedrons at the corners along the [111] direction. Such a structure would be preferably formed because of the overgrowth of {111} than the {100} facets. An HRTEM image of 30 nm (diagonal length) octopod-shaped nanoparticles is shown in Figure 11. It is obvious that the octopods are single crystalline as their corresponding FFT along the [100] projection was observed. The measured distance between adjacent lattice fringes in the core is 0.208 nm, which is close to the lattice spacing of the (200) plane of FeO, whereas this distance is found to be 0.294 nm towards the edge of the particles, which is close to the (220) plane of Fe₃O₄ (0.296 nm).

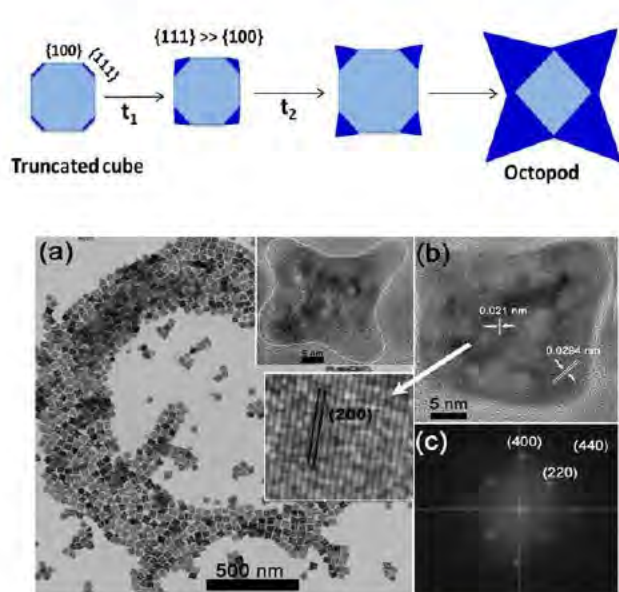


Figure 11: TEM image of octopods (a), HRTEM image of an octopod (b), and the corresponding FFT of the HRTEM image (c). The inset in ‘a’ shows the shape of an octopod with boundaries outlined to highlight its morphology. Schematic of the formation of octopods from cubic particles, where ‘t’ represents the growth time, is illustrated on the top.

This indicates that the octopods also have a core/shell structure with both the core of FeO and shell of Fe₃O₄ being well crystallized, consistent with the results obtained from the XRD analysis. The effect of particle shape on the magnetic properties was studied by conducting

systematic magnetometry studies. Figure 12 shows the temperature dependence of magnetization in the zero-field cooled (ZFC) and field-cooled warming (FCW) protocols within the temperature range of 5 – 340 K under an applied field of 50 Oe for all the samples.

The Neel temperature (T_N) of FeO is found to be ~ 198 K and is marked by a change in slope of the $M(T)$ curves for the samples. Interestingly, below the T_N , a kink is noticed in the ZFC curves, which can be associated with the thermally activated first-order Verwey transition (T_V) ~ 120 K of the Fe₃O₄ shell. In the case of nanoparticles, such first-order transitions are often associated with a structural change and are suppressed due to surface effects and associated stress. It has been noted that the Verwey transition is mostly size dependent; it shifts towards a lower value and eventually vanishes when the size of Fe₃O₄ particles decreased from 150 nm to 30 nm [17]. However, the situation is rather different for the case of FeO/Fe₃O₄ core/shell nanoparticles. As one can see clearly in Figure 12, the T_V appears in all the particle samples with different shapes. This seems to suggest that the T_V is independent of particle shape in the FeO/Fe₃O₄ systems, and that the Fe₃O₄ present in the shell may have better crystallinity than reported in single-component systems of Fe₃O₄. Above the T_N , the magnetization increases and peaks at a particular temperature (T_B), followed by a decrease due to thermal instability of the magnetization. The contribution to magnetization results mainly from the Fe₃O₄ shell, and the T_B can be attributed to the

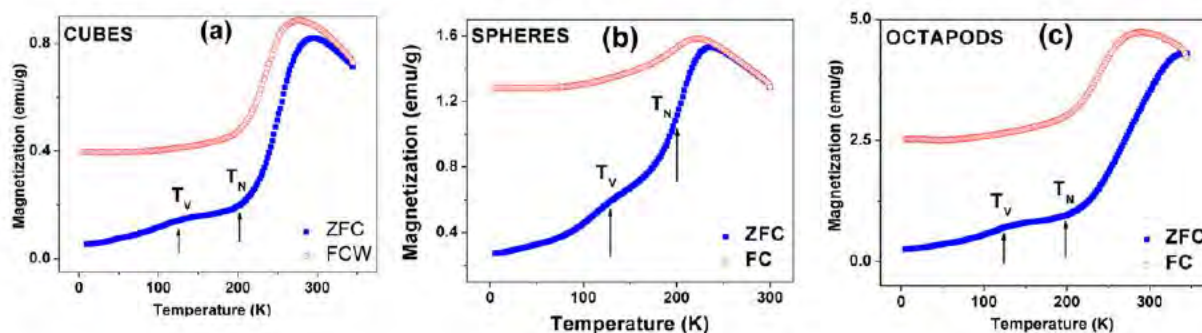


Figure 12: Temperature dependent zero-field cooled (ZFC) and field-cooled warming (FCW) magnetization curves for (a) cubic, (b) spherical, and (c) octopod-shaped FeO/Fe₃O₄ nanoparticles.

blocking of the Fe_3O_4 moments. At the T_B , the thermal energy becomes comparable to magneto-crystalline energy and above this temperature, superparamagnetic behavior sets in. As one can see in [Figure 12](#), T_B depends on the relative volume of the Fe_3O_4 shell and the core/shell $\text{FeO}/\text{Fe}_3\text{O}_4$ morphology.

Finally, we performed EB experiments by cooling down the sample to a low temperature in the presence of a magnetic field and measuring the hysteresis loop. The EB field has been calculated as ($H_{EB} = \frac{|(H^+ + H^-)|}{2}$), where H^+ and H^- are the coercive fields for the ascending and descending curves, respectively. The ZFC and FC hysteresis loops were measured at 5 K for the $\text{FeO}/\text{Fe}_3\text{O}_4$ nanoparticles with different shapes. A step-like feature in the $M(H)$ loop at low field is observed under FC conditions. Such a feature was also observed in core/shell $\text{Fe}/\text{Fe}_3\text{O}_4$ nanoparticles and was associated with the low field switching of the magnetic moments in the Fe_3O_4 shell [18]. It is noteworthy that while the EB has been observed in all $\text{FeO}/\text{Fe}_3\text{O}_4$ nanoparticles, the low-field switching behavior appears to vary with particle shape.

In conclusion, a novel chemical reaction route has been developed for the synthesis of core/shell $\text{FeO}/\text{Fe}_3\text{O}_4$ nanoparticles with controlled size and shape by varying the reaction conditions. We show that depending upon the reaction kinematics and thermodynamics, FeO particles can grow in either isotropic or anisotropic shapes. There is a correlation between particle's shape and reduction mechanism (kinetics or thermodynamics) in the case of $\text{FeO}/\text{Fe}_3\text{O}_4$ and Fe_3O_4 nanoparticles. FeO particles can be oxidized chemically or thermally to form inverse spinel Fe_3O_4 nanoparticles. Following the same synthesis procedure, it is possible to synthesize rods and triangles of Fe_3O_4 by introducing twinings and defects into the crystal structure of the seed. This synthesis process provides an efficient way for fabrication of different isotropic and anisotropically grown iron-oxide nanoparticles for a wide variety of technological applications. These main findings have been reported in *Nanoscale* 2013.

Controlled synthesis and magnetic characteristics of core-shell $\text{Fe}/\gamma\text{-Fe}_2\text{O}_3$ nanoparticles: Manipulating the magnetic anisotropy and exchange coupling in chemically synthesized nanoparticles is extremely important for the advancement of fields as diverse as information storage and biomedical applications [19]. Core-shell $\text{Fe}/\gamma\text{-Fe}_2\text{O}_3$ nanoparticle systems have attracted growing attention due to their outstanding magnetic properties including EB. However, it has remained challenging to fabricate these nanostructures with controlled core diameters and shell thicknesses.

In this project, we have advanced our thermal decomposition technique for the synthesis of $\text{Fe}/\gamma\text{-Fe}_2\text{O}_3$ nanoparticle systems with uniform and tunable particle sizes, and investigated their magnetic properties systematically. Our finding yields new insights into the collective contributions of interface and surface spins to the EB in core-shell nanoparticle systems, knowledge of which is the key to manipulating EB in magnetic nanostructures for spintronics and biomedical applications [18]. Here we will show how to distinguish the spin dynamics of the Fe core and the $\gamma\text{-Fe}_2\text{O}_3$ shell separately, in order to trigger EB in these nanostructures, by performing static and dynamic magnetic measurements on an assembly of ~ 10 nm $\text{Fe}/\gamma\text{-Fe}_2\text{O}_3$ nanoparticles.

[Figure 13](#) (a) shows a conventional bright field TEM image of these nanoparticles along with a (SAD) pattern in the inset. The average size of the nanoparticles is determined to be 9.8 ± 0.7 nm. Contrast variation at the interface clearly suggests a core and shell morphology in these nanoparticles. The (SAD) pattern is indexed to the structure of bcc iron and fcc iron-oxide. HRTEM images (Fig. 13 (b,c)) reveal the crystalline structure of both core and shell with lattice spacing of the core and shell

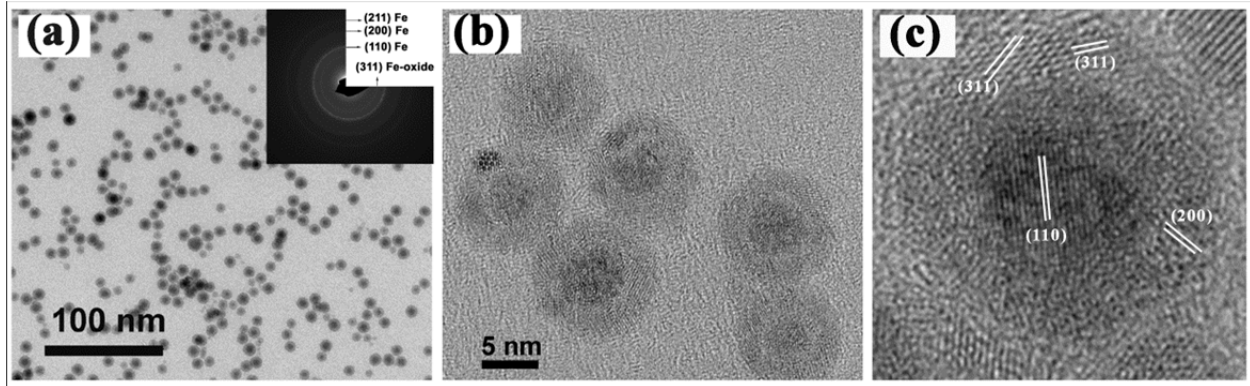


Figure 13: Bright field (a) TEM and (b,c) HRTEM images of Fe/ γ -Fe₂O₃ core-shell nanoparticles. Inset 1(a) shows selected area diffraction (SAD) pattern.

corresponding to (110) planes of bcc iron and (311) planes of fcc iron oxide, respectively. The Fe core is single crystalline. However, the shell of γ -Fe₂O₃ is composed of small crystallites which are oriented randomly.

Figure 14 presents the M-T data measured in 50 Oe under the ZFC, FCW and FCC protocols. In the present case, there exists irreversibility in the ZFC and FCW curves even at room temperature, which suggests the presence of inter-particle interactions or some particles in the blocked state. It has been reported earlier that the FCW magnetization monotonically increases with decreasing temperature for SPMs, while it tends to saturate to a constant value or even decrease with decreasing temperature for super spin glass materials (SSGs). This feature in the FCW curve gives us a first indication that the nanoparticles show a collective glassy behavior at low temperature. There also exists a thermal hysteresis in the FCW and FCC curves below ~ 68 K. The onset of thermal hysteresis is marked by a sharp rise ($\sim T_g$) in $M_{FCC}-M_{FCW}$ as shown in inset (b).

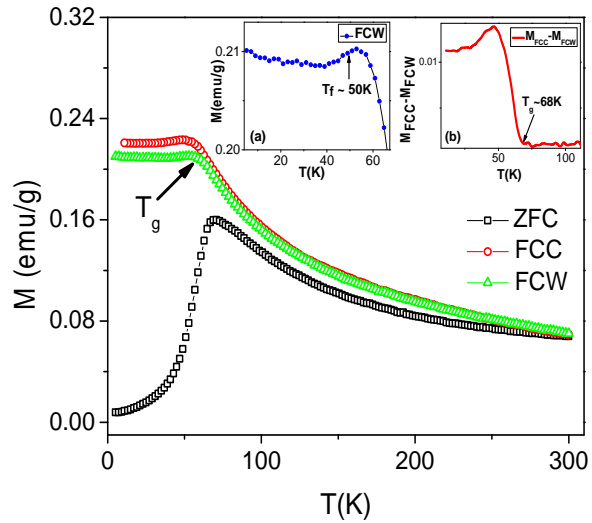


Figure 14: Temperature dependence of magnetization for zero-field-cooled (ZFC -□-), field cooled-cooling (FCC -○-) and field cool-warming (FCW -Δ-). Insets: (a) the dip in M_{FCW} is associated with onset of spin freezing ($T_f \sim 50$ K) and (b) the difference ($M_{FCC}-M_{FCW}$) plotted against temperature, where a sharp rise ($T_g \sim 68$ K) marks the onset of thermal hysteresis.

To probe the spin dynamics of these nanoparticles, ac susceptibility measurements were systematically performed on the sample by applying an AC magnetic field of 10 Oe within the frequency (f) range of 10 Hz-10 kHz. An attempt to fit to the NA model yielded unphysical results. This clearly

indicates that the dynamics of these nanoparticles cannot be explained with a non-interacting particle model. Thus we extended our analysis to the VF model, which takes into account weak inter-particle interactions. The obtained fitted parameters have reasonable values of $E_a/k_B = 571$ K, $\tau_o = 6.9 \times 10^{-13}$ s and $T_o = 48$ K. This successful fit confirms the presence of weak interactions in the nanoparticles that undergo collective freezing at $T_o \sim 48$ K, henceforth referred to as freezing temperature (T_f). The fact that these nanoparticles fall in this range ($\sim 10^{-13}$ s) indicates that they individually relax like SPM particles above blocking temperature. However, in order to understand their collective behavior, the peak temperatures T_p are fitted to a critical power law as

$$\tau = \tau_o \exp\left[\frac{T}{T_g} - 1\right]^{-zv}, \quad (1-3)$$

where T_g is the static spin glass temperature which marks the onset of critical slowing and collective glassy behavior; zv is the dynamical critical exponent which is related to the correlation length ξ that diverges at T_g [18]. The use of such phenomenological activation law is usually done for cluster glass magnetic systems, especially SSG. It is known that for a SSG system, the value of τ_o ranges between 10^{-6} - 10^{-9} s. The obtained fit parameters for our nanoparticles are $\tau_o = 2.8 \times 10^{-7}$ s, $T_g = 68$ K and $zv = 3.8$. The value of zv is very close to that calculated for 3D-Ising model³⁰ and the value of τ_o further strengthens the case for SSG type of behavior.

Now the question that arises is, *at what temperature does the crossover from SSG to SPM occur in the present system?* The answer to this is rather non-trivial. Usually an ensemble of nanoparticles is said to be in the SPM state above the blocking temperature identified as the temperature corresponding to the peak in ZFC curve. This is true for mono-disperse nanoparticles with negligible or no interactions. But, in the case of nanoparticles with finite distribution in size, there is always a precursor effect associated with unblocking of smaller particles at temperatures lower than T_{p-ZFC} . Moreover, the presence of inter-particle interaction and formation of clusters further shifts T_{p-ZFC} to higher temperature. In case of core-shell nanoparticles, since the core and shell are composed of different materials, they have different magneto-crystalline anisotropy, thermal activation, uncompensated spins, lattice strain etc. Hence, all these factors together suggest that T_{p-ZFC} may not be the true blocking temperature, at least in case of core-shell nanoparticles. We define the mean blocking temperature ($\langle T_B \rangle$) as the temperature corresponding to the fastest change in the separation of ZFC from FCW curve, which, in turn is associated with the maximum number of nanoparticles unblocking as the temperature increases. This can be easily determined by identifying the peak position in $\frac{d(M_{FCW}-M_{ZFC})}{dT}$. Figure 15a shows the $M(T)$ curves (left axis) measured at 100 Oe indicating the peak in ZFC curve (T_{p-ZFC}), while on the right axis, $-\frac{d(M_{FCW}-M_{ZFC})}{dT}$ is plotted against temperature whose peak marks $\langle T_B \rangle$ as defined above. Figure 15b shows the magnetic field dependence of $\langle T_B \rangle$, separating the SSG from SPM region.

Furthermore, we find that the freezing temperature $T_f \sim 48$ K as calculated from χ' corresponds to the freezing of the core (T_{f-cr}). Based on the same argument, the maximum at T_2 (~ 21 K) can be attributed to the freezing of shell (T_{f-sh}). This seems reliable since freezing temperature $T_{f-sh} \sim 21$ K is less than the mean blocking temperature of the shell ($T_{B2} \sim 24$ K) calculated from the AT-line fit (Fig. 15b). Thus, we can identify two sets of mean blocking temperatures (T_{B1} , T_{B2}) and freezing temperatures (T_{f-cr} , T_{f-sh}) for the core and the shell respectively (Figure 15c,d). Finally we have investigated the EB in this core-shell system and find that the onset of EB depends on the magnetic state of the core and shell. The

EB is found to develop at the temperature that marks the onset of shell blocking below the freezing

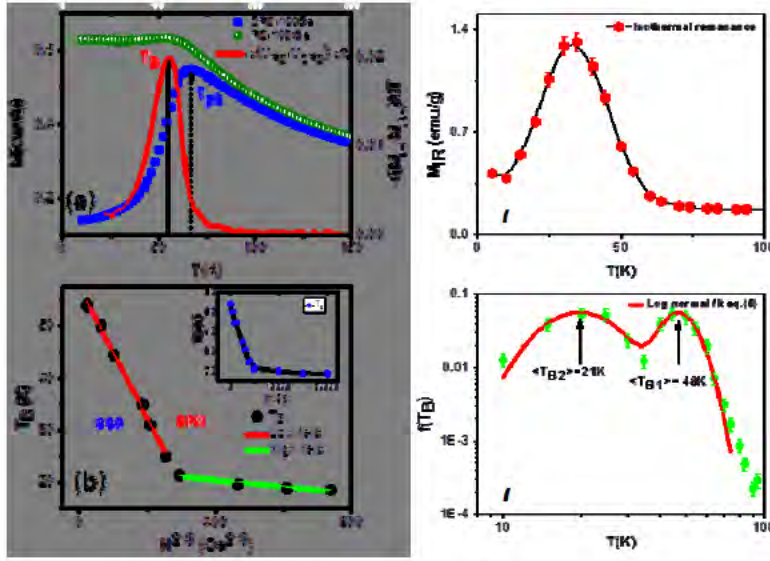


Figure 15: (a) ZFC/FC curve and the derivative $d[M_{FC} - M_{ZFC}]/dT$ indicating peak temperature of M_{ZFC} (T_{pk}) and mean blocking temperature (T_B); (b) Two straight AT-line fits for low and high field regime. Inset shows the evolution of blocking temperature (T_B) with measurement field; (c) Temperature dependence of isothermal remanance (d) Distribution function of T_B .

temperature of the core. These observations open up the possibility of tailoring EB and its onset temperature by suitably choosing different materials for the core and shell that show blocking and freezing phenomena at a desired temperature range. These new findings have been reported in *Physical Review B* 2012.

1.4. Synthesis, functionalization and characterization of magnetic fluids:

Magnetic fluids (or ferrofluids) are colloidal solutions of single domain magnetic nanoparticles (e.g. magnetite) covered with a surfactant (e.g. a long chain polar molecule). Owing to the desirable combination of normal liquid behavior of a solvent (e.g.

water, oil or diester), ferrofluids are technologically important for a variety of applications ranging from biomedicine, hydraulics to power generation [20]. In order to use ferrofluids effectively in such applications, it is essential to understand how the magnetic properties and relaxation mechanism of magnetic nanoparticles vary in different liquid environments.

In this project, we have performed the first comparative study of ferrofluids, with particle blocking and carrier fluid freezing temperatures being close or far apart from each other, yielding evidence for distinctly different behaviors seen in the magnetic response in the liquid, frozen and mixed states [21]. We demonstrate that the physical origins of relaxation peaks in the complex susceptibility or the spin-glass-like cusps in the ZFC magnetization are associated with the particle blocking and carrier liquid freezing effects. Quantitative fits of the frequency-dependent AC susceptibility to the Vogel-Fulcher model clearly delineates the difference in glassy nature in the frozen and mixed states. The blocking effect of magnetic nanoparticles in the frozen state significantly affects the interparticle dipole-dipole interaction, causing spin-glass-like slow dynamics. The coexistence of Néel and Brown relaxations in the mixed and frozen states is observed. A correlation between the blocking temperature of magnetic nanoparticles and the freezing temperature of the solvent in ferrofluids is established [22]. In our study, $CoFe_2O_4$ (mean size, 11 nm), Fe_3O_4 (mean size, 14 nm) and Fe_3O_4 (mean size, 6 nm) nanoparticles were synthesized by a chemical co-precipitation method [22]. These nanoparticles were coated using oleic acid as surfactant. The ferrofluids were prepared by dispersing the particles in hexane and dodecane with room temperature viscosities of 0.294 cP and 1.35 cP, respectively. The freezing point for hexane is ~ 178 K and ~ 264 K for dodecane. These two solvents were chosen to have freezing

points well above and close to the blocking temperature of the nanoparticles, to analyze the blocking and freezing effects on the magnetic properties of ferrofluids as discussed in further detail below. The concentrations of the ferrofluids were approximately 0.2 g/ml. For clarity, we will use the following labels in the rest of the manuscript to refer to specific samples:

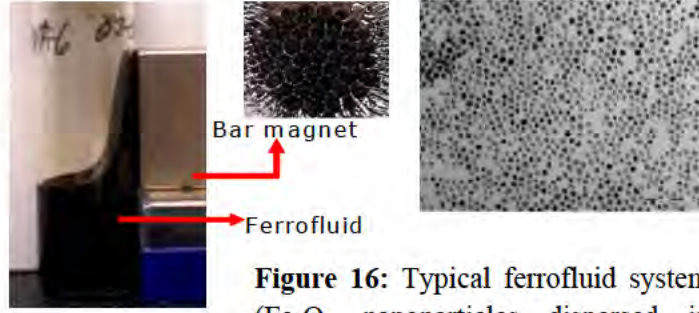


Figure 16: Typical ferrofluid system (Fe_3O_4 nanoparticles dispersed in hexane) synthesized in the project. Photographs on the left show the response of the ferrofluid to a bar magnet. TEM image of 11 nm Fe_3O_4 nanoparticles used in the ferrofluids is also shown.

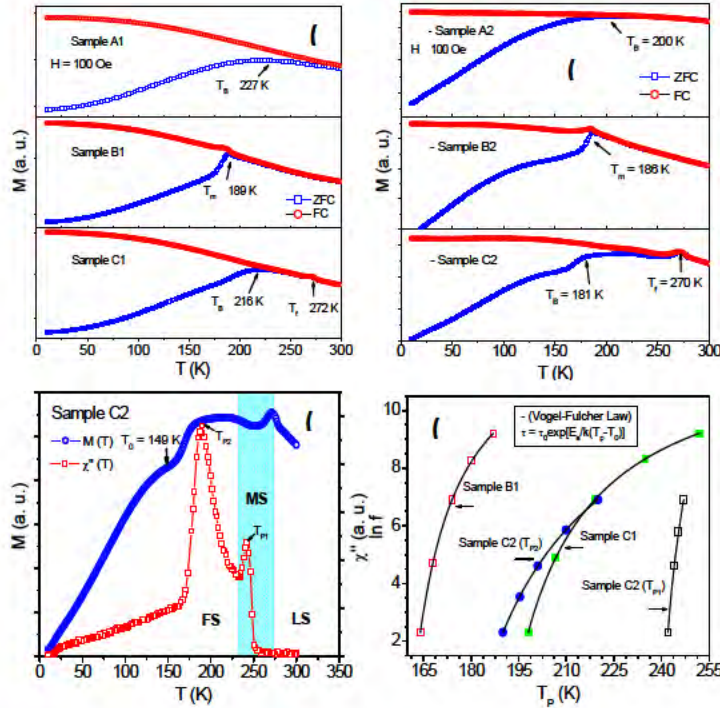


Figure 17: (a) ZFC-FC M-T curves of 11 nm CoFe_2O_4 (a) dry powder (Sample A1), dispersed in hexane (Sample B1) and dispersed in dodecane (Sample C1); (b) ZFC-FC M-T curves of 14 nm Fe_3O_4 dry powder (Sample A2), dispersed in hexane (Sample B2) and dispersed in dodecane (Sample C2); (c) Temperature dependence of ZFC magnetization and imaginary part of magnetic susceptibility, χ'' , of Sample C2 (14 nm Fe_3O_4 in dodecane). LS: Liquid State; MS: Mixed State; FS: Frozen State. T_0 is the temperature at which the system enters a glassy state. T_{p1} and T_{p2} represent the χ'' peaks in the mixed and frozen states, respectively; (d) The best fits of $T_p(f)$ data to the VF model extracted from AC susceptibility of Sample C2 (for the cases of T_{p1} and T_{p2}), Sample B1 and Sample C1.

Sample A1 (11 nm CoFe_2O_4 in dry powder form), Sample B1 (CoFe_2O_4 in hexane), Sample C1 (CoFe_2O_4 in dodecane), Sample A2 (14 nm Fe_3O_4 in dry powder form), Sample B2 (14 nm Fe_3O_4 in hexane) and Sample C2 (14 nm Fe_3O_4 in dodecane), Sample A3 (6 nm Fe_2O_4 in dry powder form), Sample B3 (6 nm Fe_2O_4 in hexane) and Sample C3 (6 nm Fe_2O_4 in dodecane). Figure 16 shows how a magnetic fluid responds to a permanent magnet.

Static and dynamic magnetic measurements performed on all these samples reveal several interesting features; the selected data are shown in Figure 17. We find that for Samples A1 and A2, the relatively broad peak observed in the ZFC curves is consistent with the polydisperse nature of the magnetic nanoparticles with broad particle size distribution. However, the case is very different for the ferrofluids. The ZFC curves exhibit a sharp peak for Samples B1 and B2, while a

small peak followed by the broad curve are observed for Samples C1 and C2. We note that the sharp peak in the ZFC curve observed for Sample A3 is attributed to the monodisperse nature of 6 nm Fe₃O₄ nanoparticles with narrow particle size distribution. As compared to Sample A3, the peak temperature (T_B) shifts to a lower temperature in the cases of Samples B3 and C3.

To understand the physical origins of the above noted peaks, we note that the T_B of magnetic nanoparticles for Sample A1 (~227 K) and Sample A2 (~200 K) are higher than the freezing temperature (T_F) of the hexane (~178 K) but are lower than the freezing temperature (T_F) of dodecane (~264 K). The T_B of magnetic nanoparticles for Sample A3 (~35 K) is much lower than those of both hexane (~178 K) and dodecane (~264 K). This clear distinction in the samples allows us to attribute the observed peaks to the freezing effect of the solvent and the blocking effect of magnetic nanoparticles, respectively. The origin of the cusp at ~270 K for the dodecane ferrofluids (Samples C1 and C2) is solely associated with the freezing of the dodecane (~264 K), while the cusp at ~190 K for the hexane ferrofluids (Samples B1 and B2) results from both the carrier liquid freezing and particle blocking effects. It is the combined freezing and blocking effect that resulted in a sharper change in the ZFC magnetization at ~190 K for Samples B1 and B2. Since the freezing of the carrier liquid abruptly stops physical motion of the nanoparticles and alignment of moments in the field direction, the cusps at ~186 K and ~270 K are sharper compared with that at ~200 K relating to the blocking mechanism of the spins within the nanoparticles which is due to a competition between thermal energy ($k_B T$) and anisotropy energy (KV). For the case of Samples B3 and C3 ($T_B < T_F$), the sharp peaks at ~19 K result dominantly from the particle blocking effect, although the features related to the freezing of the solvent are still observed at high temperatures (~184 K for Sample B3 and ~274 K for Sample C3). We recall that the blocking temperature of magnetic nanoparticles for the powder sample (Sample A3, $T_B \sim 35$ K) is larger than that for the ferrofluids (Sample B3, $T_B \sim 18$ K and Sample C3, $T_B \sim 19$ K). These findings point to the important consequences that the presence of magnetic nanoparticles in the solvent increases its T_F , whereas magnetic nanoparticles dispersed in the solvent possess lower T_B relative to the powder sample. This consistently attributes the broad cusp at ~216 K for Sample C1 (~181 K for Sample C2) to the blocking effect of the nanoparticles. These results shed light on the physical mechanisms behind the spin-glass-like cusps observed in the ZFC magnetization in ferrofluids, and provide important clues for assessing the complex nature of the glassy states in ferrofluids [22].

To correlate the physical origin of the two peaks in the ac complex susceptibility to the freezing and blocking peaks in the ZFC dc magnetization, we carried out AC susceptibility measurements on the ferrofluid samples. We have observed the two characteristic relaxation peaks in $\chi''(T)$ for Samples C1 and C2 with $T_B < T_F$. It has been shown that there exist three characteristic states (e.g. liquid, mixed and frozen states) in a ferrofluid or a solvent [23]. For temperatures above the pour point (T_{pour}) a *liquid* phase exists as the system flows like a fluid, whereas a *solid* phase (or a frozen state) is present at low temperatures below T_{s-m} , and a *mixed* phase exists in the temperature range between T_{s-m} and T_{pour} , where T_{s-m} is the transition temperature from the solid phase to the mixed phase. Importantly, the first peak in χ'' (at high temperature) has been found to belong to the temperature range of $T_{s-m} < T < T_{\text{pour}}$ (in the mixed state), while the second peak in χ'' (at low temperature) to the frozen state. Figure 17c presents an excellent correlation between features in the dc and ac magnetization for Sample C2 in the combined plots. It is inferred that the second peak in $\chi''(T)$ is ascribed to the blocking of magnetic nanoparticles, while the first peak in $\chi''(T)$ is associated with the freezing of the solvent. The first peak reflects the magnetic behavior in the mixed state, while the second peak represents the magnetic behavior in the frozen state. This important finding allows us to correctly classify the two peaks in $\chi''(T)$ as due to

freezing and blocking for Fe_3O_4 ferrofluids with kerosene solvent and for Fe_3O_4 ferrofluids with hexane solvent. We note that it is only our comparative analysis between ferrofluids with varying blocking and freezing temperatures that leads to this clarification of the origin of the peaks and the conclusion would not be apparent just by looking at the data on one type of ferrofluid alone as in the case of past studies.

To clarify the blocking and freezing effects on the glassy behaviors in the mixed and frozen states, we analyze the frequency dependence of the peaks of $\chi''(T)$ by fitting the data using both NA and VF models. Our results reveal that the $\chi''(T)$ data of all ferrofluid samples can be fit using the NA model, but the meaningful fitting parameters are only obtained for Samples B3 and C3 ($\tau_0 = 2.07 \times 10^{-11}$ s, $E_a/k = 3.45 \times 10^2$ K for Sample B3; $\tau_0 = 1.69 \times 10^{-10}$ s, $E_a/k = 4.22 \times 10^2$ K for Sample C3). This suggests that Samples B3 and C3 are non-interacting systems, while the remaining ferrofluids (Samples B1, C1, B2, C2) belong to the class of interacting particle systems for which the NA model is invalid [22]. Figure 17d presents the fitting results for these ferrofluids using the VF model. The best fits for Sample C2 yield $\tau_0 = 1.0 \times 10^{-7}$ s, $E_a/k = 1.38 \times 10^2$ K and $T_0 = 232$ K for the case of the first peak (T_{p1}), and $\tau_0 = 1.77 \times 10^{-6}$ s, $E_a/k = 4.51 \times 10^2$ K and $T_0 = 149$ K for the case of the second peak (T_{p2}). The difference in τ_0 and E_a/k for the cases of T_{p1} and T_{p2} indicates that for the ferrofluid having $T_B < T_F$, the glassy behavior is different in nature between the mixed and frozen states. This is understandable as the magnetic particles are unblocked in the former case, whereas they are already blocked in the latter case. The larger values of τ_0 and E_a/k for the case of T_{p2} indicate that the blocking effect of magnetic nanoparticles on the glassy behavior in the frozen state is simply to cause slowing down of the dynamics of the system. In addition, we find that $T_0 = 232$ K for the case of T_{p1} which coincides with the temperature at which the ferrofluid enters into the frozen state from the mixed state and this transition is the origin of the divergence in the viscosity of the ferrofluid, whereas the divergence of the relaxation time at $T_0 = 149$ K for the case of T_{p2} suggests that the system enters a glassy state at this temperature. In view of these results, we propose that the blocking of magnetic nanoparticles in the frozen state significantly affects the interparticle dipole-dipole interaction, causing characteristic spin-glass-like dynamics. This also allows one to reconcile the observations of spin-glass-like states, magnetic relaxation and aging effect in ferrofluids [21,22].

Finally, we attempt to clarify the relaxation mechanisms in the frozen and mixed states by investigating the frequency dependence of the complex susceptibility. We have observed the $\chi'(f)$ curves at three different temperatures for two representative ferrofluids (Sample B2 and Sample C1), as shown in Figure 18. We consistently note that for ferrofluids having $T_B > T_F$ (Sample B2), a double slope feature in $\chi'(f)$ is observed in the mixed state which evidently

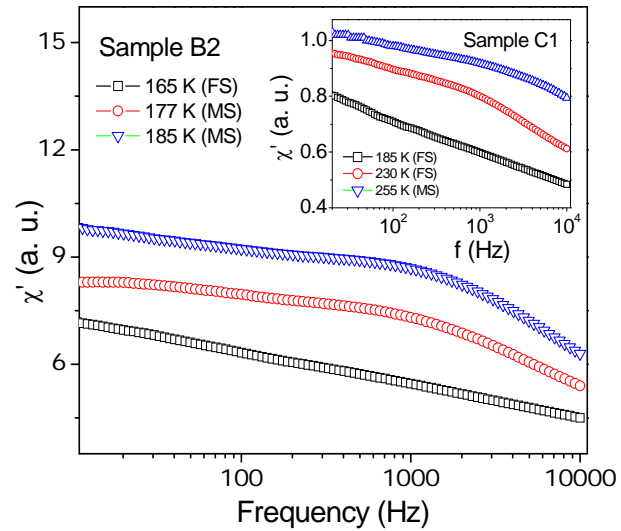


Figure 18: Real part of magnetic susceptibility, χ' , as a function of frequency of Sample B2 in the mixed state (at 177 K and 185 K) and in the frozen state (at 165 K). The inset shows the $\chi'(f)$ curves of Sample C1 in the mixed state (at 255 K) and in the frozen state (at 185 K and 230 K).

indicates coexistence of both Brownian and Néel relaxation in this state, while $\chi'(f)$ shows only a linearly monotonic decrease in the frozen state, signifying the presence of Néel relaxation only. For the ferrofluids having $T_B < T_F$ (Sample C1), the non-monotonic, double slope feature in $\chi'(f)$ is observed at temperatures above T_B even in the frozen state, and $\chi'(f)$ only shows a linear feature as the temperature is lowered below T_B . This indicates the presence of Brownian relaxation in addition to Néel relaxation even in the frozen state in the ferrofluids having $T_B < T_F$. This trend seen in our samples is consistent with the recent observation that thermal motion of magnetic nanoparticles in ferrofluids continues well below the freezing temperature of the solvent or in the frozen state [5]. These important findings have been reported in *Journal of Applied Physics* 2009 and *Physics Express* 2010.

1.5. Controlled synthesis and characterization of FeCo and core/shell Fe- γ -Fe₂O₃ nanoparticles for MRI contrast enhancement:

Iron and iron-cobalt alloy nanoparticles exhibit much higher magnetic moments than those of iron-oxide of comparable size, due to intrinsic magnetic properties. Therefore, recent efforts have been devoted to the synthesis and functionalization of iron-cobalt and iron nanoparticles with high magnetic moments [3,19]. However, not much attention is paid to controlling the size and shape of these nanoparticles during synthesis.

To address this important issue, in this project we have advanced the chemical method based on high temperature reduction of organometallic compounds for the first-time synthesis of cube-shaped iron-cobalt alloy nanoparticles with controlled size and composition. In order to achieve biocompatibility and water dispersibility, pluronic-F127 (PEO-PPO-PEO) triblock copolymer was used for surface modification of nanoparticles via physical adsorption. The hydrodynamic particle size was measured using a dynamic light scattering technique, which showed an average increase of 20 nm in the particle size after surface functionalization. In-vitro T_2 contrast studies were performed using a 7 Tesla Agilent ASR 310 MRI scanner. Changes in T_2 -contrast are evident in the T_2 -weighted image, and show the potential utility of these nanoparticles as negative contrast agents. We present below selected results that highlight the usefulness of these nanostructures for biomedical applications.

Figure 19a shows the XRD pattern of FeCo nanoparticles taken from dry particles on a silicon substrate. Strong FeCo reflections of (110), (200) and (211) planes were observed. No reflections were

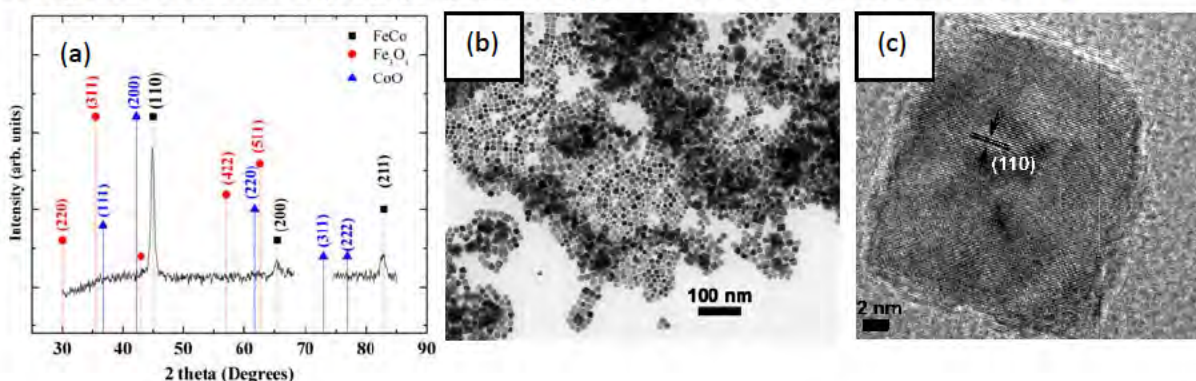


Figure 19: (a) XRD pattern of nanoparticles corresponding to FeCo alloy crystal structure without any oxide phases present. The scan at 2 theta = 68-73° is removed to avoid the sharp peak from the Si substrate at 2 theta = 69°; (b) Bright Field TEM image of FeCo nanoparticles, capped with OA and OY and (c) HRTEM of one the particles.

observed from Co, Fe and their oxides. The grain (crystalline) size was calculated to be 20 nm from XRD using the Scherrer's formula ($0.9\lambda/\beta\cos\theta$). Separately, the particle size was determined from transmission electron

microscopy (TEM) micrographs by counting more than 200 particles. Figure 19b shows a TEM image of the OA- and OY-capped FeCo nanoparticles. Particles show a clear cubic shape with an average size 20 ± 1.5 nm. The close correspondence between particle size determined from TEM and calculated from XRD indicates that particles are single crystalline. Further high-resolution TEM (HRTEM) images also reveal the single crystal structure in these nanoparticles (Figure 19c). Elemental analysis using energy dispersive X-ray (EDX) spectroscopy revealed that particles are composed of 52 % atomic Fe and 48 % atomic Co.

It is seen that when OY was replaced with trioctyl phosphine (TOP) during synthesis, while keeping the molar concentration the same, the average particle size was reduced to 15 nm, while a broad particle size distribution was introduced. In addition, particle shape also became non-uniform with a predominantly spherical shape (Figure 20a). It is well known from literature that the nucleation rate plays a very important role in obtaining particles of a uniform shape and size. A single rapid nucleation event favors particle growth with a uniform size and shape, whereas in the case of a slower nucleation rate, reactants are unevenly depleted from solution, leading to variations in growth rate for seeds formed at different times. It is likely that the use of TOP slows the nucleation rate and hence, both particle size and shape appeared non-uniform. Particle composition also varies from 52% to 60% atomic Fe (with 48% to 40 % atomic Co) when OY is replaced with TOP, as concluded from the EDX analysis.

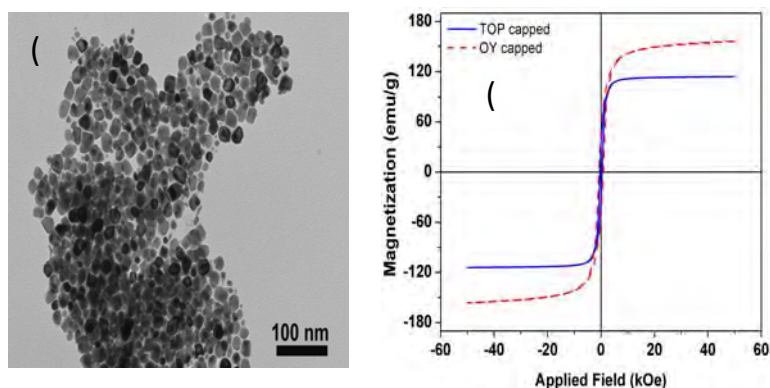


Figure 20: (a) Bright field TEM image; (b) Hysteresis curves for OY and TOP-capped FeCo particles.

Figure 20b shows the M-H curves measured at 300 K for the OY and TOP capped particles. The OY capped particles have a room temperature magnetization above 160 emu/g where as TOP capped particles show a room temperature magnetization of 120 emu/g. This effect could be due to the presence of small nanoparticles, which

are in the superparamagnetic regime. This is further evidenced by the reduced coercivity in TOP capped particles, when compared to OY capped particles. The non-collinearity of magnetic moments on the particles' surface, combined with spin canting, could have caused a lower magnetic moment in the case of small particles [18]. It is worth mentioning that this value is estimated without correction for the surfactant present at the surface of the particles. The iron nanoparticles were synthesized by the thermal decomposition in an inert atmosphere in the presence of OA and OY. These particles exhibit a core/shell morphology where core is single crystalline bcc iron and shell is composed of randomly oriented iron oxide crystallites.

The hydrocarbon chains from OA and OY make these OA/OY coated particles hydrophobic and they are soluble only in nonpolar or weakly polar solvents via steric repulsions. However, for biomedical applications, these particles must be water dispersible and stable under various conditions, such as at pH ranging from 5-9, under salt concentrations of up to a few hundred mmol/L and at temperatures up to 95°C. This can be achieved by surface functionalization (phase transformation) of hydrophobic nanoparticles by depositing hydrophilic agents (polymers, surfactants) at the particle's surface or by ligand exchange.

In the first approach, a double layer structure forms over the surface of nanoparticles due to hydrophobic interaction between hydrocarbon chains, and immobilizes the new ligand with a functional group over the original surfactant shell. Such kind of surface functionalized particles can be dispersed in various solvents, depending upon the functional group of modifying ligand. A common example of such a ligand is pluronic (F-127) copolymer. In the second approach, strong chemical interactions between the nanoparticle surface and modifying ligand causes the replacement of the original surfactant (OA, in our case) with the newly added one (F-127, in our case). The functional group at the other end of the ligand provides water dispersibility via electrostatic repulsion. F-127 is known to reduce the adsorption of proteins and adhesion of cells onto surfaces, and hence increase biocompatibility and solubility of hydrophobic drugs. It is made from two chains of polyethylene oxide (PEO) and one chain of polypropylene oxide (PPO) in a PEO-PPO-PEO PEO-PPO-PEO triblock copolymer configuration. Previously F-127 has been reported to obtain water dispersibility of magnetite nanoparticles. [Figure 21a](#) shows relative signal intensity due to presence of nanoparticles, modifying the T_2 relaxation. The blue line represents the T_2 relaxation of water, while the red line represents the T_2 relaxation in the presence of nanoparticles. The proximity of such nanoparticles to water molecules shortens the T_2 relaxation of water protons, yielding lower intensity over the relaxation time. Core/shell structured Fe/ γ -Fe₂O₃ nanoparticles of average size 10.2 ± 1.5 nm were used for T_2 -Weighted MR Imaging (Fast Spin Echo), with TR = 3196 ms, and TE = 8.31 ms using a 7 Tesla Pre-clinical MRI scanner ([Figure 21b](#)).

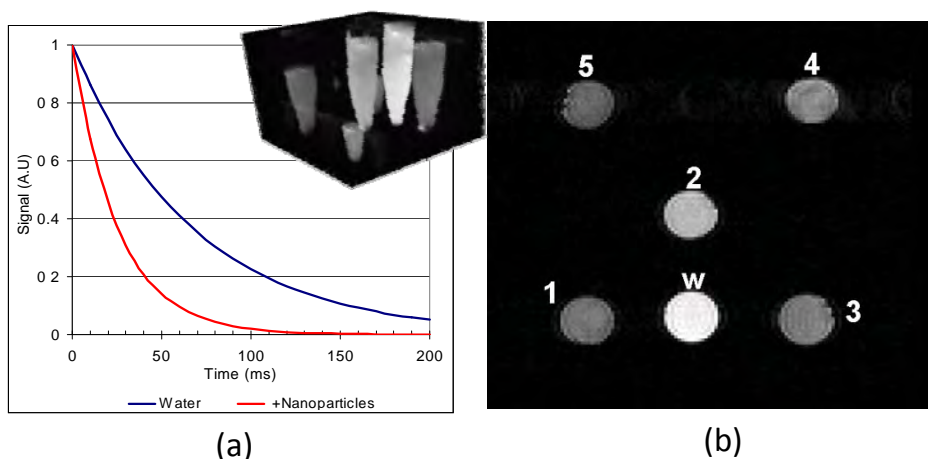


Figure 21: Theoretical nanoparticle induced negative contrast (left panel); T_2 -weighted phantom image displaying negative contrast agent concentration dependence of transverse relaxation (right panel). The concentration of particles in each tube is **1 = 20 $\mu\text{g/ml}$, 2 = 10 $\mu\text{g/ml}$, 3 = 25 $\mu\text{g/ml}$, 4 = 42 $\mu\text{g/ml}$, 5 = 55 $\mu\text{g/ml}$, W = 0 $\mu\text{g/ml}$ (water only).**

In conclusion, we have successfully synthesized shape-controlled FeCo nanoparticles possessing high magnetic moment by thermally decomposing Fe-acac and Co-acc without any partial oxidation. The water dispersibility and biocompatibility of the oleate-coated particles can be obtained via surface modification with F-127, which is known to be adsorbed at

the particles' surface via Van der Waals interactions between the aliphatic chain of (OA) and the hydrophobic part (PPO) of pluronic. Measurements of the transverse relaxation time T_2 of the core/shell $\text{Fe}/\gamma\text{Fe}_2\text{O}_3$ nanoparticle solution at 7 Tesla with varying concentration confirms that these particles are an excellent T_2 contrast agent for use in magnetic resonance imaging (MRI).

1.6. Magneto-inductive heating measurements of ferrofluids containing functionalized magnetic nanoparticles for hyperthermia applications:

Hyperthermia is a type of cancer treatment in which body tissue is exposed to high temperature, using external and internal heating devices. Research has shown that high temperature can destroy or kill cancer cells while having negligible influence on healthy tissues [23]. The human body naturally uses heat to fight disease. For example, when viruses and bacteria proliferate at normal body temperatures, the body defends itself by increasing its temperature to slow the rapid multiplication of such disease-causing agents. This phenomenon is referred to as a fever. The body temperature can also be elevated for therapeutic reasons. Cancer cells are more temperature-sensitive as compared to their normal body cells. So when the temperature of a cancer-affected body is raised above 42 °C, the cancer cells start getting destroyed. This approach can destroy tumors with minimal damage to healthy tissues and, therefore, limit negative side effects. Magnetic hyperthermia is based on the phenomenon that magnetic nanoparticles subjected to an alternating magnetic field can produce heat high enough to destroy cancer cells when magnetic nanoparticles are localized at the tumor site.

During this project, we have successfully set up a new magneto-inductive heating system in our lab at USF for hyperthermia studies of specimens containing magnetic nanoparticles. Magneto-inductive heating measurements were performed on various forms of magnetic nanoparticles and their solutions. We report below selected results of magneto-inductive heating of functionalized Fe_3O_4 nanoparticles having three different shapes (spherical, cubic and octopod), demonstrating the important role of particle shape in tuning the magnetic properties of nanoparticles for biomedical applications. Figure 22 shows TEM images of (a) spherical Fe_3O_4 particles with an average size 12.5 ± 1.1 nm, (b) cubic Fe_3O_4 particles with an average size 20.1 ± 1.5 nm and, (c) octopod-shaped Fe_3O_4 with an average size of 25.2 ± 1.8 . The synthesis of these particles has been described earlier in Section 1.1 of this report. To make the nanoparticles biocompatible as simulated in human body fluid, the particles were transformed into a water soluble state by changing the surfactant ligands via and 11-mercaptoundecanoic acid (MUA, $\text{C}_{11}\text{H}_{22}\text{O}_2\text{S}$). To perform the ligand exchange 1 g of MUA was dissolved in 5 ml of chloroform, 100 mg of Fe_3O_4 nanoparticles dispersed in 5 ml chloroform was added to the first dispersion and a mild stirring was performed for 2 hours. Afterwards, the particles were precipitated with water by centrifuging.

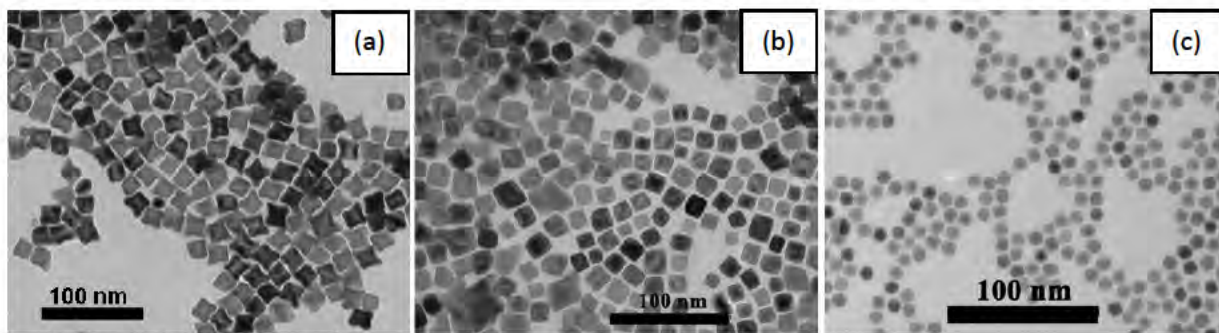


Figure 22: TEM images of (a) Octopod-shaped, (b) cubic, and (c) spherical Fe_3O_4 nanoparticles used for hyperthermia experiments.

To perform inductive heating experiments, MUA coated particles were dispersed in water and a suspension of 1mg/ml was used. In this work we have used 7 turns' coils with an inner radius of 12.5 mm and length of 43 mm. For a 100A current, it can generate 4.6 kA/m, and at 200A it induces 9.2 kA/m AC magnetic fields.

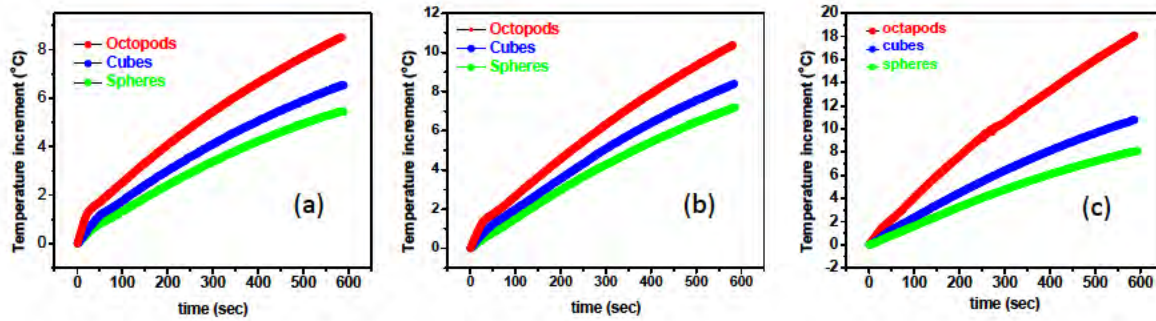


Figure 23: The heating curves for octopods (red solid symbols), cubes (blue solid symbols) and spheres (green solid symbols) shape nanoparticles at 12 KA/m (a), 14 KA/m (b) and 16 KA/m (c) respectively.

The field was applied for 600 s and temperature variation was monitored by inserting a fiber optic temperature probe directly into the specimen (the suspension of Fe_3O_4 particles in water). Figure 23 shows the heating curves for spheres, cubes, and octopod-shaped Fe_3O_4 particles under an applied AC current of (a) 150A, (b) 170A and, (c) 200A, each with a suspension of 1mg/ml H_2O . An applied current of 150A, 175A and 200A would generate AC fields of 12 kA/m, 14kA/m and 16kA/m inside the coil, respectively. It can be seen that the maximum heating obtained is higher with higher current, due to the enhanced magnetic field in the center of coil. For each value of applied field, the heating rate is higher for octopods than those of cubes and spheres. The SAR was calculated for each curve using the equation

$$SAR = \left(\frac{m_s}{m_n} \right) C_p \left(\frac{dT}{dt} \right) \quad (1-4)$$

where m_s and m_n are the masses of the solution and nanoparticles, respectively. C_p is the heat capacity of the dispersion. dT/dt is the initial slope of the heating curve.

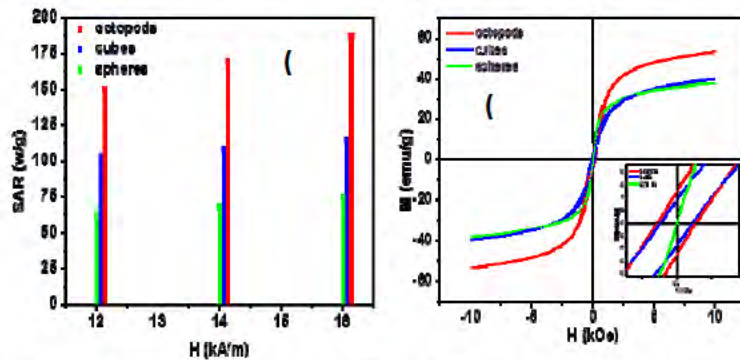


Figure 24: The calculated SAR for the cube, sphere and octopod-shaped Fe_3O_4 nanoparticles at various AC fields (a) and the M-H curves for the corresponding shapes (b).

The calculated SAR is shown in Figure 24 at different current densities and ac fields. It can be seen that the octopods provide the highest SAR among the particles used. This is true for all applied ac fields. Considering the important factors contributing to the heat generation of magnetic nanoparticles, the coercivity or area under the hysteresis loop plays an important role. We have measured the MF curves at room temperature for the spheres, cubes

and octopods at a 10 kOe dc magnetic field. It can be seen that, although the cubes and spheres exhibit almost identical values of the room temperature magnetization at 10 kOe, the coercivity is much higher for the cubes than for the spheres. The octopods possess the highest coercivity and magnetization, as compared to those of the cubes and spheres. Such higher values of coercivity in the cubes and octopods are believed to be due to their higher surface to volume ratios as compared to the spheres. Since the nanocubes are more prone to chaining, they are expected to display higher SAR values compared to the spherical particles. The octopods have the highest magnetization among the particles used, so they tend to form in a chain inside a solution, resulting in the highest SAR.

In conclusion, our hyperthermia measurements and comparative analysis of specific absorption rates and AC power losses of ferrofluids containing magnetic nanoparticles synthesized by us in this project indicate that our nanoparticles with controlled size and shape are excellent candidates for a wide range of biomedical applications, including MRI, hyperthermia and biomolecular detection. In particular, we have demonstrated that the octopod-shaped Fe_3O_4 nanoparticles exhibit a superior magnetic heating efficiency as compared to their spherical and cubic particle counterparts.

Project 2: Nanoparticle/nano-wire structures and polymer nanoparticles for sensing and molecular manipulation

2.1. Synthesis and characterization of Au templates with variable spacing and formation of In nano-pore structures:

This research was aimed at developing a metallic film with ordered nano-pores for applications requiring large surface areas for molecular attachment. Applications include gas and bio sensors. The approach was two fold: (1) synthesize a 2-D template of spatially ordered Au nanoparticles by self-assembly, (2) use the template as a substrate to deposit In while heating the Au nanoparticles with a pulsed laser beam at 532 nm wavelength. As Au particles have a plasma resonance absorption peak near 520 nm, only the nanoparticles would heat above the melting point of In and prevent In deposition on particle sites, creating a film with ordered nano-pores. An SEM of an In film deposited on a Au template by this method is shown in [figure 25](#). This image shows complete coverage of Au nanoparticles by In and the nano-pores structures were not formed. The main difficulty in reaching the project goal was the inability to heat the Au nanoparticles selectively by the pulsed laser to achieve temperatures much above its melting point of 156°C.

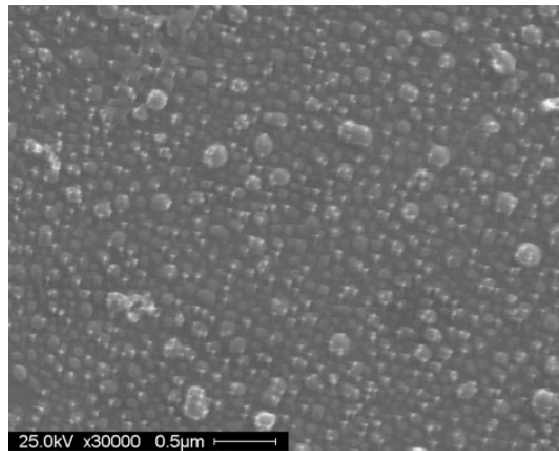


Figure 25: In film deposited on a self-assembled Au nano-template that is heated by a pulsed YAG laser at 532 nm wavelength.

2.2. Growth of nano-wires of inorganic compounds with variable diameters:

Zinc oxide (ZnO) is a material with multiple applications as a transparent conducting oxide for gas sensors, photocatalysis, and electrodes for photoelectrochemical cells. By appropriate doping electrical properties of ZnO can be altered and produce potentially important materials such as room temperature ferromagnetic semiconductors. In addition a variety of nanostructured ZnO morphologies have been synthesized by solution or vapor transport methods with and without the use of metal catalysts. In this project ZnO- nanowires have been grown by pulsed laser deposition (PLD).

In terms of growth parameters at higher pressure and temperatures the growth mode in PLD converts from a continuous film to a columnar growth that eventually results in the growth of free-standing micro(nano)-pillars. The materials transport and atomic processes that cause such a dramatic change in the growth are currently not well understood and need further investigation. Compared to the growth parameters the choice of substrate, i.e. $\text{Al}_2\text{O}_3(0001)$ or $\text{YSZ}(111)$, affects the film morphology to a lesser extent. However, some clear trends are noteworthy. XRD investigations have shown that the FWHM of the rocking curves have been always less for $\text{YSZ}(111)$ substrates compared to $\text{Al}_2\text{O}_3(0001)$ substrates for otherwise identical growth conditions ([Figure 26](#)). This indicates that the orientational c-axis alignment of the ZnO film is better on YSZ than on sapphire. On the other hand, growth of nano-pillars at elevated temperatures and pressures resulted in more uniform surface morphologies on sapphire than on YSZ. These differences may be associated with the different lattice mismatch between the two

substrates. Therefore YSZ(111) is a better substrate for the growth of c-axis oriented films while $\text{Al}_2\text{O}_3(0001)$ makes a better substrate for nano-pillar growth.

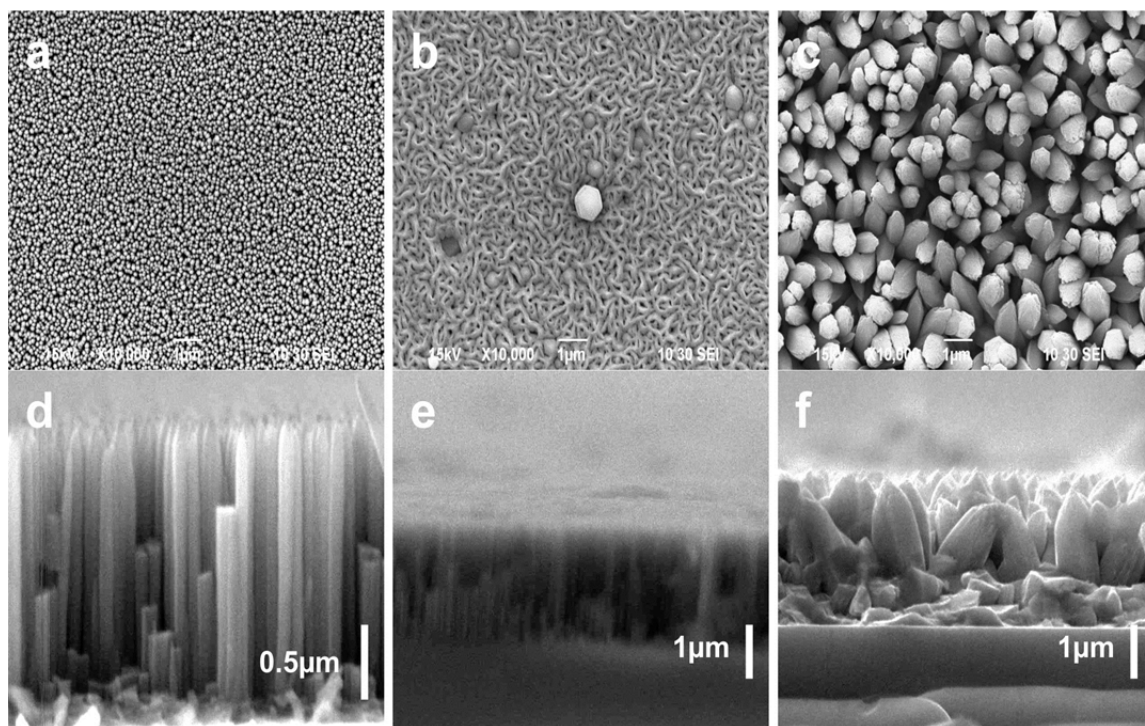


Figure 26: SEM images of ZnO nanowires grown by laser deposition on substrates of (a) $\text{Al}_2\text{O}_3(0001)$ (b) YSZ(111) (c) Si(100) (d) Cross-section SEM on $\text{Al}_2\text{O}_3(0001)$ (e) Cross-section SEM on YSZ(111) (f) Cross-section SEM on Si(100)

2.3. Formation of polymer nano-templates:

The aim of this project was to develop polymer nano-templates for biological cell attachment by a technique similar to that used in Task 2.1. The two-dimensional nanotemplate of gold particles formed by molecular self-assembly on a quartz substrate that is coated with ITO (as previously described) was spin-coated with a thermoset polymer solution. The Au nano template was heated with a pulsed laser tuned to the plasmon resonance wavelength for the nanoparticles. It was expected that the solution that is in contact with the Au nanoparticles would polymerize to form a coating on only the Au nanoparticles while the space between the particles would remain uncoated leading to a polymeric nanotemplate. The spatial uniformity and ordering of the nano features produced by this technique were not sufficient for quantitative analysis of biological cell attachment and manipulation.

2.4. Manipulation of molecules using electrical stimulation:

The first goal of this project is to use magnetic particles to apply mechanical stress to adherent cells and study the frequency-dependent cell growth. Many essential functions of mammalian cells, including movement, proliferation, and differentiation, can involve cellular recognition of and response

to mechanical stimulation. Our first step is to validate the force application system and to investigate the effect of prolonged static or cyclic stress on cellular viscoelastic parameters and on the cell-substrate adhesion of human umbilical vein endothelial cells (HUVECs). With collagen-coated iron oxide beads ($\sim 5 \mu\text{m}$ in diameter) attached to the dorsal surfaces of HUVECs, we were able to apply constant stress to the cells by placing the culture dishes close to a permanent magnet.

For cyclic force, the cell culture dish with the cells was placed on a stage that moved periodically left and right under the stationary magnet. Following static or cyclic stress application of a few hours duration, viscoelastic parameters of the cells were obtained from the measured time-dependent deformation produced by constant stress, analyzed using a suitable viscoelastic model. The time-dependent changes of cell morphology were measured by Electric Cell-substrate Impedance Sensing (ECIS). Our data show that applying 4 to 7 dyne/cm^2 of static stress to HUVECs for a few hours caused an increase of the elastic moduli and the viscosity of the cell body, and the elastic modulus of cell-substrate adhesion as well. On the other hand, cyclic stress of the same magnitude caused a decrease in all of these values. These observations indicate that the cellular viscoelastic properties and the cell-substrate adhesion of adherent epithelial cells can be altered by applied mechanical stress, either static or cyclic, but that the effects are strongly depend on the time course of stress application (figure 27).

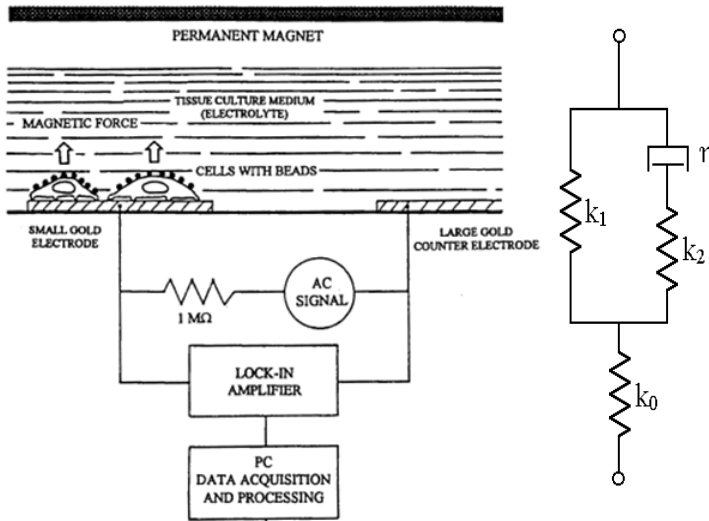


Figure 27: Viscoelastic model for an adherent HUVECs, in which the springs represent elasticity and the dashpot represents viscosity. A spring (k_1) connected in parallel with a Maxwell body, which consists of a spring (k_2) and a dashpot (η) in series, is used to describe the viscoelasticity of the cell body, and another spring (k_0) in series with the cell body system is used to describe the elasticity of cell-substrate adhesion.

	k_0	k_1	k_2	η
	(10 dyne/cm^2)	(10^3 dyne/cm^2)	(10^3 dyne/cm^2)	(10^4 poise)
Control ($n = 7$)	4.1 ± 0.6	5.5 ± 0.7	6.6 ± 0.4	2.2 ± 0.3
Static ($n = 10$)	6.5 ± 0.8	7.2 ± 0.9	10.6 ± 1.5	3.1 ± 0.5
Cyclic ($n = 12$)	1.6 ± 0.3	2.3 ± 0.3	4.3 ± 0.3	1.6 ± 0.1

Table 2-1 Summary of measured viscoelastic parameters of adherent HUVECs following a three hour application of static and cyclic mechanical stress via collagen-coated iron oxide beads. The values in this table are mean \pm standard error of the mean for n independent measurements.

2.5. Molecular dynamics simulations of structural and mechanical properties of oxide nanostructures and density functional theory studies of electronic properties of nano-wires and nano-ribbons:

Density functional theory (DFT) calculations of atomic and electronic structure of extended line defect in graphene have been performed. The 1D topological line defect consists of 5 and 8 member rings of sp² hybridized carbon atoms. The DFT calculations confirmed the stability of this defect and provided fully relaxed geometry. The calculated band structure and density of states demonstrate the metallic character of the line defect. The electronic states close to the Fermi level produce a local doping in a narrow stripe along the line defect, thus making a perfect one- dimensional metallic wire embedded in the perfect graphene sheet. These results were published in the journal *Nature Nanotechnology* [24]

2.6. Development and testing of amorphous magnetic ribbons for GMI-based sensing technologies:

Research on soft ferromagnetic materials with the giant magnetoimpedance (GMI) effect for making highly sensitive magnetic sensors is of current interest [25]. GMI is a large change in the ac impedance of a ferromagnetic conductor subject to a dc magnetic field. The impedance (Z) of a ferromagnetic ribbon can be calculated by

$$Z = R_{dc} \cdot jka \coth(jka), \quad (2-1)$$

where a is half of the thickness of the ribbon, R_{dc} is the electrical resistance for a dc current, j =imaginary unit, and $k = (1+j)/\delta_m$. It is related to the skin effect characterized by the skin depth (δ_m), which, in a magnetic medium, is given by

$$\delta_m = \sqrt{\frac{\rho}{\pi\mu_T f}}, \quad (2-2)$$

where ρ is the electrical resistivity, μ_T is the transverse magnetic permeability, and f is the frequency of the ac current. The application of a dc magnetic field H_{dc} changes μ_T , and consequently δ_m and Z . A large GMI effect should exist in soft ferromagnetic materials, such as Co-based amorphous and Fe-based nanocrystalline ribbons [25]. Since GMI is observed at high frequencies (>1 MHz), the skin effect is significant enough to confine the ac current to a sheath close to the surface of the conductor; GMI is therefore a surface-related magnetic phenomenon. As such, the surface roughness of a material is important and can considerably reduce the GMI magnitude if the surface irregularities exceed the skin depth. On the other hand, if one can reduce the surface roughness of a ribbon, the GMI response will be increased.

The overall goal of our research is to investigate the GMI effect in a variety of magnetic materials to explore its potential for applications ranging from magnetic sensors to bio-molecular detection. In particular, we have developed new approaches to tailoring the ribbon surface by capping it with a thin magnetic layer for improving both the GMI effect and its magnetic response of the ribbon [26,27]. We present below selected results from these studies.

Enhanced GMI Effect and field sensitivity in soft ferromagnetic ribbons with Co coating: We have demonstrated that the presence of the Co coating layer enhances both the GMI effect and field sensitivity in the Co-coated ribbons [26]. The largest values of the GMI effect and field sensitivity are achieved in the sample coated with Co on the free ribbon surface having the smaller surface roughness as compared to that coated with Co on the wheel-side ribbon surface with the larger surface roughness. Our findings are therefore of practical importance, demonstrating a way to tailor the GMI effect and field sensitivity in surface-modified ferromagnetic ribbons for use in highly sensitive magnetic sensors. In this work, $\text{Co}_{84.55}\text{Fe}_{4.45}\text{Zr}_7\text{B}_4$ amorphous ribbons with a width of 2 mm and a thickness of 30 μm were prepared by the melt-spinning method. X-ray diffraction confirmed the amorphous nature of the ribbons. The surfaces of the ribbons were then coated with 50 nm-thick Co layers using magnetron sputtering. The surface morphology of the samples was analyzed using atomic force microscopy (AFM). We denote the free surface of the ribbon as that which had no contact with the surface of the copper wheel and the wheel-side ribbon surface as that which had direct contact with the surface of the copper wheel. Magnetic measurements were performed at room temperature using a VSM. Magneto-impedance measurements were conducted along the ribbon axis using an impedance analyzer HP4192A by the four point technique. The dc field from -120Oe to +120Oe and ac current of constant magnitude 5 mA, over the frequency range 0.1 – 13 MHz were supplied along the sample axis. Two important figures of merit for evaluating the GMI effect in a material include the GMI ratio ($\Delta Z/Z$) and the field sensitivity (η), which are calculated as

$$\frac{\Delta Z}{Z} (\%) = \frac{Z(H) - Z(H_{\max})}{Z(H_{\max})} \times 100 \quad (2-3)$$

$$\eta = \frac{2 \times [\Delta Z/Z]_{\max}}{\Delta H}, \quad (2-4)$$

where H_{\max} (= 120 Oe) is the magnetic field sufficient to saturate the impedance and ΔH is the full width at half maximum of the field-dependent GMI curve. The ac magnetoresistance (MR) ratio $[\Delta R/R]$ and the magnetoreactance (MX) ratio $[\Delta X/X]_{\max}$, as well as their field sensitivity are defined in an analogous manner.

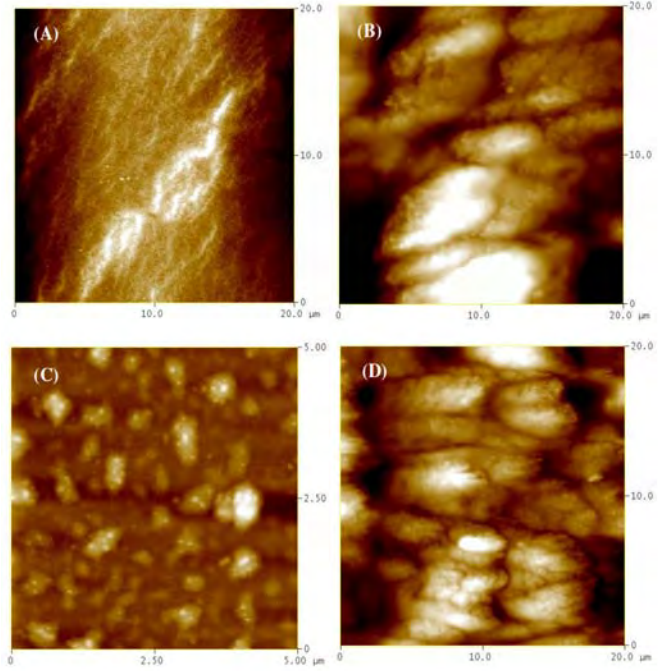


Figure 28: 2D topography images of (a) the free ribbon surface of the uncoated ribbon (Sample #1), (b) the wheel-side surface of the uncoated ribbon (Sample #2), (c) the free ribbon surface of the Co-coated ribbon (Sample #3), and (d) the wheel-side surface of the Co-coated ribbon (Sample #4).

First we studied the surface topography of the uncoated and Co-coated ribbon samples using AFM. Figure 28 shows the AFM images of these samples for both surfaces. The AFM image indicates the distribution of protrusions with very high and uniform density for the free surface of the ribbon, unlike in the case of the wheel-side surface of the ribbon. The root mean squared (rms) surface

roughness ($R_q = \frac{1}{n} \sqrt{\sum_{i=1}^n z_i^2}$, where z is the average amplitude of the topographical feature) was

determined from the corresponding topographical data of Figure 28 to be about 5.6 nm, 147 nm, 3.2 nm, and 61 nm for the free surface of the uncoated ribbon (Sample #1), the wheel-side surface of the uncoated ribbon (Sample #2), the free ribbon surface coated with Co (Sample #3), and the wheel-side ribbon surface coated with Co (Sample #4), respectively. Since Sample #1 and Sample #2 are both uncoated control samples, they have the same magnetic properties and GMI effect; we discuss below the M-H and GMI results of only samples #1, #3, and #4.

Figure 29a,b shows the dc magnetic field dependence of GMI ratio ($\Delta Z/Z$) for samples #1, #3, and #4 at two representative frequencies $f = 5$ MHz and 10 MHz. The frequency dependence of maximum GMI ratio ($[\Delta Z/Z]_{\max}$) and the maximum field sensitivity of GMI (η_{\max}) of these samples are displayed in Figure 29 c,d, respectively. It can be observed that a double-peak structure in GMI profile is present for all samples investigated, with a more pronounced dip at zero field in Samples #3 and #4 than in Sample #1. From a sensor application perspective, it is very interesting to note that in the frequency range of 0.1 to 10 MHz, larger values of $[\Delta Z/Z]_{\max}$ and η_{\max} are achieved in Sample #3 and Sample #4

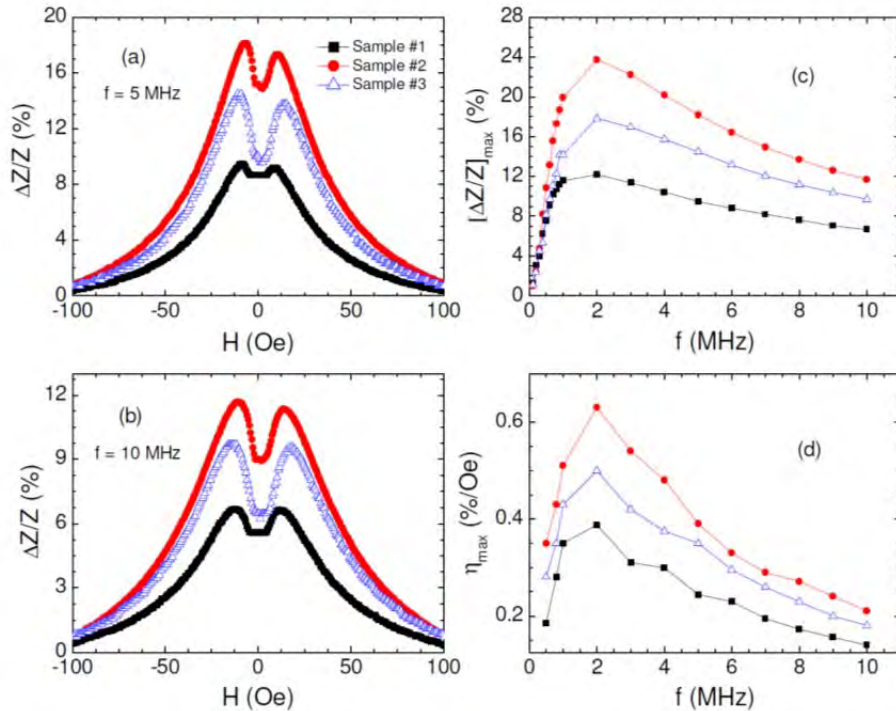


Figure 29: (a,b) Magnetic field dependence of GMI ratio ($\Delta Z/Z$) at 5 MHz and 10 MHz for Sample #1, Sample #3, and Sample #4; (c,d) Frequency dependence of the maximum GMI ratio ($[\Delta Z/Z]_{\max}$) and the field sensitivity of GMI (η) for these samples.

when compared to Sample #1. At $f = 2$ MHz, $[\Delta Z/Z]_{\max}$ and η_{\max} reach the largest values of 12.18% and 0.39%/Oe for Sample #1, 23.71% and 0.74%/Oe for Sample #3, and 17.85% and 0.50%/Oe for Sample #4. This clearly indicates that the Co coating enhances the GMI ratio and field sensitivity. Depositing the Co on the free ribbon surface with the smaller surface roughness ($R_q \sim 6$ nm) results in the larger $[\Delta Z/Z]_{\max}$ and η_{\max} when compared to that on the wheel-side ribbon surface having the larger surface roughness ($R_q \sim 147$ nm).

Overall, we have shown that the presence of the Co coating layer enhances both the GMI effect and field sensitivity in the Co-coated ribbons, demonstrating a new way to tailor the GMI effect and field sensitivity in surface-modified ferromagnetic ribbons for use in highly sensitive magnetic sensors. These results have been published in *Journal of Applied Physics* 2011.

Impact of field-induced exchange anisotropy on GMI in ribbon/FeMn bilayers: We show how the GMI of a Co-based amorphous ribbon is affected by tuning the surface anisotropy of the ribbon by capping it with an antiferromagnetic material FeMn in the presence of a 200 Oe field applied in the longitudinal or transverse directions. We find that the orientation of the deposition field greatly impacts the GMI of the bilayer structures. Our studies provide further guidance for tailoring GMI in surface modified soft ferromagnetic ribbons as well as optimizing specific frequency ranges for particular sensors. In this work, cobalt based Metglas® Inc 2705M ribbons of width 2mm and thickness of 30 μm were coated with 150 Å of FeMn by using magnetron sputtering.

X-ray diffraction confirmed the amorphous structure of the ribbons pre-deposition. During the deposition, a field of 200 Oe was applied either perpendicular or parallel to the sample length. The samples were also rotated 90 degrees so that the applied DC field was perpendicular to the sample length before impedance measurements were again carried out. Magnetic measurements were performed at room temperature using a VSM. Magneto-impedance measurements were conducted along the ribbon axis.

Figure 30a,b shows the magnetic field dependence of GMI ratio at a representative frequency of 1 MHz and the maximum GMI ratio as a function of frequency for the plain ribbon, FeMn/ribbon bilayer in an applied transverse field of 200 Oe (conf. 1), and FeMn/ribbon bilayer in an applied longitudinal field of 200 Oe (conf. 2).

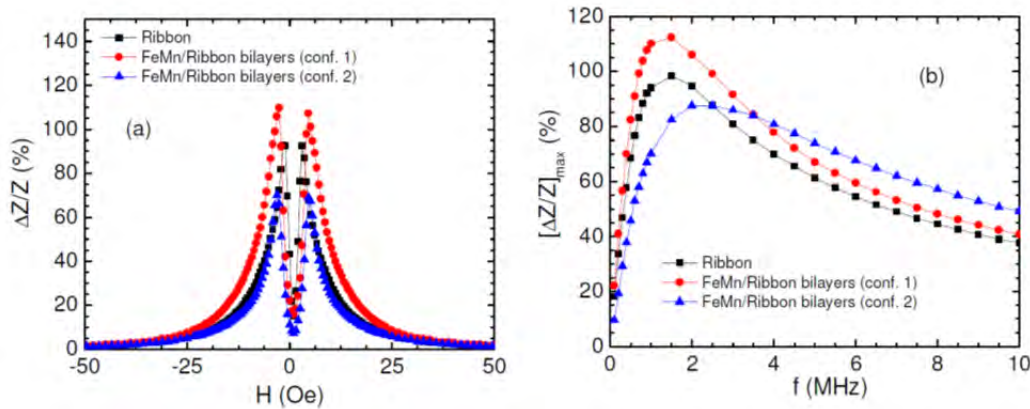


Figure 30: (a) Magnetic field dependence of GMI ratio and (b) frequency dependence of maximum GMI ratio for the plain ribbon, the FeMn/ribbon bilayer in a transverse magnetic field of 200 Oe and the FeMn/ribbon bilayer in a longitudinal magnetic field of 200 Oe.

As one can see from Figure 30a, the GMI profiles with a double-peak structure have been obtained for all samples investigated. At 1 MHz, the sample with conf. 1 has the largest value of GMI ratio among the three samples. It is very interesting to note in Figure 30b that while the sample with conf. 1 has larger values of GMI ratio compared with those of the plain ribbon in the whole frequency range of 0.1-10 MHz, the sample with conf. 2 possesses smaller values of GMI ratio at $f < 4$ MHz, but larger values of GMI ratio for $f > 4$ MHz. This clearly indicates the important impact of exchange bias on the GMI profile in the FeMn/ribbon bilayer structures. To understand the frequency dependence of

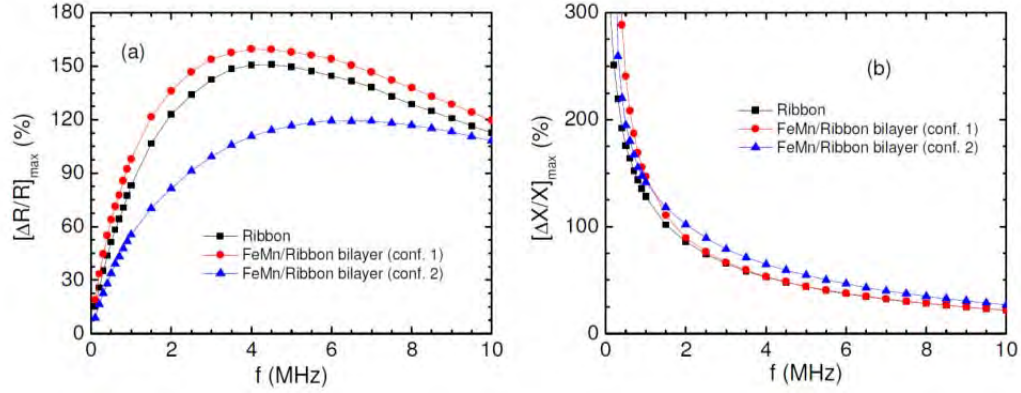


Figure 31: Frequency dependence of (a) maximum $\Delta R/R$ and (b) $\Delta X/X$ ratios for the plain ribbon, the FeMn/ribbon bilayer in a transverse magnetic field of 200 Oe and the FeMn/ribbon bilayer in a longitudinal magnetic field of 200 Oe.

maximum $\Delta Z/Z$ of the plain ribbon, the FeMn/ribbon bilayer in a transverse magnetic field of 200 Oe and the FeMn/ribbon bilayer in a longitudinal magnetic field of 200 Oe, we have studied the frequency dependence of maximum $\Delta R/R$ and $\Delta X/X$ ratios for these samples (Figure 31). In the frequency range 0.1 – 10 MHz the $\Delta R/R$ ratio is largest for the FeMn/ribbon bilayer in a transverse magnetic field of 200 Oe (the sample with conf. 1). The $\Delta R/R$ ratio of the FeMn/ribbon bilayer in a longitudinal magnetic field of 200 Oe (the sample with conf. 2) is smaller than that of the plain ribbon. However, the $\Delta X/X$ ratio is largest for the sample with conf. 2 at high frequencies ($f > 1$ MHz). These relative contributions of $\Delta R/R$ and $\Delta X/X$ to $\Delta Z/Z$ allow us to interpret the frequency dependence of maximum $\Delta Z/Z$ in these three samples.

Overall, we have systematically studied the GMI effect in field-grown FeMn/Metglas® Inc bilayer structures. Both the FeMn layer and the direction of the field during deposition have a substantial impact on the GMI. Depending on the frequency range and field range desired, we have shown that it is beneficial to use a bilayer structure over a control sample. These improvements could be used for improving the sensitivity and functionality of highly sensitive magnetic sensors.

Enhanced GMI effect in soft ferromagnetic amorphous ribbons with pulsed laser deposition of cobalt ferrite: We have developed a new method of using a pulsed laser deposition (PLD) technique for the controlled growth of a thin magnetic oxide (CoFe_2O_4) layer on the surface of Co-based amorphous ribbons to improve the GMI response [27]. Our study indicates that both the surface roughness of the ribbon and closure of magnetic flux paths due to the presence of the additional magnetic layer play important roles in tailoring the GMI effect and field sensitivity. Below, we highlight some of the main

findings. Two types of ribbons $\text{Co}_{65}\text{Fe}_4\text{Ni}_2\text{Si}_{15}\text{B}_{14}$ (Type-I) and $\text{Co}_{69}\text{Fe}_4\text{Ni}_1\text{Mo}_2\text{B}_{12}\text{Si}_{12}$ (Type-II), with corresponding thicknesses of 15 and 22 μm were prepared by a rapid quenching method. A 50 nm CoFe_2O_4 (CFO) layer was deposited on the ribbons using PLD. The structure and surface morphology of the samples were characterized using X-ray diffraction (XRD) and Atomic Force Microscopy (AFM). Magnetoimpedance measurements on plain and CFO-coated Type-I and Type-II ribbons with a width of 2 mm and a length of 1 cm were performed using an HP4192A analyzer with a constant ac current of 5 mA supplied along the ribbon over a frequency range 0.1-13 MHz in axial dc fields up to ± 120 Oe.

Our studies reveal that the presence of the 50 nm thick CFO layer enhanced both the GMI effect and field sensitivity. As shown in Figure 32, the CFO-coated ribbon samples of both types have higher $[\Delta Z/Z]_{\text{max}}$ and η as compared to their corresponding plain samples over a wide frequency range of 0.1 – 13 MHz, with a maximum change at a particular frequency f_0 . In particular, the deposition of a 50 nm thick CFO film on the Co-based ribbons greatly enhanced the GMI ratio, by 97% for Type-I and 42% for Type-II. A similar trend is found for the field sensitivity of GMI for both Type-I and Type-II. For Type-I, the η increased from 0.76%/Oe for the plain sample to 1.02%/Oe for the CFO-coated sample, which represents an enhancement by 34%. Also, for Type-II the η increased from 3.84%/Oe for the plain sample to 5.74%/Oe for the CFO-coated sample, representing an enhancement of 50%. These improvements of the GMI and η in the CFO-coated ribbons are significantly larger than those reported in the ribbons coated with Co, CuO, ZnO, or a diamagnetic organic material [28]. The enhancement of the GMI and η in the CFO-coated ribbons can be attributed to the reduced stray fields on the ribbon surface due to reduced surface irregularities and the enhanced closure of magnetic flux paths, with a similar explanation given for the case of Co-based amorphous ribbons coated with Co [26]. These findings open the possibility of developing a new generation of biosensors for biomedical applications. The main results have been published in *Journal of Applied Physics* in 2013.

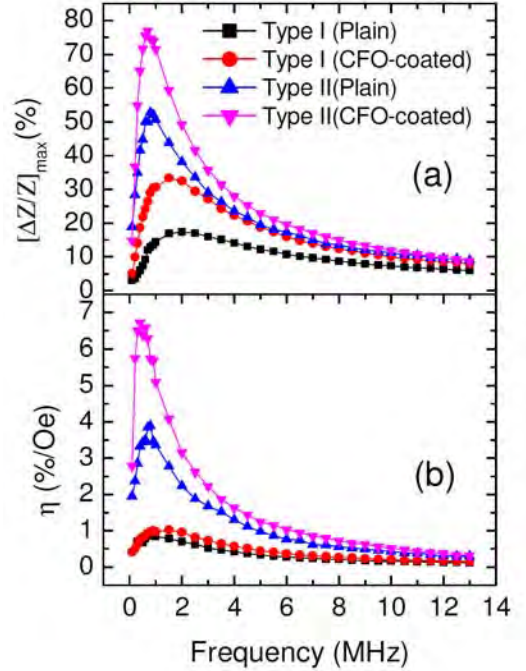


Figure 32: (a) Frequency dependence of the maximum GMI ratio $[\Delta Z/Z]_{\text{max}}$ for both Type-I and Type-II; (b) Frequency dependence of GMI sensitivity (η).

2.7. Improving the field sensitivity and figure of merit of wire-based GMI materials for biosensing and microwave device applications:

The overall goal of this research is to tailor the GMI effect in soft ferromagnetic microwires and explore it for biodetection and microwave device applications. We have demonstrated that it is possible to improve the GMI effect and its field sensitivity by forming individual wires into a multi-wire system. This multi-wire system is shown to be more promising for detection of weak magnetic fields coming from biological systems. Instead of using the GMI effect, we have demonstrated the possibility of

improving the sensor sensitivity further by using the ac magneto-reactance (MX) effect, which is later explored for biodetection with greatly improved sensitivity.

Tailoring the GMI response in magnetic multi-wire systems for magnetic sensor applications:

It has been reported that soft ferromagnetic amorphous glass-coated microwires are one of the most attractive candidate materials for use in GMI-based sensors [27]. Interestingly, Garcia et al. [29] reported that both the GMI effect and its field sensitivity could be greatly improved in a system consisting of multiple wires in a parallel arrangement. Chiriac et al. [30] showed that this multi-wire system could have a great potential for highly sensitive detection of biomolecules. However, the origin of the observed GMI effect and the influence of wire spacing on the GMI signal remain to be investigated. From a magnetic sensor application perspective, it is essential to investigate the effects of multi-wire configuration on the magneto-impedance (MI), but also on the magneto-resistance (MR) and magneto-reactance (MX) of the system, both of which may provide alternative approaches for improving the field sensitivity of existing sensors.

To address these important issues, we have performed a systematic study of the MR, MX, and MI effects in an array of amorphous glass-coated $\text{Co}_{82.9}\text{B}_{3.4}\text{Si}_{5.8}\text{Mn}_{7.9}$ microwires. The amorphous wires were prepared by glass coated melt spinning technique [31]. The dc field from -120 Oe to +120 Oe and ac current of constant magnitude 5mA, over the frequency range 0.1 – 13 MHz were supplied along the sample axis. The impedance of all the samples was measured over the length of 10mm on the impedance analyzer HP4192A by four point technique.

Our studies reveal that the MR, MX, and MI ratios and their corresponding field sensitivities

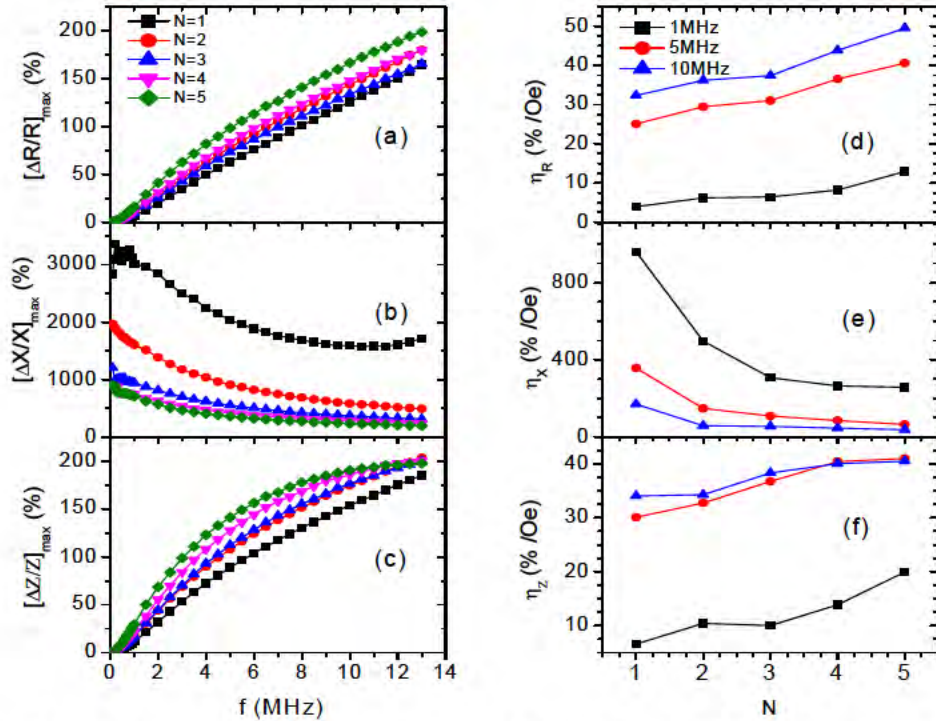


Figure 33: Frequency dependence of maximum MR (a), MX (b), and MI (c) ratios for $N = 1, 2, 3, 4$, and 5 and corresponding field sensitivities (d-f) as a function of number of wires at frequencies $f = 1, 5$, and 10 MHz.

strongly depend on the number of microwires in an array and on the distance between them. As shown in Figure 33, we have found that increasing the number of microwires increases the MR and MI ratios and their field sensitivities but decreases the MX ratio and field sensitivity. A similar trend is observed for the frequency dependence of these parameters. Increasing the distance between the wires is also found to decrease the MR, MX, and MI ratios of the array considerably. From a sensor application perspective, it is interesting to note that for the case of a single microwire [Figure 33 (d-f)], the η_X reaches a value as high as 960 %/Oe at a frequency of 1 MHz, which is about 192 times the η_R and η_Z (~5 %/Oe), revealing the possibility of developing ultrahigh sensitivity magnetic field sensors based on the principle of the MX effect. These findings are of practical importance in developing single- and multi-wire systems for advanced sensor technologies. The important results have been published in *Journal of Alloys and Compounds* in 2013.

Based on these research achievements, we have recently developed a new generation of coil-based inductive sensors for highly sensitive biodetection of functionalized magnetic nanoparticles as magnetic markers in biological systems. The coil is made of glass-coated soft ferromagnetic amorphous microwires. This type of sensor not only enables the detection of low-concentration magnetic nanoparticles, but also the study of the dynamic phenomena of magnetic fluids flowing through a tube located inside the magnetic coil.

A new type of microwave field sensor using fiber Bragg grating and soft ferromagnetic glass-coated microwires: The fiber Bragg grating (FBG), which is a periodic variation of the index of refraction of an optical fiber, forms the basis of numerous sensors [32]. For the most part, strain and temperature are the primary environmental parameters that can be detected with FBGs. Other variables can be measured by using a probe design that converts the desired variable to a strain or temperature change. For example, an FBG bonded to the wall of a vacuum chamber might be used to measure pressure if the wall strain vs. pressure calibration were known. Increasing the sensitivity and developing a cost-effective probe are challenging tasks for these types of sensors. Traditionally, probes based on gold and other metals have been used to absorb the heat energy in these sensors (Figure 34).

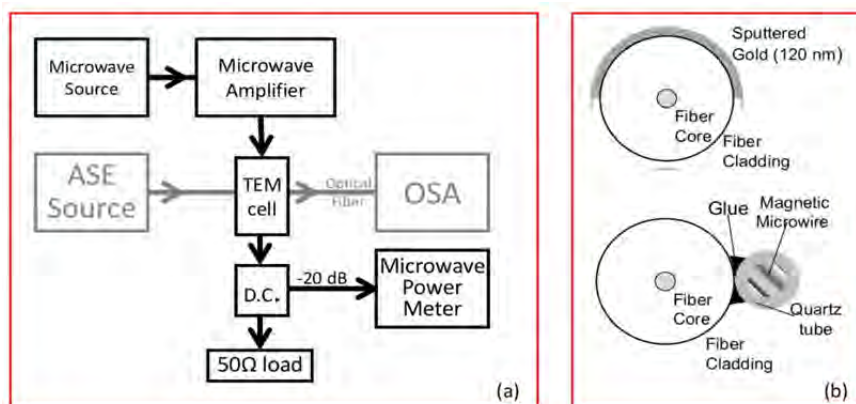


Figure 34.: Diagram of experimental setup: (a) Optical (microwave) components and paths are shown in gray (black). Abbreviations are as follows: ASE--amplified spontaneous emission; TEM cell--50 Ω microstrip transmission line; OSA--optical spectrum analyzer; D.C.--directional coupler. (b) Cross-section of gold-based probe; and c) cross-section of microwire-based probe (not to scale).

In this project, we have developed a new type of microwave energy sensor that relies on Joule heating of a soft ferromagnetic glass-coated microwire to change the temperature of an FBG. We show below that the proposed sensor probe, with a relatively poor thermal coupling with FBG, has better performance compared to the gold-based probe with a better thermal coupled gold-based probe.

For a fiber grating designed to reflect a single wavelength, the Bragg condition can be written as $\lambda_{\text{FBG}} = 2n\Lambda$ where λ_{FBG} is the Bragg wavelength, n is the effective index of refraction of the core, and Λ is the grating pitch. As the temperature of an FBG changes, the center wavelength of the grating will shift according to the formula [32]:

$$\Delta\lambda_{\text{FBG}} = \left[\alpha + \frac{\left(\frac{dn}{dT}\right)}{n} \right] \Delta T \quad (2-5)$$

where α is the coefficient of thermal expansion, n is the effective index of refraction, and ΔT is the temperature change. This wavelength shift is exploited to use an FBG as a temperature sensor. By monitoring the transmitted or reflected optical spectrum, we can determine the average temperature of the FBG.

A probe based on the microwave-absorbing soft ferromagnetic glass-coated microwire of diameter 14 μm and composition $\text{Fe}_{4.97}\text{Co}_{64.63}\text{B}_{16}\text{Si}_{11}\text{Cr}_{3.4}\text{Ni}_{0.02}$ was designed by gluing it to the cladding

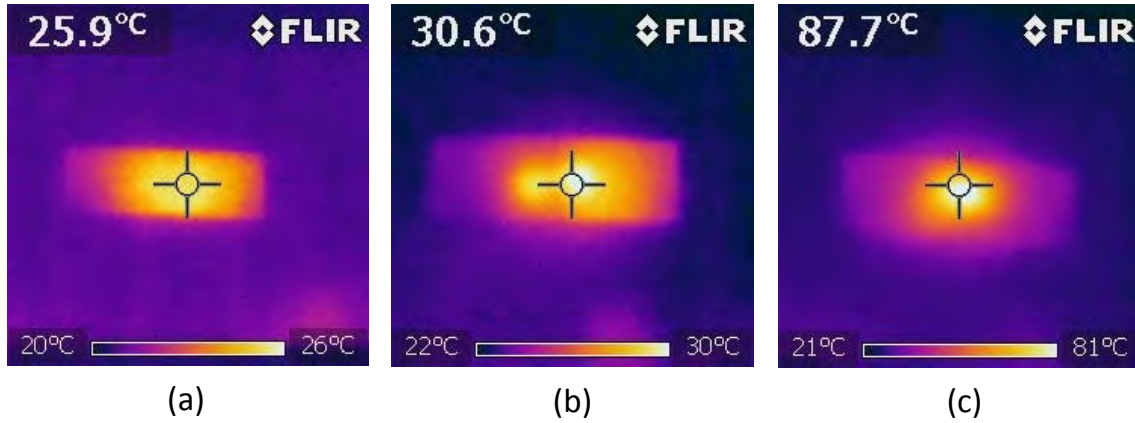


Figure 35: Temperature increase for (a) polymer, (b) polymer with a magnetic ribbon, and (c) polymer with a magnetic microwire after 10 seconds of microwave heating.

of a commercial FBG. We have chosen this type of microwire because it absorbs microwave energy and convert it into heat most efficiently, as compared to other materials like a magnetic ribbon (Figure 35). For comparison, a gold-based probe was created by sputtering approximately 120 nm of the metal onto the FBG's cladding. Obviously; the latter probe had a better thermal coupling with the FBG to absorb microwave energy. Any temperature increase of the microwire or gold due to Joule heating was transmitted to the FBG and appeared as a shift of the notch in the FBG's transmission spectrum. Light from a broadband amplified spontaneous emission source (JDSU M/N BBS1560+1FP) was launched into the optical fiber that contained the FBG. Light transmitted through the optical fiber was monitored with an optical spectrum analyzer (HP M/N 70951B). The sensor was placed into a homemade 50 Ω microstrip transmission line. As microwave energy of different frequencies and powers was sent through the transmission line, the optical spectrum transmitted by the FBG was recorded. The

microwaves were generated by an HP M/N 8703A, amplified by either a Mini-Circuits M/N ZHL-42W or Avantek M/N APT-10555, and monitored with an HP M/N E4419B. The experimental set up is shown in Figure 36.

We have found that the performance of the microwire probe is linear with the microwave energy at several frequencies (Figure 36a). The result demonstrates that the slope of $\Delta\lambda_{\text{FBG}}$ vs. microwave energy is a function of the microwave frequency. The performance of the microwires and gold was compared by calculating the FOM at a particular microwave frequency as

$$\text{FOM} = \frac{\text{linear slope of } \Delta\lambda_{\text{FBG}} \text{ vs. microwave power}}{10^{(S_{11}/10)}}. \quad (2-6)$$

As shown in Figure 36b, at microwave frequencies the microwire-based probe has a larger FOM than the gold-coated FBG in general. At $f = 3.25$ GHz, the microwire-based probe has shown the best performance (~ 10 times) relative to the gold-based probe. These results demonstrate that using the microwires as a microwave absorber, it is possible to fabricate a fiber Bragg grating-based microwave energy sensor with improved sensitivity and less perturbation of the microwave field. Applications that require a strong response and minimal perturbation of the EM-field would benefit from such a probe. Additionally, the microwave resonances of the microwires are tunable and so one can imagine sensors that are even more appropriate at particular microwave frequencies. Recently, we have performed a comparative study of the magnetic softness, GMI effect, and microwave absorption capacity of glass-coated amorphous $\text{Co}_{68}\text{B}_{15}\text{Si}_{10}\text{Mn}_7$ and $\text{Co}_{64.63}\text{Fe}_{4.97}\text{B}_{16}\text{Si}_{11}\text{Cr}_{3.4}\text{Ni}_{0.02}$ microwires. We find that the

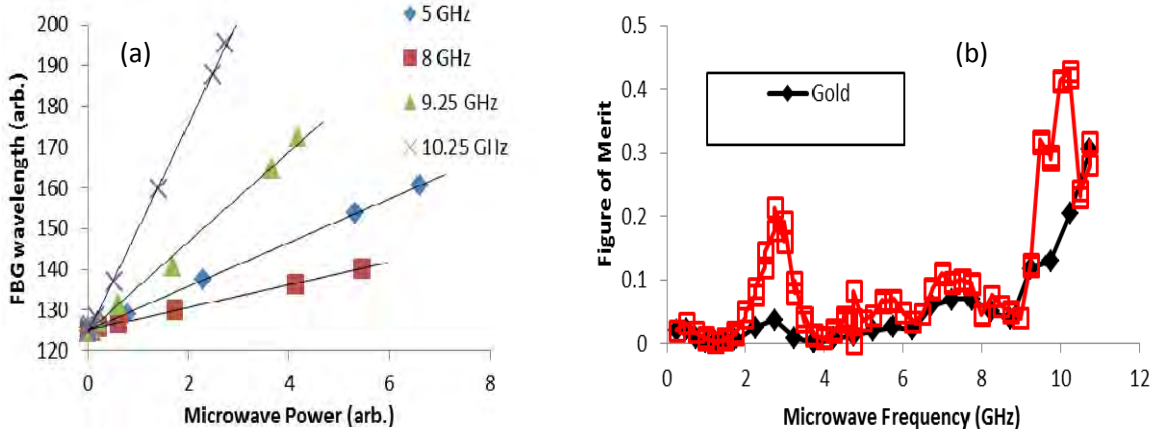


Figure 36: (a) λ_{FBG} vs. microwave power at several microwave frequencies for a probe using one of the ferromagnetic glass microwires. Linear fits to each dataset are shown; (b) FOM of the microwire-based probe and the gold-based probe.

$\text{Co}_{68}\text{B}_{15}\text{Si}_{10}\text{Mn}_7$ wire exhibits larger values of the saturation magnetization, GMI ratio, and microwave absorption capacity as compared to the $\text{Co}_{64.63}\text{Fe}_{4.97}\text{B}_{16}\text{Si}_{11}\text{Cr}_{3.4}\text{Ni}_{0.02}$ wire. As a result, the former is a more promising microwave absorber for fabrication of a new class of microwave energy sensor based on FBG. Our study emphasizes a correlation between the magnetic softness, GMI and microwave absorption in the microwires, and paves the way to improving the performance of this sensor by tailoring their soft magnetic properties. The results featuring these new findings have been submitted for publication in *Sensors and Actuators A: Physical* 2013 and *Journal of Applied Physics* 2013.

Project 3: Carbon nanotube based sensors

In recent years, carbon nanotubes (CNTs) have been used in many potential applications including nano-devices, sensors, ultra high strength engineered fibers, quantum wires and catalyst supports [33-38]. Carbon nanotubes are attractive candidates for supercapacitors due to their high electrical conductivity and controllably mesoporosity arising from the central nanotube canal and voids formed from nanotube entanglements. Hybrid nanocomposite materials composed of carbon nanotubes loaded with nanoparticles have also been studied for supercapacitors. Recently, it has been reported that Fe_3O_4 filled CNTs may be used as diffraction gratings, optical filters and polarizers [34]. Other applications of these materials include cantilever tips in magnetic force microscopes, magnetic stirrers or magnetic valves in nanofluidic devices. Since the biocompatibility of magnetite and CNTs are somewhat well established in the literature [35,37], the combination of these two nanostructured elements could be of potential interest for improved drug delivery systems. Korneva *et al* proposed that these magnetically filled CNTs can potentially be used as nanosubmarines driven through blood vessels by an external magnetic field and transporting drugs to specific locations in the body, as well as for medical diagnosis without surgical interference [38]. To realize such applications, it is technologically important to retain the desirable magnetic properties of magnetic nanoparticles in CNTs through control over the particle size and uniformity of packed particles. Despite a number of previous studies, filling CNTs completely with monodisperse magnetic nanoparticles has remained a challenging task. Moreover, it is essential to understand the magnetic interactions that are likely to influence the magnetic properties of magnetic particle-filled CNTs.

The goal of this project is to develop multifunctional materials by combining the superior properties of carbon nanotubes and superparamagnetic nanoparticles for a wide range of applications from smart RF sensors and microwave devices to biodetection. We have demonstrated an effective method for filling CNTs completely with monodisperse superparamagnetic nanoparticles of different compositions (Fe_3O_4 , CoFe_2O_4 , NiFe_2O_4) [39]. We have developed a new approach for carbon nanotube-based gas and chemical sensing using the GMI technology [40]. We show that the synthesized magnetic carbon nanotubes are not only attractive candidate materials for RF sensors and microwave devices, but also as excellent magnetic biomarkers in biological systems. In addition, we have demonstrated a novel approach to using functionalized superparamagnetic nanoparticles and the GMI technology for highly sensitive detection of cells and biomolecules. Finally, the synthesis and characterization of integrated ferroelectric-ferromagnetic high aspect ratio nanostructures are reported.

3.1. Chemical synthesis and characterization of magnetic carbon nanotubes for RF sensor and biomedical applications:

Carbon nanotubes filled with monodisperse Fe_3O_4 nanoparticles: A facile, multi-step process is utilized to fabricate these structures. First we synthesized the magnetite nanoparticles chemically and separately used chemical vapor deposition (CVD) to grow multi-walled CNTs within the pores of alumina templates. The Fe_3O_4 NPs were incorporated inside the CNTs using a magnetically assisted capillary action method [38]. We demonstrate that the optimization of loading conditions in a magnetically assisted capillary action technique allows production of CNTs filled completely with uniformly dispersed Fe_3O_4 nanoparticles and that the increased dipolar inter-particle interaction leads to the enhanced magnetic properties of these nanostructures. Detailed magnetic characterization was performed using DC and AC susceptibility experiments. To our knowledge this is the first report of

uniformly filled CNTs displaying large saturation magnetization which would render them useful for various applications.

We briefly describe the multi-step process involved in the fabrication of magnetic nanoparticle loaded carbon nanotubes. The entire process consisted of three different steps (Figure 37): (i) synthesis of Fe_3O_4 nanoparticles; (ii) carbon nanotubes grown by CVD technique; (iii) filling of the carbon nanotubes by as prepared Fe_3O_4 nanoparticles.

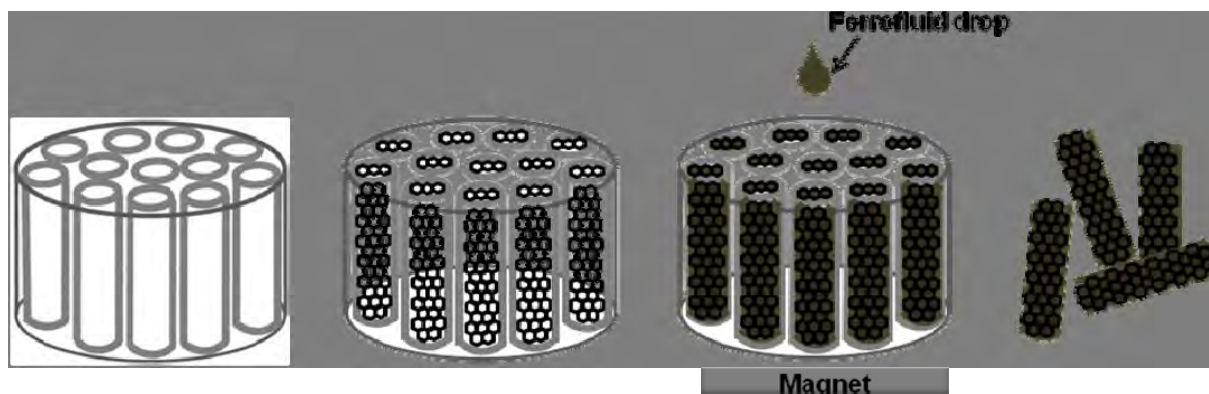


Figure 37: Scheme of the synthesis steps: (i) Alumina template, (ii) CNT grown by CVD technique inside the template, (iii) CNTs filled by ferrofluids dropwise keeping a magnet underneath the template, (iv) CNTs filled with ferrofluid after removing the template.

First, Fe_3O_4 nanoparticles were synthesized using the thermal decomposition method. Briefly, 2mmol Iron (III) acetylacetonate ($\text{Fe}(\text{acac})_3$), 10 mmol 1,2- hexadecanediol, 6 mmol oleic acid, 6 mmol oleylamine, 20 ml benzyl ether were mixed together and magnetically stirred under the flow of argon at 200°C for 2 h. Then the mixture was heated to reflux at 300°C for 1 h. The black colored material was cooled down to room temperature. 40 ml ethanol was added to the mixture and the precipitate was separated by centrifugation. The product was dissolved in hexane in the presence of oleic acid and oleylamine. This solution was centrifuged to remove the undispersed residue. The product was precipitated again with ethanol and centrifuged to remove the solvent and finally dissolved in hexane for further characterization.

Next, carbon nanotubes were produced using a CVD method and directly grown inside the pores of alumina membranes. The procedure was similar to that reported by Miller *et al* [41]. Before the growth of CNTs, the alumina template membranes were placed between two quartz slides and heated to 740°C for 1h to prevent the bending of templates during the CNT synthesis. The heat – treated alumina template membrane (13 mm diameter, $60\mu\text{m}$ thick and $0.2\mu\text{m}$ pore size purchased from Whatman) was placed vertically inside the quartz tube. The quartz tube loaded with the alumina template was placed inside the CVD reactor furnace and its temperature was increased to 670°C under the flow of argon (flow rate 20 sccm). When the temperature stabilized at 670°C , the gas flow was switched to 30% ethylene and 70% helium at a flow rate of 20 sccm. The reaction was continued for 6 h and the gas flow was switched back to argon at the flow rate of 20 sccm. The furnace was turned off and allowed to cool down to room temperature still maintaining the flow of argon. Note that while attempts were made to use alumina with smaller pore size as quoted by the manufacturers, the nanotubes grown were on average much larger (in the 250 to 300 nm range). This is most likely due to pore size being not uniform through the depth of the $60\mu\text{m}$ thick alumina templates.

The next step was filling the carbon nanotubes (open at both ends) encased in the alumina templates with the organic solvent containing the suspended Fe_3O_4 nanoparticles. Before filling the nanotubes, a permanent magnet ($\mu_0 H = 0.4$ T) was placed underneath the template and the hexane solution of Fe_3O_4 was poured dropwise on the top end of the template. The ferrofluid invaded the pores due to capillary action and the homogeneous magnetic field helped to increase the rate and depth of penetration. After the evaporation of hexane at room temperature, the template was broken into tiny pieces and dipped into 4.0 M NaOH solution and sonicated till the template dissolved completely. After sonication, the solution was vacuum filtered through a polyester nucleopore membrane (pore size ~ 0.2 μm). After filtration, the residue was rinsed with toluene to remove the stray ferrofluid particles from the surface of the membrane. Then the residue was washed with isopropanol and deionized water for several times and finally dried at room temperature. The dry sample was collected for structural characterization and magnetic measurements.

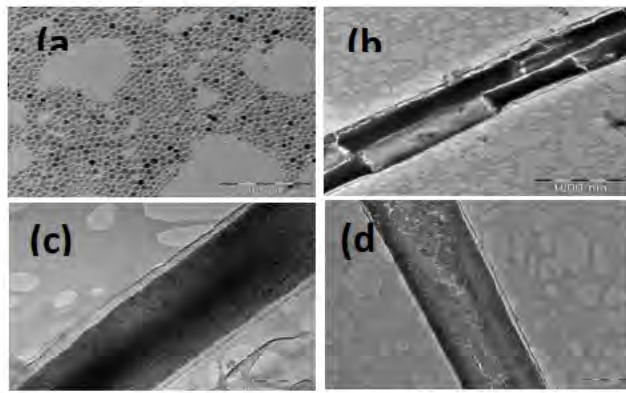


Figure 38: TEM micrographs of (a) Fe_3O_4 nanoparticles and (b,c,d) carbon nanotubes filled with Fe_3O_4 nanoparticles.

Figure 38 shows TEM images of Fe_3O_4 nanoparticles and CNTs filled with these nanoparticles. The average particle size of Fe_3O_4 was estimated from a histogram analysis to be 6 ± 0.5 nm (figure 10a). Several different views of the nanoparticle loaded CNTs are shown in figure 10((b), (c), (d)). It can be seen that the particle packing within the cross-section of the nanotubes is very uniform. The average length of CNT is 5-6 μm and diameter is 250-300 nm with 30 nm wall thickness. So the aspect ratio of these magnetic nanotubes turns out to be ~ 20 .

Figure 39a shows the ZFC and FC M-T curves for Fe_3O_4 nanoparticles and CNTs filled with Fe_3O_4 nanoparticles (labeled as Fe_3O_4 -CNTs) taken at a field of 200 Oe. The ZFC M-T curve for the Fe_3O_4 nanoparticles exhibits the typical blocking process of an assembly of superparamagnetic particles with a distribution in blocking temperature around an average $T_B \sim 31$ K. However, the case is quite different for Fe_3O_4 -CNTs, which exhibit a broad ZFC curve with its peak at ~ 58 K. For this sample, the gradual decrease in

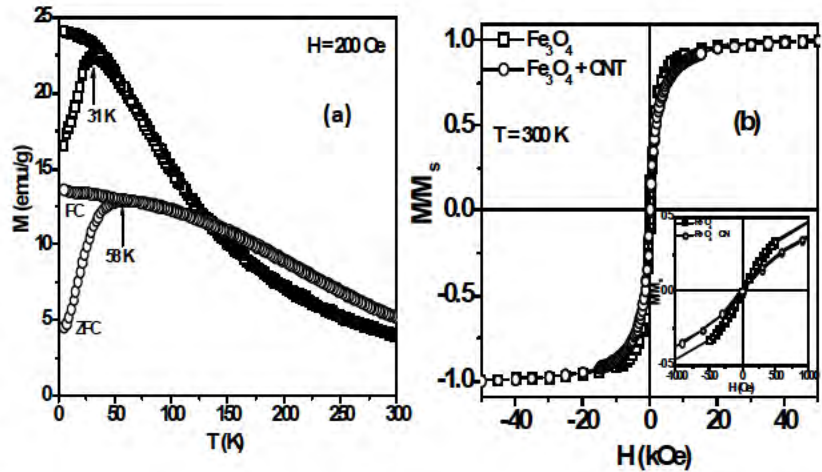


Figure 39: M vs T plot of Fe_3O_4 nanoparticles (\square) and carbon nanotubes filled with Fe_3O_4 nanoparticles (\circ); M vs H plot of Fe_3O_4 nanoparticles (\square) and carbon nanotubes filled with Fe_3O_4 nanoparticles (\circ) at 300 K. ($M_s = 60$ emu/g for Fe_3O_4 NPs and 63 emu/g for carbon nanotubes filled with Fe_3O_4 NPs).

magnetization above 58 K, deviating from Curie type $1/T$ dependence, is characteristic of the presence of particle interactions in this system.

Figure 39b and its inset shows the magnetic field dependence of magnetization (the M-H curves) taken at 300 K. It can be observed that for both Fe_3O_4 NPs and Fe_3O_4 -CNTs the M-H curves at 300 K do not show any hysteresis, consistent with superparamagnetic behavior. At 5 K the values of saturation magnetization (M_S) of Fe_3O_4 NPs and Fe_3O_4 -CNTs are determined to be about 60 emu/g and 63 emu/g, respectively. Subtracting the diamagnetic contribution of CNTs, the M_S of Fe_3O_4 -CNTs is ~ 63.7 emu/g. This value is smaller than that of bulk Fe_3O_4 ($M_S \sim 92$ emu/g) but is larger compared with that of Fe_3O_4 NPs ($M_S \sim 60$ emu/g). The enhancement of M_S for Fe_3O_4 -CNTs is very important from magnetic-field guided applications point of view. The slight enhancement of the magnetization in Fe_3O_4 -CNT system in comparison with the as-synthesized Fe_3O_4 nanoparticles is also consistent with enhanced inter-particle interactions (due to tight packing of the particles within the confined region of the hollow nanotubes) that is discussed and quantitatively analyzed in our publication in *Nanotechnology* 2009.

Carbon nanotubes filled with monodisperse CoFe_2O_4 nanoparticles: In this work, spherical monodisperse CoFe_2O_4 nanoparticles with diameter of $7 \text{ nm} \pm 1 \text{ nm}$ were filled inside CNTs. Figure 40 shows TEM images of CNTs with an average diameter of 250-300 nm and those filled with CoFe_2O_4 nanoparticles. The magnetic properties of CoFe_2O_4 nanoparticles and CoFe_2O_4 -filled CNTs were investigated using our PPMS.

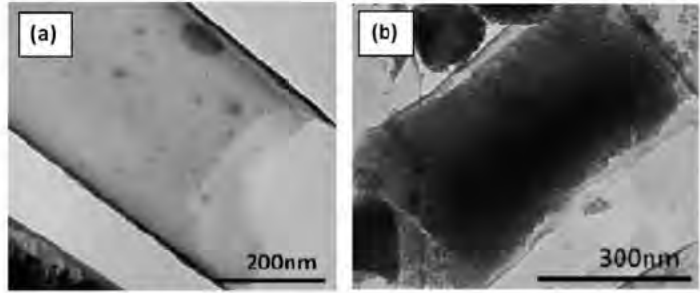


Figure 40: TEM images of (a) as-synthesized CNT; (b) CoFe_2O_4 -filled CNT.

Figure 41a shows the ZFC and FC M-T curves in a magnetic field of 100 Oe for CoFe_2O_4 nanoparticles and CoFe_2O_4 -filled CNTs. It is very interesting to note in this figure that the blocking temperature ($T_B = 264 \text{ K}$) of the CoFe_2O_4 -filled CNTs is significantly larger than that of the CoFe_2O_4 nanoparticles ($T_B = 224 \text{ K}$). As one can see clearly in Figure 41b, $M_S = 37.1$ emu/g for the CoFe_2O_4 -filled CNTs, which is slightly larger compared with that of the CoFe_2O_4 nanoparticles ($M_S = 36$ emu/g). These results indicate that inter-particle interactions are stronger in the CoFe_2O_4 -filled CNTs than in the CoFe_2O_4 nanoparticles.

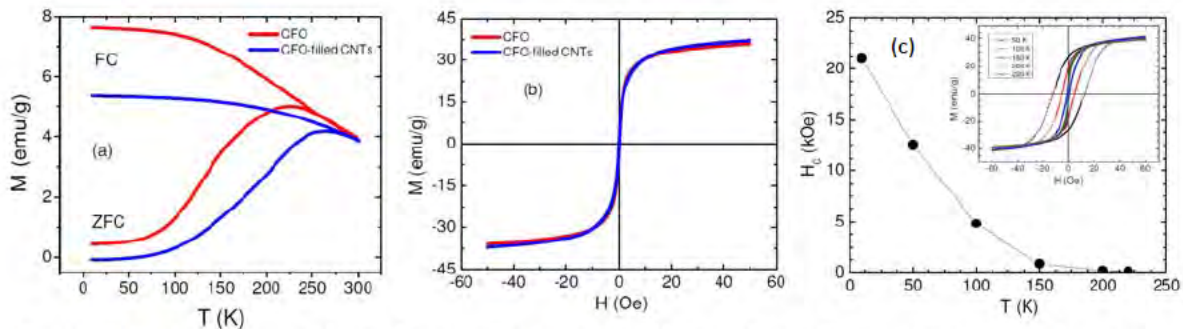


Figure 41: Temperature dependence of coercivity (H_C) of CoFe_2O_4 nanoparticles. The insets shows M-H loops measured at different temperatures below T_B .

In the ferromagnetic regime ($T < T_B$), we have found that the saturation magnetization (M_S) increases and the coercivity (H_C) decreases as temperature decreases (Figure 41c). The temperature dependence of H_C , as extracted from the M-H curves, can be described by

$$H_C = H_{co} \left[1 - \left(\frac{T}{T_B} \right)^{\frac{1}{2}} \right], \quad (3-1)$$

where $T_B = K_u V / 25 k_B$ and $H_{co} = 2\alpha K_u / M_S$ with $\alpha = 0.48$ being a phenomenological constant. From fitting the $H_C(T)$ data using Eq. 4, we have determined $T_B \sim 225$ K for the 7 nm Fe_3O_4 nanoparticles. This value of T_B is consistent with that obtained from the M-T data.

Measurements of the ac susceptibility and analysis give important clues about the spin dynamics and the role of interactions between nanoparticles forming clusters or arrays. Therefore, we have conducted temperature-dependent ac susceptibility measurements at different frequencies. Figure 42a,b shows these data. The magnetic relaxation processes in the nanoparticle systems were studied by analyzing the frequency dependence of the peaks in $\chi'(T)$ and $\chi''(T)$ and fitting these experimental data to the NA and VF models. We have found that the data of both samples fit the VF model, indicating dipolar inter-particle interactions in these systems. Interestingly, the CoFe_2O_4 -filled CNTs show enhanced inter-particle interactions relative to the CoFe_2O_4 nanoparticles. These results are fully consistent for other CNT systems filled with Fe_3O_4 and NiFe_2O_4 nanoparticles, which all reveal the new possibility of tuning the magnetic properties of CoFe_2O_4 -filled CNTs for sensor and microwave device applications.

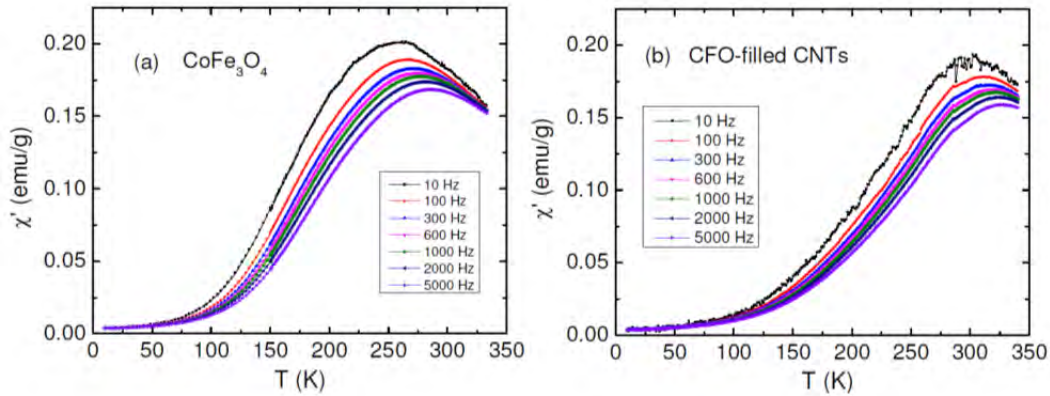


Figure 42: (a) Temperature dependence of the real component of ac susceptibility of CoFe_2O_4 nanoparticles; (b) Temperature dependence of the real component of ac susceptibility of CoFe_2O_4 nanoparticle-filled CNTs.

In conclusion, we have demonstrated that the high compacting of superparamagnetic nanoparticles (Fe_3O_4 , CoFe_2O_4 , NiFe_2O_4) inside CNTs can enhance the saturation magnetization and shape anisotropy, both of which are desirable for enhancing the microwave absorption properties for sensor and microwave device applications. High saturation magnetization and shape anisotropy achieved in our magnetic nanotubes indicate their usefulness not only for microwave and sensor device applications, but also for others such as cantilever tips in magnetic force microscopes, CNT-based biomedical agents, and as interconnects in hybrid CMOS spintronic devices. Recently, we have

introduced a new concept of incorporating superparamagnetic nanoparticles such as Fe_3O_4 and CoFe_2O_4 into a polymer matrix to create a new class of nanocomposite materials with tunable microwave response [41,42]. It is therefore expected that the microwave response can be further enhanced in high-aspect ratio magnetic nanostructures, such as CNTs filled with superparamagnetic nanoparticles, where the magnetic anisotropy can easily be tuned by varying the size and density of magnetic nanoparticles inside CNTs.

3.2. Carbon nanotube-based gas and chemical sensors using RF magneto-impedance technology:

Carbon nanotubes (CNTs) based gas sensors with high sensitivity and selectivity (where sensing is achieved by the DC resistance change upon adsorption of analytic molecules) are critically needed for leakage detections of explosive gases such as hydrogen, and for real-time detections of toxic or pathogenic gases in industries [43]. Due to the extremely high surface-to-volume ratio, CNTs are ideal for gas molecule adsorption and storage. However, these resistive sensors possess limited sensitivities ($\Delta\rho/\rho \sim 2\text{-}10\%$). Therefore it is essential to develop alternative techniques that allow detecting gases with a higher degree of sensitivity.

In this project, we have demonstrated that detecting field-induced impedance change (known as the GMI effect) in CNTs deposited on magnetic ribbons would be a radically new concept which would lead to developing a new class of gas sensors with improved sensitivity. We present below some of the main results of this research.

Carbon nanotubes were grown in commercial porous alumina templates using the chemical vapor deposition (CVD) method without using metal catalysts. The alumina templates were etched away leaving free standing CNTs. The resulting CNTs were between 250 and 300 nm in diameter on average (see inset of Figure 43). The CNTs were then drop-casted onto a Metglas® 2714A ribbon before measuring GMI. Three different concentrations were used and compared to a plain ribbon with no CNTs. Magneto-impedance measurements were conducted along the ribbon axis in dc magnetic fields up to 120 Oe over a frequency range of 0.1 ~ 10 MHz with a constant ac current of 5 mA.

Figure 44 shows that the presence of CNTs increased the $\Delta Z/Z$ ratio in the case of the sample with CNTs. The $\Delta Z/Z$ ratio increased from 34% for the ribbon to 40% for the ribbon with CNTs. With increasing CNT concentration, the $\Delta Z/Z$ ratio first increased, reached a maximum, and decreased as the CNT concentration was saturated. Interestingly, the large $\Delta Z/Z$ ratio was achieved only high frequencies ($f > 1$ MHz), where the skin effect is strong and the surface effect becomes important.

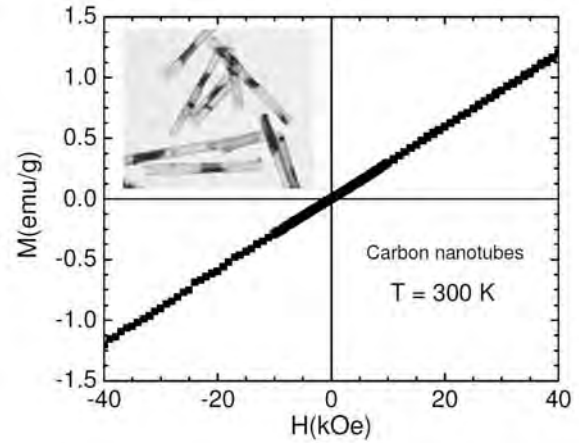


Figure 43: M-H loop of CNTs at 300 K. In inset: TEM of CNTs synthesized using CVD.

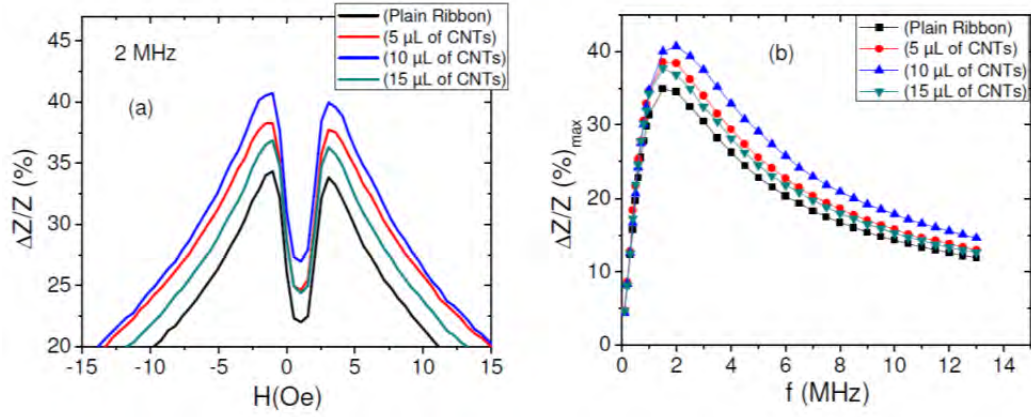


Figure 44: (a) GMI profiles at 2 MHz for the magnetic ribbon with and without CNTs and (b) Frequency dependence of maximum GMI ratio for these samples.

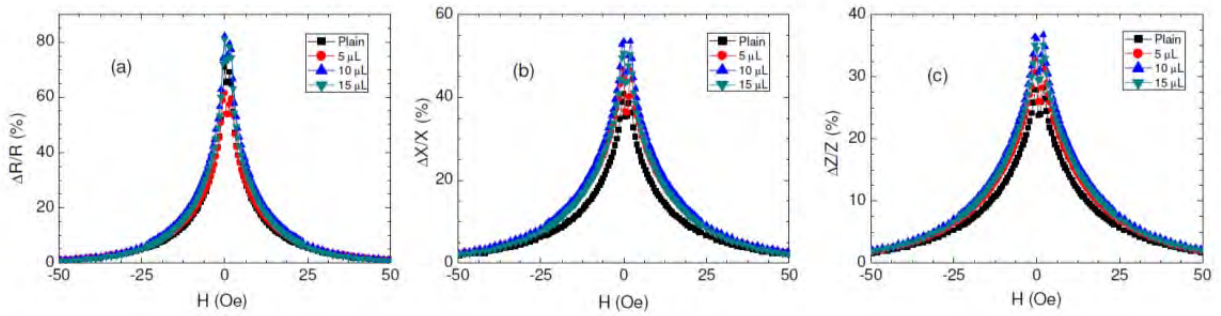


Figure 45: Magnetic field dependence of $\Delta R/R$, $\Delta X/X$ and $\Delta Z/Z$ ratios taken at 5 MHz for the ribbon with and without CNTs.

To elucidate this further, we measured the M-H loop of CNTs at 300 K and the result obtained is shown in Figure 45. It is evident that CNTs showed a paramagnetic behavior. Therefore, the physical mechanism leading to the observed increase of the $\Delta Z/Z$ ratio in the ribbons with CNTs must be different from what has been proposed for the case of supermagnetic nanoparticles. To elucidate this, we have investigated the influence of CNTs on the electrical resistance R and reactance X response ($Z = R + jX$). Figure 45(a-c) shows the magnetic field dependence of $\Delta R/R$, $\Delta X/X$, and $\Delta Z/Z$ ratios for all the samples at $f = 5$ MHz. At this frequency both $\Delta R/R$ and $\Delta X/X$ are larger for the ribbon coated with CNTs. The double-peak feature significantly varied at low magnetic fields in the samples with CNTs. This pointed to the important fact the presence of CNTs could compensate stray fields due to surface irregularities that are present on the surface of the ribbon and consequently increased the GMI effect. The relative contributions of $\Delta R/R$ and $\Delta X/X$ to $\Delta Z/Z$ are different in the investigated frequency range 0.1 – 10 MHz.

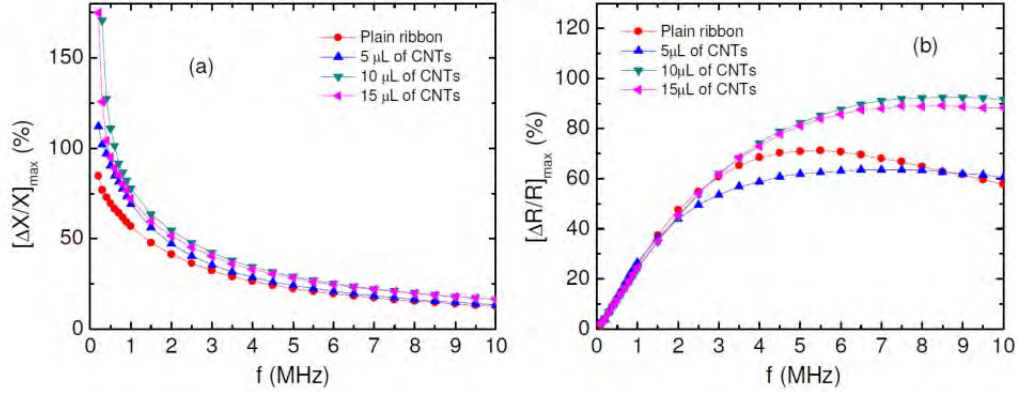


Figure 46: (a) Frequency dependence of (a) maximum $\Delta X/X$ and (b) $\Delta R/R$ ratios for the magnetic ribbon with and without CNTs.

As shown in Figure 46, the presence of CNTs strongly changed $\Delta X/X$ in the low frequency range ($f < 3$ MHz) and $\Delta R/R$ in the high frequency range ($f > 3$ MHz). These findings provide important clues towards a complete understanding of the enhanced GMI effect in the ribbons coated with CNTs. From a practical application perspective, it is very interesting to note that the $\Delta R/R$ ratio (the magnetic field-induced AC resistance change) increases up to 35% for the ribbon coated with CNTs with respect to the plain ribbon. This reveals the new possibility of developing CNT-based gas sensors operating based on the principle of the MI effect with higher field sensitivity compared with current state-of-the art sensors based on the DC resistance change.

In conclusion, we have demonstrated that the presence of carbon nanotubes on the surface of a Co-based amorphous ribbon enhances the GMI effect of the ribbon. This reveals a new perspective for developing a new class of CNT-based gas sensors operating on the principle of the GMI effect. A change in the electrical resistance of the CNTs, when exposed to gases such as NO_2 , NH_3 , H_2O , CO , iodine, and ethanol, may alter the GMI of the ribbon. We have also studied the effect of CNTs filled with magnetic nanoparticles on the GMI effect of a ribbon and found that these magnetic nanotubes are interesting candidates for magnetic biodetection. The results featuring these important findings have been reported in *Journal of Applied Physics* 2012.

3.3. Sensitive detection of magnetic nanoparticle-embedded cancer cells and biomolecules using RF magnetoimpedance technology:

Detection of cancer cells at their earliest stages in the human body, often before symptoms occur, can greatly increase the chances of successful treatment. For this purpose, several methods, such as visual identification of malignant changes, cell growth analysis, specific-ligand receptor labeling or genetic testing have been proposed [44]. However, these methods require lengthy and complicated analysis thus limiting them for practical use. A combination of magnetic sensors with magnetic nanoparticles offers an alternative approach for a highly sensitive, simple, and quick detection of cancer cells [45]. Improving the sensitivity of existing magnetic biosensors for detection of magnetic nanoparticles as biomarkers in biological systems is an important and challenging task.

In this project, we have successfully developed a new class of magnetic biosensor based on the RF magnetoimpedance technology. In particular, we have developed a new method of combining the magneto-resistance (MR), magneto-reactance (MX), and magneto-impedance (MI) effects to develop an integrated magnetic biosensor with tunable and enhanced sensitivity [46]. We show that by exploiting

the MR and MX effects it is possible to improve the detection sensitivity of the biosensor by up to 50% and 100%, respectively. The MX-based approach shows the most sensitive detection of superparamagnetic (Fe_3O_4 , ~10 nm diameter) nanoparticles at low concentrations, demonstrating a sensitivity level comparable to that of a SQUID-based biosensor. Unlike a SQUID, however, the proposed MX technique is cryogen-free and operates at room temperature, providing a promising avenue to the development of low-cost highly sensitive biosensors. A novel biosensor based on the MX effect of a soft ferromagnetic ribbon with a nanohole-patterned surface has been developed for detection of low-concentration functionalized magnetic nanoparticles as magnetic biomarkers in biological systems [47,48]. This biosensor has recently proved its usefulness for the detection and quantification of anticancer drugs (e.g. Curcumin) tagged to superparamagnetic (e.g. Fe_3O_4) nanoparticles [47]. Since such magnetic nanoparticles are widely used as magnetic resonance imaging (MRI) contrast agents, our biosensing technique can also be used as a new, low-cost, fast and easy pre-detection method before MRI.

Detection of low concentration superparamagnetic nanoparticles using a novel RF magnetic sensor: While previous efforts have been focused mainly on developing a biosensor based on the MI effect which has limited sensitivity [49], we have demonstrated a new method of using the principles of radio frequency MR, MX, and MI effects to produce a functional magnetic biosensor with tunable and enhanced sensitivity [46]. In our study, a biosensor prototype was designed by using an amorphous MATGLAS® 2714A ribbon and composition $\text{Co}_{65}\text{Fe}_4\text{Ni}_2\text{Si}_{15}\text{B}_{14}$ as a magnetic sensing element. It was covered by a thin parafilm paper. The ribbon piece was stacked on a non-magnetic glass support and placed at the center of a Helmholtz coil that provided a dc magnetic field ranging up to ± 120 Oe and parallel to its length. A driving current of magnitude 5 mA over the frequency range of 0.1 – 13 MHz was supplied along the ribbon axis, and the DC magnetic field induced magneto-impedance (MI), magneto-resistance (MR), and magneto-reactance (MX) changes were measured by a four-probe technique on a HP4192A impedance analyzer over the length of 10 mm of the ribbon at room temperature. These measurements were performed for 20 μL of various concentrations (0, 124 pM, 1.24 nM, 12.4 nM, 62 nM, 124 nM, 620 nM, and 1.24 μM) of SPIO (superparamagnetic iron oxide) nanoparticles in water.

The change in MR, MX, and MI with the applied field at a frequency of the driving current (also known as the MR, MX, and MI ratios) was calculated. The changes in the MR, MX, and MI ratios due to the presence of SPIO nanoparticles at different concentrations were obtained by subtracting the corresponding responses observed for the blank prototype as, $\Delta\eta = [\xi]_{\max, \text{SPIO}} - [\xi]_{\max, \text{Blank}}$, where $[\xi]_{\max}$ with $\xi = \frac{\Delta R}{R}, \frac{\Delta X}{X}$, and $\frac{\Delta Z}{Z}$ are the maximum values of the MR, MX, and MI ratios, respectively.

Through a systematic study of the magnetic particle (Fe_3O_4 , mean size ~7 nm) concentration dependence of MR, MX, and MI ratios of a soft ferromagnetic amorphous ribbon, we find that these ratios first increase sharply with increase in particle concentration (0 - 124 nM) and then become unchanged for higher concentrations (>124 nM) (Fig. 47 and Fig. 48).

These observations point to the existence of a certain sensing region and an upper limit to detection of the biosensor. While the biosensor with sensitivity optimized at a certain frequency can easily function using each principle, the MX-based biosensor shows the highest sensitivity.

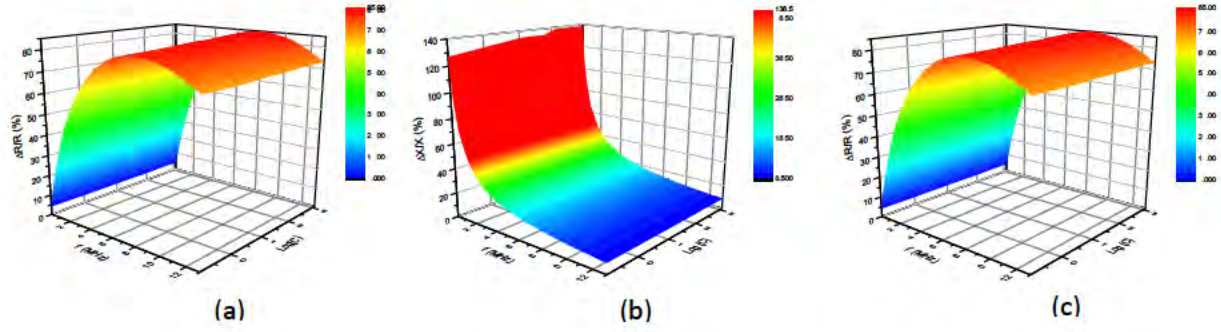


Figure 47: Frequency dependence of (a) MR, (b) MX, and (c) MI for various concentrations of Fe_3O_4 nanoparticles in water.

With this sensor, 3.6×10^{11} 7nm Fe_3O_4 nanoparticles can be detected over a detection area of $2.0 \times 10^7 \mu\text{m}^2$, which is comparable to a SQUID biosensor that detects the presence of 1×10^8 11nm Fe_3O_4 nanoparticles over a detection area of $6.8 \times 10^4 \mu\text{m}^2$. Given that the present biosensor works at room temperature, it is indeed promising for biosensing applications. These findings have been reported in *Journal of Applied Physics* 2013.

A nanoholes-patterned magnetic biosensor with tunable and enhanced sensitivity for highly sensitive detection of functionalized Nanomag-D beads: We have demonstrated a new approach to

improving the detection sensitivity of a ribbon-based GMI biosensor by patterning nanoscale holes on the ribbon surface. We highlight here main results of the GMI detection of functional magnetic beads, Nanomag-D, using a Co-based amorphous ribbon (Fig. 49).

The Metglas® 2714A amorphous ribbon of dimension $16\text{cm} \times 2\text{mm} \times 0.015\text{mm}$ was chosen as the sensing element and impedance was measured over the length of 1cm for 5 mA axial ac current by same techniques and experimental set-up as described above. The impedance was first measured for a plain ribbon (P), then 30 μl of a Nanomag-D suspension (Nmag, 100 $\mu\text{g}/\text{ml}$) was drop-cast on it for comparison. The surface of the ribbon was then treated with 5 μl of dilute (~ 4.5 vol-%) HNO_3 for 24 hrs and washed with distilled water (Figure 49 a,b). The impedance was measured again for the acid-treated ribbon (A), with 5 μl of water, and the same volume of Nanomag-D suspension sequentially. The magneto-resistance (MR) and magneto-reactance (MX) ratios are defined similarly to the case of the MI ratio defined in Eq. (3). The changes in the MR, MX, and MI ratios due to the presence of Nanomag-D

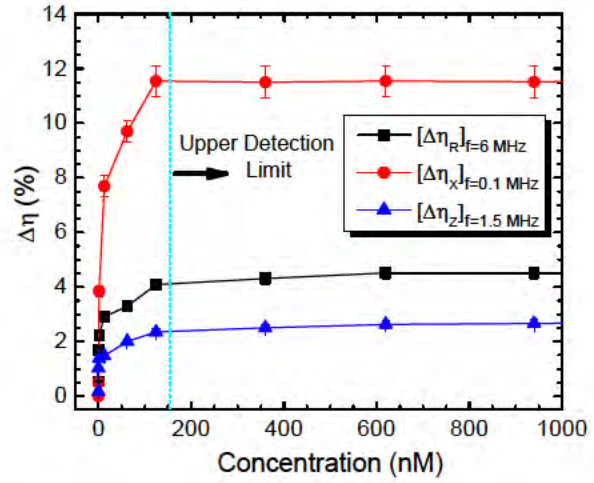


Figure 48: Relative SPIO particle concentration dependence of MR, MX, and MI showing the sensitivity and upper limit of the detection of the biosensor.

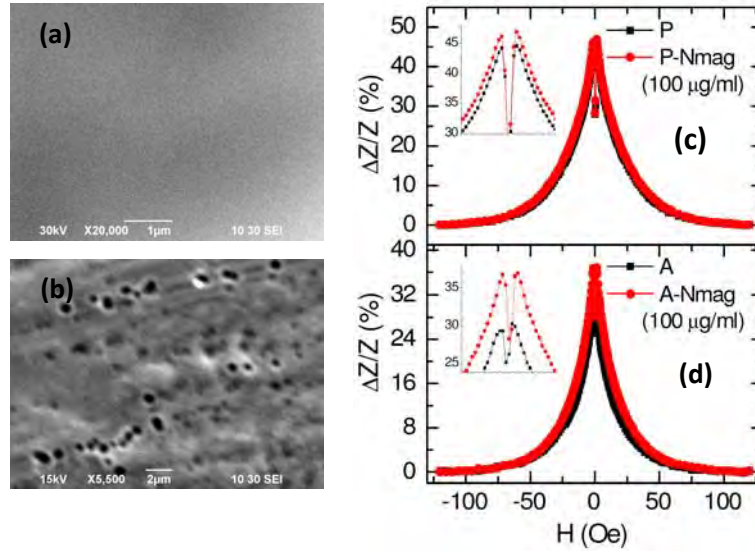


Figure 49: SEM images of plain (a) and Nitric acid ~4 vol -%) treated (b) ribbons, and corresponding GMI profiles (c – d) with and with Nanomag-D bead suspension (5 µl).

beads are obtained by subtracting the corresponding responses observed for the plain ribbon, representing the sensitivity of the biosensor detection, $\Delta\eta_{\xi}$.

Figure 50(c,d) shows the field dependence of GMI ratio at a frequency 1.5 MHz for both plain and acid-treated ribbons. As one can see clearly, the GMI effect of the ribbon is altered due the presence of functionalized Nanomag-D beads on its surface. It is worth noting that the etch pits due to the HNO_3 treatment (Figure 49 b) enhances the Nanomag-D detection sensitivity by about three times compared to that observed for the plain ribbon (Figure 7d). This indicates that treating the surface of a ribbon with an appropriate concentration of acid can be an effective way of creating nano-traps and improving the detection of a ribbon-based GMI biosensor. As seen in Figure 50, there are large enhancements in the maximum of MR, MX, and MI ratios and corresponding field sensitivities of the acid-treated ribbon over a wide frequency range of 0.1 – 13 MHz due to the presence of Nanomag-D bead suspension, while a negligible effect was found in the case of the ribbon with the presence of equal volume of water. The highest values of $\Delta\eta_{\xi}$ observed for MR, MX, and MI due to the presence of Nanomag-D beads are 16%, 23%, and 7% at $f = 10, 0.1, \text{ and } 0.7 \text{ MHz}$, respectively. These findings indicate that it is possible to use the combined measurements and analysis of MR, MX, and MI for making a functional biosensor with enhanced

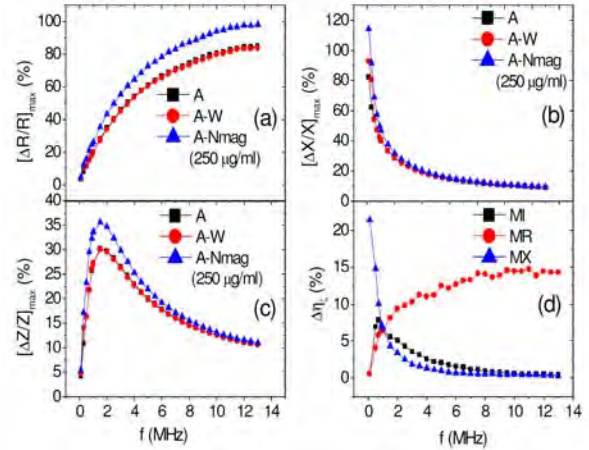


Figure 50: Frequency dependence of maximum (a) magneto-resistance, (b) magneto-reactance, (c) magneto-impedance for samples A, A-W, and A-Nmag (250 µg/ml), and (d) the difference in MR, MX, and MI between the A-W and A-Nmag (250 µg/ml).

sensitivity and tunable working frequency. These important results have been published in *IEEE Transactions on Magnetics* 2013.

An ultrasensitive magnetic biosensor for detection and quantification of anticancer drugs tagged to superparamagnetic nanoparticles: Based on our previous achievements, we have developed an ultrasensitive MX-based magnetic biosensor for detection and quantification of anticancer drug Curcumin (Cur) tagged to superparamagnetic (Fe_3O_4) nanoparticles via bio-functionalized nanoconjugates (Fe_3O_4 -Alg-Cur), where Alginate (Alg) was used to chemically stabilize the surface of Fe_3O_4 nanoparticles. In this work, Fe_3O_4 nanoparticles of 10 ± 2.5 nm diameter were chemically stabilized by coating with Alg (which is a polysaccharide extracted from brown algae), then functionalized with Cur (which is a yellow compound isolated from rhizome of *Curcuma longa* L. plant and is widely used as an anticancer drug for applications in drug delivery and hyperthermia) to obtain the Fe_3O_4 -Alg-Cur nanoparticles of 120 ± 15 nm diameter. The detail of the synthesis of these functionalized nanoparticles has been reported elsewhere [48]. The inset of Figure 51 shows a typical SEM image of the Fe_3O_4 -Alg-Cur nanoparticles. The room-temperature superparamagnetic nature of the Fe_3O_4 -Alg-Cur nanoparticles is evident with the absence of the coercivity ($H_C \sim 0$) in the magnetic hysteresis $M(H)$ loop taken at 300 K and the best fit of the $M(H)$ data to the Langevin function (Figure 51).

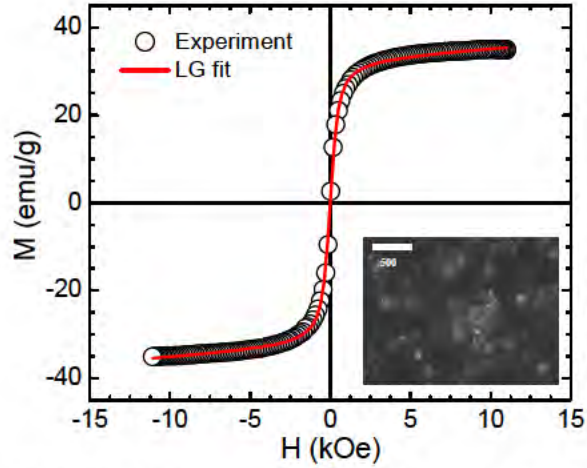


Figure 51: Magnetic hysteresis loop of the Fe_3O_4 -Alg-Cur nanoparticles. The inset shows a typical SEM image of the Fe_3O_4 -Alg-Cur nanoparticles.

Figure 52(a) shows the magnetic field dependence of the MX ratio ($\Delta X/X$) taken at 0.5 MHz for a plain ribbon, with 10 μl of DI water, 10 μl of a 250 ng/ml Fe_3O_4 -Alg-Cur nanoparticle solution, and after removing the solution completely. The inset shows the enlarged view of the $\Delta X/X$ profiles. The presence of water and Fe_3O_4 -Alg-Cur nanoparticles on the surface of the ribbon has negligible influence on the double-peak structure of the $\Delta X/X$ profile. The presence of water (with and without dispersed Fe_3O_4 -Alg-Cur nanoparticles) also does not alter the $\Delta X/X$ ratio of the plain ribbon, indicating a negligible corrosion effect of water on the presently used ribbon. It is worth noting here that the presence of Fe_3O_4 -Alg-Cur nanoparticles on the surface of the ribbon results in an increase in the $\Delta X/X$ ratio by 18%. This increase in the MX ratio can be explained by considering the effect of the fringe fields of Fe_3O_4 -Alg-Cur nanoparticles on the superposition of the applied axial dc magnetic field and the induced transverse ac field (due to an ac current flowing along the axis of the ribbon). To probe the effects of water and Fe_3O_4 -Alg-Cur nanoparticles on the MX response of the ribbon at different frequencies, we have measured the MX of the plain ribbon, with water (10 μl), and with 10 μl of a 250 ng/ml Fe_3O_4 -Alg-Cur nanoparticle solution over a frequency range of 0.2 – 2.5 MHz.

Figure 52b shows the frequency dependence of maximum MX ratio (i.e. $[\Delta X/X]_{\max}$) for these samples. It can be observed that $[\Delta X/X]_{\max}$ is largest at 0.2 MHz and decreases sharply with increasing frequency in the range of 0.2 – 2.5 MHz. From a biosensing perspective, it is interesting to highlight that while almost identical values of $[\Delta X/X]_{\max}$ are obtained for the plain ribbon with and without water, the presence of Fe_3O_4 -Alg-Cur nanoparticles results in significantly larger values of $[\Delta X/X]_{\max}$ in the frequency range of 0.2 – 2.5 MHz. We have defined the detection sensitivity of the sensor (η), as the difference in $[\Delta X/X]_{\max}$ between the plain ribbon and the ribbon with Fe_3O_4 -Alg-Cur nanoparticles. The variation in η with frequency is plotted in inset of Figure 52b. As one can see in this figure, η has a maximum value of ~30% at 0.2 MHz and decreases sharply with increase in the frequency. This value of η is about 4-5 times higher than that of a GMI-based biosensor reported in the literature. For this reason, a frequency of 0.2 MHz was chosen for studies of detection of Fe_3O_4 -Alg-Cur nanoparticles of varying concentrations.

Figure 52c displays the magnetic field dependence of the MX ratio at 0.2 MHz for the ribbon with Fe_3O_4 -Alg-Cur nanoparticles at various concentrations. The detection sensitivity (η) has been calculated for all particle concentrations, and its variation with particle concentration is depicted in Figure 52d. It can be seen that η first increases sharply in the range of 0 – 50 ng/ml (from ~3.5% for 10 ng/ml to ~30 % for 50 ng/ml) and then remains almost unchanged for higher concentrations (50 ng/ml – 250 ng/ml). A similar trend has recently been reported by us for the case of non-functionalized Fe_3O_4 nanoparticles. This can be understood by considering the disturbance of the applied dc longitudinal and ac transverse fields due to the presence of the fringe fields of the Fe_3O_4 -Alg-Cur nanoparticles on the surface of the ribbon. As the concentration of Fe_3O_4 -Alg-Cur nanoparticles is increased, the strength of the fringe fields also increases, thus disturbing the dc and ac magnetic fields on the ribbon to a greater degree and consequently altering the MX. This superposition effect becomes independent of Fe_3O_4 -Alg-Cur nanoparticles as particle concentration exceeds a critical value (~50 ng/ml in the present case), setting an upper limit of the sensor detection.

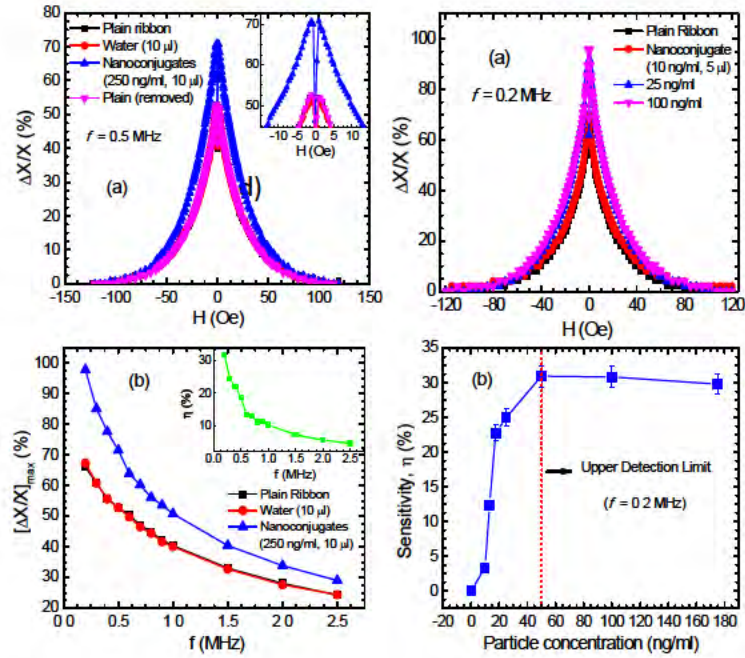


Figure 52: (a) Magnetic field dependence of the MX ratio ($\Delta X/X$) at 0.5 MHz for the plain ribbon, with water (10 μ l), with 10 μ l of a 250 ng/ml Fe_3O_4 -Alg-Cur nanoparticle solution, and after removing the solution. The inset shows an enlarged view of the $\Delta X/X$ profiles; (b) Frequency dependence of the maximum MX ratio ($[\Delta X/X]_{\max}$) for these samples. The inset shows the frequency dependence of the sensor detection sensitivity (η); (c) Magnetic field dependence of the MX ratio ($\Delta X/X$) at 0.2 MHz for various concentrations of Fe_3O_4 -Alg-Cur; (d) Particle concentration dependence of the sensor's detection sensitivity.

In conclusion, we have demonstrated the possibility of using the magneto-reactance effect of a soft ferromagnetic amorphous ribbon to develop a highly sensitive magnetic biosensor for detection and quantification of anticancer drugs (Curcumin) tagged to superparamagnetic (Fe_3O_4) nanoparticles. This type of biosensor is particularly suited for detection of low-concentration superparamagnetic nanoparticles as magnetic biomarkers in biological systems. It can also be used as a new, low-cost, fast and easy pre-detection method before MRI. These important findings have been submitted for publication in *Journal of Applied Physics* 2013.

A new type of coil-based magnetic biosensor for detection of Au- Fe_3O_4 nanoparticle-embedded human embryonic kidney cells: We have developed a new type of magnetic biosensor using a tunnel diode oscillator (TDO)-based radio-frequency (RF) transverse susceptibility technique for detection of Au- Fe_3O_4 nanoparticles taken up by human embryonic kidney (HEK) cells [51]. Since this resonant method can detect small changes in the magnetic signal of even small amounts of nanoparticles taken up by cells, it is a very promising tool for biosensing applications. We present below briefly how Au-coated Fe_3O_4 nanoparticles were synthesized, functionalized and transfected into cells and finally detected using a RF magnetic biosensor.

In this work, Au-coated Fe_3O_4 nanoparticles were synthesized using a micellar method. First, a stock solution was made by dissolving ferric ammonium sulfate (0.128 M with respect to the Fe(III) ion) and ferrous ammonium sulfate (0.064 M with respect to the Fe(II) ion) in 100 mL 0.40 M aqueous sulfuric acid. A separate solution of 1.0 M NaOH was added to 0.01 M poly(oxyethylene)isooctyl phenylether (TX-100) to make a concentration of 0.01 M TX-100. This solution was heated to 70–80 °C, and 25 mL of the iron stock solution was added dropwise while stirring. Heating and stirring continued for 30 min while Fe_3O_4 nanoparticles were formed. The particles were centrifuged to separate them from the solution and washed. The resulting Fe_3O_4 particles were then coated with Au. For this step 0.5 g of glucose was added to a solution of 1:1 molar ratio Fe_3O_4 to HAuCl_4 . The solution was sonicated for 15 min and then heated at 80 °C in a water bath for 1 hour.

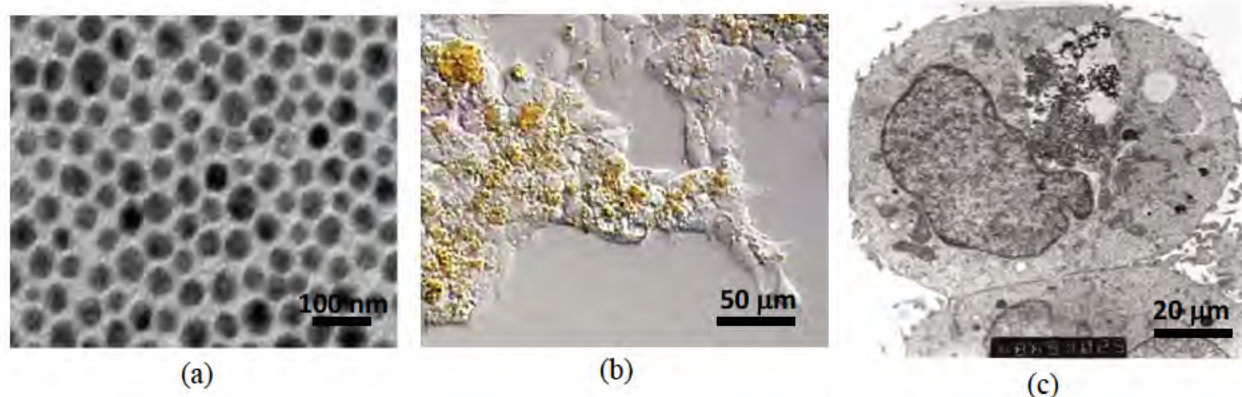


Figure 53: (a) TEM image of Au- Fe_3O_4 nanoparticles; (b) Optical and (c) TEM images of the nanoparticles (circled) inside HEK cells.

Human embryonic kidney (HEK293) cells were obtained from the American Type Culture Collection (ATCC). Cells were cultured on a plastic substrate at 37 °C in minimum essential medium containing 10% fetal bovine serum and 100 units/mL each of penicillin and streptomycin in an atmosphere of 5% CO_2 /95% air. Au- Fe_3O_4 nanoparticles were introduced to the medium at

concentrations of 0.05 mg/mL, 0.1 mg/mL, 0.5 mg/mL, and 1 mg/mL, where they were phagocytosed by the cells. Cells were then detached from the substrate by removing excess medium, rinsing the cell layer with 0.25% (w/v) trypsin-0.53 mM EDTA solution and incubating them for 3–5 min with the trypsin-EDTA solution. A complete growth medium was then added to the cells for incubation. Figure 53a shows a TEM image of Au-Fe₃O₄ particle sizes of 60 nm ± 10 nm. This size of particle is desirable because the cells to be used in this experiment preferentially take up particles of 60–70 nm. Figure 53b,c show optical and TEM images of cells after uptake of nanoparticles. The circle indicates the region where the nanoparticles are located, and the particles appear as dark, filament-like structures. The nanoparticles can be recovered from the cells through homogenization. The particles are being phagocytosed or endocytosed at a maximum concentration (1 mg/mL) of approximately 70%.

We now demonstrate that the RF transverse susceptibility technique can be used as a biosensor for the detection of biological cells that have taken up magnetic nanoparticles. A simple schematic of the RF transverse susceptibility circuit and a cut-away view of our existing set-up mounted on a cryogenic insert are shown in Figure 54. The TDO is housed outside of a commercial physical property measurement system (PPMS by Quantum Design) which serves to modulate the applied DC magnetic field ($\mu_0 H$ up to ± 7 T), as well as the measurement temperature ($2 \text{ K} < T < 350 \text{ K}$). The sample is placed in an inductive coil which is part of an ultrastable, self-resonant tunnel-diode oscillator (operating frequency around 10 MHz to 20 MHz) with

a perturbing small amplitude RF field perpendicular to the externally applied DC field (in the PPMS). Transverse susceptibility is defined as $\chi_t = \frac{dM_x}{dH_z}$ and

in our experiment this is measured from the shift in resonance frequency as a function of variable field and temperature. Because the change in frequency of the circuit is a direct consequence of the change in inductance as the sample is magnetized, the quantity Δf is directly proportional to $\Delta \chi_T$. We are therefore most interested in the quantity:

$$\frac{\Delta \chi_T}{\chi_T} (\%) = \frac{|\chi_T(H) - \chi_T^{\text{sat}}|}{\chi_T^{\text{sat}}} \times 100 \quad (3-3)$$

as a function of H_{DC} where χ_T^{sat} is the transverse susceptibility at the saturating field, H_{sat} . This quantity, which represents a figure of merit, does not depend on geometrical parameters and is useful for comparing the transverse susceptibility data for different samples, or for the same sample under different conditions.

Since this is a technique based on finding the change in the resonant frequency of the circuit in the presence of a magnetic field, the uncertainty in a specific data point is determined by the uncertainty in each resonant frequency measured and the change in each resonant frequency in the presence of a field. Usually a TS spectrum in a unipolar field scan from positive to negative saturation should consist

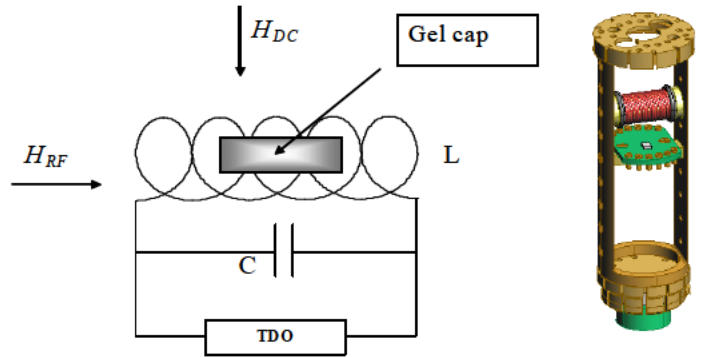


Figure 54: Schematic of the TDO circuit and sample space (a) and computer-aided design (CAD) drawing of the inductance coil which serves as the sample holder (b).

of three singularities, of which two occur at the anisotropy fields ($\pm H_K$) and one at the switching field ($\pm H_S$). However, for an array of nanoparticles with a distribution in size, the switching peak is often merged with one of the anisotropy peaks and a marked asymmetry in both peak location heights can be seen. Since the high sensitivity comes from our ability to detect changes of the order of a few Hz in the overall resonance of 10 MHz to 20 MHz, the TS technique is well suited for biosensing where the signal from even a small number of target cells that have taken up magnetic nanoparticles can be detected. This technique is also good for evaluating magnetic nanoparticles for MRI contrast enhancement since the set-up geometry is nearly identical.

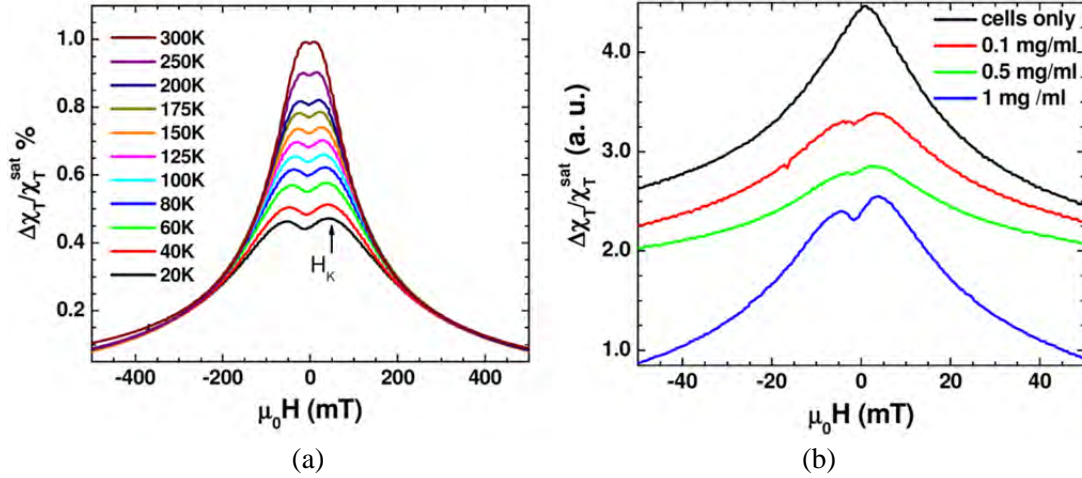


Figure 55: (a) Transverse susceptibility scan taken at different temperatures for Au-Fe₃O₄ nanoparticles; (b) Transverse susceptibility measurements of HEK cells with varying concentrations of Au-Fe₃O₄ nanoparticles. The black scan is for the cells without any nanoparticles. The scans have been shifted vertically to better compare the characteristics of each sample.

Figure 55a shows unipolar TS scans with magnetic fields sweeping from 0.5 T to -0.5 T for different temperatures between 20 K and 300 K for the Au-Fe₃O₄ nanoparticles. It is observed that in the temperature range of 20 K to 300 K the TS profiles show a double-peak and the peak locations (which correspond to $\pm H_K$) shift to smaller fields as the temperature is increased. This trend can be reconciled with the fact that the particle system transitioned from the ferromagnetic state to the superparamagnetic state. However, the presence of H_K detected even at 300 K indicates that not all of the Au-Fe₃O₄ particles have undergone the ferromagnetic to superparamagnetic transition. This feature will be used to distinguish the difference in TS signal between the cells with and without Au-Fe₃O₄ nanoparticles, and the cells containing different amounts of Au-Fe₃O₄ nanoparticles. For each sample, TS measurements were performed on cells that were not exposed to nanoparticles, as well as cells after uptake of Au-Fe₃O₄ nanoparticles at different concentrations (0.05 mg/mL, 0.1 mg/mL, 0.5 mg/mL, and 1 mg/mL buffer). A sample of cells was placed inside a liquid-safe, 1 mL sample holder.

Figure 55b shows the unipolar TS scan of the cells with several concentrations of the Au-Fe₃O₄ nanoparticles, as well as a scan of cells without nanoparticles. It can be seen that the TS probe was able to detect a signal from the nanoparticles inside the cells, whereas the cells by themselves left no signal. While the highest concentration of the Au-Fe₃O₄ nanoparticles (1 mg/mL) gives the best signal, it is important to note that at concentrations as low as 0.1 mg/mL, the signal of the Au-Fe₃O₄ nanoparticles can still be detected. The anisotropy peaks seen for nanoparticles inside cells appear more defined than

those seen at room temperature for Au-Fe₃O₄ particles alone. This experiment demonstrates how transverse susceptibility as a measurement technique can act as a biosensor for the presence of magnetic nanoparticles inside targeted cells. This could be used in a diagnostic capacity if the nanoparticles were functionalized with a biomarker specific to a type of cancer cell. Targeting and uptake of the nanoparticles would only occur if the cells were cancerous. Transverse susceptibility could then be used to determine if the cells had taken up the particles and, hence, were cancerous. Selected results have been published in *Sensors* 2013.

3.4. Controlled synthesis and excellent magnetic properties of core-shell CoFe₂O₄-PZT nanotubes:

Multiferroic composite materials consisting of both ferro/ferrimagnetic and ferroelectric phases have drawn an increasing amount of interest due to their capability of efficient energy transfer between electric energy and magnetic energy, and their potential applications in many multifunctional devices [50]. Such materials can display the magnetoelectric effect, a dielectric polarization variation as a response to an applied magnetic field, or an induced magnetization by an external electric field.

In this project, we have successfully synthesized a new class of core-shell ferromagnetic/ferroelectric nanorod structures with CoFe₂O₄ (CFO) core and Pb(Zr_{0.52}Ti_{0.48})O₃ (PZT) shell using an alumina template and investigated their structural and magnetic characterization. To our best knowledge, it is the first report on such nanostructures. We briefly describe how they were fabricated and characterized.

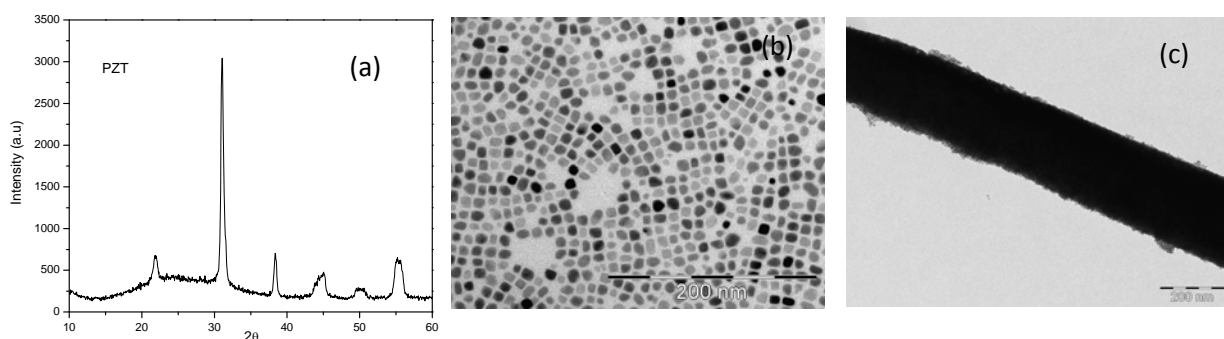


Figure 56: (a) XRD of PZT nanotubes; TEM images of (b) CFO nanoparticles and (c) the PZT nanotube filled with CFO nanoparticles.

In this work, a 0.3M PZT precursor with the molar ratio of 1.1:0.52:0.48 was prepared by dissolving lead acetate Pb(CH₃CO₂)₂·3H₂O, zirconium propoxide Zr(CH₂CH₂CH₃O)₄, and titanium butoxide Ti(C₄H₉O)₄ into 2-methoxyethanol. An alumina (AAO) template with pore diameter of 200 nm was immersed into the PZT precursor solution for 20 min then the wet template was baked in air at 300 °C for solvent removal and annealed in air at 725 °C for 1 h to grow the PZT nanorods. After annealing the alumina template, a few drops of CoFe₂O₄ ferrofluid (synthesized in our lab) was deposited on to the membrane keeping a permanent magnet (μ₀H = 0.4 T) underneath the template. CoFe₂O₄@PZT core-shell nanorods were collected from the AAO template by dissolving the template in NaOH solution. XRD has been done on PZT nanorods and CoFe₂O₄ separately and the perovskite PZT phase (Figure 56a) and spinel CoFe₂O₄ phase were observed. The TEM images of CoFe₂O₄ and CoFe₂O₄-filled PZTs are shown in Figure 56b,c. The TEM image shows the cube-shaped CFO nanoparticles with an average particle size 8 ± 1 nm. These particles were nicely packed inside the PZT nanotubes. The average length of PZT is 4-5 μm and diameter is 250-300 nm with 30 nm wall thickness.

So the aspect ratio of these magnetic nanotubes comes out to be ~ 20 . The magnetic properties of CoFe_2O_4 nanoparticles and CoFe_2O_4 -filled PZTs were done using our PPMS. For these measurements, the dry samples were loaded in a standard, non-magnetic gelatin capsule. The blocking temperature is $T_B \sim 294$ K for the CoFe_2O_4 nanoparticles and 307 K in the CoFe_2O_4 -filled PZT nanotubes. The increase in T_B indicates that the anisotropy energy density of the nanoparticles increases, due to the confinement of the nanoparticles inside the PZT nanotubes.

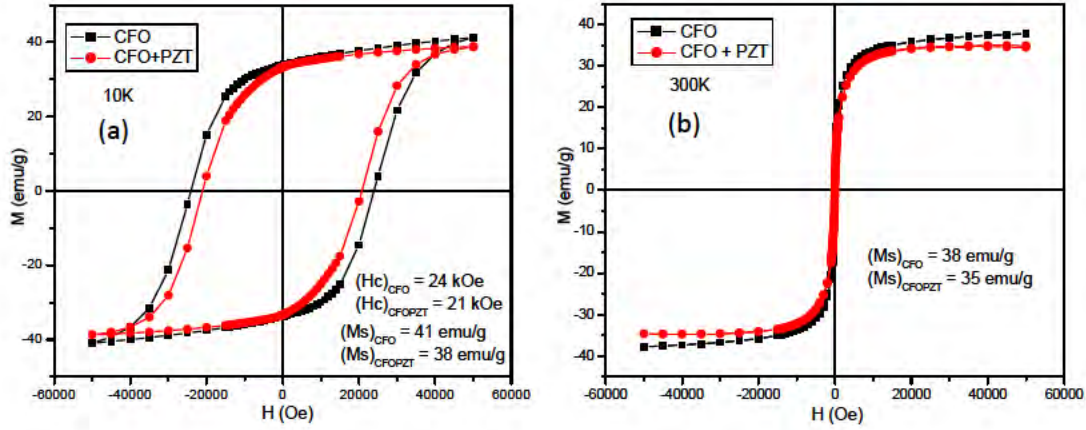


Figure 57: M-H loops at 10 K (a) and 300 K (b) for the CFO and CFO-filled PZT nanotubes

Magnetic field-dependent magnetization (M-H) measurements at 10 K show a hysteresis loop with large values of coercivity (H_c) for both CFO and CFO-PZT samples (Figure 57). The coercivity of CoFe_2O_4 nanoparticles is ~ 24 kOe and it is ~ 21 kOe for the CFO-PZT sample. The saturation magnetization M_s of CFO nanoparticles is 41 emu/g, which is almost identical to that of the CFO-PZT system ($M_s = 38$ emu/g). The room temperature M-H data show no coercivity for both the samples, indicating the superparamagnetic nature of the nanoparticles. It is worth highlighting that the coercivity and the saturation magnetization do not change considerably in the CFO-PZT system, which is desirable from magnetic-field guided applications point of view. A manuscript featuring these important results is being written for publication in *Applied Physics Letters* 2013.

Project 4: Functional materials for affecting cell proliferation and locomotion

4.1. Magnetic nanoparticle attachment to cell membranes:

In this project, we are looking at several nanoscale structures where the basic functionality such as magnetic and metallic properties can be used for biomedical diagnostics and cell manipulation. We have synthesized water-soluble, biocompatible nanoparticles and conducted studies on cell uptake using optical microscopy and electric cell substrate impedance sensing (ECIS).

Superparamagnetic iron oxide nanoparticles have drawn special attention for various biomedical applications such as diagnosis, therapeutics, separations, contrast agent for magnetic resonance imaging. [52-54] This is because they possess high saturation magnetization and are also less toxic than the other metal or metal oxide nanoparticles. In general nanoparticles suitable for biomedical applications should be (i) highly water dispersible, (ii) monodisperse (iii) surface modified by biocompatible reagents. In this work we have synthesized highly water dispersible polyethylene glycol (PEG) diacid surface modified iron oxide nanoparticles.

We have synthesized Fe_3O_4 nanoparticles and functionalized them with polyethylene glycol (PEG). PEG is an amphiphilic polymer and coating on Fe_3O_4 by PEG makes iron oxide particles biocompatible. Synthesis procedure is outlined below:

Synthesis of Fe_3O_4 nanoparticles: The synthesis and surface functionalization of Fe_3O_4 nanoparticles were followed the procedure described by Sun et al [54]. Briefly 2 mmol of iron (III) acetylacetonate [$\text{Fe}(\text{acac})_3$], 10 ml benzyl ether and 10 ml oleylamine were mixed together. The solution was heated to 110°C for 1h and finally to 300°C for 2h. The solution was cooled to room temperature and 50 ml ethanol was added to it. The black precipitate was collected by centrifugation and this procedure was repeated three times. Finally the product was redispersed in hexane and 0.25 ml of oleic acid was added to stabilize the particles.

Surface functionalization of Fe_3O_4 nanoparticles: PEG diacid (20 mg), 2 mg N-hydroxysuccinimide, 3 mg N, N' dicyclohexylcarbodiimide and 1.27 mg dopamine hydrochloride were dissolved in a solvent mixture of 2 ml chloroform and 1 ml dimethyl formamide. Anhydrous Na_2CO_3 (10 mg) was added to the reaction mixture. Then the reaction mixture was stirred at room temperature for 2h. 5 mg Fe_3O_4 nanoparticles were added and the reaction mixture was stirred overnight in presence of argon at room temperature. The modified Fe_3O_4 nanoparticles were precipitated by adding hexane. The precipitate was collected by a permanent magnet and dried under Ar. The particles were dispersed in water. Figure 58 shows the XRD and TEM characterization of these nanoparticles. XRD shows pure Fe_3O_4 phases present in the sample and TEM image shows

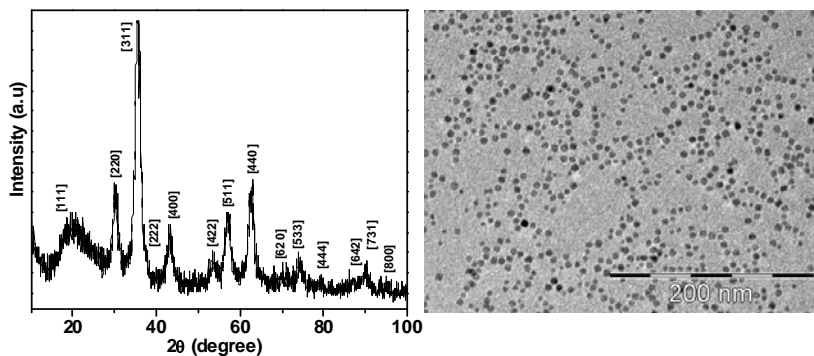


Figure 58: Structural characterization (XRD and TEM) of water-soluble, biocompatible nanoparticles

the particles are nicely dispersed in water without any agglomeration. The particle size is 4-5 nm.

Cell culture:

The 3T3 cells and the water dispersed Fe_3O_4 nanoparticle-loaded 3T3 cells were incubated at 37 °C (5% CO_2) overnight. Three different concentrations (10, 100 and 300 μl) of nanoparticles were added to a certain number of cells. The nanoparticles uptake by cells was studied by optical microscopy and electric cell substrate impedance sensing (ECIS) measurement (Figure 59).

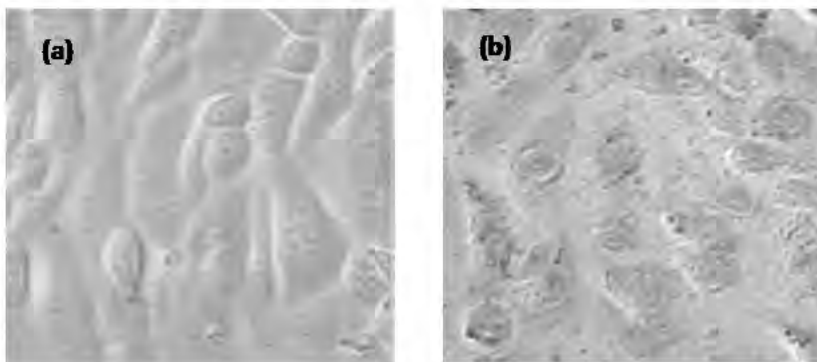


Figure 59: Optical microscopy image of (a) 3T3 cells as control/medium and (b) Fe_3O_4 nps labeled 3T3 cells.

Optical microscopy study:

The microscopic images show the intercellular dispersion of the particles and no adverse effect has been observed upon nanoparticle labeling in cells.

Electric cell substrate impedance sensing (ECIS) measurement:

In this measurement we have studied the resistance with time for all samples including the control (see Figure 60). Electrode arrays, relay bank, lock-in amplifier and software for the ECIS measurement and data analysis were from the instrument commercialized by Applied BioPhysics (Troy, NY). Each electrode array consisted of eight wells which was 1 cm in height and 0.8 cm^2 in bottom area; each well contained a 250 μm diameter gold electrode (area $\sim 5 \times 10^{-4} \text{ cm}^2$) and a much larger gold counter electrode. The large electrode and one of the small electrodes were connected via the relay bank to a phase-sensitive lock-in amplifier. A 1V AC signal at 4 kHz was applied to the sample through a 1M Ω resistor to maintain an approximately constant current of 1 μA through the sample i.e. the in-phase voltage was proportional to the resistance, and the out-of-phase voltage was

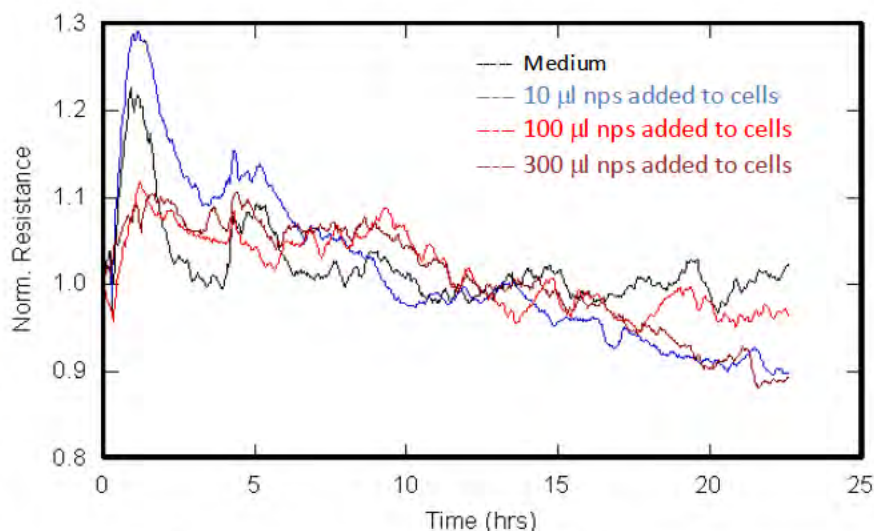


Figure 60: ECIS spectra of cells loaded with different concentrations of biocompatible nanoparticles

proportional to the capacitive reactance. For impedance measurement of 3T3 cells upon addition of Fe_3O_4 particles, the samples were cultured for 24 h.

The time-series data were normalized and numerically analyzed by calculating power spectrum and variance (the square of the standard deviation). The normalized resistance with time plot and variance with time plot of the nanoparticle loaded samples are similar to the control sample which indicate that the cell viability is not affected by the nanoparticle loading upto 300 μl concentration of nanoparticles.

4.2. Design and fabrication of lithographically patterned metallic micro-wires:

Micro-wires of Al have been fabricated on silicon substrates by the following steps:

- (1) Lithographically define the areas where the metal strips are to be deposited,
- (2) Using thermal evaporation deposit an Al film on the patterned substrate.
- (3) Chemically etch the photoresist. A scanning electron microscopy (SEM) image of the micro-wires fabricated by the above method is shown in Figure 61.

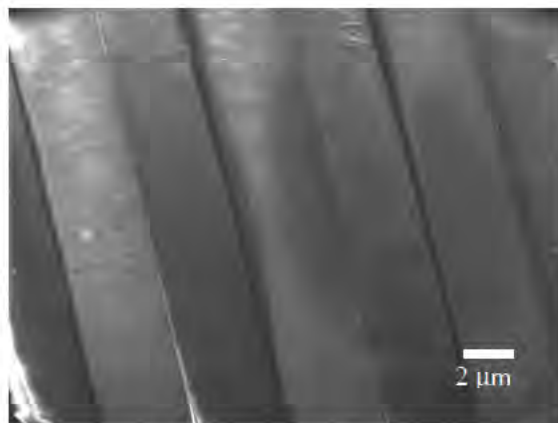


Figure 61: Metallic electrodes fabricated on glass substrates by

4.3. Design and fabrication of substrates with controlled nanotopography

4.4. Study of cell migration, cell-substrate adhesion, and cell growth

4.5. Stimuli-response studies using ECIS of magnetic nanoparticle loaded cells:

Tasks 4.3, 4.4, and 4.5 have been merged with Task 4.6 (described below). The change to the project tasks were presented in the Year 3 annual report.

4.6. An integrated functional materials approach to the development of an artificial Matrigel:

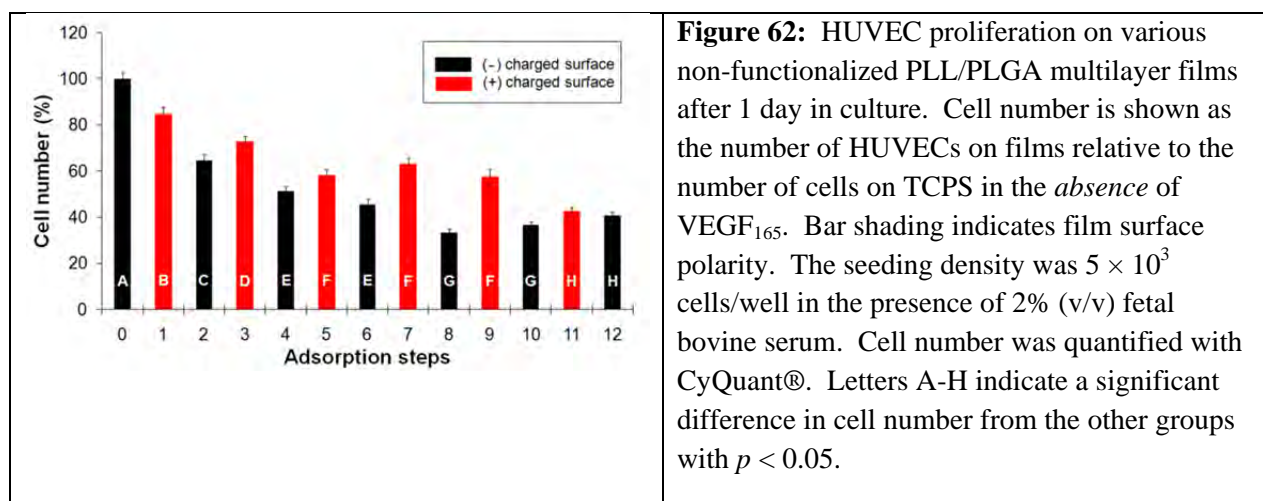
This project is an investigation of the combined effects of physical and biochemical stimuli on adhesive mammalian cells *in vitro*. Polypeptide multilayer films provided a means of controlling substrate charge, viscoelasticity, and functionalization. Adhered collagen I (CI)-derived peptides and soluble vascular endothelial growth factor (VEGF) represented means of controlling exposure of cells to specific biochemical cues. All polymers utilized for film fabrication were produced synthetically; VEGF was recombinant. This work focused on human umbilical vein endothelial cells (HUVECs) as a model cell type.

HUVECs are commonly employed in physiopharmacological investigations such as bioactive-molecule transport, blood coagulation and fibrinolysis [55-57]. These cells respond to cytokine concentration, cell adhesion molecule surface density, and other environmental stimuli [58-60]. Under some conditions, proliferative cell morphology can be transformed into tubular structures, as in neovascularization, a usual prerequisite for tumor progression [61, 62]. HUVEC culture conditions are thus determinative of cell fate.

Responses of cells to mechanical properties of the adhesion substrate have been investigated for many years [63-67]. Such studies have shown that adherent cells tend to spread more, adhere better, and survive longer on comparatively stiff substrates. Similar tendencies have been found for polyelectrolyte multilayer film-coated materials [68]. Multilayer films made of polyaminoacids (e.g., PLL) and polysaccharides (e.g., chitosan) show poor cell adhesion or anti-adhesion if the films are “thick”, i.e., consist of more than 12 “layers” [68-71]. Surprisingly, the present study has revealed that HUVECs adhere less to multilayer films of any thickness than tissue-culture poly(styrene) (TCPS), despite the apparent greater similarity of a polypeptide multilayer film than TCPS to the extracellular matrix. HUVECs also appear to proliferate rapidly on TCPS than the films.

Cell adhesion:

Figure 62 shows HUVEC adhesion on various PLL/PLGA films after 1 day of culture in serum-containing medium. Varying the number of polypeptide adsorption steps led to differences in HUVEC behavior. Specifically, cell adhesion decreased on increasing the number of adsorption steps (decreasing substrate rigidity). The buildup of PLL/PLGA proceeded exponentially (Figure 63), similar to various reported polyelectrolyte systems [72-76]; film thickness increased with the number of adsorption steps. As expected, thicker films were softer than thinner films (Figure 64).



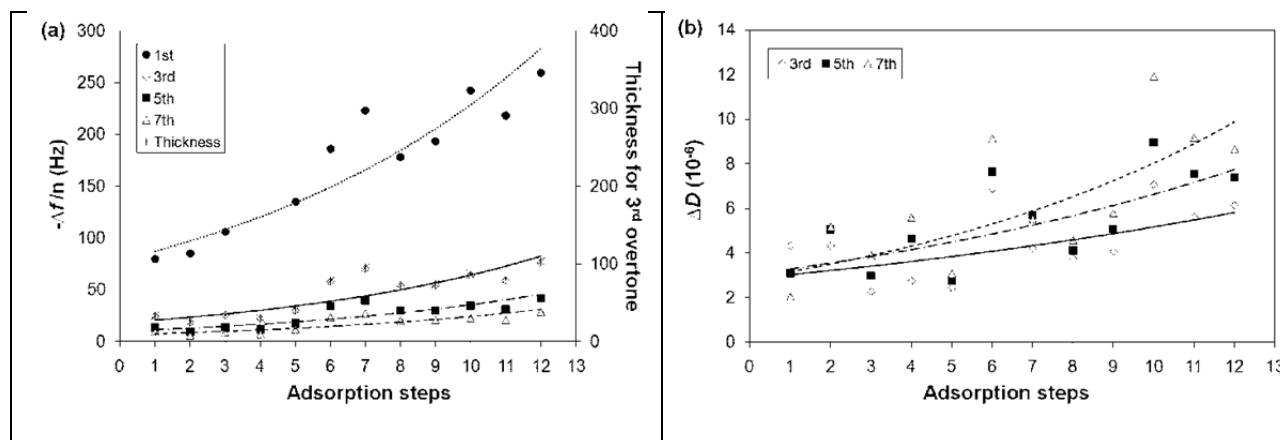


Figure 63: Film buildup as monitored by QCM-D. (a) Measured frequency shift ($-\Delta f/n$) for different overtones and calculated hydrated film thickness for the 3rd overtone (eq. 2) as a function of PLL/PLGA film buildup, (b) measured dissipation shift (ΔD) for different overtones. All lines are fits of an exponential model to empirical data points. The fundamental frequency was 5 MHz; the overtones were 15 MHz, 25 MHz and 35 MHz.

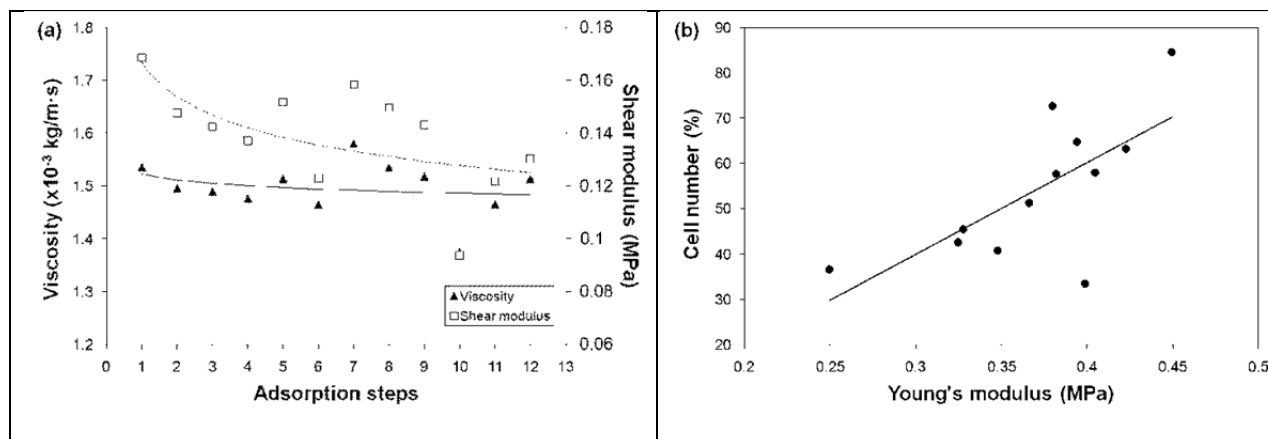


Figure 64: Mechanical properties of various non-functionalized PLL/PLGA films and their relationship to HUVEC proliferation. (a) Viscosity and shear modulus and (b) the relationship of Young's modulus to cell proliferation. Data from the 5th and 7th overtones were used for viscoelasticity modeling. Cell number is shown as the number of HUVECs on films with respect to the number of cells on TCPS in the absence of VEGF after 1 day in culture. All curvilinear lines are visual aids. The straight line in panel (c) was obtained by regression analysis.

Cell behavior on a given substrate is well known to depend heavily on cell type. Nevertheless, HUVEC attachment to 7-adsorption-step poly-(D-lysine)/PLGA films ($78 \pm 10\%$), reported by Boura et al. (2003), resembles attachment to 7-adsorption-step PLL/PLGA films in this work ($63 \pm 7\%$ relative to TCPS). The first polymer 5 adsorption steps in the Boura et al. work consisted of one precursor layer of poly(ethylenimine) followed by two bilayers of poly(sodium 4-styrenesulfonate)/poly(allylaminehydrochloride). The “5-layer” film was then coated with poly-(D-lysine) and PLGA. Surprisingly, Boura et al. found that cell count had increased after 3 days in culture relative to TCPS, despite decreased rigidity relative to the corresponding PLL/PLGA film substrate in this work. The

difference from the present results can perhaps be ascribed to film architecture. Films made of strong polyelectrolytes tend to be stiffer and thinner per adsorption step than ones made of weak polyelectrolytes like PLL and PLGA [77, 78]. Nevertheless, the present data make it difficult to understand how HUVECs could display increased proliferation on a less rigid substrate after 1 day of culture. Several studies have increased multilayer film rigidity by covalent crosslinking, for instance, by EDC and sulfo-NHS chemistry [79-81]. Stiffer substrates have consistently promoted cellular attachment and growth, despite the greater similarity of a polyelectrolyte multilayer film than TCPS to key properties of the extracellular matrix.

PLL-ending films gave greater cell proliferation than PLGA-ending films in the presence of serum. The result may be explained by the sign of the surface charge. Richert et al. (2002) found that chondrosarcoma cells bound more strongly to films with a positive (PLL) surface than a negative (PLGA) surface in a serum-free environment. Although the zeta potential of PLL-ending films decreased after exposure to serum-containing medium, cell attachment to PLL-ending films was still higher than for PLGA-ending films. Ideally, one could dissect the binding affinity of cells from the number of sites, an extensive quantity and site occupancy. In Kim et al. (2009), HUVEC attachment to a polyelectrolyte hydrogel increased on increasing the positive charge concentration [82]. Hydrogel, even if highly charged, is obviously more flexible than TCPS. A similar tendency was found when a negatively charged polyurethane membrane was coated with a positively charged polyelectrolyte [83]. HUVECs anchored to the substrate and spread well when the substrate surface charge was changed from negative to positive.

Film functionalization:

Multilayer films have been functionalized with specific biochemical signals by different investigators in different ways. One approach has been to conjugate a short peptide to a long polymer (e.g., PLGA), and to adsorb the resulting branched structure onto the film surface. For example, a 14-amino-acid peptide containing the laminin-5 sequence or a 15-amino-acid peptide containing the RGD sequence of fibronectin have been grafted to PLGA with the crosslinking reagents EDC and sulfo-NHS. Film functionalization resulted from a subsequent grafted-polymer adsorption step. A downside of the approach is the need for conjugation and separation steps. The present study took a simpler route. 12 lysine residues at the N-terminus of designed peptides CI-1 and CI-2, which are based on collagen I, were for binding to a negatively charged surface. The functional regions of the same peptides were for increased control over cell adhesion and proliferation. Film functionalization was achieved by LBL, the same process used to make the underlying film. No peptide grafting or corresponding separation step was required. The UV absorption data shown in Figure 65 indicate that the functional peptides remained bound to the film at equilibrium subsequent to several rinse steps. Such functional peptides can be adsorbed onto virtually any oppositely-charged surface, regardless of film architecture or surface roughness. Moreover, the peptides are readily utilized

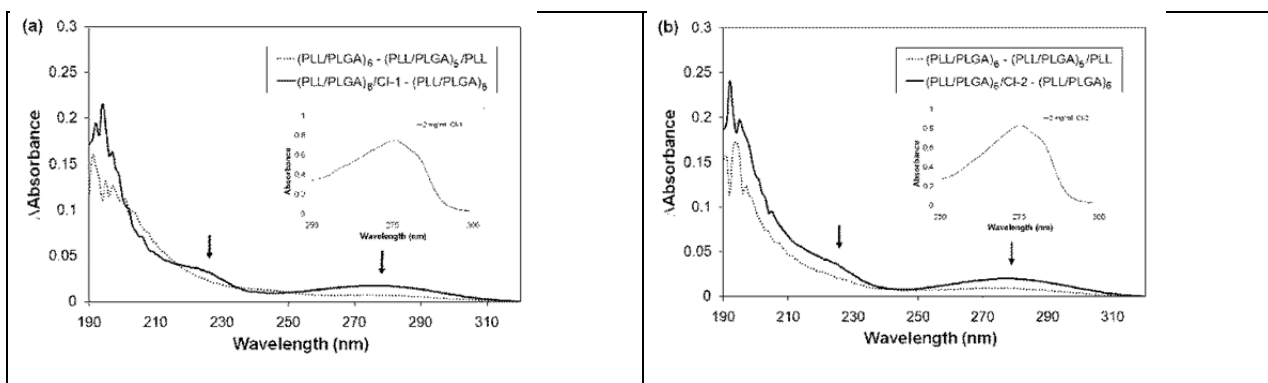


Figure 65: Film functionalization. (a, b) UV difference spectra of multilayer films for CI-1 (a) and CI-2 (b) functionalization. The broken line represents the 12th layer of the non-functionalized film, the solid line, the corresponding functionalized film layer in each case. Arrows indicate absorption bands clue to the aromatic ring of tyrosine. Insets are UV absorbance spectra of functional peptides in solution at 2 mg/mL.

individually or in combination and under considerable control over a broad range of surface densities and molar ratios.

The data show that film functionalization with CI-1 and CI-2 had a significant impact on adhesion and other aspects of cell behavior. There was at least 25% increase in HUVEC adhesion after 2 h of culture (Figure 66).

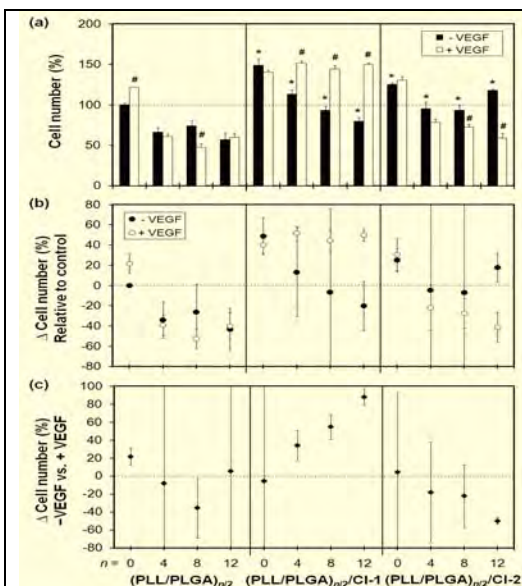


Figure 66: Short-term HUVEC adhesion on functionalized films. Cells were incubated 2 h in culture medium on different film architectures. (a) HUVEC cell number adhered to various substrates, (b) HUVEC adhesion difference relative to TCPS in the *absence* of VEGF₁₆₅ and (c) VEGF effect on cell adhesion after 2 hr incubation. TCPS and 4-, 8- and 12-adsorption-step films, which have a negative surface charge, were functionalized with CI-1 or CI-2 as in Fig. 4. Black bars represent cells cultured in the *absence* of VEGF₁₆₅; white bars, with VEGF₁₆₅. The seeding density was 3×10^4 cells/well. An asterisk (*) indicates a significant difference in proliferation between the functionalized film and the corresponding non-functionalized film with $p < 0.05$. A pound sign (#) indicates a significant difference between the *presence* and *absence* of VEGF₁₆₅ in culture medium with $p < 0.05$.

The GFPGER sequence, included in peptide CI-1, corresponds to a high-affinity binding site in collagen type I and IV for integrin $\alpha_2\beta_1$ and in collagen type I for $\alpha_1\beta_1$ [84]. GFPGER-peptide coatings have previously been employed to elicit a specific osteogenic cellular response and promote bone tissue ingrowth into scaffolds [85, 86]. Bone formation occurred significantly faster on GFPGER-coated scaffolds than uncoated scaffolds in the absence of exogenous growth factors. A GFPGER peptide has also been found to increase HUVEC attachment and spreading on stiff polyacrylamide gels [87]. GTPGPQGIAGQRGVV (P15)-coated materials have been shown to enhance cell adhesion and proliferation *in vitro*. P15 promoted the growth of primary HUVECs and the proliferation of endothelial cells on P15-treated expanded polytetrafluoroethylene (ePTFE) grafts compared to untreated controls. [88] The GTPGPQGIAGQRGVV sequence motif was included in peptide CI-2.

Despite initial enhancement of attachment on CI-1- or CI-2-functionalized PLL/PLGA films, HUVEC density decreased with time (Fig. 67). Only a few cells remained after 7 days in culture. Increasing the number of adsorption steps resulted in somewhat fewer cells adhered after 1 day in culture and a dramatic decrease in cell density after 7 days. On TCPS, by contrast, cells proliferated and became confluent with time, with or without functional peptide coatings. It therefore appears that substrate stiffness had a greater effect on cellular behavior on the films than the chemical stimulus provided by the

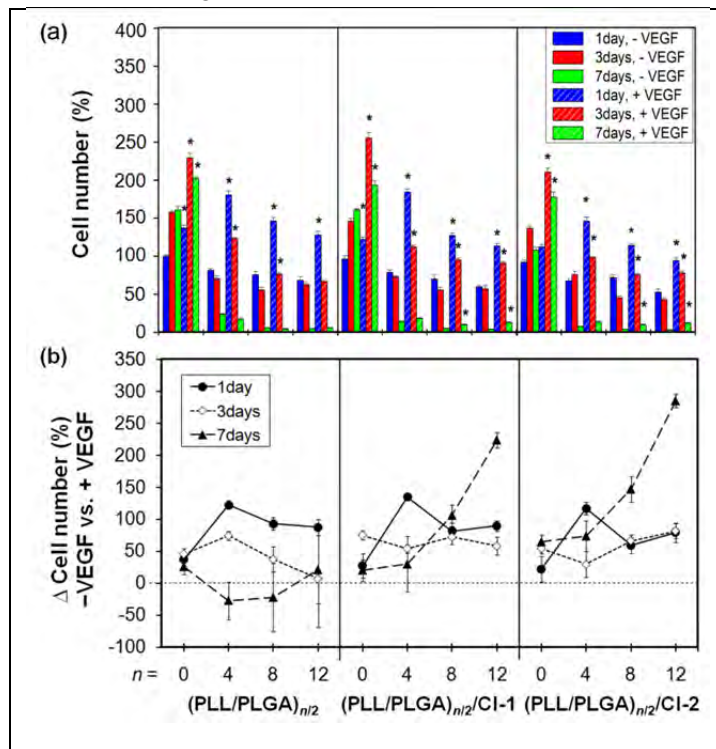


Figure 67: Long-term HUVEC proliferation on multilayer films. (a) HUVEC adhesion after 7 days relative to TCPS in the *absence* of VEGF₁₆₅ and (b) VEGF effect on cell adhesion over time. TCPS and 4-, 8- and 12-adsorption-step films were functionalized with CI-1 or CI-2. The seeding density was 3×10^4 cells/well. An asterisk (*) indicates a significant difference for cells without and with VEGF₁₆₅ in culture medium with $p < 0.05$.

functional peptides.

It has been suggested that the spacing between a peptide sequence and its anchoring moiety could influence functionality [89]. Presumably, a specific attachment peptide will have to be sufficiently prominent on a substrate surface to attach to the corresponding cell receptor. Here, the lysine residues of the attachment region of designed peptides will have formed a complex with PLGA molecules on the

film surface. There was a 9-residue “linker” ((GPO)₃) between the film and the functional region of CI-1, and no linker in CI-2. The present results may therefore be attributable to linker length in some measures. Examples are known of effective cell adhesion in the absence of a linker in an RGD peptide [90], and increasing linker length has been found to reduce cell attachment [91]. Picart et al., using a 15-amino-acid RGD peptide (CGPKGDRGDAGPKGA), found improved osteoblast adhesion on functionalized 12-adsorption-step PLL/PLGA film. The same study found that film crosslinking had a comparable effect to biochemical functionalization on cell adhesion. It therefore seems that no definite conclusion can be reached at this time, concerning the linker length and the adhesion data of the present work.

Exponential growth of multilayer films is well known for different polyelectrolyte systems [92]. It is probable that the number of functional peptide binding sites increases with film thickness in such cases. One might therefore expect a greater surface density of functional peptides on 12-adsorption-step than 4- or 8-adsorption-step PLL/PLGA films. In the present work, nevertheless, there was no clear difference in peptide-specific biochemical effects for the various film thicknesses. The reasons are uncertain. Future experiments could increase the emphasis on known details of receptor-ligand interactions.

The effects of VEGF₁₆₅ in this work cannot be distinctly separated from the effects of substrate mechanics and chemical signaling. VEGF had inconclusive impact on the short-term adhesion of HUVECs on the various multilayer systems. While film functionalization with CI-1 and CI-2 improved cell adhesion, synergism of the film-bound biochemical signals with soluble VEGF is less certain. Cells on CI-2-functionalized films showed similar trends with regard to adhesion as non-functionalized films and bare TCPS, whereas cells on CI-1-functionalized films displayed a significant increase in cell numbers on films in the presence of VEGF (Fig. 66).

Fig. 67 shows how VEGF affected HUVEC proliferation over 7 days in culture. In general, this endothelial cell-specific mitogen and angiogenic factor [93-95] increased cell survival after 1 day in culture. VEGF is well known to regulate endothelial cell survival, proliferation, migration and differentiation. Nevertheless, there was little evidence that VEGF influenced HUVEC proliferation beyond the first day of culture. It seems probable that more cells remained at later time points in VEGF-treated cell populations because of increased initial cell adhesion after 1 day of culture, not because of effects of VEGF on adhered cells. In any case, soluble VEGF is a means of controlling cell behavior on multilayer films.

Cell morphology and cytoskeletal organization:

A qualitative comparison of cell morphology and cytoskeletal organization was done to gain further information on possible synergistic effects of mechanical stimuli, substrate-bound biochemical stimuli and soluble biochemical stimuli (Fig. 68-70). That endothelial cells are mechano-sensitive is well known. In 2- and 3-dimensional models of *in vitro* angiogenesis, capillary-like structures are favored on or in more flexible substrates [96-98].

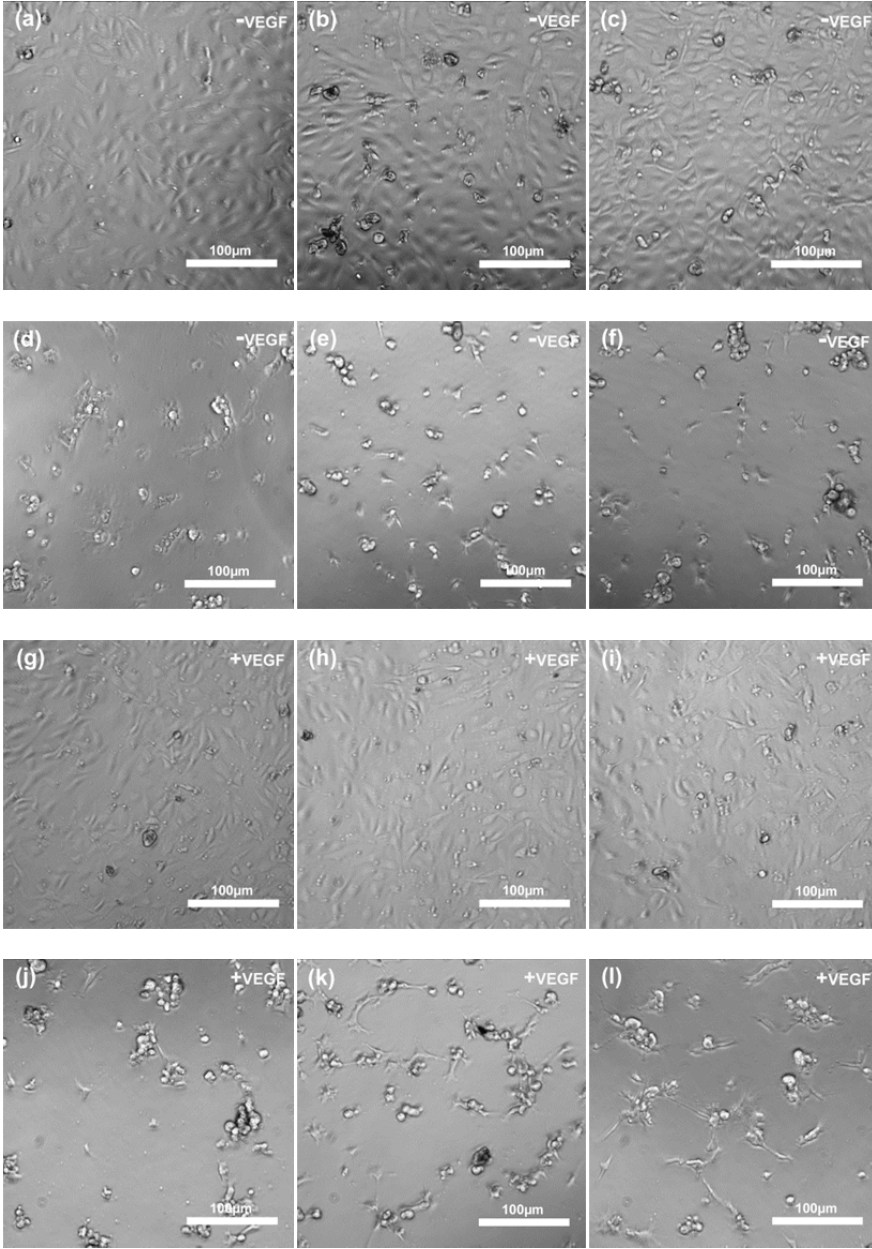
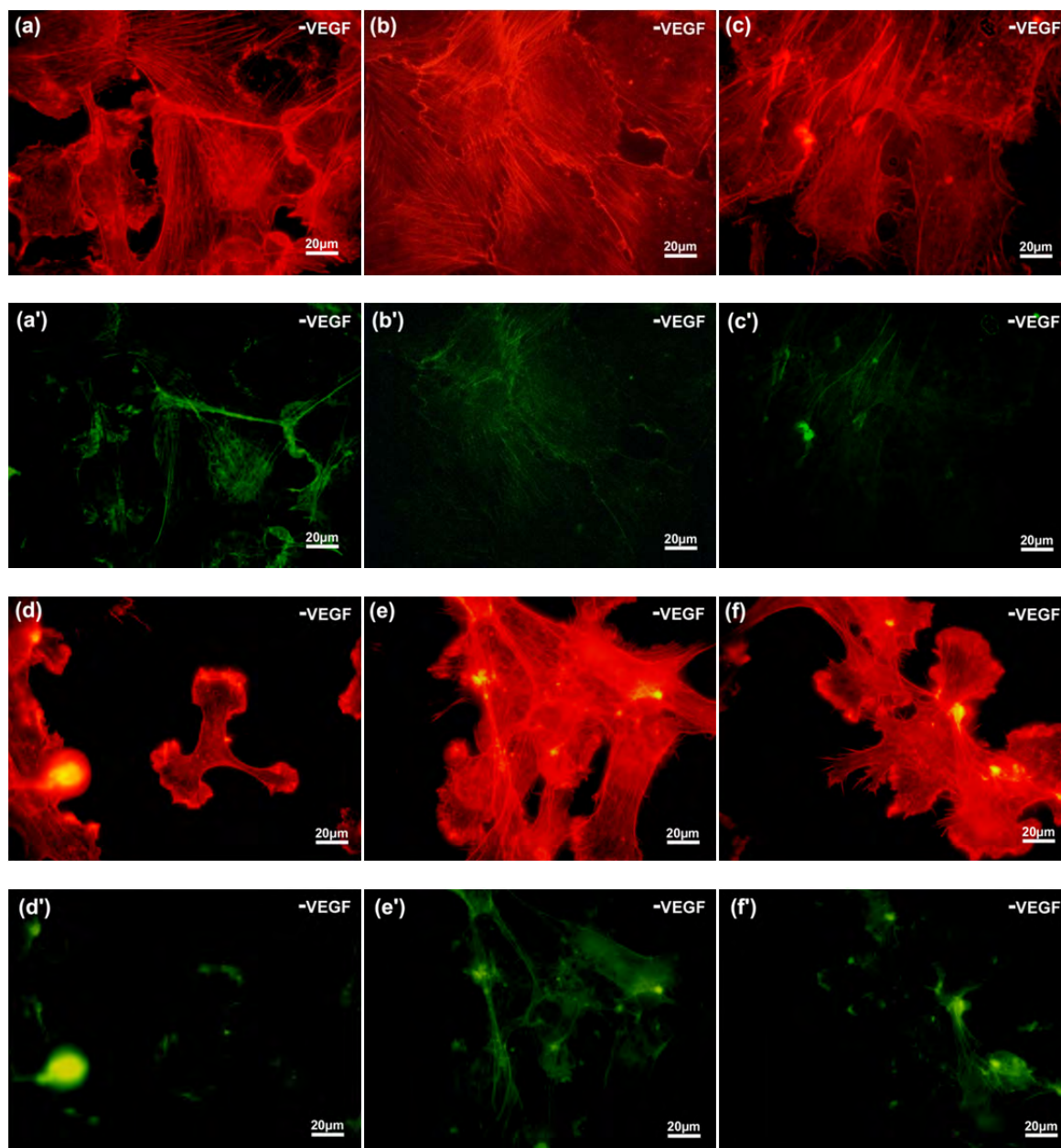


Figure 68: HUVEC density and morphology on multilayer films after 1 day in culture. The films were built on a 96-well plate. The seeding density was 3×10^4 cells/well on (a, g) TCPS, (b, h) CI-1-functionalized TCPS, (c, i) CI-2-functionalized TCPS, (d, j) 12-adsorption-step, non-functionalized films, (e, k) CI-1-functionalized 12-adsorption-step films, and (f, l) CI-2-functionalized 12-adsorption-step films. VEGF₁₆₅ was absent (a-f) or present (g-l) in the culture medium. The phase contrast images were obtained at a magnification of 10 \times . Scale bars, 100 μ m.

Saunders et al. have reported stable network formation by HUVECs on gels with a Young's modulus of 140 Pa, whereas gels with a Young's modulus of 2.5 kPa supported cell attachment but showed no cell organization into vascular networks, with or without VEGF and basic fibroblast growth factor. Under the cell culture conditions of this work, for which Young's modulus was close to 0.4 MPa, HUVECs did not form vascular networks on non-functionalized or functionalized 12-adsorption-step

films, regardless of VEGF treatment (Fig. 68(d-f)). Nor was there evidence of angiogenesis, nevertheless, HUVECs did seem to migrate, especially on functionalized films in the presence of VEGF (Fig. 28(j-l)). VEGF-stimulated migration may decrease the stability of cell networks, as it leads to crawling along adjacent cells or stretching/moving. If the cell density is relatively low, as on the 12-adsorption step films of the present study, cells are all the less apt to form a network assembly [99].

VEGF-stimulated cell migration is associated with regulation of the cytoskeleton and long and highly structured actin stress fibers. As shown in Fig. 68, VEGF-treated cells displayed long and condensed stress fibers reaching into the cell body. VEGF had a striking effect on cells cultured on 12-adsorption-step films: fibers were disorganized throughout the cells on non-functionalized and on functionalized films in the absence but not the presence of VEGF (Fig. 68(g-i)).



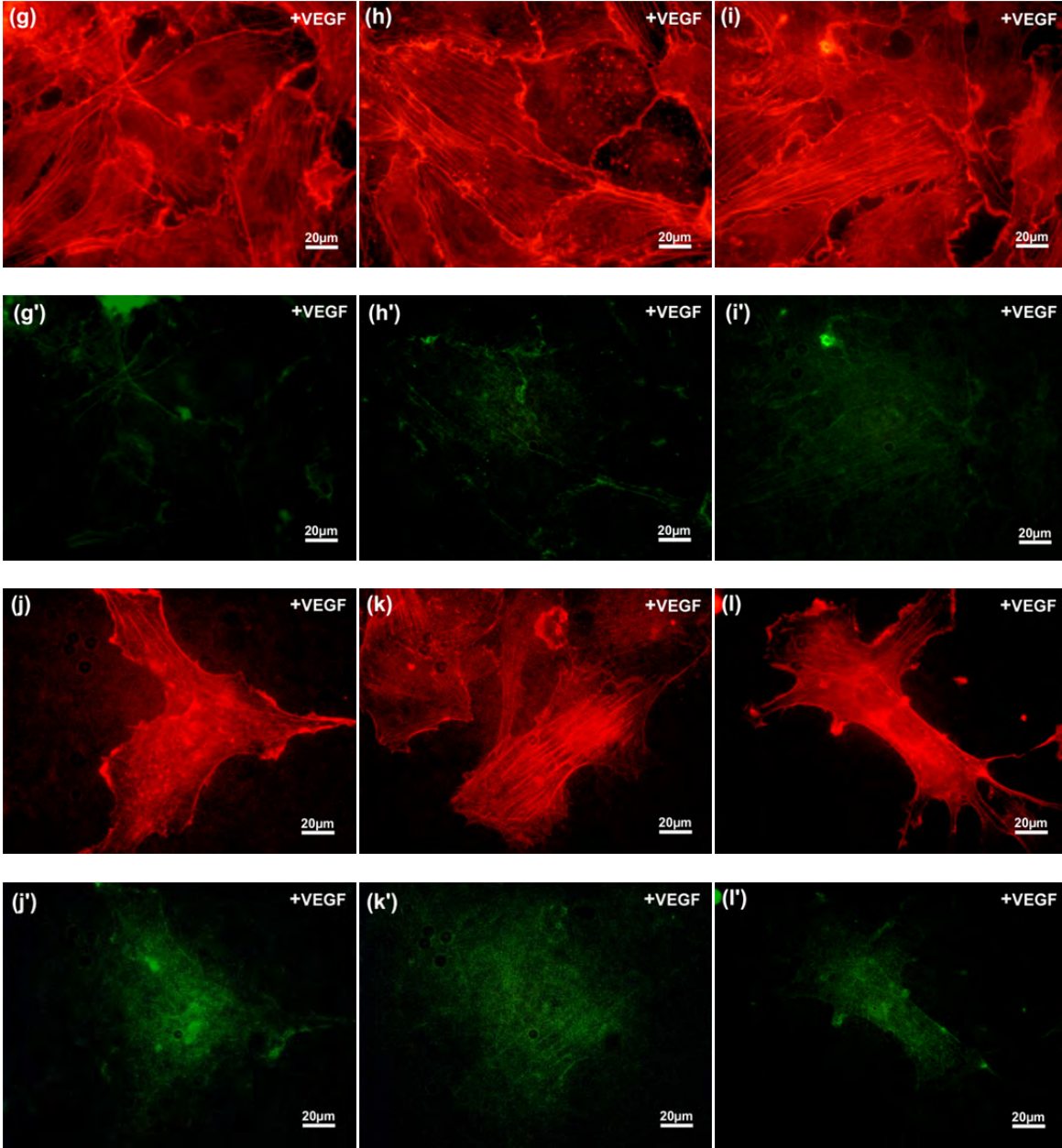


Figure 69: F-actin organization and distribution of vinculin in HUVECs on multilayer films after 1 day in culture. The films were built on microscope cover glass. The seeding density was 1×10^5 cells/cover glass on (a, a', g, g') TCPS, (b, b', h, h') CI-1-functionalized TCPS, (c, c', i, i') CI-2-functionalized TCPS, (d, d', j, j') non-functionalized 12-adsorption-step films, (e, e', k, k') CI-1-functionalized 12-adsorption-step films, and (f, f', l, l') CI-2-functionalized 12-adsorption-step films. Cells were stained with (a-l) rhodamine phalloidin or (a'-l') FITC-labeled anti-vinculin for visualization of microfilaments or focal adhesions, respectively. VEGF₁₆₅ was absent (a-f, a'-f') or present (g-l, g'-l') in the culture medium. Scale bars, 20 μ m.

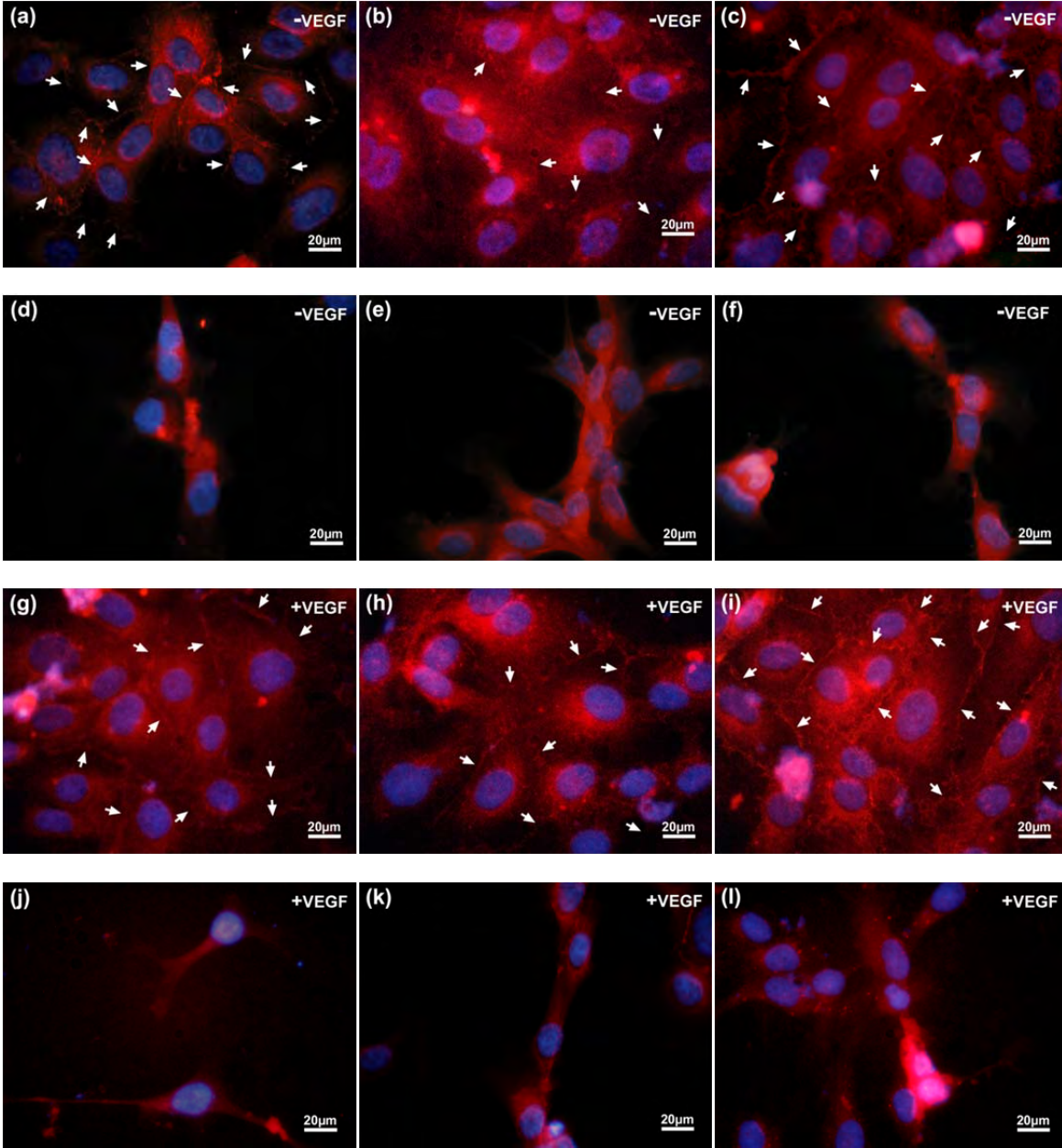


Figure 70: VE-cadherin-mediated cell-cell adhesion in HUVECs on multilayer films after 1 day in culture. The films were built on microscope cover glass. The seeding density was 1×10^5 cells/cover glass on (a, g) TCPS, (b, h) CI-1-functionalized TCPS, (c, i) CI-2-functionalized TCPS, (d, j) non-functionalized 12-adsorption-step films, (e, k) CI-1-functionalized 12-adsorption-step films, and (f, l) CI-2-functionalized 12-adsorption-step films. Cells were stained with anti-human VE-cadherin/CD144-PE and DAPI for visualization of adhesion contacts and cell nuclei, respectively. VEGF₁₆₅ was absent (a-f) or present (g-l) in the culture medium. Arrows indicate VE-cadherin staining at cell-cell junctions. Scale bars, 20 μ m.

VEGF is also known to induce cell edge ruffling. In the present work, VEGF-untreated groups showed more edge ruffles on multilayer films than TCPS, consistent with the view that effects due to substrate mechanical properties dominated effects due to VEGF. The immune-cytochemistry data show that the distribution of vinculin, a focal adhesion protein, correlated with substrate stiffness. For VEGF-treated HUVECs on non-functionalized or functionalized 12-adsorption-step films, vinculin was irregularly distributed throughout the cell, despite the presence of actin filament bundles. As before, although VEGF influenced the reorganization of actin filaments, it would appear the mechanosensitivity of HUVECs was greater than their responsiveness to the soluble growth factor, and that focal adhesion stability decreased with decreasing film stiffness. The present data are consistent with other studies [100-102].

Finally, although substrate mechanical properties dominated over biochemical stimuli with regard to cell adhesion, it appears that VEGF influenced VE-cadherin abundance in cell-cell junctions (Fig. 67). An apparent locomotive effect of VEGF on cells was correlated with a decreased abundance of cell-cell junctions. A cytoplasmic target of VE-cadherin is α -catenin, which is related to F-actin [103]. Details of the relationship between the abundance of cell-cell junctions and vinculin distribution will be discussed elsewhere.

Conclusion:

Films were also functionalized by adsorbing collagen type I-derived peptides onto the surface. VEGF₁₆₅ served as a soluble biochemical stimulus. Whereas primary HUVECs adhered poorly on all non-functionalized multilayer films in comparison to TCPS, functionalization increased adhesion in short-term culture. After 7 days in culture, however, cell density was lower on films than on TCPS, even with functionalization, even though VEGF stimulated cell growth during 1 day in culture. The mechanical properties of multilayer films therefore appear to have had a more significant long-term effect than the biochemical signals in this work. VEGF enhanced initial cell survival and stress fiber formation on films. In addition, HUVECs appeared more mobile on the softer films in the presence of VEGF. This study specifically focused on HUVEC response to the combined effects of film functionality and mechanical properties, with or without a soluble growth factor. The same mechanochemical stimuli could be applied to many other cell types, and the stimuli used here could easily be changed. The general approach is therefore a relatively straightforward means of probing the response of a cell to a controlled and specific cellular environment. The film functionalization procedure employed here is simpler than the grafted polymer approach. A strictly designed multilayer film system of mechanochemical properties could also be employed in the diagnosis of disease, perhaps in cancer research. The cellular activity, morphology and malfunction can be identified under the strict conditions.

4.7. Formation and delivery of functionalized artificial platelets for rapid cessation of internal bleeding:

This project is continuing under the no-cost extension till September 2015. Results will be reported in future quarterly and annual reports.

Task II: Nanoparticle/nano-wire structures and polymer nanoparticles for sensing and molecular manipulation

Project 5: Nanoparticle/nano-wire structures and polymer nanoparticles for sensing and molecular manipulation

5.1. Chemical synthesis of ferrite nanoparticles and fabrication of polymer nanocomposite films, analysis of structural, electrical and magnetic properties:

Polymer nanocomposites have received much attention because of their unique electrical, thermal, mechanical, and optical properties. Polyvinylidene fluoride (PVDF) is one of the promising systems for different types of sensor applications [104]. It is a ferroelectric polymer exhibiting efficient piezoelectric and pyroelectric properties. These characteristics make it useful in sensor and battery applications. However, the dispersion of nanoparticles into a polymer matrix has been a bottleneck for nanocomposite fabrication. One of the best ways to uniformly disperse nanoparticles in a polymer matrix is to functionalize the particle surface with organic surfactants. If the particles are surface functionalized with organic surfactants, they will become more compatible with the polymer matrix, resulting in a homogeneous dispersion of nanoparticles.

In this project, we have successfully developed a new way of making novel magnetic polymer nanocomposites, including PVDF-Fe₃O₄ and Rogers-CoFe₂O₄ nanocomposite systems, and their structural, magnetic, and microwave properties have been studied systematically [105,106]. We have demonstrated the possibility of tuning the magnetic and microwave responses of these nanocomposites by varying concentrations of the particle loading, indicating that these newly developed magnetic polymer nanocomposites are excellent candidate materials for applications in biomedical sensing and microwave communication devices.

Synthesis and characteristics of novel PVDF-Fe₃O₄ nanocomposites: First we synthesized Fe₃O₄ nanoparticles and functionalized them with polyethylene glycol (PEG). PEG is an amphiphilic polymer and coating on Fe₃O₄ by PEG makes iron oxide NPs soluble in different solvents. In this work, dried Fe₃O₄ was added to the dimethylformamide solution of PVDF by 30 wt%, 50 wt% and 80 wt% ratio. The polymer nanocomposites were dried at room temperature. The TEM image (Figure 71 a) shows that the average particle size of Fe₃O₄ is ~ 7 nm with uniform dispersion. The TEM image (Figure 71 b) of the PVDF-Fe₃O₄ nanocomposite shows that the particles are well dispersed in the polymer matrix.

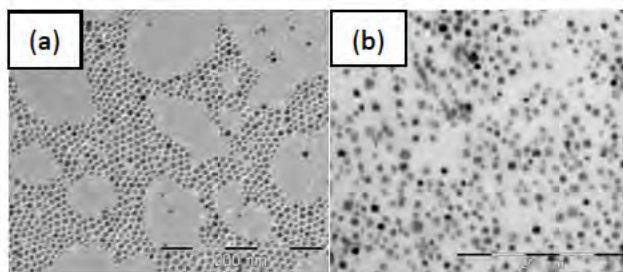


Figure 71: TEM images of (a) Fe₃O₄ nanoparticles and (b) PVDF-Fe₃O₄

All magnetic measurements including the temperature dependence of ZFC and FC magnetization, M-H hysteresis loops were done using our PPMS. For these measurements, the dried samples were loaded in a standard, non-magnetic gelatin capsule. The blocking temperature (T_B) is determined to be ~40 K for Fe₃O₄ nanoparticles, which remains almost the same for all PVDF-Fe₃O₄ nanocomposite samples with different Fe₃O₄ concentrations. The M-H loops taken at 10 K show the same coercivity (H_c) of ~ 185 Oe for Fe₃O₄ and PVDF-Fe₃O₄ samples. However, the saturation magnetization (M_s) of Fe₃O₄ particles is 7

emu/g, and the M_s decreases with decreasing the percentage loading of Fe_3O_4 in the PVDF- Fe_3O_4 composites (Figure 72). The M-H data at 300 K shows no coercivity for all the samples, indicating the superparamagnetic nature of the PVDF- Fe_3O_4 nanocomposites, which is desirable for sensor and microwave device applications.

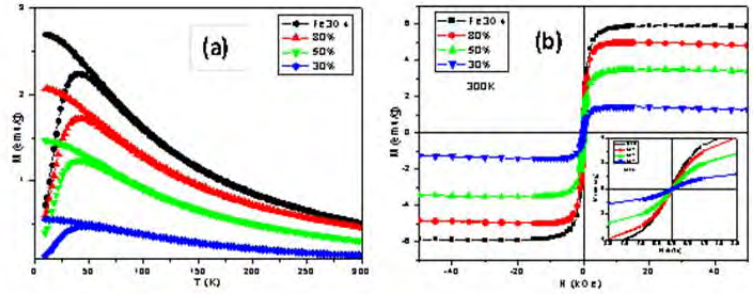


Figure 72: (a) The M-T data of the PVDF- Fe_3O_4 nanocomposites; (b) The M-H curves taken at 300 K showing the superparamagnetic response in all the

Synthesis and characteristics of

novel Rogers – CoFe_2O_4 nanocomposites: In our continued efforts to create novel magnetic polymer nanocomposites with improved and tunable microwave responses, we have synthesized and investigated the structure, magnetic and microwave properties of Rogers – CoFe_2O_4 nanocomposites. In this case, CoFe_2O_4 nanoparticles were synthesized using a thermal decomposition method and were dissolved in hexane in the presence of oleic acid and oleylamine ($\sim 0.05\text{ml}$ each) to create a ferrofluid. The polymer nanoparticle composites (PNCs) were made by adding the synthesized particles to Rogers Polymer (a low-loss, high-temperature thermosetting resin provided by the Rogers Corporation). A calculated amount nanoparticles and polymer were then mixed together to create composites with different loadings. Each sample was left stirring with a magnetic stir bar overnight to ensure uniform dispersion of nanoparticles within the polymeric matrix. Once the solutions were formed, the PNC material was drop-casted onto a multilayer microstrip linear resonator and heated in a vacuum oven to evaporate the solvent and cure the polymer. PNCs were made to be 30 wt%, 50 wt% and 80 wt% in films as thick as $435\text{ }\mu\text{m}$. Figure 73a shows the XRD plot of the pure CoFe_2O_4 nanoparticles compared to the highest and lowest weight percentages. The synthesized nanoparticles and the composites alike are of the same phase, indicating that any heating of the PNCs did not affect the phase of the nanoparticles. Figure 73b and 73c show TEM images of the $10\pm 1\text{ nm}$ CoFe_2O_4 nanoparticles alone and within the 50 wt% composite, respectively. In both cases, the particles are well-separated and free from any agglomeration.

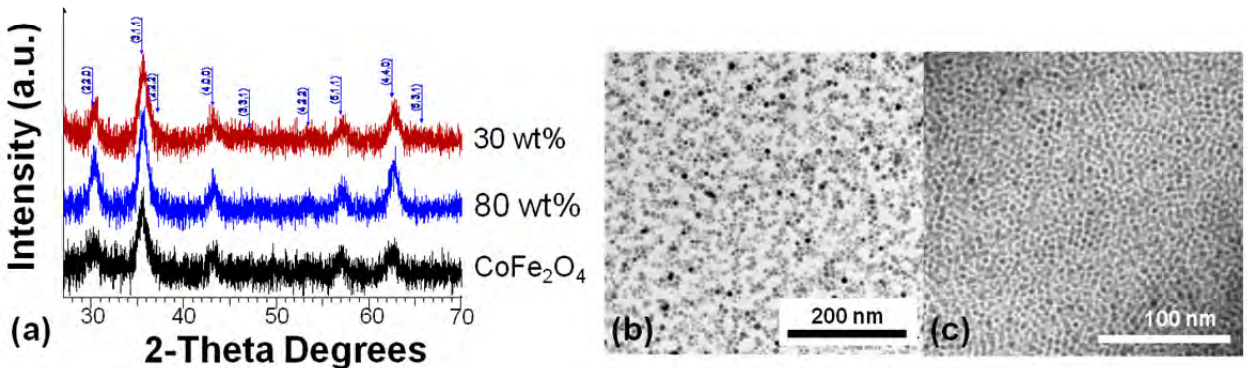


Figure 73: (a) XRD plot of pure CoFe_2O_4 nanoparticles, 30 wt% PNC, and 80wt% PNC; (b) TEM image of pure CoFe_2O_4 nanoparticles; and (c) TEM image of 50 wt% composite.

Magnetization vs. magnetic field (M-H) measurements at 300 K show curves of varying saturation magnetizations (M_s) based on the different loadings of the PNCs all with zero coercivity, confirming the superparamagnetic behavior of the samples at room temperature (Figure 74a). Figure 74 shows that M-H measurements at 10 K display the same pattern of varying M_s with loading of particles and also a coercivity of ~ 18 kOe for all samples. Note that the large coercivity in this system is expected because of large magnetic anisotropy of the CoFe_2O_4 system. Magnetization vs. temperature (M-T) measurements reveal a blocking temperature (T_B) of ~ 298 K for the CoFe_2O_4 nanoparticles and all three PNCs, shown in Figure 4c. This is beneficial for many commercial applications as both the ferromagnetic and superparamagnetic states of the material are accessible near room temperature. Also note that since the M_s changes with particle loading, but the T_B does not, these PNCs display a tunable magnetization.

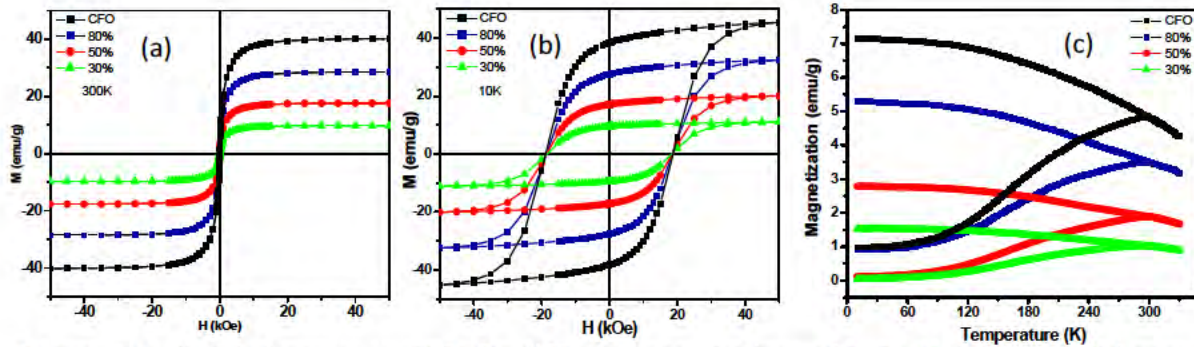


Figure 74: (a) M-H curves at 300K for different concentrations of CoFe_2O_4 in Rogers Polymer with inset showing zero coercivity; (b) M-H curves at 10K for the same concentrations showing coercivity of 18 kOe; and (c) M-T curves for same concentrations showing a T_B of ~ 298 K for all samples.

To test the microwave response of the Rogers- CoFe_2O_4 PNCs, a two-port microstrip linear resonator was designed using the multilayer structure shown schematically in Figure 75a. The resultant frequency of the resonator relies on the effective material properties of the implemented substrate following the relation, $F_r \sim 1/(\epsilon\mu)^{1/2}$ with μ and ϵ being the effective permeability and permittivity, respectively, for the multilayer system. Figure 75b presents the measured transmission characteristics of the aforementioned resonator with embedded PNC as a function of frequency for several different magnetic fields, ranging from zero

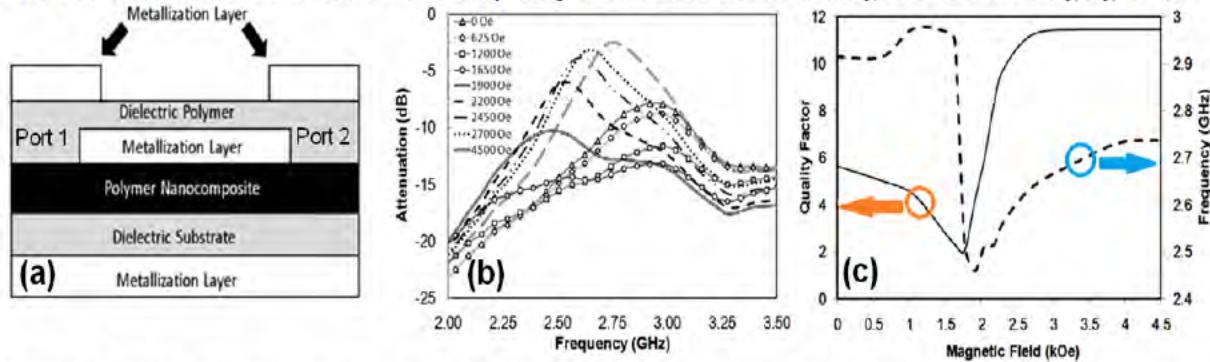


Figure 75: (a) Cross-sectional diagram of the multilayer microstrip resonator; (b) Measured transmission characteristics of the microstrip linear resonator with embedded CoFe_2O_4 -Rogers nanocomposite of 80%loading; and (c) Quality factor and frequency as a function of magnetic field.

magnetic field to 4500 Oe for the 80 wt% sample. The observed variations in the resonance frequency are due to the changes in the permeability and permittivity of the PNC. Figure 75c shows a plot of the quality factor and the frequency as a function of magnetic field, also of the 80 wt% sample. Observe the sharp increase in both of these parameters as the magnetic field is increased.

Note that the changes in the magnitude of the transmission characteristics and the quality factor of the device are also partially related to the variation in the effective losses of the nanocomposite material.

In conclusion, we have demonstrated excellent control over nanoparticle dispersion in two new types of magnetic polymer nanocomposites, namely the PVDF-Fe₃O₄ and Rogers-CoFe₂O₄ nanocomposite systems. Their tunable magnetic and microwave properties make them truly attractive for applications in biomedical sensing and microwave communication devices. The results featuring these achievements have been reported in *Nanotechnology* 2011 and *IEEE Transactions on Magnetics* 2011.

5.2. PLD growth of ferroelectric/ferrite heterostructures with controlled interface strain. RF and microwave measurements of polymer composites and oxide films:

Integration of ferromagnetic (FM) thin films with ferroelectric (FE) thin films to enable electrical manipulation of the magnetic properties holds attractive possibilities for novel magneto-electronic (ME) devices [107, 108]. These multifunctional structures offer possible applications in several advanced technologies, including ME memory devices that allow electrical encoding and magnetic readout, voltage gain devices, ultra sensitive magnetic field sensors that operate at room temperature, and microwave frequency transducers [109-111].

This research task was aimed at fabricating artificial multiferroic heterostructures consisting of alternate layers of the FM spinel CoFe₂O₄ (CFO) with the FE perovskite PbZr_{0.52}Ti_{0.48}O₃ (PZT) together to form interfaces that will enable the coupling of the magnetization and electric polarization via interfacial strain. Since the manifestation of the coupling between the order parameters in these structures is due to the strain at the interfaces of the magnetic and ferroelectric layers, epitaxial growth of the layers was essential to maximize the transfer of stress from one material system to the other. The initial phase of the project involved the growth and characterization of epitaxial single-layered CFO and PZT thin films using PLD technique. In the final phase, epitaxial PZT/CFO heterostructures were fabricated and their room temperature FM and FE properties were measured.

Magnetic anisotropy and strain in epitaxial CFO thin films: In the initial stage of the proposed task, epitaxial CFO thin films were grown on lattice-matched single-crystal on MgO (100) and STO (100) substrates by PLD. Figure 76 shows the XRD peaks for the CFO powder target and for the films grown on MgO and STO substrates. The peaks that correspond to CFO *fcc* lattice belong to the space group Fd-3m (227). The films grown on MgO (100) and STO (100) show peaks corresponding only to (400) peak of CFO indicating high degree of alignment. The insets in Figure 1b and Figure 1c show the XRD rocking curves about CFO (400) plane in CFO films on STO and MgO substrates, respectively. The full width at half maximum (FWHM) of the peak for MgO is 0.076°, showing excellent crystallographic orientation along the (100) direction that is indicative of high degree of epitaxy. FWHM of the rocking curve patterns of films grown on STO is 0.915° due to the large lattice mismatch with CFO. Since (200) of MgO and (400) of CFO diffraction peaks are very close to each other, ϕ scan measurements were conducted using Bragg's reflection from the (311) plane of cobalt ferrite. The peaks of the ϕ spectra occur at intervals of 90°, confirming the cubic symmetry and epitaxial growth. Because of larger lattice mismatch, (400) peak of CFO is shifted significantly in films that were grown on STO. Inset in Figure 76 b also shows the ϕ

scan curves from (311) reflection of CFO films that were deposited on STO substrates. In-plane lattice parameters were obtained from the asymmetric scan of the two CFO planes, viz. (511) and (440).

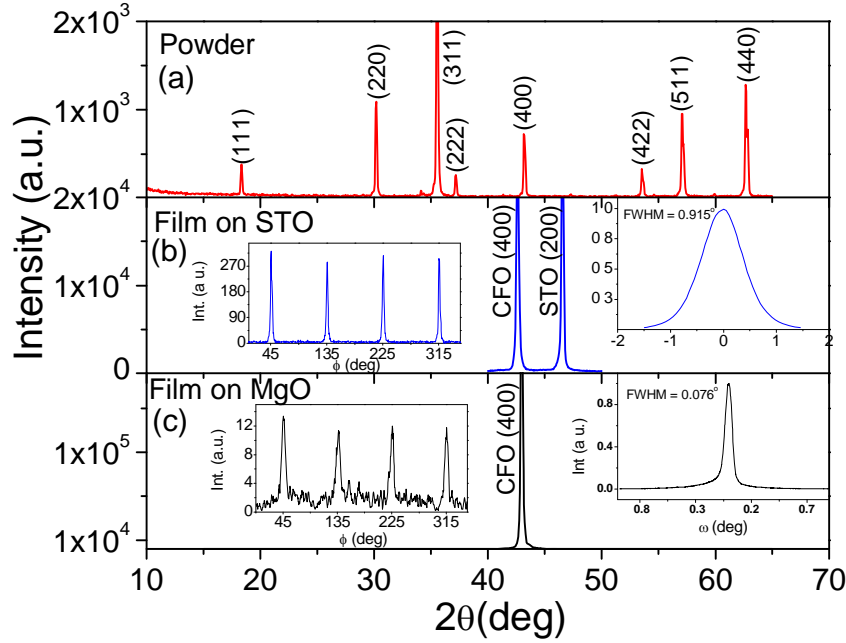


Figure 76: (a) XRD θ - 2θ patterns of CFO powder target, and epitaxial CFO films grown on (b) STO (100) and (c) MgO (100) substrates, respectively. The left insets show the corresponding ϕ scan spectra from CFO (311) Bragg reflection. The right insets show rocking curves of the CFO (400) peaks.

Table 5-1. Co to Fe ratio obtained by energy dispersive X-ray analysis (EDS), in plane and out of plane lattice parameters obtained from x-ray diffraction (XRD) peaks and the strain calculated using in plane lattice parameters.

CFO Film on	Co/Fe Ratio	a_{\perp} (Å)	a_{\parallel} (Å)	In plane Strain	Stress (dyn/cm ²)	Anisotropy (K α) (erg/cm ³)
MgO	2.04	8.388	8.401	0.0013	-12.19×10^9	10.79×10^6
STO	2.014	8.486	8.297	-0.011	-16.50×10^9	14.60×10^6

The value of the in-plane lattice parameter given in Table 5-1 is the average of the values obtained from the reflections off of these two planes. The difference between the out-of-plane lattice parameter ($a_{\perp} = 8.486$ Å) and the in-plane lattice parameter ($a = 8.297$ Å) confirmed the tetragonal distortion of the CFO unit cell in the film grown on STO. In the case of the film grown on MgO, in-plane and out-of-plane lattice parameters differ by only 0.15%. Values of in-plane strain presented in the Table 5-1 were calculated by using the formula $(a_{\parallel} - a_0)/a_0$, where a_0 is the bulk lattice parameter of CFO. To

confirm the stoichiometry, energy dispersive spectroscopy (EDS) was used. In each of the thin films of CFO it was found that the Fe:Co ratio was very close to 2 (Table 5-1). This confirmed the single crystalline stoichiometric growth of CFO thin films.

Figure 77 shows the magnetization vs. magnetic field (M-H) hysteresis loops measured at 300K and at 10K for the epitaxial CFO thin films of the same thickness (200 nm). The hysteresis graphs in Figure 77 were obtained after subtracting the diamagnetic contribution from the substrates.

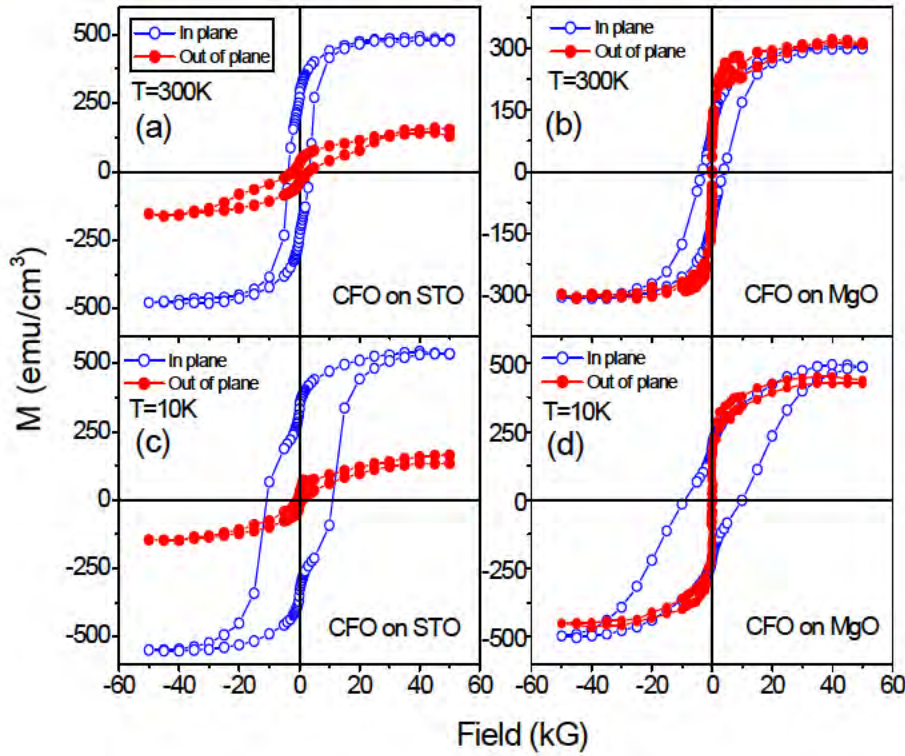


Figure 77: (a) and (c) M-H loops measured at 300K and 10 K respectively of the 200 nm thin film grown on STO (100) for in plane and out of plane configuration. (b) and (d) M-H loops measured at 300K and 10 K respectively of the 200 nm thin film grown on MgO (100) for in plane and out of plane configuration.

The saturation magnetization (M_s) value of the film grown on STO at 300K is around 490 emu/cm³ which corresponds to 3.9 μ_B per Co-site. This value is around 2.6 μ_B per Co-site in case of the film grown on MgO. However, at low temperature (10K), the saturation magnetization is closer to the bulk value of the cobalt ferrite [112]. It can be observed that the easy axis of magnetization of the films grown on MgO is out of the plane of the film along the [100] direction, whereas the films grown on STO have the easy axis of magnetization along the plane of the film. Although, the saturation field is smaller for the out of plane magnetization, the coercivity is small, atypical for an easy axis. However, the difference in magnetic anisotropy for these two films could have arisen from the fact that the CFO films (lattice constant=8.39 Å) grow with tensile strain on MgO (2 x lattice parameter=8.42 Å) substrate and undergo compression when grown on STO (2 x lattice parameter=7.81 Å). In particular, the stress present

due to the mismatch between the film and the substrate may have played a significant role in the observed anisotropy.

To summarize, we showed that stress is a dominant factor in the observed anisotropy in single crystalline thin films of CFO. The film with larger strain (on STO substrate) showed larger stress anisotropy. Films grown on STO experienced compression and showed in-plane anisotropy. On the other hand, films grown on MgO with tensile strain exhibited easy out of plane switching, which will have a good application in magneto-optical recording devices.

Enhanced ferroelectricity in epitaxial PZT thin films: In this section, we describe the epitaxial growth of stoichiometric $\text{PbZr}_{0.52}\text{Ti}_{0.48}\text{O}_3$ (PZT) thin films using PLD. Laser ablation of PZT is complicated by the high volatility of Pb in PZT that leads to its preferential evaporation during the ablation process resulting in Pb-deficient PZT films with poor FE properties [113-125]. We investigated the Pb depletion in laser-ablated PZT films through a systematic study of PZT target-laser interactions for both single laser (PLD_{SL}) and dual-laser ablation (PLD_{DL}) methods [126-130]. The films were deposited on single crystal SrTiO_3 (STO) (100) and MgO (100) substrates at 550 °C with a background oxygen pressure of 500 mT.

Figure 78 (a and b) shows SEM images of typical conical structures formed on the PZT target surface after laser-ablation using low and high fluences of 1 and 5 J/cm², respectively. The cones formed at low fluences (Figure 3 a) exhibited well-defined tips that were Pb deficient as compared to their bodies. Such conical structures were associated with the preferential evaporation of Pb in PZT. PZT films deposited under these conditions were non-stoichiometric and highly Pb-deficient [78]. At high fluences the conical structures (Figure 78 b) exhibited hemispherical cone tips and not so distinct bodies. Figures 78 (c, and d) shows the ICCD images of the laser-induced plasma plumes for the PLD_{SL} and PLD_{DL}, respectively. In order to compare the images, the intensities were normalized to the PLD_{SL} plume (Figure 78 c). The overall total intensity of the PLD_{DL} plume was 145% greater than that of PLD_{SL} emission. Also, the broader transverse expansion, measured on-axis 1 cm from the target, of the plume in dual-laser (28.0 mm FWHM) compared to single-laser (18.7 mm FWHM) clearly exhibits coupling of the laser energies in dual-laser ablation. This allowed the growth of more uniform film over a larger area and led to enhanced film properties.

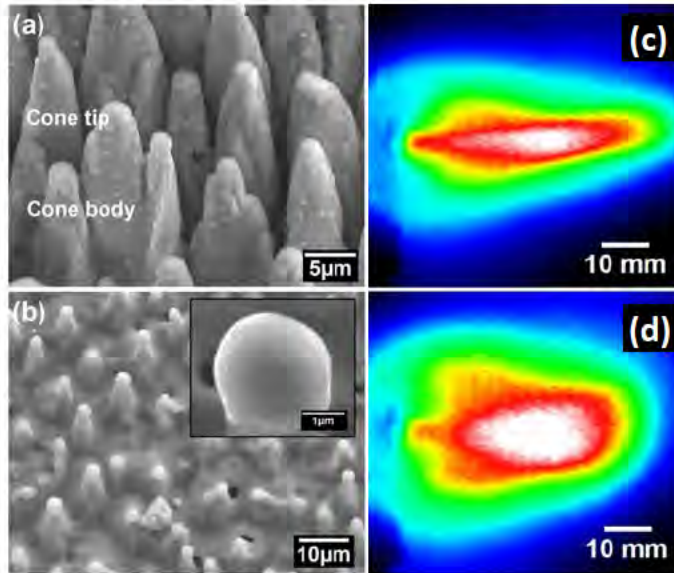


Figure 78: SEM images of laser-target interaction sites on a PZT target surface after laser ablation using (a) low fluence and (b) high fluence, respectively. Time integrated ICCD images of the visible emission spectra of laser-induced plumes for (c) single-laser ablation and (d) dual-laser ablation.

Table 5-2 lists the atomic (at.) % ratios of Pb/(Zr + Ti), Zr/(Zr + Ti), and Ti/(Zr + Ti), obtained from EDS analysis, at the laser-target interaction sites after ablation at increasing laser (KrF) fluences for a PZT target with 30 at. % excess PbO, under both PLD_{SL} and PLD_{DL} conditions. From Table 5-2, it can be seen that for PLD_{SL} the at. % ratio of Pb in PZT target decreased from 1.30 before ablation to 0.83 after ablation at 1 J/cm² while the Zr and Ti ratios remained almost the same. This suggested that PLD_{SL} at low KrF fluence led to non-congruent evaporation. However above 3 J/cm², the at. % ratio of Pb

Table 5-2. Atomic % ratios of Pb/(Zr + Ti), Zr/(Zr + Ti), and Ti/(Zr + Ti), obtained from EDS analysis, at laser-target interaction sites after ablation using increasing laser (KrF) fluences on a PZT target with 30 atomic % excess PbO, under single-laser (PLD_{SL}) and dual-laser (PLD_{DL}) conditions. For PLD_{DL}, the CO₂ fluence and interpulse p-p delay were kept constant at 2 J/cm² and 100 ns, respectively.

Laser (KrF) fluence (J/cm ²)	PLD _{SL}			PLD _{DL}		
	Atomic % ratio					
	Pb / (Zr + Ti)	Zr / (Zr + Ti)	Ti / (Zr + Ti)	Pb / (Zr + Ti)	Zr / (Zr + Ti)	Ti / (Zr + Ti)
0	1.30 ± 0.03	0.55 ± 0.01	0.45 ± 0.04	1.30 ± 0.03	0.55 ± 0.01	0.45 ± 0.04
1	0.83 ± 0.06	0.59 ± 0.04	0.40 ± 0.04	1.03 ± 0.09	0.58 ± 0.04	0.41 ± 0.02
3	1.03 ± 0.05	0.57 ± 0.03	0.42 ± 0.01	1.14 ± 0.01	0.58 ± 0.03	0.42 ± 0.02
5	1.02 ± 0.03	0.57 ± 0.02	0.43 ± 0.02	1.15 ± 0.02	0.58 ± 0.02	0.42 ± 0.03

reached saturation at ≈1.0, with the Zr and Ti ratios still the same. This implied that the preferential evaporation of Pb from the target was limited at high KrF laser fluences (> 3 J/cm²) where the high energy facilitated the congruent evaporation of materials from the target surface. From Table 5-2 it is clearly observed that the at. % of Pb in PLD_{DL} (using CO₂ fluence of 2 J/cm² and inter-pulse p-p delay (Δt) of 100 ns) at all KrF fluences is higher than PLD_{SL} while Zr and Ti ratios remain the same. This confirmed the role of PLD_{DL} in minimizing the Pb depletion in PZT.

Figure 79 (a and b) shows the XRD θ-2θ scans for PZT films deposited on STO (100) substrates using PLD_{DL} and PLD_{SL} with KrF fluence of 3 J/cm², denoted as PZT_{DL}-STO and PZT_{SL}-STO, respectively. In both cases, only strong (100) (*l* = 1, 2, and 3) diffraction peaks of PZT were observed along with those of the single-crystal STO (100) substrates suggesting the epitaxial growth of the film in relation to the substrate. The PZT peaks were indexed with the tetragonal phase with space group P4mm (99). The higher intensity of XRD peaks in PZT_{DL}-STO (Figure 79 a) as compared to PZT_{SL}-STO (Figure 79 b) suggested better crystallinity in these films.

This was also confirmed from the XRD rocking curves about the PZT (100) planes, as shown in inset (I) and (II) in Figure 79. The FWHM of the rocking curve for PZT_{DL}-STO (FWHM value of 0.1°) was much smaller than that of PZT_{SL}-STO (FWHM value of 0.5°), confirming a better in-plane crystal orientation. The insets (III) and (IV) in Figure 79 show the XRD θ-2θ scans for PZT films deposited on MgO (100) substrates using PLD_{DL} and PLD_{SL}, respectively. Epitaxial growth was also observed for PZT_{DL} and PZT_{SL} films on MgO substrates. However, the rocking curves about the PZT (100) plane of

PZT_{DL}-MgO exhibited better in-plane epitaxy with a FWHM of 0.5° as compared to PZT_{SL}-MgO with

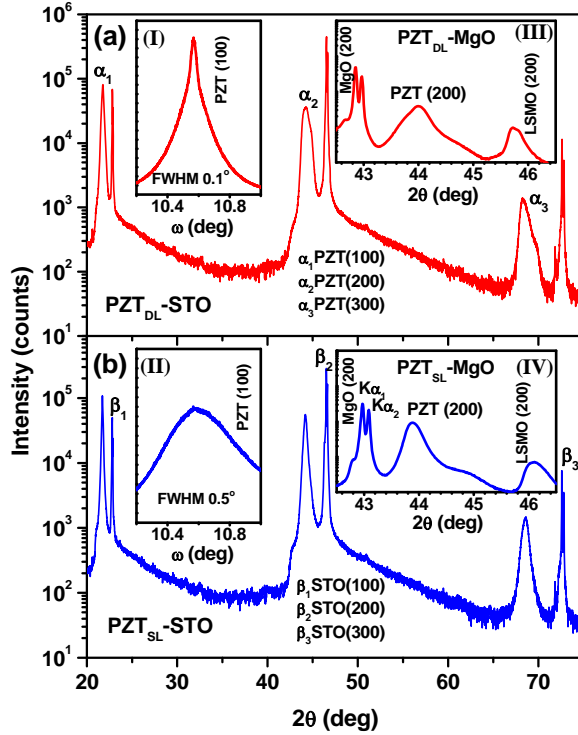


Figure 79: XRD patterns of PZT thin films deposited on SrTiO₃ (STO) (100) substrates, using dual-laser and single-laser ablations, denoted as (a) PZT_{DL}-STO and (b) PZT_{SL}-STO, respectively. Insets (I) and (II) show the XRD rocking curves about the PZT (100) planes for the PZT_{DL}-STO (FWHM value of 0.1°) and PZT_{SL}-STO films (FWHM value of 0.5°), respectively. Insets (III) and (IV) shows the θ -2 θ scans for PZT films deposited on MgO (100) substrates using PLD_{DL} and PLD_{SL}, respectively.

FWHM as 0.8°.

Figure 80 (a, and b) show the AFM images of PZT_{DL} and PZT_{SL} films on STO substrates, respectively grown using high KrF fluence of 3 J/cm². Clearly, PZT_{DL} (Figure 5 a) film exhibited a smoother surface ($R_{\text{rms}} = 1.6$ nm) and smaller grain size as compared to PZT_{SL} (Figure 80 b) film ($R_{\text{rms}} = 11.5$ nm). This suggested a higher nucleation of grains along the preferred PZT (100) direction in PZT_{DL}.

Polarization versus electric field (P-E) curves for PZT_{SL} and PZT_{DL} films on MgO and STO substrates, respectively, measured for driving voltages between 1 to 9 V are shown in Figure 81 (a, b). The curves have been plotted on the same scale for comparison. From Figure 6 it is clear that PZT_{DL} films showed enhanced polarization for all driving voltages as compared to PZT_{SL} films. From the figure, it can be seen that the P_r values showed a 70 % enhancement

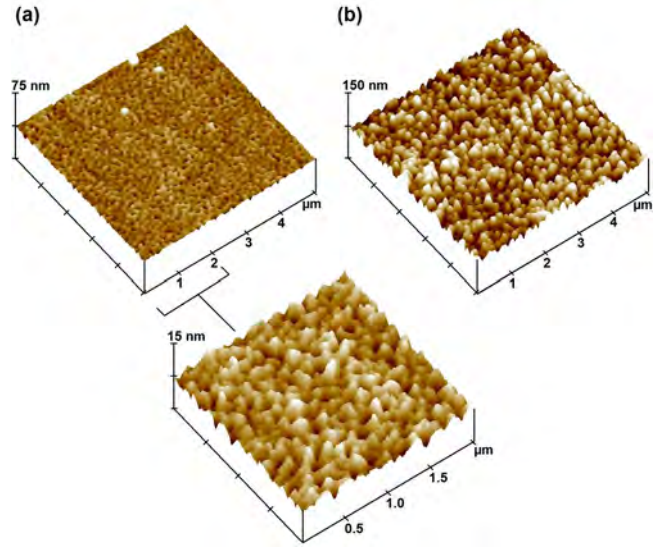


Figure 80: AFM images of PZT thin films on SrTiO₃ (100) substrates deposited using (a) dual-laser deposition (PLD_{DL}) with KrF fluence of 3 J/cm², CO₂ fluence of 2 J/cm², and 100 ns inter-pulse delay and (b) single-laser deposition (PLD_{SL}) with same KrF fluence, respectively.

from $P_r = 45 \mu\text{C}/\text{cm}^2$ for $\text{PZT}_{\text{SL}}\text{-MgO}$ to $P_r = 77 \mu\text{C}/\text{cm}^2$ for $\text{PZT}_{\text{DL}}\text{-MgO}$ and a 167 % enhancement from $P_r = 34 \mu\text{C}/\text{cm}^2$ for $\text{PZT}_{\text{SL}}\text{-STO}$ to $P_r = 91 \mu\text{C}/\text{cm}^2$ for $\text{PZT}_{\text{DL}}\text{-STO}$, respectively, under the same conditions. Such enhanced P_r could be attributed to the higher nucleation of grains along the preferred (100) direction of PZT_{DL} as compared to PZT_{SL} films. To our knowledge, the P_r values of $77 \mu\text{C}/\text{cm}^2$ and $91 \mu\text{C}/\text{cm}^2$ observed for PZT_{DL} films are the highest values ever reported for any in situ grown PZT films. Reported P_r values vary from 15 to $54 \mu\text{C}/\text{cm}^2$ for PLD_{SL} grown PZT films with one of the highest P_r values reported as $\approx 70 \mu\text{C}/\text{cm}^2$ for PLD_{SL} grown PZT films, but required ex situ post annealing at 750°C in air by rapid thermal annealing (RTA) technique. [131] The P-E loops for PZT_{DL} films showed much higher degrees of squareness (80 – 84 %) (Table III) and were more symmetric ($+P_r \sim -P_r$) (table III) as

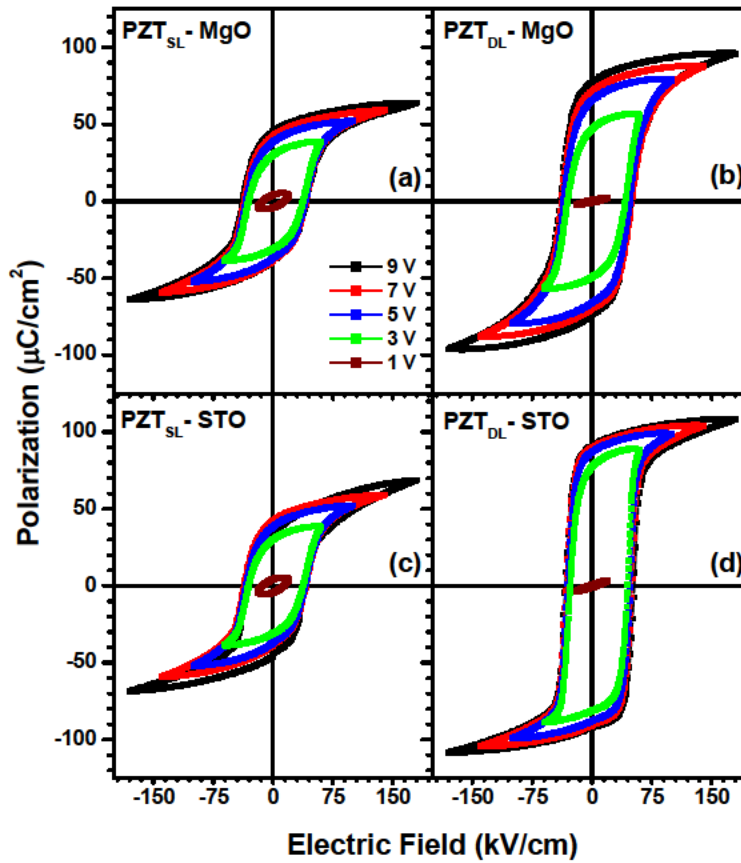


Figure 81: Polarization versus electric field (P-E) hysteresis loops for single-laser (PZT_{SL}) and dual-laser (PZT_{DL}) deposited PZT films on MgO and STO substrates, respectively. Data was measured for driving voltages between 1 to 9 V.

dual-laser ablated films exhibited record high remanent polarization and squareness, compared to data reported so far.

Enhanced ferroelectricity and ferromagnetism in epitaxial PZT/CFO heterostructures: In the final stage of the proposed task, PZT/CFO (FE/FM) heterostructures were fabricated using PLD. Recently, there have been numerous reports on the growth of PZT/CFO heterostructures mostly grown on Pt/Ti/SiO₂/Si

compared to PZT_{SL} films. Since it has been shown that asymmetric P-E loops give imprint failures in FE devices as a consequence of high built-in field, PZT_{DL} films were better suited for device application. [132] PZT_{DL} films showed much lower leakage current densities as compared to PZT_{SL} films, which indicated a lower concentration of defects in PZT_{DL} films. [133, 134].

To summarize, particulate-free smooth epitaxial $\text{Pb}(\text{Zr}_{0.52}\text{Ti}_{0.48})\text{O}_3$ thin films were grown on STO (100) and MgO (100) substrates using the dual-laser ablation process that exhibited enhanced ferroelectric properties as compared to films grown by single-laser ablation. Laser-target interaction studies showed that the preferential evaporation of Pb during ablation was minimized using high KrF fluences, however, leading to particulate laden films. The FE properties of

substrates and only a few on MgO or STO substrates [135-142]. The observed ME effect was primarily attributed to the residual strain at the interface [143,145].

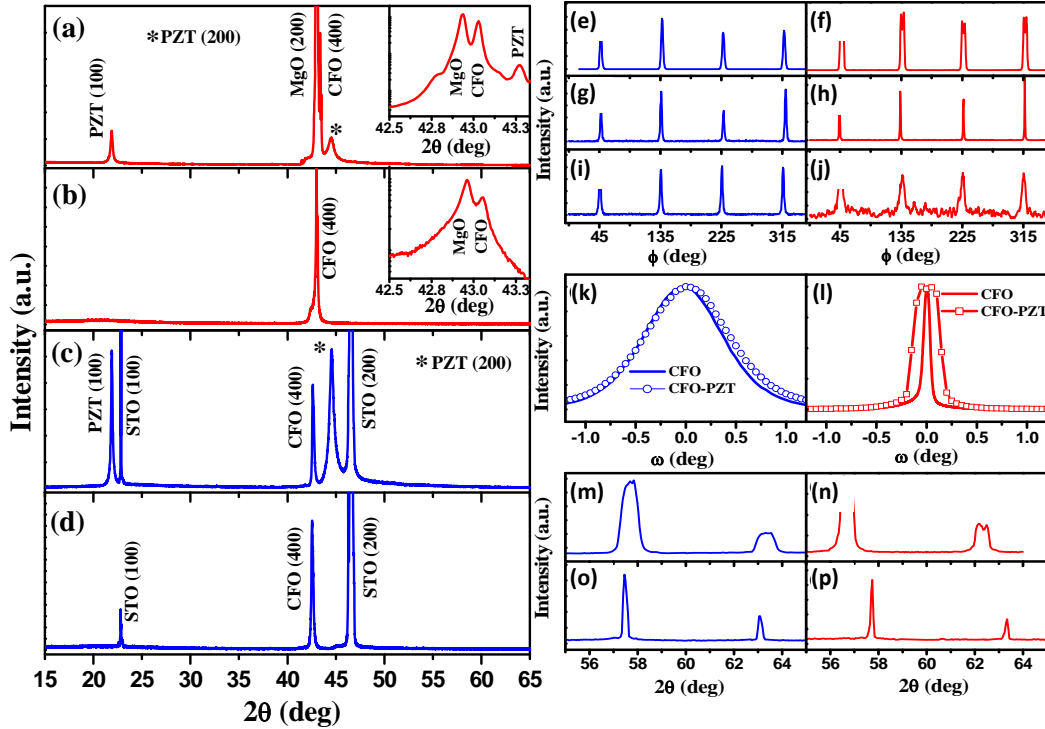


Figure 82: XRD θ - 2θ scans for single layer CFO and bilayer CFO-PZT films grown on MgO (a and b) and STO substrates (c and d), respectively. The insets to (a) and (b) show the details of the MgO (200), CFO (400) and PZT (200) peaks around 43° . (e-j) ϕ scan spectra from PZT (101) and CFO (311) reflection in CFO-PZT bilayer film. (k and l) Rocking curves of CFO (400) peaks. (m and n) and (o and p) are asymmetric scans of (511) and (440) CFO planes for single layer CFO films and bilayer layer CFO-PZT films respectively.

In this section epitaxial thin films of CFO-PZT bilayers were grown on single crystal MgO and SrTiO₃ (STO) substrates by PLD. The small lattice mismatch (0.04 %) between PZT (tetragonal perovskite, lattice parameters, $a=b= 4.036 \text{ \AA}$, $c= 4.146 \text{ \AA}$) and CFO (face-centered cubic, lattice parameter, $a = 8.391 \text{ \AA}$) as well as between CFO and the substrates allowed for the growth of the epitaxial films. Figure 82 (a, b) and 82 (c, d) show the XRD θ - 2θ spectra for PZT/CFO/MgO and CFO/MgO, and PZT/CFO/STO and CFO/STO respectively. In all the samples the single phase nature and epitaxial relationship with the substrates were observed. The XRD peak in CFO was assigned to the (400) plane, corresponding to the face-centered cubic (fcc) phase of CFO with space group Fd-3m (227). For PZT/CFO/MgO and PZT/CFO/STO films, the PZT peak was indexed to the (100) plane of tetragonal PZT with space group P4mm (99) (Figure 82 (a) and (c)). Due to the small lattice mismatch between MgO (face-centered-cubic, $2 \times$ lattice parameter = 8.42 \AA) and CFO, the MgO (200) and CFO (400) peaks were in close occurrence to each other in the θ - 2θ spectra. Figures 82 (e - j) show the ϕ scan spectra from the PZT (101) plane and CFO (311) plane for PZT/CFO/STO, PZT/CFO/MgO, CFO/STO and CFO/MgO, respectively. In all cases, the peaks in the ϕ spectra occurred at intervals of 90° suggesting four-fold cubic symmetry and cube-on-cube growth. Figures 82 (k) and (l) show the rocking curves (ω

scans) about the CFO (400) planes for PZT/CFO/STO and CFO/STO, and PZT/CFO/MgO and CFO/MgO, respectively. The small full-width at half maximum (FWHM) values ($< 1^\circ$) of the rocking curves confirmed a good degree of in-plane orientation for CFO in all the samples (see Table 5-3 for FWHM values). However the (400) texture was sharper in the films grown on MgO which may be attributed to the smaller lattice mismatch between CFO and MgO. In addition, the degree of (400) texturing of CFO weakened slightly in PZT/CFO/STO and PZT/CFO/MgO compared to PZT/STO and PZT/MgO, respectively. Figures 7 (m) and (n) show the asymmetric scans of (511) and (440) planes of CFO for CFO/STO and CFO/MgO, respectively. Figures 82 (o) and (p) show the similar asymmetric scans for PZT/CFO/STO and PZT/CFO/MgO, respectively. For Figures 82 (m) to (p) the left peaks are from CFO (511) plane and the right peaks are from CFO (440) planes. The average in-plane lattice parameters ($a_{||}$) for CFO in the samples were calculated from the asymmetric scans shown in Figures 82 (m) to (p) (see Table 5-3).

The strain (ϵ) in the CFO layer was calculated by using the formula $\epsilon = (a - a_o)/a_o$, where a is out-of-plane (a_{\perp}) or in-plane ($a_{||}$) lattice parameter and a_o is the bulk unstressed lattice parameter of CFO ($a_o = 8.39 \text{ \AA}$). The in-plane stress ($\sigma_{||}$) in the film was calculated using the relation $\sigma_{||} = Y \epsilon_{||}$ where $\epsilon_{||}$ is the in-plane strain (ϵ) and the Young's modulus value for CFO ($Y = 1.5 \times 10^{12} \text{ dyne/cm}^2$). Table 5-3 summarizes the lattice parameters and strains calculated for the out-of-plane and in-plane configurations. From the strain values listed in Table 5-3 it is seen that the CFO/MgO films grew with slight in-plane tensile ($\epsilon_{||} = 0.0015$) and out-of plane compressive ($\epsilon_{\perp} = -0.0005$) strains. On the other hand, the CFO/STO film grew with larger in-plane compressive ($\epsilon_{||} = -0.0116$) and out-of plane tensile ($\epsilon_{\perp} = 0.0124$) strains. This could be attributed to the different lattice mismatches of CFO with MgO and STO substrates. The lattice mismatch at room temperature was calculated using the relation $(a_s - a_o)/a_s$ (%) where a_s is the lattice parameter of the substrate. The calculated values for CFO/MgO and CFO/STO were 0.36% and 7.8%, respectively. It was also observed that the in-plane lattice parameter ($a_{||}$) of CFO for the PZT/CFO/MgO film ($a_{||} = 8.294 \text{ \AA}$) was smaller than that of the CFO/MgO film ($a_{||} = 8.403 \text{ \AA}$).

Table 5-3. FWHM of rocking curves about CFO (400) plane, in-plane ($a_{||}$) and out-of-plane (a_{\perp}) lattice parameters obtained from XRD peaks, in-plane ($\epsilon_{||}$) and out-of-plane (ϵ_{\perp}) strains calculated using $\epsilon = (a - a_o)/a_o$, where a is $a_{||}$ or a_{\perp} and a_o is the bulk lattice parameter of CFO ($a_o = 8.39 \text{ \AA}$), and the in-plane stress calculated from in-plane strain and Young's modulus of CFO ($Y = 1.5 \times 10^{12} \text{ dyne/cm}^2$) for CFO and CFO-PZT films on MgO and STO substrates.

Sample	FWHM of Rocking curve ($^\circ$)	Out-of-plane a_{\perp} (\AA)	strain ϵ_{\perp}	In-plane $a_{ }$ (\AA)	In-plane strain $\epsilon_{ }$	In-plane stress (dyne/cm^2)
CFO/MgO	0.076	8.386	-0.0005	8.403	0.0015	2.25×10^9
PZT/CFO/MgO	0.321	8.338	-0.0062	8.294	-0.0114	-17.1×10^9
CFO/STO	0.915	8.494	0.0124	8.292	-0.0116	-17.5×10^9
PZT/CFO/STO	0.986	8.479	0.0106	8.33	-0.0071	-10.7×10^9

This suggested that possibly with the deposition of the PZT layer on top, the CFO layer experienced an in-plane compression that compelled it to match its a_n to the smaller lattice parameter of PZT ($a = b = 4.036 \text{ \AA}$, $c = 4.146 \text{ \AA}$). As a consequence the in-plane strain and consequently the stress was amplified in PZT/CFO/MgO. However, an opposite trend was observed for the films grown on STO substrates. The CFO/STO film was already highly strained due to the large mismatch between the STO substrate and CFO. With PZT layer on top of it, the PZT/CFO/STO film was slightly relaxed to a lower strain state.

In order to analyze the surface morphologies of the thin films and predict their mechanisms of growth, AFM was employed. Figure 83 (a) illustrates an AFM image of the CFO top layer for CFO/MgO film. The image revealed a very smooth and compact surface with a root mean square roughness (R_{rms}) value of 2.084 nm and small grain size with relatively uniform size

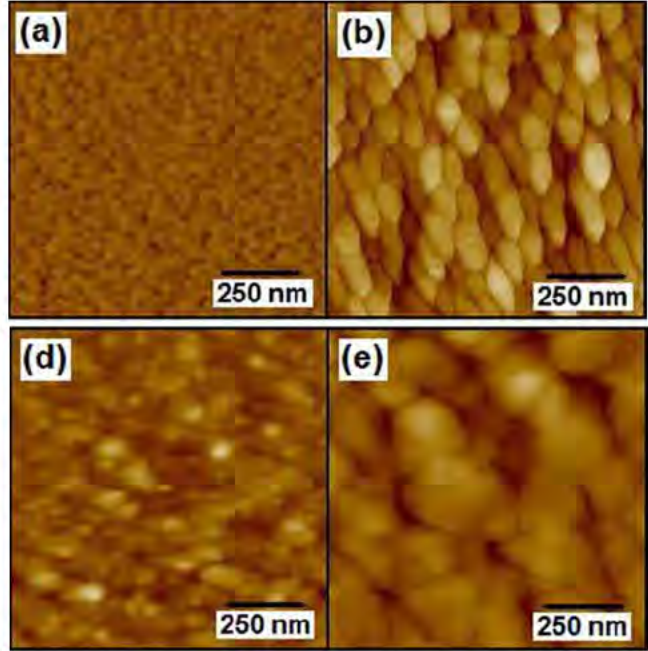


Figure 83: AFM images of the CFO and PZT surfaces of PZT/CFO bilayers on MgO and STO substrates, respectively.

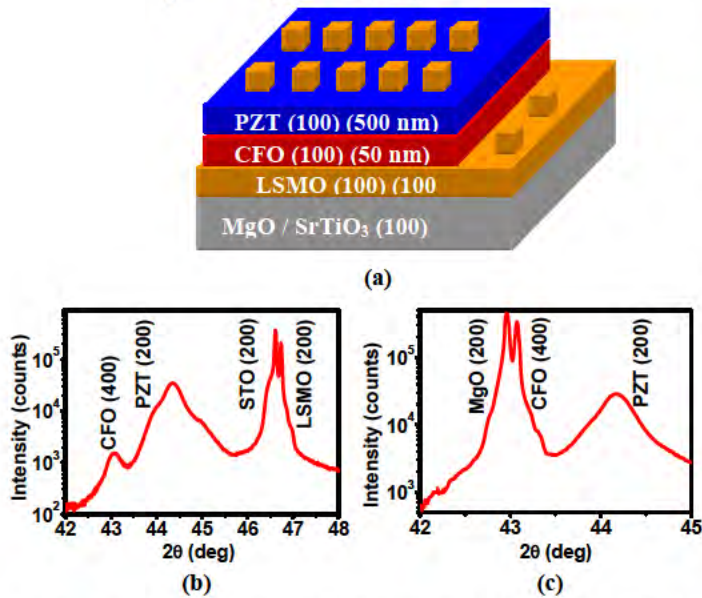


Figure 84: (a) Schematic diagram of PZT/CFO/LSMO heterostructure grown on MgO or STO (100) substrate and (b, c) XRD θ - 2θ scans of PZT/CFO/LSMO heterostructures grown on STO and MgO (100) substrates, respectively.

distribution, indicative of a layer-by-layer growth mechanism. Figure 83 (b) shows an AFM image of the PZT top layer for PZT/CFO/MgO film. The PZT layer was relatively less smooth with R_{rms} value of 11.456 nm and larger grain size as compared to CFO/MgO. Uniform grain size distribution was also observed for PZT. Films grown on STO substrates showed distinctively different surface morphology. Figure 83 (c) shows the surface of CFO/STO film. The surface appears rougher than CFO/MgO with R_{rms} value of 7.502 nm. It also consisted of grains with various shapes and sizes, attributed to the island growth mode. Figure 83 (d) shows the PZT top surface for PZT/CFO/STO film. The various grain sizes with larger grain growth and R_{rms} value of 22.683 nm still conformed to the island growth mechanism.

For FE measurements, LSMO/PZT/CFO/LSMO capacitors were fabricated as shown schematically in Figure 84 (a). Figure 9 (b and c) show the XRD θ - 2θ scans of PZT/CFO/LSMO heterostructures grown on STO and MgO (100) substrates, respectively. In both cases, only strong (100) ($l = 1, 2, \text{ and } 3$) diffraction peaks of PZT, CFO and LSMO were observed along with those of the single-crystal STO (100) and MgO (100) substrates confirming the epitaxial growth of the film in relation to the substrate. While the PZT peaks were indexed with the tetragonal phase with space group $P4mm$ (99), the CFO peaks matched with CFO face-centered-cubic (fcc) lattice with space group $Fd-3m$ (227). Figure 85 (a) shows a cross-sectional TEM image of the PZT/CFO/LSMO thin film on STO substrate. From the image it is evident that the individual layers in the heterostructure are flat and of uniform thicknesses.

Figure 85 (b, and c) shows high resolution TEM (HRTEM) cross-sectional images of the PZT-CFO and CFO-LSMO interfaces, respectively. The images clearly exhibit good epitaxial cube-on-cube growth morphology from LSMO to CFO (Figure 85 c) and then from CFO to PZT (Figure 85 b). The measured d-spacing values were consistent with those obtained from XRD. Figure 85 (d) shows a typical selected area electron diffraction (SAED) pattern taken near the PZT-CFO interface. The linear dotted SAED pattern corresponds to the single crystalline nature of the PZT and CFO layers. Due to the close lattice parameters of PZT and CFO a twinning pattern (as shown by the red and yellow arrows) is observed in the SAED patterns. Such twinning patterns were not observed in SAED patterns captured away from the interface excluding the possibility of defect-generated twin patterns. To illustrate the above, the SAED pattern for the LSMO layer in Figure 85 (e) shows single crystal nature and cubic symmetry with no indication of twins. Similar single crystalline SAED patterns were observed for all layers corroborating the XRD observations.

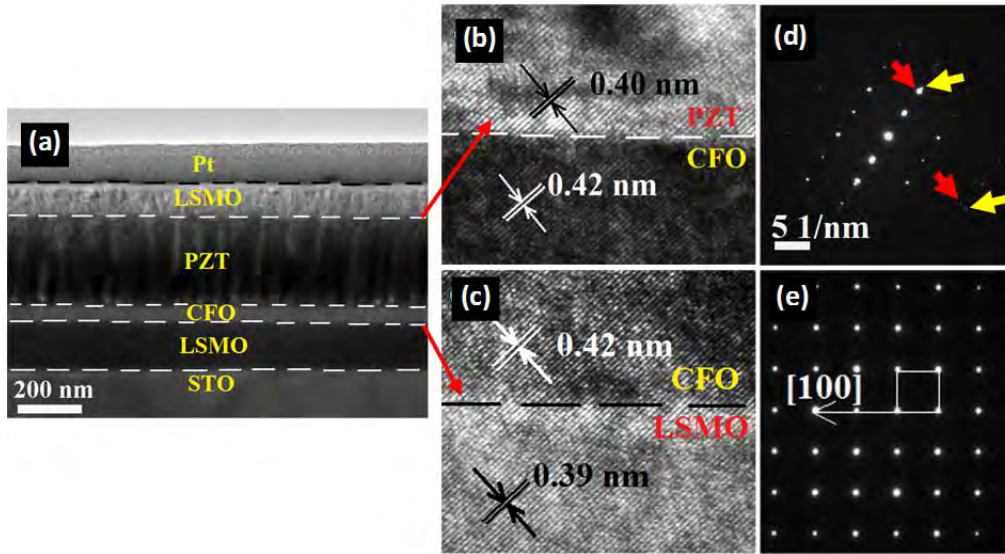


Figure 85: (a) Cross-sectional TEM image of the PZT/CFO/LSMO heterostructure with the LSMO top electrode grown on STO (100) substrate using dual-laser ablation. Cross-sectional HRTEM images and SAED patterns of (b, c) PZT-CFO interface and (d, e) CFO-LSMO interface for the PZT/CFO/LSMO heterostructure grown on STO (100) substrate.

Figure 86 (a, b) shows the in-plane M-H curves at 300 K for the PZT/CFO/LSMO and PZT/LSMO films on STO (100) and MgO (100) substrates, respectively. PZT/CFO/LSMO showed enhanced saturation magnetization (M_s) values of 370 emu/cm^3 and 290 emu/cm^3 as compared to 280 emu/cm^3 and 230

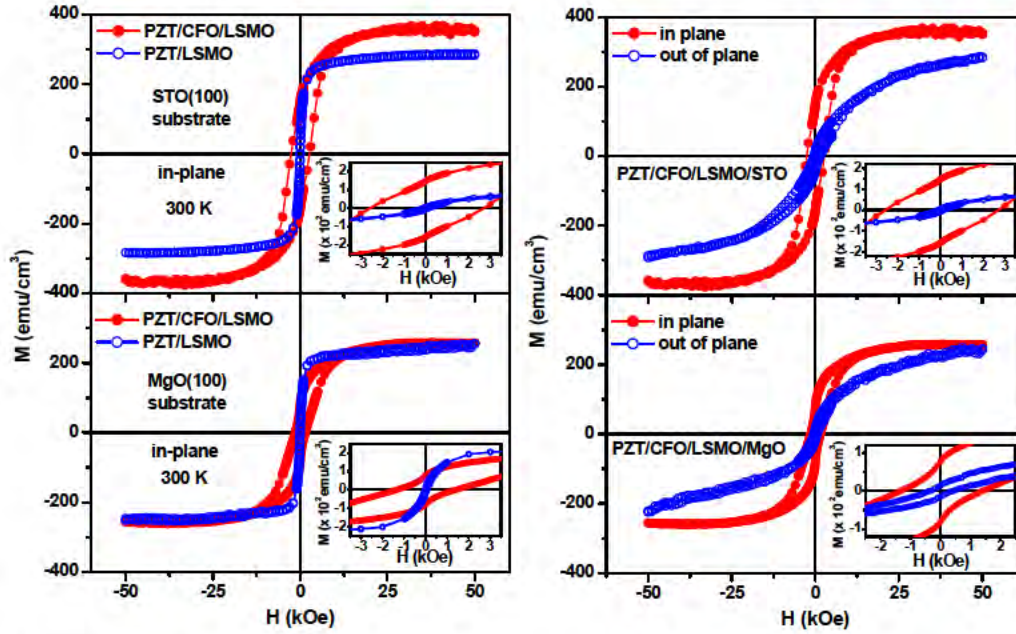


Figure 86: In-plane M-H curves at 300 K for the PZT/CFO/LSMO and PZT/LSMO films on STO (100) and MgO (100) substrates

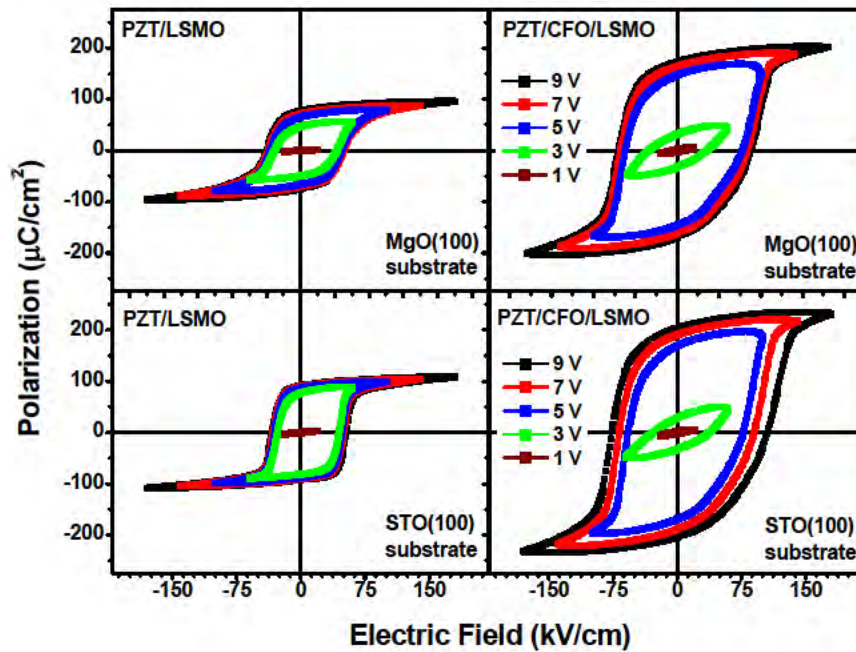


Figure 87: P-E loops for PZT/LSMO and PZT/CFO/LSMO thin films on MgO (100) and STO (100) substrates, respectively

emu/cm³ for PZT/LSMO on both STO and MgO substrates, respectively. With the introduction of hard magnetic material CFO, the low coercivity of PZT/LSMO increased from 0.1 kOe to 2.6 kOe, on both

types of substrates. In- and out-of-plane M-H loops for PZT/CFO/LSMO as shown in Figure 86 (c and d) demonstrate the in-plane uniaxial magnetic anisotropy in this heterostructure, similar to epitaxial PZT/LSMO thin films with the easy axis of magnetization along the film plane.

Figure 87 shows the P-E curves for the PZT/LSMO and PZT/CFO/LSMO heterostructures on MgO (100) and STO (100) substrates, respectively, measured at varying driving voltages of 1 V to 9 V. All the samples show well-saturated and square hysteresis loops corroborating the high crystalline quality of the samples. The PZT/CFO/LSMO heterostructures show higher remanent polarization in comparison to the PZT/LSMO thin films. The enhanced remnant polarization (P_r) values of $121 \mu\text{C}/\text{cm}^2$ and $182 \mu\text{C}/\text{cm}^2$ in PZT/CFO/LSMO on MgO and STO substrates, respectively, as compared to $77 \mu\text{C}/\text{cm}^2$ and $91 \mu\text{C}/\text{cm}^2$, for PZT/LSMO/MgO and PZT/LSMO/STO, respectively, indicate a charge screening mechanism for increased polarization.

In conclusion, PZT/CFO heterostructures were grown on lattice matched single crystal MgO and STO (100) substrates. X-ray diffraction (XRD) revealed the single crystalline nature and the epitaxial relationship between the layers. Cross-sectional TEM analysis exposed atomically sharp and defect-free interfaces in the structure. FE and FM measurements showed enhanced properties in PZT/CFO heterostructures in comparison to their single-phase films.

5.3. Materials growth efforts continued with piezoelectric films containing nanoparticle inclusions, experiments to study the magneto-electric and multiferroic coupled response in materials and prototype device structures:

In this task we have doped PZT thin films with the rare earth ion La^{3+} to enhance its FE properties. Aliovalent doping of La in PZT influences its microstructure and confers it with enhanced dielectric [146] and piezoelectric properties, both in bulk and thin film form [147, 148]. In terms of FE properties, the effect of La doping in bulk PLZT ceramics have been relatively less investigated, although increased the squareness of the FE hysteresis loop and decreased coercive fields (E_c) in bulk PLZT ceramics have been reported [149, 150]. On the other hand, detailed literature survey shows that the FE properties of PLZT thin films have been rarely reported [151-153].

In this work, we report on the epitaxial PLZT/LSMO heterostructures with atomic (at.) % of La varying as 0.1 %, 0.5 % and 1 % that were deposited on single crystal SrTiO_3 (STO) (100) substrates using PLD. Figure 88 (a) shows a schematic diagram of the layered PLZT/LSMO thin film on STO substrate and representative AFM images of the PLZT and LSMO surfaces. The as-deposited LSMO thin films exhibited similar smooth surface morphologies with roughness values as low as 1-2 nm (as shown in Figure 88a) and uniform grain size distribution ($\approx 60 \pm 9 \text{ nm}$), consistent with earlier reports [154]. The good surface quality of the underlying LSMO layers provided an optimum platform for the subsequent growth of the PLZT layers. AFM analysis revealed that all the PLZT thin films showed similar particulate-free surfaces features with roughness values ranging from 10-12 nm and uniform grains of sizes $\approx 170 \pm 10 \text{ nm}$ [155]. Figure 88 (b) shows the XRD θ -2 θ patterns for the undoped PZT and the PLZT thin films. In all cases, only strong (00 l) ($l = 1, 2, \text{ and } 3$) diffraction peaks of PZT were observed along with those of the LSMO layers and the single-crystal STO substrates suggesting the epitaxial relationship of the thin films in relation to their substrates. The in-plane epitaxial relationship of the undoped PZT and the PLZT layers were confirmed from ϕ scans performed about the PZT (101) plane.

As shown in Figure 89 (a), the repeated occurrence of the XRD peaks in the ϕ spectra at intervals of 90° indicate the four-fold cubic symmetry of the undoped PZT and the PLZT layers.

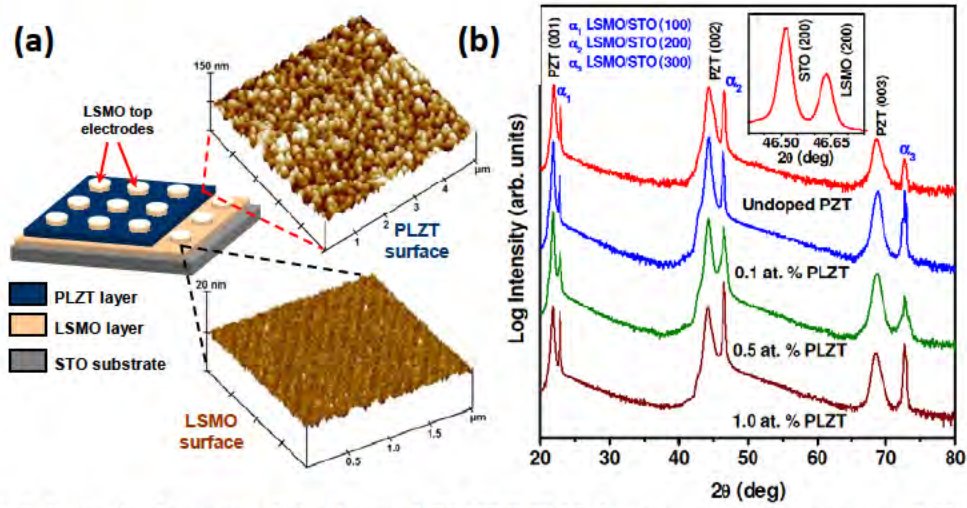


Figure 88: (a) Schematic diagram of the layered PLZT/LSMO heterostructure grown on SrTiO₃ (STO) (100) substrate and representative AFM images of the surface morphologies of PLZT and LSMO layers. (b) XRD θ - 2θ patterns for the undoped PZT and the PLZT thin films at varying La concentrations of 0.1 atomic (at.) %, 0.5 at. % and 1.0 at. %; denoted as 0.1 at. % PLZT, 0.5 at. % PLZT and 1.0 at.% PLZT; grown on LSMO-STO (100) substrates. Inset to (b) shows the details of the STO (200) and LSMO (200) peaks at small 2θ range.

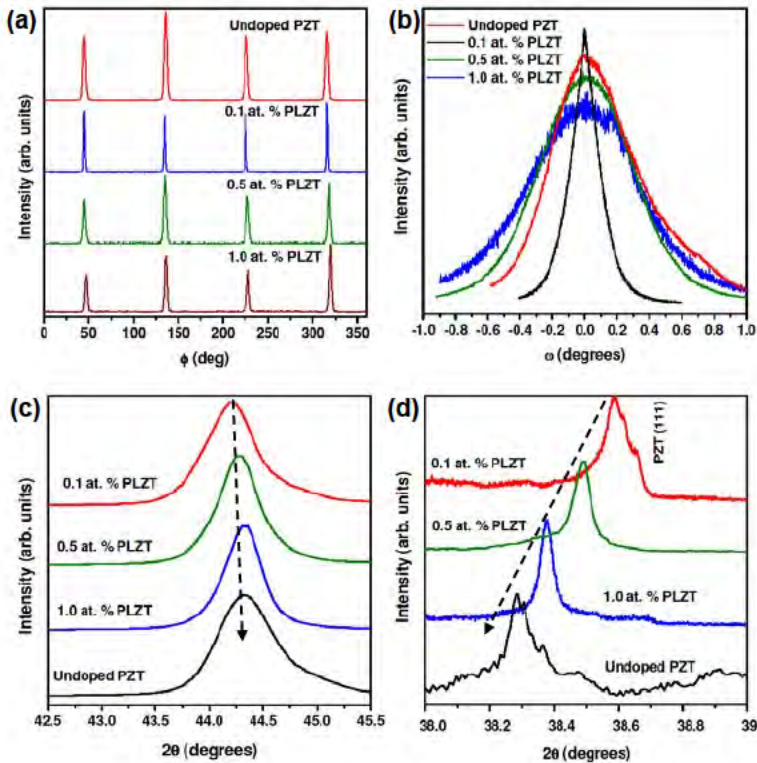


Figure 89: XRD (a) ϕ scans about the PZT (101) plane, (b) rocking curves about the PZT (002) plane, (c) symmetric θ - 2θ scans about the PZT (002) plane and (d) asymmetric 2θ - ω scans about the PZT (111) plane for the undoped PZT and the PLZT thin films at varying La concentrations of 0.1 atomic (at.) %, 0.5 at. % and 1.0 at. %; denoted as 0.1 at. % PLZT, 0.5 at. % PLZT and 1.0 at.% PLZT, respectively.

Figure 89 (b) shows the XRD rocking curves performed about the PZT (002) planes for the PZT and the PLZT thin films. The small full-width-at-half-maximum (FWHM) values ($< 1^\circ$) of the rocking curves confirmed the excellent in-plane orientation in all the samples (see Table 5-4 for the FWHM values).

Table 5-4. FWHM of X-ray rocking curves about the PZT (002) plane, out-of-plane (a_\perp) and in-plane (a_\parallel) lattice parameters, out-of-plane (ε_\perp) and in-plane (ε_\parallel) strains, saturation polarization (P_{sat}), remanent polarization (P_r), coercive field (E_c) measured at 9 V driving voltage for PLZT films with varying La-doping concentrations and undoped PZT thin film.

Sample	FWHM of Rocking curve ($^\circ$)	Lattice parameters		Strain		Polarization		
		a_\perp (\AA)	a_\parallel (\AA)	ε_\perp (%)	ε_\parallel (%)	P_{sat} ($\mu\text{C}/\text{cm}^2$)	P_r ($\mu\text{C}/\text{cm}^2$)	E_c (kV/cm)
0.1 at. % PLZT	0.18	4.121 ± 0.007	3.931 ± 0.005	0.26	-3.05	102 ± 4	91 ± 2	32 ± 2
0.5 at. % PLZT	0.57	4.119 ± 0.006	3.967 ± 0.003	0.22	-2.17	76 ± 5	65 ± 3	30 ± 3
1.0 at. % PLZT	0.66	4.116 ± 0.005	3.987 ± 0.006	0.15	-1.67	60 ± 7	50 ± 4	39 ± 4
Undoped PZT	0.52	4.115 ± 0.007	4.001 ± 0.002	0.12	-1.33	45 ± 3	41 ± 4	38 ± 4

However, as is evident from Figure 89 (b), the (002) texturing was the highest in the 0.1 at. % PLZT thin film with the sharpest and narrowest XRD peak (FWHM = 0.18°) as compared to the other samples. The degree of (002) texturing weakened slightly in the 0.5 at. % (FWHM = 0.57°) and 1.0 at. % (FWHM = 0.66°) PLZT thin films. This could be associated with the development of different residual strains in the samples at higher doping levels. Figures 89 (c and d) show the XRD symmetric θ -2 θ scans and asymmetric 2θ - ω scans about the PZT (002) and PZT (111) planes, respectively, for all the samples. From Figure 89 (c), a small shift in the XRD peaks to higher 2θ values is observed in the PLZT thin films as the La doping increased from 0.1 at. % to 1 at. %, suggesting a very slight decrease in the out-of-plane d-spacings and lattice parameters. However, from the asymmetric scans in Figure 89 (d), a larger shift in XRD peaks to higher 2θ values is observed in the 0.1 at. % PLZT thin film as compared to the undoped PZT thin film. This indicates the in-plane d-spacings and lattice parameters were the lowest in the 0.1 at. % PLZT and gradually increased in the higher doped samples with the undoped PZT film exhibiting the highest lattice parameter.

Similar results were obtained from the symmetric scans about PZT (001) and (003) planes, and asymmetric scans about PZT (101), (110), and (211) planes. The PZT planes for the asymmetric scans were chosen such that there were no contributions to XRD peaks from the underlying LSMO or STO layers. The average out-of-plane (a_\perp) and in-plane (a_\parallel) lattice parameters in all the samples calculated from the symmetric and asymmetric scans, respectively, have been summarized in Table 5-4. Subsequently, the out-of-plane (ε_\perp) and in-plane (ε_\parallel) strains in the PLZT and PZT layers were calculated by using the formula $\varepsilon = (a - a_o)/a_o$, where a is a_\perp or a_\parallel and a_o is the bulk unstressed lattice parameter of

PZT (tetragonal, $a_{o\perp} = 4.11 \text{ \AA}$, $a_{o\parallel} = 4.055 \text{ \AA}$) as measured from powder XRD pattern (summarized in Table 5-4).

From the lattice parameter and strain values in Table 5-4, the following observations are evident:

I. For the undoped PZT thin film, the strain values ($\epsilon_{\perp} = 0.12 \%$ and $\epsilon_{\parallel} = -1.33 \%$) indicate that although there is no significant out-of-plane strain, the PZT layer in PZT/LSMO experienced an in-plane compressive strain in order to match the smaller lattice parameter of the LSMO (pseudo cubic, $a_o = 3.878 \text{ \AA}$) bottom layer. This resulted in a slightly larger out-of-plane tetragonal distortion of the PZT lattice increasing the a_{\perp}/a_{\parallel} (or c/a) ratio to 1.03 from that of 1.01 in unstrained PZT unit cell, consistent with earlier reports [144].

II. For the PLZT thin films, a decrease in a_{\parallel} values but with similar a_{\perp} values is observed as compared to the undoped PZT thin film. This is consistent with the earlier reports where the cell parameters of the PZT thin film decreased with the addition of La dopant [142]. Substitution of A-site in ABO_3 -type PZT, with the La^{3+} ion having smaller radii than the Pb^{2+} ion leads to the shrinking of the lattice parameter.

III. In-plane compressive strains in PLZT films have been reported earlier [156]. From Table 5-4, a systematic increase from $\epsilon_{\parallel} = -1.67$ for 1.0 at. % PLZT to $\epsilon_{\parallel} = -3.05$ for 0.1 at. % PLZT is observed. The lower ϵ_{\parallel} values at higher La-doping concentrations could be associated with some of the La^{3+} occupying the interstitial sites in addition to the substitutional sites in the PLZT unit cell. The 0.1 at. % PLZT sample has the highest out-of-plane tetragonal distortion with the a_{\perp}/a_{\parallel} ratio of 1.05 as compared to 1.02 for the undoped PZT thin film.

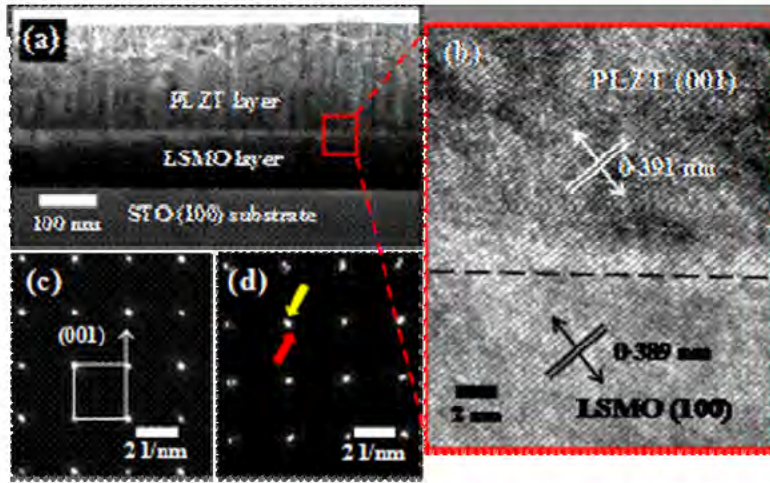


Figure 90: (a) Cross-sectional TEM image of the 0.1 at. % PLZT/LSMO layered heterostructure. (b) HRTEM image of the PLZT-LSMO interface captured from the 0.1 at. % PLZT/LSMO layered structure. (c, d) SAED patterns captured near the (c) PLZT-LSMO interface of the 0.1 at. % PLZT/LSMO thin film and the (d) PZT-LSMO interface of the undoped PZT thin film, respectively.

To summarize, both the epitaxial strain from the lattice mismatch and smaller ionic radius of the dopant La^{3+} lead to higher compressive strains in PLZT thin films as compared to undoped PZT thin films. The cross-sectional TEM image of the 0.1 at. % PLZT thin film as shown in Figure 90 (a) demonstrates distinctly sharp and flat interfaces along with uniform thicknesses of the individual layers.

Similar cross-sectional microstructure was obtained for all the samples and corroborated to their

optimized growth using PLD. Figure 90 (b) shows the HRTEM image of the PLZT-LSMO interface. The atomically sharp and flat interface along with the continuous lattice fringes from the bottom LSMO layer to the top PLZT layer clearly demonstrate their single crystalline nature and the cube-on-cube epitaxial growth morphology, with no evidence of any structural defects. The measured d-spacing values (in Figure 90 b) are consistent with those obtained from XRD. HRTEM images of the LSMO-STO interface also showed atomically sharp and flat interfaces with no structural defects, similar to our earlier reports. The linear dotted single-crystalline SAED pattern in Figure 90 (c) captured near the PLZT-LSMO interface confirms the close lattice parameters and crystal structure of the PLZT and LSMO layers. In comparison, the SAED pattern obtained near the undoped PZT-LSMO interface shows the presence of slightly-displaced lattice planes (as shown by arrows in Figure 90 d) indicating a lattice mismatch between the PZT and LSMO layers. From the TEM analysis it is concluded that PLZT and LSMO have close lattice parameters indicating an in-plane compression of the PLZT unit cell, while undoped PZT and LSMO have slightly mismatched lattice parameters with slightly strain-relaxed PZT unit cell having larger lattice parameter than the underling LSMO layer. These results are consistent with those obtained from the XRD strain analysis shown earlier.

Figures 91 (a, b, c, and d) show the polarization versus electric field (P-E) curves for undoped PZT, 0.1 at. % PLZT, 0.5 at. % PLZT, and 1 at. % PLZT thin films, respectively, measured at driving voltages varying from 1 to 9 V. While both the saturation polarization (P_{sat}) and remnant polarization (P_r) consistently increase with increasing driving voltages, the coercive fields (E_c) show almost constant values as function of driving voltages suggesting that space charge effects are negligible in the samples [157]. Such well behaved P-E curves could be attributed to the high crystalline quality of the samples and almost defect-free nature of their interfaces as observed earlier in their XRD and TEM analysis, respectively. The P-E curves for the PLZT thin films (Figure 91 b, c and d) show higher P_{sat} and P_r values than the undoped PZT thin film at all driving voltages (Figure 91 a) with the highest values observed in the

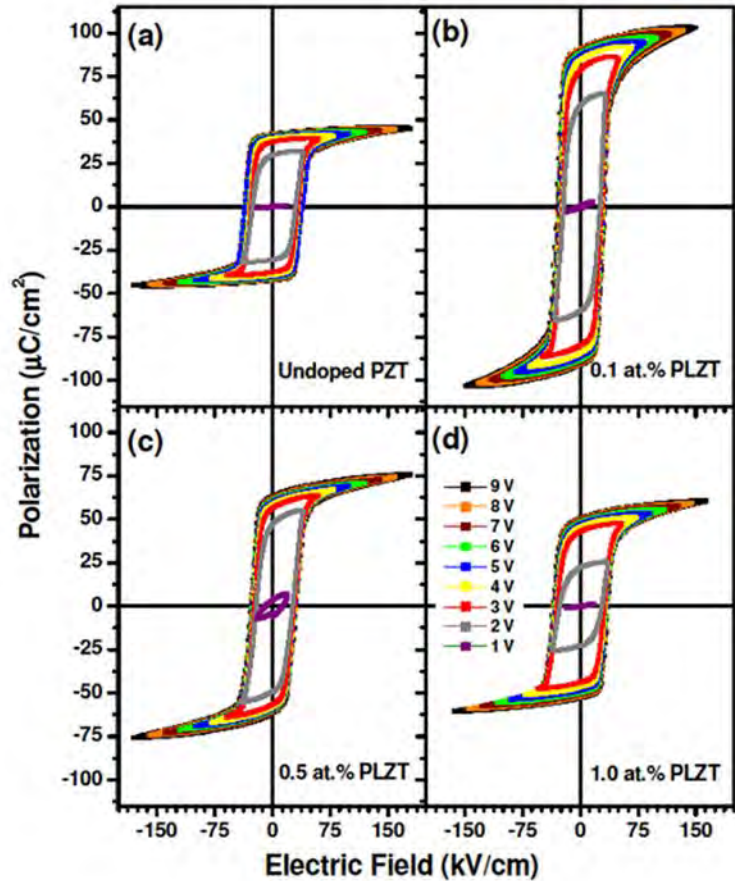


Figure 91: Polarization versus electric field (P-E) curves for (a) undoped PZT, (b) 0.1 atomic (at. %) PLZT, (c) 0.5 at. % PLZT, and (d) 1 at. % PLZT thin films, respectively, measured at driving voltages varying from 1 to 9 V (shown by different colors).

0.1 at. % PLZT sample. The decrease in P_r values at higher doping of La has been recently reported for bulk PLZT ceramics of the same composition, and attributed to the internal strain created at higher doping [158], however, no such observation has been reported for PLZT thin films. To clearly demonstrate the enhanced FE properties of PLZT thin films, at lower La-doping concentrations, the P-E curves for the PLZT and undoped PZT thin films measured at the maximum driving voltage of 9 V and the trends in the recorded P_r and E_c values as a function of La-doping concentrations have been plotted in Figures 92 (a and b). The P_r value for the undoped PZT film of $41 \mu\text{C}/\text{cm}^2$ at E_c of 38 kV/cm match well with earlier reports on epitaxial PZT films [159].

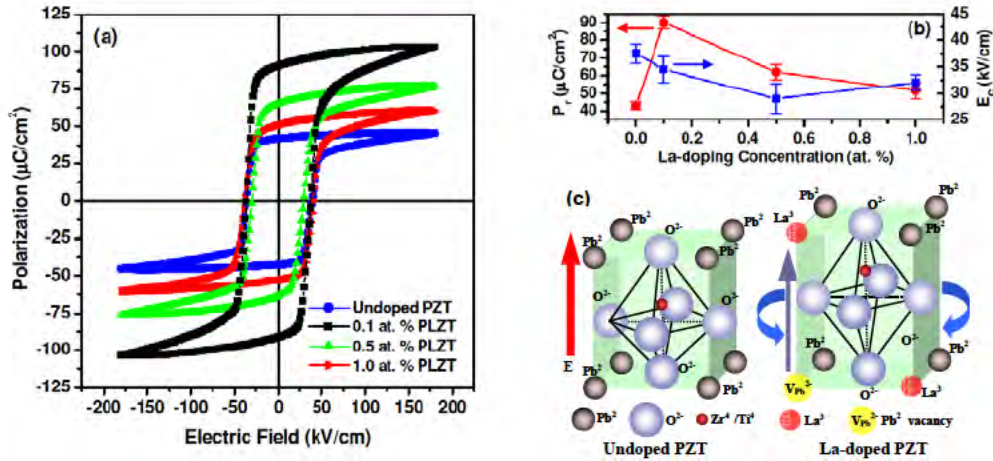


Figure 92: (a) Polarization versus electric field (P-E) curves for undoped PZT, 0.1 atomic (at. %) PLZT, 0.5 at. % PLZT, and (d) 1 at. % PLZT thin films, respectively, measured at driving voltage of 9 V. (b) Variation of remnant polarization (P_r) and coercive field (E_c) as function of La-doping concentrations. (c) Schematic diagrams of the tetragonal undoped PZT unit cell and La-doped PZT unit cell with enhanced tetragonality under in-plane compressive strain and the La^{3+} - $\text{V}_{\text{Pb}}^{2-}$ defect dipole moments under external applied field (E).

Reported P_r values vary from 15 to 36 $\mu\text{C}/\text{cm}^2$ at higher E_c (≈ 194 kV/cm) for polycrystalline PZT films with higher P_r values of 45 to 54 $\mu\text{C}/\text{cm}^2$ at lower E_c of 35-40 kV/cm recorded for epitaxial PZT/LSMO thin films [160]. From Table 5-4, it can be observed that compared to the undoped PZT film, the P_r values in the PLZT films progressively increase from 50 $\mu\text{C}/\text{cm}^2$ for 1.0 at. % PLZT (22 % enhancement) to 65 $\mu\text{C}/\text{cm}^2$ for 0.5 at. % PLZT (58 % enhancement) to 91 $\mu\text{C}/\text{cm}^2$ for 0.1 at. % PLZT (122 % enhancement). To our knowledge, such high P_r values have been observed for the first time in PLZT thin films, and the record high P_r of 91 $\mu\text{C}/\text{cm}^2$ for the 0.1 at. % PLZT is the highest P_r observed in any doped or undoped PZT system. Reported P_r values vary from 11 $\mu\text{C}/\text{cm}^2$ at E_c of 40.6 kV/cm for sol-gel derived PLZT films [156] to 19 $\mu\text{C}/\text{cm}^2$ at E_c of 70 kV/cm for PLD deposited polycrystalline PLZT thin films on Pt(Si) substrates [161]. A similar trend in increased P_r values at lower doping concentrations compared to the undoped PZT thin films and the decrease in P_r values at higher doping concentrations have been reported for similar aliovalent donor-type Nb doped PZT thin films [162]. From Table 5-4, it is also observed that the E_c values for the 0.1 at. % ($E_c = 32$ kV/cm) and 0.5 at. % ($E_c = 30$ kV/cm) PLZT films are lower than the undoped PZT film ($E_c = 38$ kV/cm) which is consistent with earlier reports on bulk PLZT ceramics [163].

When La^{3+} substitutes Pb^{2+} in PZT, it induces lead vacancies ($\text{V}_{\text{Pb}}^{2-}$) into the PZT unit cell to maintain its electrical neutrality and the doping concentration governs the density of such defects. However, it creates the possibility of producing immobile ($\text{La}^{3+}-\text{V}_{\text{Pb}}^{2-}$)-type defect dipoles within the PZT unit cell. In polycrystalline samples, due to the different crystal orientations, these defect dipoles produce random fields that locally destabilize the domain structure. The lowered stability of the domain structure against external mechanical or electrical fields facilitates domain wall motion in PLZT, consequently enhancing its piezoelectric and dielectric properties as have been experimentally observed [164]. On the other hand, in epitaxial PLZT films, due to the unidirectional orientation of the PZT unit cells, there is a higher probability that the defect-dipoles are aligned parallel to the external applied field during poling (as shown schematically in Figure 92 c), which in turn can increase the polarization in PLZT thin films. Also the higher in-plane compressive strain in PLZT thin films, as observed from XRD analysis, causes an out-of-plane tetragonal distortion of the PLZT unit cell, and consequently displaces the Zr^{4+} or Ti^{4+} ions further from the body-center of PZT unit cell and enhances its polarization (Figure 92c). From Table 5-4, a strong correlation between the compressive strains (ϵ_n) and P_r values can be observed in the PLZT thin films, with the higher strain giving rise to higher polarization. Thus, contributions from both the defect-dipoles and the increased tetragonality cause the enhanced polarization in PLZT thin films.

In conclusion, epitaxial undoped PZT/LSMO and PLZT/LSMO thin films were grown on STO (100) substrates using PLD. Structural characterization using AFM, XRD, and cross-sectional TEM showed smooth surface morphologies, single crystalline nature, and atomically-sharp and defect-free interfaces, respectively. Polarization measurements showed enhanced P_r in PLZT thin films as compared to undoped PZT thin films. A strong association among the doping concentrations, residual strains, and the polarization was observed. The donor-induced defect-dipole contribution coupled with a strain-compression relaxation mechanism was proposed to explain the enhanced FE properties in the PLZT thin films

5.4. Fabricate and characterize ZnO:V, ZnO:Mn and ZnO:V/ZnO:Mn heterostructures. Investigate the multiferroic coupling in these structures:

This task involved the growth of ZnO:Mn and ZnO:V thin films and a study of their FM and FE properties. Finally, the individual layers were combined to fabricate ZnO:V/ZnO:Mn heterostructures for the investigation of multiferroic coupling.

Room temperature ferromagnetism in epitaxial Mn-doped ZnO thin films: In recent times, it has been reported that the magnetic properties of ZnO could be altered by transition metal doping such as Mn producing room temperature (RT) dilute magnetic semiconductors (DMS) [165]. Among the transition metals that have been used so far Mn has attracted more attention due to the introduction of a strong magnetic moment and the high thermal solubility in ZnO [166]. However the origins of RT FM in Mn doped ZnO still remains unresolved due to the varied experimental results obtained over the years. In this work, ZMO films were grown at different conditions on c-cut sapphire (Al_2O_3) substrates by varying the substrate temperatures (T_s) from a $\text{Zn}_{0.98}\text{Mn}_{0.02}\text{O}$ ceramic target using PLD. Figure 93 shows the θ -2 θ XRD scans of films deposited on c-cut sapphire (Al_2O_3) substrates at a T_s of RT, 200 °C, 400 °C and 600 °C, labeled as ZMO(RT), ZMO(200), ZMO(400) and ZMO(600) respectively. The films were highly textured with no observed peaks (within the resolution limits of XRD) from secondary phase formation of oxides of Mn or ZnMnO alloys which could lead to anti-ferromagnetic cluster formation. Table 5-5 lists the resistivity (ρ), carrier concentration (n_c) and Hall mobility (μ_H) measured at room temperature for

ZMO films deposited at various T_s but constant pO_2 of 10 mT. All the measured films showed n -type conduction. As the growth temperatures were increased the films became more conducting. Generally in doped samples there is an overall increase of ρ because the charged dopants (Mn^{2+}) act as scattering sites for electrons. This explains the orders of magnitude increase in ρ for ZMO(RT), ZMO(200), ZMO(400) and ZMO(600) as compared to undoped ZnO thin film ($\rho \sim 10^{-2} \Omega\text{cm}$).

Sample	Growth temperatures	$\rho(\Omega\text{cm})$	$nc(\text{cm}^{-3})$	$\mu_H(\text{cm}^2/\text{Vs})$
ZMO(RT)	RT	1.36×10^4	7.78×10^{12}	58.81
ZMO(200)	200 °C	9.69	2.89×10^{17}	2.23
ZMO(400)	400 °C	8.33	3.88×10^{17}	1.93
ZMO(600)	600 °C	0.46	2.51×10^{18}	5.45
Undoped ZnO	600 °C	0.02	1.04×10^{18}	330.19

Table 5-5. Resistivity (ρ), carrier concentration (nc) and Hall mobility (μ_H) measured at room temperature of ZnO:Mn thin films on c -cut sapphire substrates.

Further, from Table 5-5 we see that ZMO(RT) is highly insulating with very low density of free carriers. This could also be associated with the poor crystalline nature of the film which made the system strongly disordered.

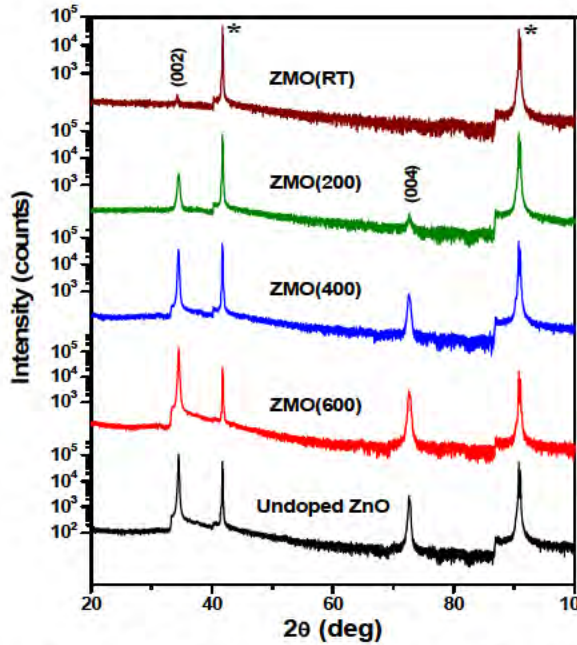


Figure 93: XRD patterns of $(\text{Zn}_{0.98}\text{Mn}_{0.02})\text{O}$ films on sapphire substrates grown at room temperature, 200 °C, 400 °C and 600 °C with a background oxygen pressure of 10 mT named as ZMO(RT), ZMO(200), ZMO(400) and ZMO(600) respectively. The sapphire substrate peaks have been denoted by *.

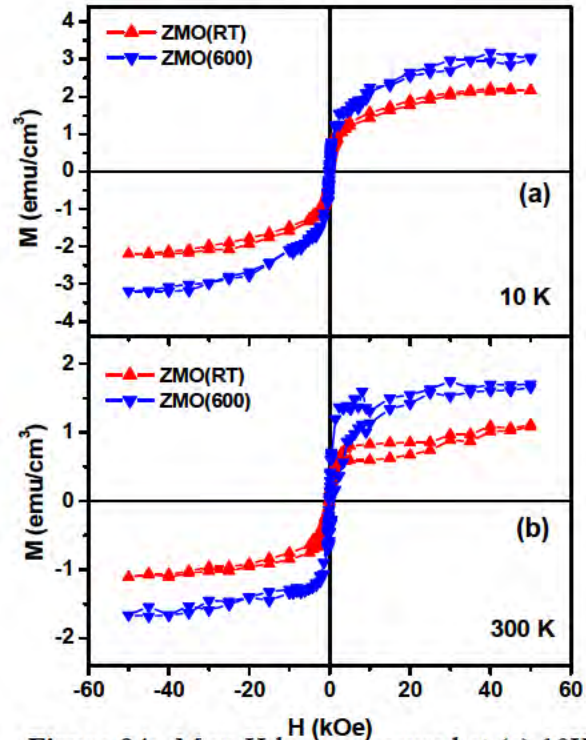


Figure 94: M vs H loops measured at (a) 10K and (b) 300K for $(\text{Zn}_{0.98}\text{Mn}_{0.02})\text{O}$ films deposited on c -cut sapphire substrates at RT and 600 °C with a constant pO_2 of 10mT named as ZMO(RT) and ZMO(600) respectively.

Figure 94 shows the in-plane M-H loops measured at (a) 10K and (b) 300K for $(\text{Zn}_{0.98}\text{Mn}_{0.02})\text{O}$ films deposited on c-cut sapphire substrates. An increase in the 300 K, M_s from 1.08 ± 0.02 to 1.67 ± 0.02 emu/cm³ and H_c from ~ 120 Oe to ~ 250 Oe were observed as the T_s was increased from RT to 600 °C. At 10K, H_c increased from ~ 110 Oe to ~ 180 Oe and M_s increased from 2.17 ± 0.03 to 3.1 ± 0.1 emu/cm³ from the film ZMO(RT) to ZMO(600). The H_c and M_s for films ZMO(200) and ZMO(400) also followed the same trend.

The most probable mechanism for the observed magnetism at low temperatures (10 K) in the highly insulating sample ZMO(RT) is due to the percolation of bound magnetic polaron (BMPs). In contrast, for films deposited at 200 °C, 400 °C and 600 °C, which are more conducting, it is the indirect RKKY mechanism which dominates the magnetic behavior [167].

RKKY exchange interaction in ZMO thin films: Figure 95 (a) shows the variation of RKKY exchange integral, $J_{\text{RKKY}}(r)$ as a function of the separation of the Mn spins (r). From the plot we can see that $J_{\text{RKKY}} > 0$ in the ranges $r < 0.11$ nm and $0.36 \text{ nm} < r < 0.59 \text{ nm}$ and $0.84 \text{ nm} < r < 1.07 \text{ nm}$. Now for 2 atomic % doping of Mn in ZnO the average separation between Mn^{2+} spins was found to be $r \sim 1.05 \text{ nm}$, which is based on the relation $r = (1/n_i)^{1/3}$ where $n_i = 8.438 \times 10^{20} \text{ cm}^{-3}$ (i.e. density of Mn^{2+} spins). Thus r falls within the range of FM RKKY interaction. This implies that at such dilute doping levels RKKY interaction would give FM.

Figure 95 (b) shows the linear fits of M vs $1/H$ data for $20 \text{ kOe} < H < 50 \text{ kOe}$. From the slopes and intercepts of the linear fits of M vs $1/H$ data points at saturation measured at 10 K, for ZMO(RT), ZMO(200), ZMO(400) and ZMO(600), n_i and V_o were calculated. The calculated values have been summarized in Table 5-6. From Figure 95 (b) and the values in Table 5-6 it was observed that the intercepts and slopes increased slightly from ZMO(200) to ZMO(600).

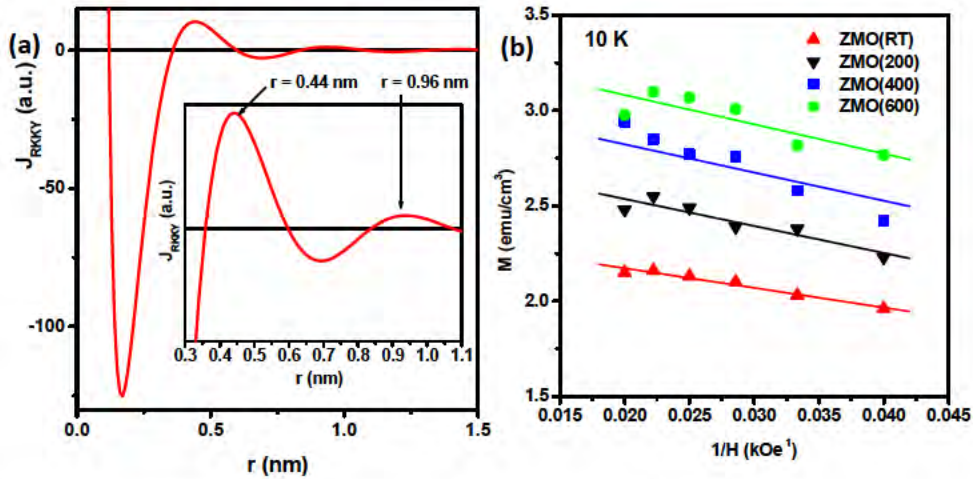


Figure 95: (a) Plot of RKKY exchange integral $J_{\text{RKKY}}(r)$ as a function of the average separation between magnetic spins (r). The inset shows the range of r when $J_{\text{RKKY}} > 0$. (b) M vs $1/H$ (kOe⁻¹) at 10 K for $(\text{Zn}_{0.98}\text{Mn}_{0.02})\text{O}$ films deposited at various growth temperatures with constant $p\text{O}_2$. (b) The solid lines are the linear fits of M vs $1/H$ data points for films named ZMO(RT), ZMO(200), ZMO(400) and ZMO(600).

This showed that the number of magnetic impurities interacting via RKKY mechanism increased with higher T_s and better crystallinity. However, the slope of the linear fit for ZMO(RT) was different

from the others showing a smaller value for n_i . The calculated value of n_i for ZMO(600) was $n_i \sim 7.31 \times 10^{19} \text{ cm}^{-3}$. It was much lower than the magnetic impurity density for 2 atomic % doping of Mn in ZnO which was $8.438 \times 10^{20} \text{ cm}^{-3}$. In other words only $\sim 8\%$ of the total number of Mn^{2+} ions in the system were involved in RKKY-mediated FM. From Figure 96 (a) for ZMO (600) the M_s was $\sim 3.1 \text{ emu/cm}^3$ which corresponded to an average magnetic moment of $0.4 \mu_B/\text{Mn}^{2+}$ assuming a uniform Mn ion distribution. This was again 8% of the theoretical value which was $5 \mu_B/\text{Mn}^{2+}$ when all the Mn spins are aligned [168, 169]. Thus, only about 8% of the incorporated Mn atoms at substitutional Zn sites contributed to FM via RKKY mechanism. The remaining Mn atoms may have formed interstitial defect sites or accumulated at the grain boundaries.

Sample	Intercept	Slope	n_i (10^{19} cm^{-3})	V_o (10^{-37} ergcm^3)	$n_i V_o$ (meV)
ZMO(RT)	2.3741	10314	5.12	6.75	0.0216
ZMO(200)	2.8173	14166	6.08	6.58	0.0250
ZMO(400)	3.1209	14782	6.73	5.59	0.0235
ZMO(600)	3.3896	15399	7.31	4.94	0.0226

Table 5-6. Summary of RKKY parameters calculated using the linear fits in Figure 93.

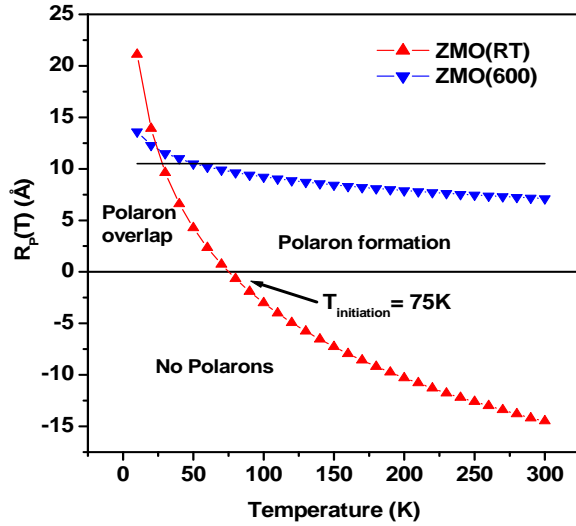


Figure 96: Variation of the radius of polarons R_p in angstroms at different temperatures for ZMO(RT) and ZMO(600), ($\text{Zn}_{0.98}\text{Mn}_{0.02}\text{O}$) films deposited at RT and 600°C respectively.

Percolation of Bound Magnetic Polarons (BMPs) in ZMO thin films: In order to explain the FM in ZMO(RT) by the BMP model, the electron confinement radius (a_B) was calculated using $a_B = \epsilon(m_0/m_e^*)a$ where ϵ is the static dielectric constant, $m_e^* = 0.28m_0$ is the electron effective mass and $a = 0.52\text{\AA}$ is the Bohr radius [131]. The electron confinement radii for ZMO(RT) and ZMO(600) were $\sim 20 \text{\AA}$ and $\sim 4 \text{\AA}$ respectively. The radius value for ZMO(RT) was larger owing to the shallower defect level ($\Delta E \sim 6.4 \text{ meV}$) [131]. The BMP model is valid only in the low carrier density regime where $n_c a_B^3 \ll 1$ and when $n_i \gg n_c$. This was true for both ZMO(RT) and ZMO(600). Following Calderon and Sarma's [167] work the temperature dependence of the radius of the polaron (R_p) was plotted using the following equation

$$R_p(T) \equiv (a_B/2) \ln (sS|J| (a_0/a_B)^3/k_B T) \dots\dots\dots (5-1)$$

where $s = 1/2$ is the spin of carriers (electrons), $S = 5/2$ is the spin of magnetic dopant (Mn^{2+}), using $J \approx 1$ eV as the local exchange coupling between carrier spin and the magnetic Mn moments [118, 125] and $a_0^3 = 47.77 \text{ \AA}^3$ is the unit cell volume for ZnO.

Figure 96 shows the curves for ZMO(RT) and ZMO(600). For ZMO(RT), polarons only start forming at a temperature of $T_{\text{initiation}} \sim sS|J| (a_0/a_B)^3/k_B \sim 75 \text{ K}$ above which there are no polarons in the system. However in ZMO(600) polarons are always present even at room temperature. The size of the BMPs in ZMO(RT) increases drastically from $\sim 0.7 \text{ \AA}$ at 70K to $\sim 20 \text{ \AA}$ at 10K whereas for ZMO(600) the increase in size is gradual from $\sim 7 \text{ \AA}$ at 300K to $\sim 13 \text{ \AA}$ at 10K. The magnetic dopant spins at a distance $r < R_p$ tend to align with the localized carrier spin. The average separation between randomly oriented magnetic dopant spins was found to be $\sim 10 \text{ \AA}$, which is based on the relation $r = (1/n_i)^{1/3}$ where $n_i = 8.438 \times 10^{20} \text{ cm}^{-3}$ for 2 at.% doping of Mn in ZnO. With lowering of temperature, polarons start overlapping with neighboring BMPs forming FM clusters which keep growing in size to form an infinite cluster (of the size of the system) i.e. when the BMP percolation occurred. The percolation radius (r_{perc}) for ZMO(RT) at 10K is $\sim 5 \text{ \mu m}$ calculated from $r_{\text{perc}} \approx 0.86/n_c^{1/3}$ [168] where n_c (10K) was estimated using $n_c(T) = n_{c0} \exp(\Delta E/k_B T)$ from $n_c(\text{RT})$ and ΔE values measured earlier. The r_{perc} in ZMO(RT) was larger than the thickness of the film and implied long range FM at 10K. The r_{perc} for ZMO(600) at 10K was 0.03 \mu m which was much smaller than the film thickness to mediate large FM via BMP percolation throughout the sample. From Figure 96 it was observed that for ZMO(600), $R_p \approx r$, in the range 10K - 300K. This implies that the BMPs are always overlapping with their spins aligned with the carriers. If there are substantial thermally activated carriers, the BMP scenario extrapolates to RKKY FM.

In conclusion, the observed FM in $Zn_{0.98}Mn_{0.02}O$ films shows characteristics of both intrinsic and carrier mediated mechanisms. The experimental results show a strong correlation between effective carrier densities due to different growth conditions and the FM in the samples.

Enhancement of ferroelectricity in V-doped ZnO thin films: V doping in ZnO is reported to create switchable spontaneous polarization [161]. Doping divalent cation Zn sites by V ions creates a mixed

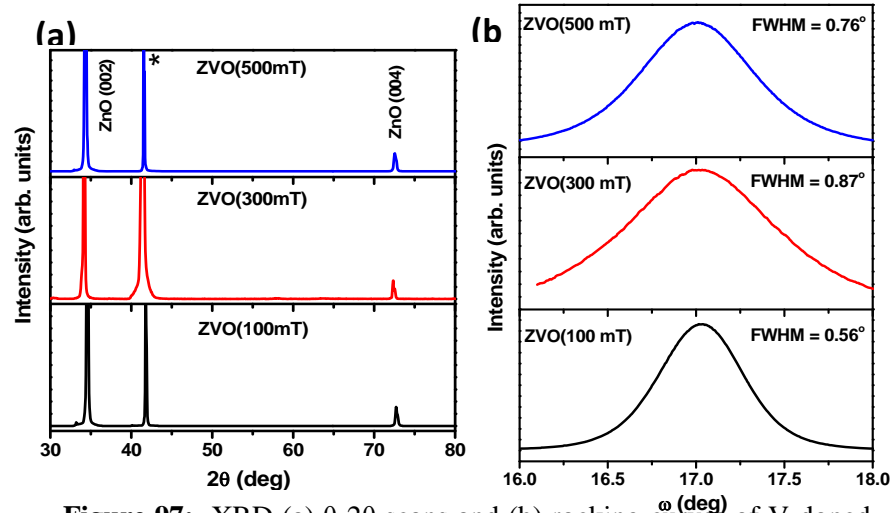


Figure 97: XRD (a) θ - 2θ scans and (b) rocking curves of V-doped ZnO thin films grown at 600°C but varying the background O_2 pressure from 100 mT, 300 mT, and 500 mT, named as ZVO(100mT), ZVO(300mT), and ZVO(500mT) respectively. The substrate peak is denoted by *.

valency as well as strain in the original ZnO hexagonal structure because of the reduced ionic size of vanadium. It is reported that the V ions which replace the Zn sites are in 5^+ valency state [162]. The mixed valency creates charge polarity between Zn-O and V-O bonds. This charge polarity and the rotation of the nonlinear V-O bonds with respect to Z-O bonds under electric field gives rise to the enhanced ferroelectricity [162]. Here, we report on the evidence of

enhancement in ferroelectricity in thin films of vanadium (V) doped ZnO grown at higher oxygen pressures. This process reduces the intrinsic oxygen deficiencies and the material becomes very insulating, which in turn lowers the leakage current through the ferroelectric capacitor. 2 at. % V-doped ZnO films with thicknesses of approximately 1 μm were grown epitaxially on c-cut sapphire (Al_2O_3) (0001) at a growth temperature of 600°C.

Figure 97 shows the XRD θ -2 θ scans of ZVO films, named as ZVO(100mT), ZVO(300mT), and ZVO(500mT), respectively. The films were highly textured with only (002) orientation. There were no observed peaks (within the resolution limits of XRD) from secondary phase formation of oxides of V or other impurities. The in-plane epitaxial relationship was verified by rocking scans about the (002) plane of ZnO as shown in Figure 97. The narrow FWHM ($< 1^\circ$) confirms the high degree of texturing in all the samples. However, the slightly larger FWHMs for ZVO(300mT) and ZVO(500mT) as compared to ZVO(100mT) imply a less preferential orientation.

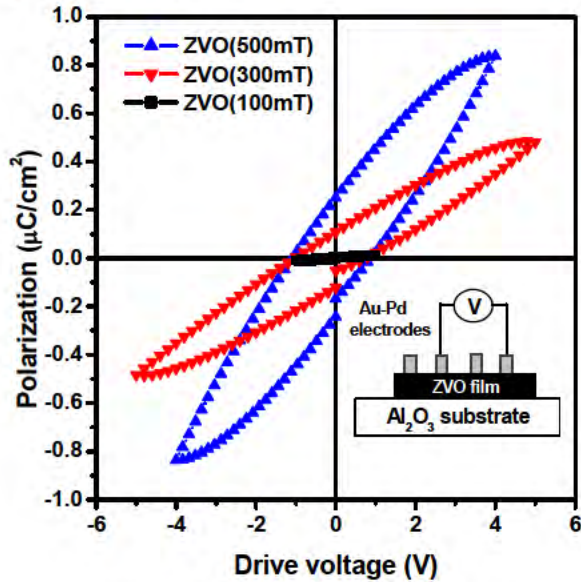


Figure 99: Polarization vs driving voltage curves for V-doped ZnO thin films grown under different $p\text{O}_2$, named as ZVO(100mT), ZVO(300mT), and ZVO(500mT), respectively. Inset shows a schematic diagram of ZVO capacitor.

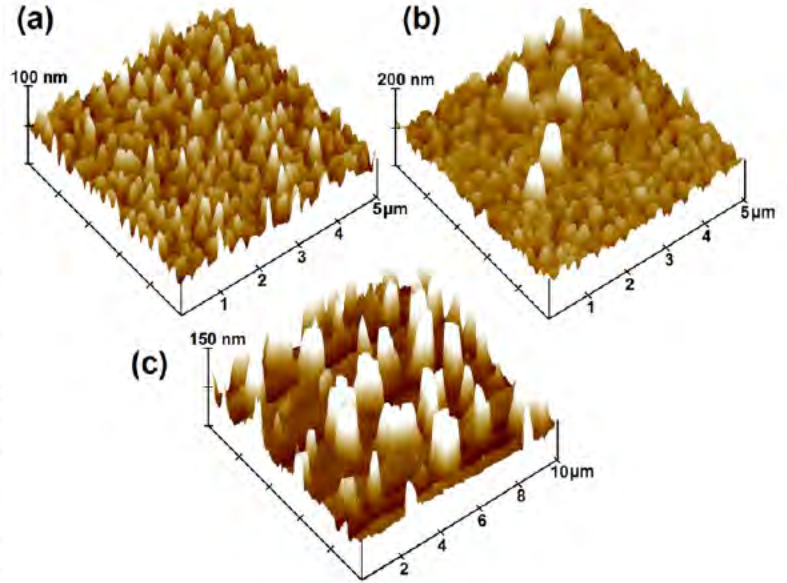


Figure 98: AFM images V-doped ZnO thin films grown at 600°C but varying the background O_2 pressure from (a) 100 mT, (b) 300 mT, and (c) 500 mT, named as ZVO(100mT), ZVO(300mT), and ZVO(500mT) respectively.

Figure 98 (a), (b), and (c) show AFM images of ZVO films, ZVO(100 mT), ZVO(300 mT), and ZVO(500 mT), respectively. The particulate density on the film surface increased as the $p\text{O}_2$ was increased. ZVO(500 mT) (Figure 98 c) shows large number of micron size droplets that were ejected from the target during ablation. To make sure that the particles are not any foreign object, EDS was performed on top of the droplets. The EDS spectra showed the presence of only Zn and O confirming that they came from the target.

Roughness analysis showed that the root mean square roughnesses (R_{rms}) for ZVO(100mT), ZVO(300mT), and ZVO(500mT) were 17.5 nm, 33.5 nm and 55.8 nm,

respectively. The R_{rms} increased by three times as the pO_2 increased from 100 mT to 500 mT.

The ferroelectric properties of the ZVO films on insulating sapphire substrates were tested using a planar electrode configuration. Gold palladium (Au-Pd) electrodes were sputter coated on top of the film using a shadow mask with 500 μm holes. Figure 99 shows polarization (P) loops for ZVO(100mT), ZVO(300mT), and ZVO(500mT) capacitors measured at 1 kHz. Table 5-7 summarizes the P values for the ZVO films. The remnant polarization (P_r) observed in ZVO(500mT) was 0.25 $\mu C/cm^2$ which was close to the value reported by Yang et. al. [159, 160]. The reported value was 0.2 $\mu C/cm^2$ for ZVO films deposited on Si (111) substrates. This trend of increasing P values with higher pO_2 could be associated with the reduction in donor type defects like oxygen vacancies created during deposition. Less number of defects within the film inhibited the percolation paths and consequently reduced the leakage current across the capacitor. This allowed the measurement of P by applying higher driving voltages without causing a dielectric break down in the capacitor.

Table 5-7. Summary of polarization data for ZnO:V thin films on c-cut sapphire substrates grown at 600°C but varying the background O_2 pressure.

Sample	Maximum Polarization P_{max} ($\mu C/cm^2$)	Remnant Polarization P_r ($\mu C/cm^2$)	Coercive Field E_c (kV/cm)
ZVO(100mT)	0.01	0.0045	2.05
ZVO(300mT)	0.48	0.1	4.4
ZVO(500mT)	0.83	0.24	4.9

In conclusion, ferroelectric switching was obtained in V-doped ZnO thin films. Higher saturation polarization was obtained for the ZVO film grown at higher oxygen pressure because of the more insulating nature of the film.

Magneto-electric coupling in ZnO:Mn-ZnO:V Heterostructure: This section describes the growth and characterization of ZnO:Mn-ZnO:V heterostructures as a potential multiferroic device. The evidence of magneto-elastic coupling in these ZnO:Mn-ZnO:V bilayer films is discussed. The electric field control of magnetization in ZnO:Mn-ZnO:V heterostructures could lead to a possibility of ME effect which is sought after in multiferroic devices.

Figure 100 (a) shows a schematic diagram of the ZnO:Mn/ZnO:V heterostructure. The undoped ZnO layer was deposited at low pO_2 to make it conducting so that it could serve as a bottom electrode. Au electrodes were sputter-coated on top using a shadow mask with 0.5 mm diameter holes. Figure 100 (b) shows the XRD θ -2 θ scan of the ZnO:Mn-ZnO:V heterostructure. The high counts from the peak intensities confirmed the good crystalline quality. Although the major peaks were from the (002) planes of ZnO, some low intensity peaks from other orientations of ZnO were also observed. This was due to the large thickness (approx. 2.6 μm) of the structure where the epitaxial relationship among the individual layers could not be maintained throughout the structure. On the other hand, no impurity peaks from

secondary phase segregation were observed even in the logarithmic scale. To sum up, the heterostructure was highly textured and exhibited only single phase of ZnO. The degree of in-plane orientation in the heterostructure was measured by rocking curves performed about the (002) plane of ZnO. The rocking curves about the (002) plane of ZnO for the ZnO:Mn-ZnO:V heterostructure and the ZnO:Mn single layer film have been shown in Figure 100 (c). The narrow FWHM (1.158°) for the heterostructure confirms the

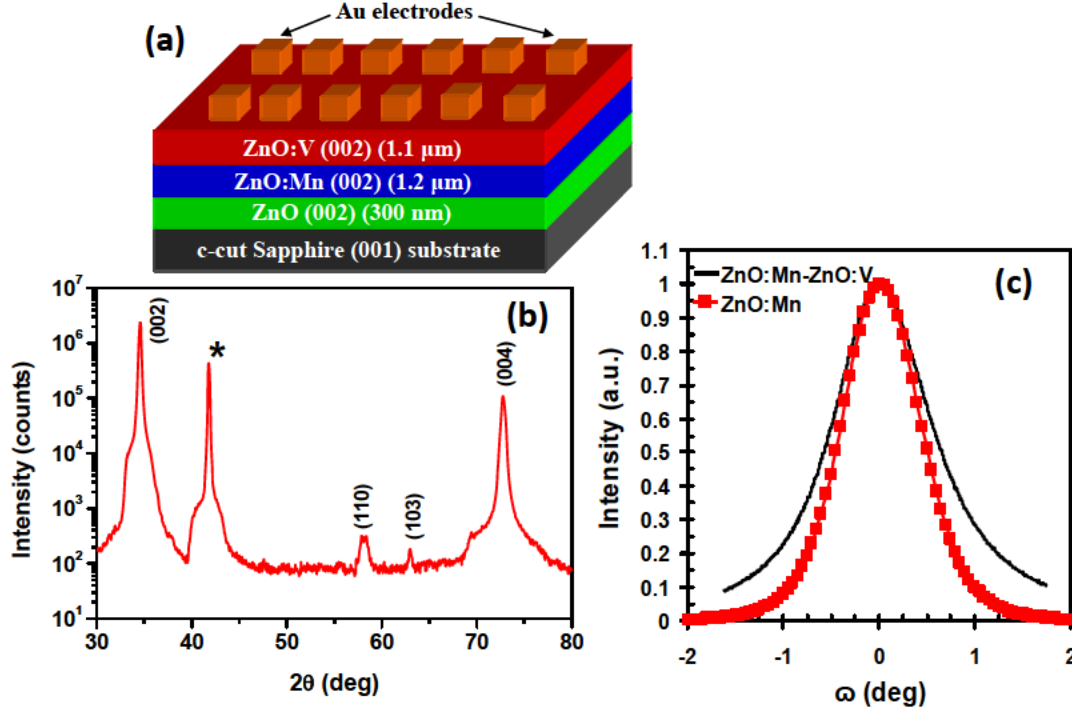


Figure 100: (a) Schematic diagram of ZnO:Mn-ZnO:V heterostructure. (b) XRD θ - 2θ scan of ZnO:Mn-ZnO:V heterostructure. The c-cut sapphire substrate peak is denoted by *. (c) Rocking curves about the (002) plane of ZnO for the ZnO:Mn-ZnO:V heterostructure and the ZnO:Mn single layer film.

high degree of in-plane texturing. The slight relaxation of the preferential orientation in the heterostructure as compared to single ZnO:Mn film (FWHM = 0.962°) is again due to the large thickness and different growth conditions of the individual layers.

In order to investigate the magnetic properties of the heterostructure and to correlate it to the FM in the individual layers, M vs H loops were measured not only for the heterostructure but also for the individual layers by depositing them separately under the same conditions. Figure 101 shows the M vs H loops measured at 10 K and 300 K for the ZnO:Mn-ZnO:V heterostructure, ZnO:Mn single layer, and ZnO:V single layer, respectively. The magnetic field was applied parallel to the film plane. Room temperature (RT) FM is observed in the heterostructure which is important for device application purpose. The ZnO:V layer exhibited RT FM which was of the same order as the undoped ZnO film. This small magnetism is associated with defects in the film and not due to V doping. It is observed that the M_s value for the ZnO:Mn-ZnO:V heterostructure is smaller than the ZnO:Mn single layer film. The ZnO:Mn film was grown under low pO_2 (10 mT) which made the film highly conducting with a high carrier concentration. This leads to higher M_s owing to the carrier-mediated mechanism. However, the high pO_2

(500 mT) deposition of the ZnO:V layer during the growth of the heterostructure allowed more O₂ incorporation into the ZnO:Mn layer effectively reducing its carrier concentration and effective M_s .

In order to test magneto-elastic coupling in ME composite materials, a change in magnetization as a function of applied electric field has to be demonstrated. Further, for multiferroic device application the measurements have to be performed at RT.

The electric field control of magnetization in the ZnO:Mn-ZnO:V heterostructure was investigated by poling the ferroelectric ZnO:V top layer by applying 4 V of d.c. bias voltage across the coplanar sputter-coated Pt electrodes as shown in Figure 101. Figure 101 (c) shows the M-H loops at 300K for the heterostructure before and after poling. A large drop in the M_s by an order of magnitude was observed. It could be an indication of possible interaction between the magnetic moments in ZnO:Mn layer and the electric polarization in ZnO:V layer. Therefore, the ZnO:Mn/ ZnO:V heterostructure showed possible magnetoelectric coupling at room temperature.

In conclusion, multiferroic composite layered ZnO:Mn-ZnO:V heterostructure was fabricated using PLD. The heterostructure retained the FM and FE properties of the parent layers. Possibility of magneto-elastic coupling through a cross interaction between the layers was observed. Further research in this direction is required to enhance the saturation values for practical device application. However, the results in this section provide substantial evidence towards the ME coupling in layered thin films. As opposed to the strain-mediated ME coupling in PZT/CFO heterostructures, the coupling in ZnO:Mn/ZnO:V structures could be charge mediated.

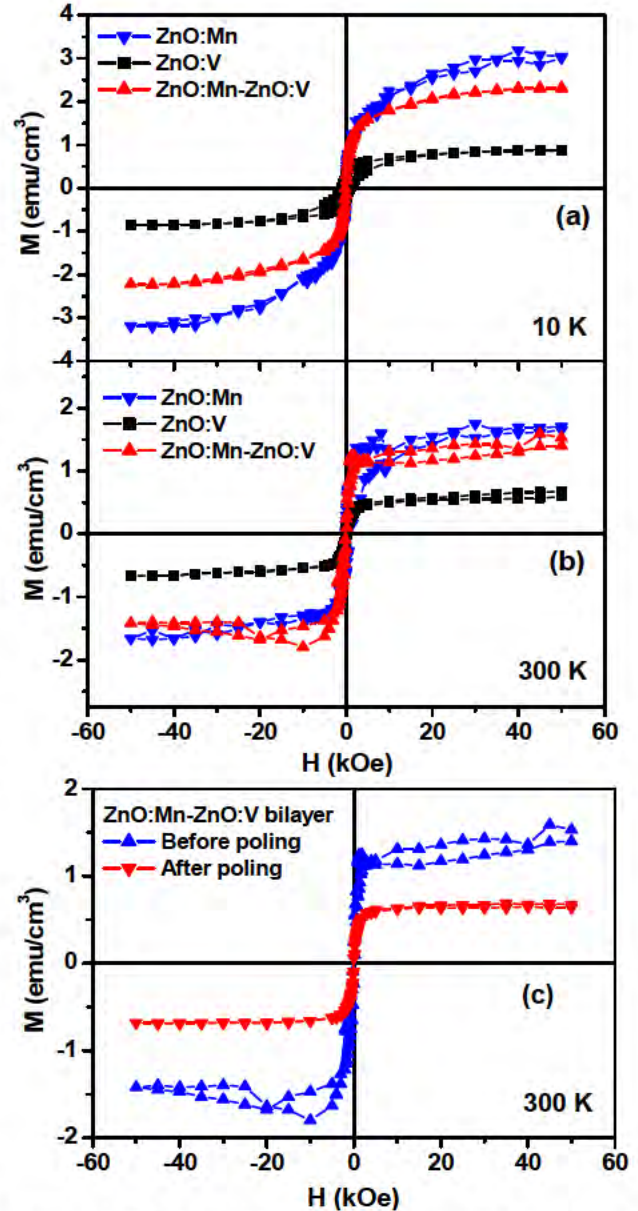


Figure 101: M vs H loops measured at (a) 10 K and (b) 300 K for the individual layers, ZnO:Mn and ZnO:V, and the ZnO:Mn-ZnO:V heterostructure, all grown on c-cut sapphire substrates. (c) Magnetization loops at 300K before and after poling the ZnO:Mn/ZnO:V epitaxial heterostructure.

5.5. Synthesis of ferroelectric-ferromagnetic nanopillar-nanoparticle structure and exploration of magnetoelectric coupling:

Since the magneto-electric coupling between the FE and FM phases is due to the interfacial strain, the increased surface area in nanopillar-nanoparticle structure is expected to enhance this effect. In the first phase of the work, our aim was to manipulate the growth conditions to fabricate structures that contain nano-pillars of CoFe_2O_4 surrounded by PZT. This was achieved by depositing CoFe_2O_4 (CFO) on the substrate at an oblique angle using PLD. In an oblique incident growth process the initial islands that grew preferentially in a specific crystal orientation show a high rate of growth in the vertical direction while suppressing growth in the other direction due to strong shadowing effect giving rise to columnar growth of CFO and other materials[164 - 168].

In the second phase of the work, we chose a combinatorial physical/chemical route to grow PZT nanowires on large area substrates. While chemical synthesis routes allowed for the growth of PZT nanostructures with precise control of size and orientation, physical deposition techniques such as pulsed laser deposition or sputtering allowed the growth of continuous thin films, resulting in PZT nanowire arrays.

Nanocolumnar growth of preferentially-oriented cobalt ferrite (CFO) thin films using oblique-angle PLD: CFO thin films were deposited on SiO_2/Si (100) substrates using oblique-angle pulsed laser deposition (α -PLD) with an oblique angle of 120° (as shown in Figure 102). A series of CFO thin films of varying thicknesses from 50 nm to 400 nm were deposited at a substrate temperature of 450°C in an

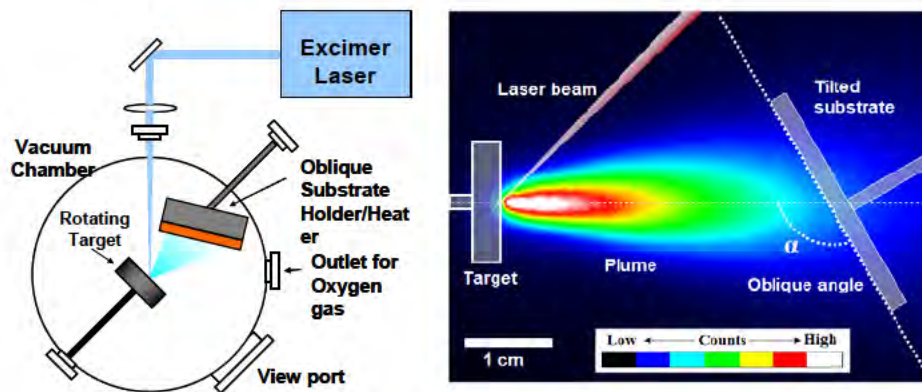


Figure 102: (a) Schematic diagram of the oblique-angle pulsed laser deposition system showing the position of the target, the laser beam and the 120° -tilted substrate. (b) Time-integrated ICCD image of the total visible emission from the laser-induced plume during the oblique-angle (α) PLD of CFO thin films with schematic diagrams of the CFO target, laser beam, tilted substrate drawn-to-scale.

ambient O_2 pressure of 10 mTorr using laser fluence of 2 J/cm^2 .

For comparison, CFO thin films were also deposited on Si substrates using normal-incidence PLD under the same conditions.

Figure 102 (a) shows the XRD θ - 2θ patterns for the α -PLD deposited CFO thin films for varying thicknesses.

The observed peaks were indexed to the face-centered cubic phase of CFO with a space

group of Fd-3m (227). The XRD pattern of the 400 nm thick film demonstrated a bulk-like polycrystalline nature while those for the 100 nm and 50 nm thick CFO films indicated that the films

were highly (111) textured. The XRD pattern for the 200 nm film showed preferred orientation in the (111) direction. [169 - 170]. The insets to Figures 102 (b and c) show the XRD rocking curves performed about the CFO (222) crystallographic plane for the α -PLD and 90°-PLD grown films, respectively. The rocking curves were performed using an in-plane grazing incidence configuration in order to maximize the signal from the in-plane direction of the films. The smaller full-width at half-maxima (FWHM) value of the rocking curve peak in the α -PLD deposited film (FWHM = 0.18°) as compared to that of the 90°-PLD film (FWHM = 0.41°) indicated the better in-plane orientation of the (111) plane (Figure 103) in the α -PLD grown film as compared to the 90°-PLD film.

The surface morphologies of the α -PLD grown CFO films at varying thicknesses of 50 nm, 100 nm, and 200 nm and that of the 200 nm thick 90°-PLD grown CFO film obtained from AFM scans are shown in Figure 104. The α -PLD deposited films exhibited smooth surfaces (Figs. 104 a-c) with R_{rms} values varying as low as 1-2 nm while the 90°-PLD grown CFO films exhibited much higher surface roughness values in the range of 10-12 nm. The α -PLD deposited films exhibited the preference of mounds to coalesce in certain regions along the direction of deposition giving non-uniform grain growth. The

Figure 104: AFM images of the surfaces of CFO thin films deposited using oblique-angle PLD at varying thicknesses of (a) 50 nm, (b) 100 nm, and (c) 200 nm, and normal-incidence PLD at thickness of (d) 200 nm, respectively.

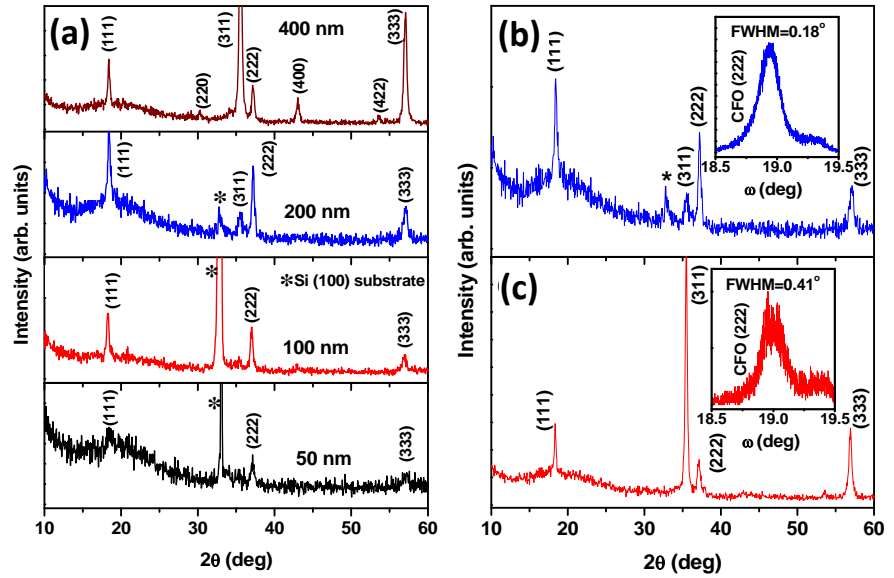
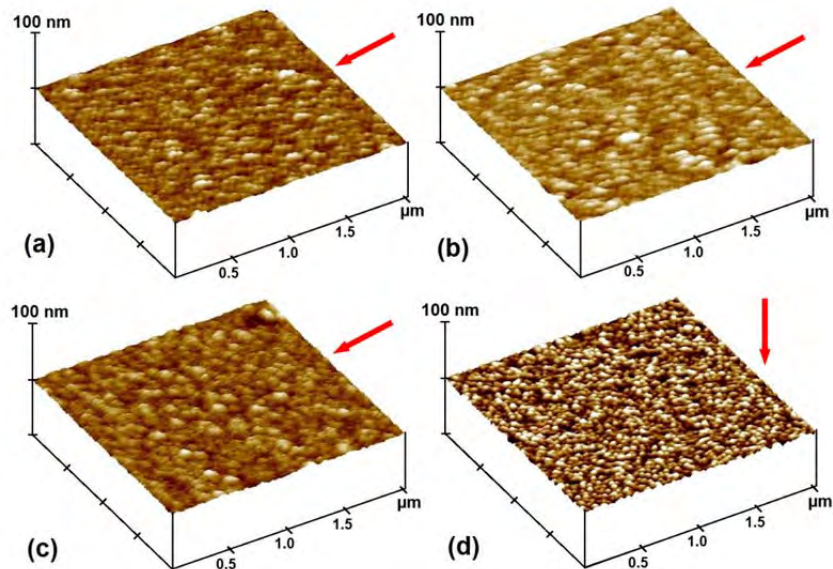


Figure 103: (a) XRD θ - 2θ patterns for oblique-angle deposited CFO thin films on Si substrates for varying thicknesses. (b and c) XRD θ - 2θ patterns for 200 nm thick CFO thin films deposited on Si substrates using oblique and normal-incidence PLD processes keeping all other parameter constant, respectively. The insets show the XRD rocking curves performed about the CFO (222) planes for the respective films. The Si substrate peaks have been marked as *.



distinctively different surface mor-phologies for α -PLD and 90°-PLD grown CFO films (Figure 104) suggested possible diff-erent growth mechanisms during the film deposition.

Figures 105 (a and b) show HRTEM images captured at different locations along the interface of the 200 nm thick α -PLD grown CFO film. From the figure it is clearly seen that the CFO layer made a distinctly sharp and flat interface with the SiO₂/Si substrate.

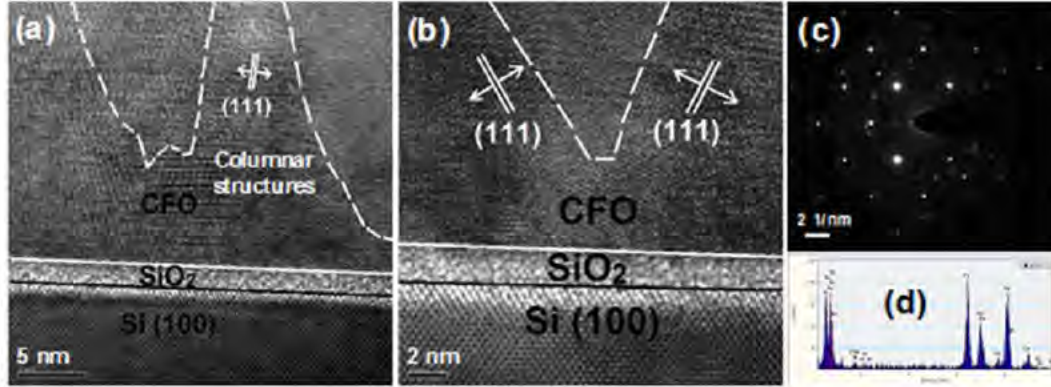


Figure 105: (a, b) Cross-sectional HRTEM images at different locations along the interface of 200 nm thick α -PLD deposited CFO thin film on Si (100) substrate with SiO₂ native amorphous layer. (c, d) Typical SAED pattern and EDS spectrum (from TEM analysis) obtained near the CFO/Si interface, respectively.

Distinct columnar structures (shown by dotted lines in Figure 105) with continuous sharp lattice fringe spacings identified with the preferred (111) orientation of CFO were observed in all the images. In the space between the columns, different order lattice fringes corresponding to the (311) or (400) orientations of CFO were observed. Figure 105 (c) shows the selected area electron diffraction pattern (SAED) obtained near the interface. Unlike the ring-patterns of a bulk polycrystalline sample, the SAED pattern in Figure 105 (c) shows dotted pattern indicating preferred growth and corroborating the preferred crystal (111) orientation that was observed in the XRD analysis earlier. EDS spectrum (as shown in Figure 105 d) captured near the film substrate interface confirmed the stoichiometric CFO composition.

Figure 106 shows the M-H hysteresis curves for the α -PLD grown CFO thin films at

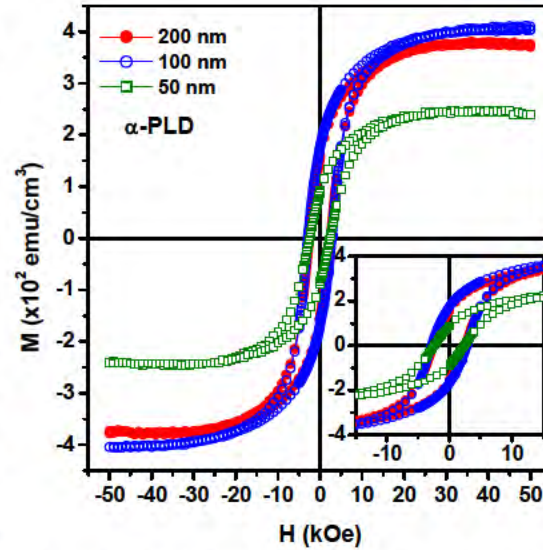


Figure 106: Magnetization vs. magnetic field (M-H) hysteresis curves for CFO thin films grown using oblique-angle PLD under the same conditions with varying thicknesses of 50 nm, 100 nm, and 200 nm. The inset shows the enlarged portion of the M-H curves at low field ranges.

varying thicknesses of 50 nm, 100 nm, and 200 nm. From the figure it can be seen that the 100 nm and 200 nm thick α -PLD grown CFO films have comparable saturation magnetization (M_{sat}) and coercive fields (H_c) while the 50 nm thick film exhibited lower M_{sat} and H_c .

In order to clearly demonstrate the enhanced magnetic properties of α -PLD grown CFO thin films, the M-H curves for both α -PLD and 90°-PLD deposited CFO films at thicknesses of 100 nm and 200 nm have been shown in Figure 107 (a) and (b), respectively. The nano-columns formed at the

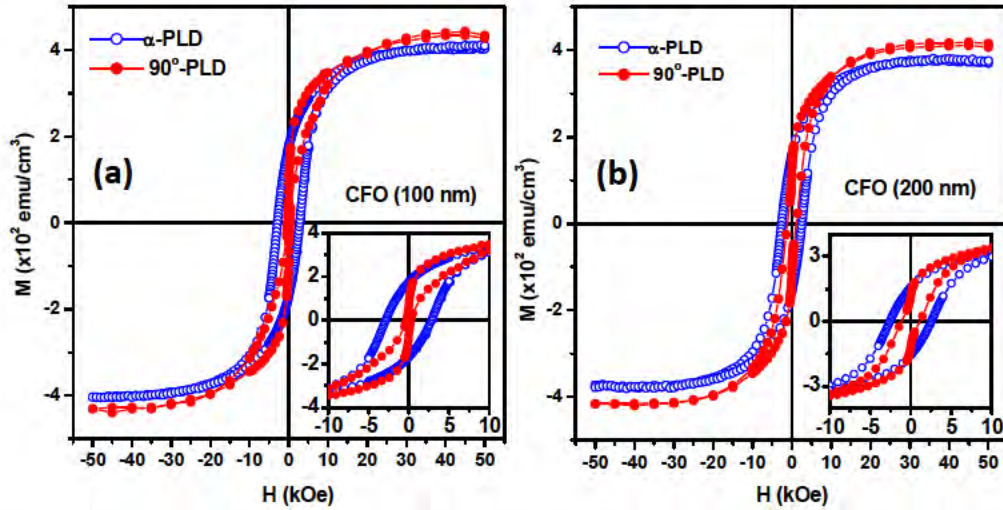


Figure 107: Magnetization vs. magnetic field (M-H) hysteresis curves for CFO thin films deposited using both oblique- and normal-incidence PLD process labeled as α -PLD and 90°-PLD at thicknesses of 100 nm and 200 nm, respectively. The insets show the enlarged portion of the M-H curves at low field ranges.

interfaces showing (111) crystal orientation (Figure 106) as a result of oblique-incidence in the α -PLD process that resulted in enhanced preferred growth along the CFO (111) direction (i.e. along the magnetic hard axis for single-crystal CFO), possibly resulted in increased magneto-crystalline anisotropy and consequently higher M_r values in the α -PLD grown CFO thin films as compared to the polycrystalline 90°-PLD grown CFO thin films. Strain-induced higher coercivity where domain wall motion is restricted as a result of strain has been reported in CFO thin films [171]. From XRD strain analysis, it was observed that the α -PLD grown CFO thin films exhibited higher compressive strains, as compared to the slightly tensile strains in the 90°-PLD grown CFO films, which most probably resulted in the higher H_c values.

In conclusion, CFO thin films were deposited under the same conditions using oblique and normal-incidence PLD processes. On one hand, XRD analyses revealed an enhanced preferred orientation along the CFO (111) plane, on the other AFM images revealed extremely smooth film surfaces with roughness values as low as 1-2 nm in the oblique-incident films. HRTEM images of the obliquely incident CFO films showed nano-columnar growth along the interfaces in the preferred CFO (111) direction. Magnetization measurements showed comparable saturation magnetizations in both oblique and normal-incident CFO films. However, a huge systematic enhancement in the coercive fields

was obtained in the obliquely incident CFO films as compared to those deposited using normal-incidence PLD.

Growth of PZT nanowires by combined physical and wet-chemical synthesis approaches: Two approaches were employed to grow PZT nanostructures.

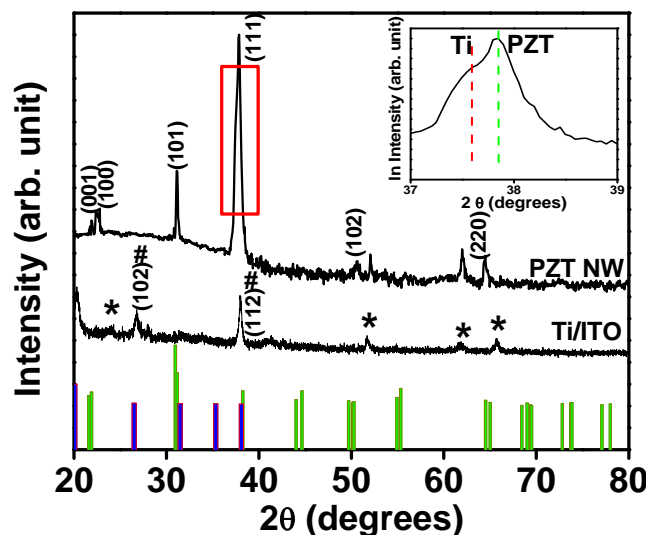


Figure 108: XRD spectra of the Ti/ITO/glass and PZT NWs on the same. ITO substrate peaks (*) and the Ti peaks (#) are shown in the Ti/ITO/glass spectrum. The (111) peak in the PZT NW XRD spectrum is deconvoluted to show Ti bottom layer peak and PZT peak in log scale. Standard database of PZT (green bar) and Ti (red bar) are also shown for comparison.

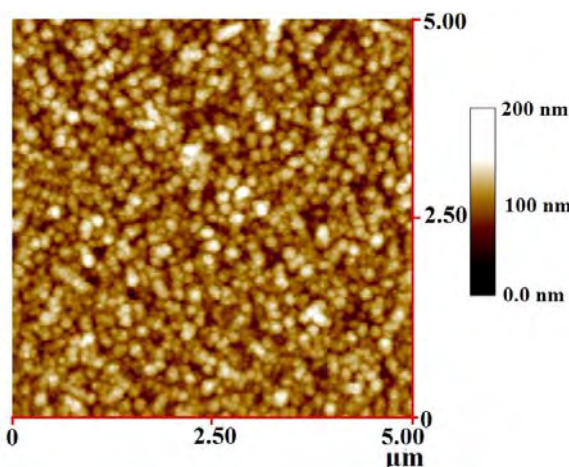


Figure 109: AFM image showing the surface morphology of the Ti coated ITO/glass used as the seed layer in the hydrothermal growth of PZT NWs.

- **Approach 1:** Promoting one dimensional (1-D) growth of PZT nanowire arrays on top of Ti sputtered ITO/glass substrates where the Ti layer acted as source for PZT nanostructure growth using chemical synthesis.

- **Approach 2:** Promoting (1-D) growth of PZT nanorods on top of nanoparticulate PZT ultrathin films deposited by pulsed laser deposition (PLD) which acted as seed layer for further 1-D growth using chemical synthesis.

Figure 108 shows the XRD spectra of the Ti-coated ITO and that of the PZT NWs deposited on Ti coating. Standard XRD patterns for Ti and tetragonal PZT are given for comparison of our samples. Both Ti-coated ITO glass and the PZT NWs samples show polycrystalline patterns without any preferential orientation. Absence of most Ti and ITO XRD peaks in the PZT NW sample is suggestive of densely covered growth of the NWs in the sample. Since 2θ value of peak (111) in tetragonal PZT closely matches that of the (112) plane in hexagonal Ti of our sample we deconvoluted the (111) XRD peak of PZT NW pattern. Two peaks, one for the Ti and the other for the PZT were observed after de-convolution (shown in the log scale in the inset of Figure 108). Ratio of the normalized intensities of the Ti/PZT peaks is calculated to be ~ 0.005 which gives an idea of the good coverage of the NWs in the sample.

Surface morphology of the Ti coating after sputtering was studied by AFM (Figure 109). The as-deposited Ti film exhibits a uniform and flat surface with a root-mean-square value of surface

roughness (R_{rms}) of 10 ± 2 nm. The average grain size measured is around 100 ± 12 nm. The as-deposited film has a thickness of 800 ± 10 nm as measured by a profilometer. SEM image of the deposited and cleaned PZT NW film on Ti/ITO is shown in Figure 110 (a). The image shows dense and uniform growth of PZT NW with a large aspect ratio (> 60), without any exposed bottom Ti layer or ITO substrate. Inset shows titled image of an array of the PZT NWs, which suggests that the NWs have grown upright to the substrate with random orientation. A part of the PZT NW film was forcefully cracked and the bottom Ti layer was observed (Figure 110 b). The PZT NWs are found to have grown from the bottom Ti layer that acted as the seed layer for the growth of the NWs.

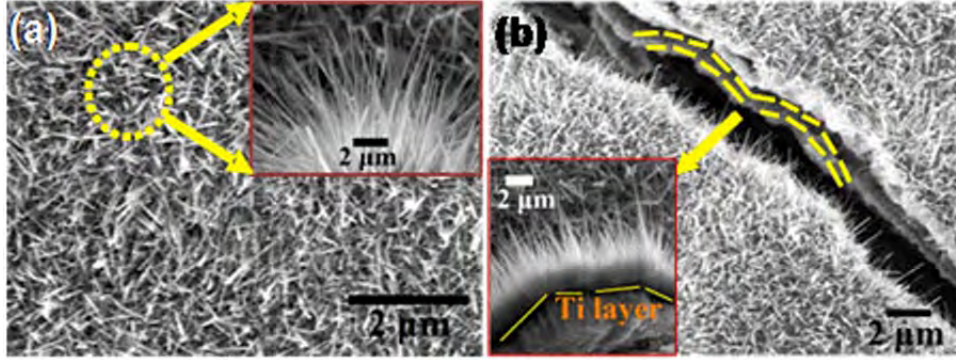


Figure 110: (a) SEM image of the PZT NW arrays showing uniform and continuous coverage over large surface area. Inset to Figure 35 (a) shows SEM image of titled PZT NWs indicating that the NWs have grown upright to the substrate with random orientation. (b) SEM image showing a region of the PZT NW arrays that was forcefully cracked to expose the bottom Ti seed layer that promoted the upright growth of the PZT NWs. Inset to the Figure 35 (b) shows the upright growth of PZT NWs from Ti seed layer from the cracked zone.

Figure 111 shows the TEM images of the PZT NWs. The NWs have sharp boundaries and uniform length with average diameter of 80 ± 5 nm. As shown in the inset of Figure 111a, Figure 111b and insets of Figure 111b majority of the NWs have rounded or tapered tip with an average tip diameter of 5 ± 2 nm. The base of the NWs are more tetragonal in shape demonstrating the inherent crystal structure of PZT. HRTEM image of a single NW near its tip is shown in Figure 111c. As indicated, the continuous and sharp lattice fringe spacing in the NW matches the (001) plane of tetragonal PZT. The particulate features at the tip are due to the surface disintegration of the NW upon long exposure to the high energy electron beam under TEM. Selected Area Electron Diffraction pattern collected from an individual PZT NW shows single crystal pattern with marked crystal planes in the tetragonal lattice structure (Figure 111d). SAED pattern also indicates that the NWs are of high crystalline nature without presence of detectable structural defects. EDS spectrum collected from different zones of a single PZT NW (Figure 111e) reveals stoichiometric composition within an error limit of 0.001 at. %.

In conclusion, FE PZT NW upright arrays were grown over a large surface area on ITO/glass substrate directed by Ti seed layer at the bottom. The Ti seed layer was first deposited through a controlled RF sputtering process which was then used as a substrate for the growth of large-scale PZT NW arrays through an optimized hydrothermal process. Position of the Ti/ITO/glass substrate and the presence of Ti coating were found to affect the uniform growth and coverage of single crystalline NWs. The results reported in this work offer a platform for introducing newer techniques for the growth of 1D

PZT nanostructures and expand the investigation of the fundamental structure-property relationships of these FE nanostructured thin films.

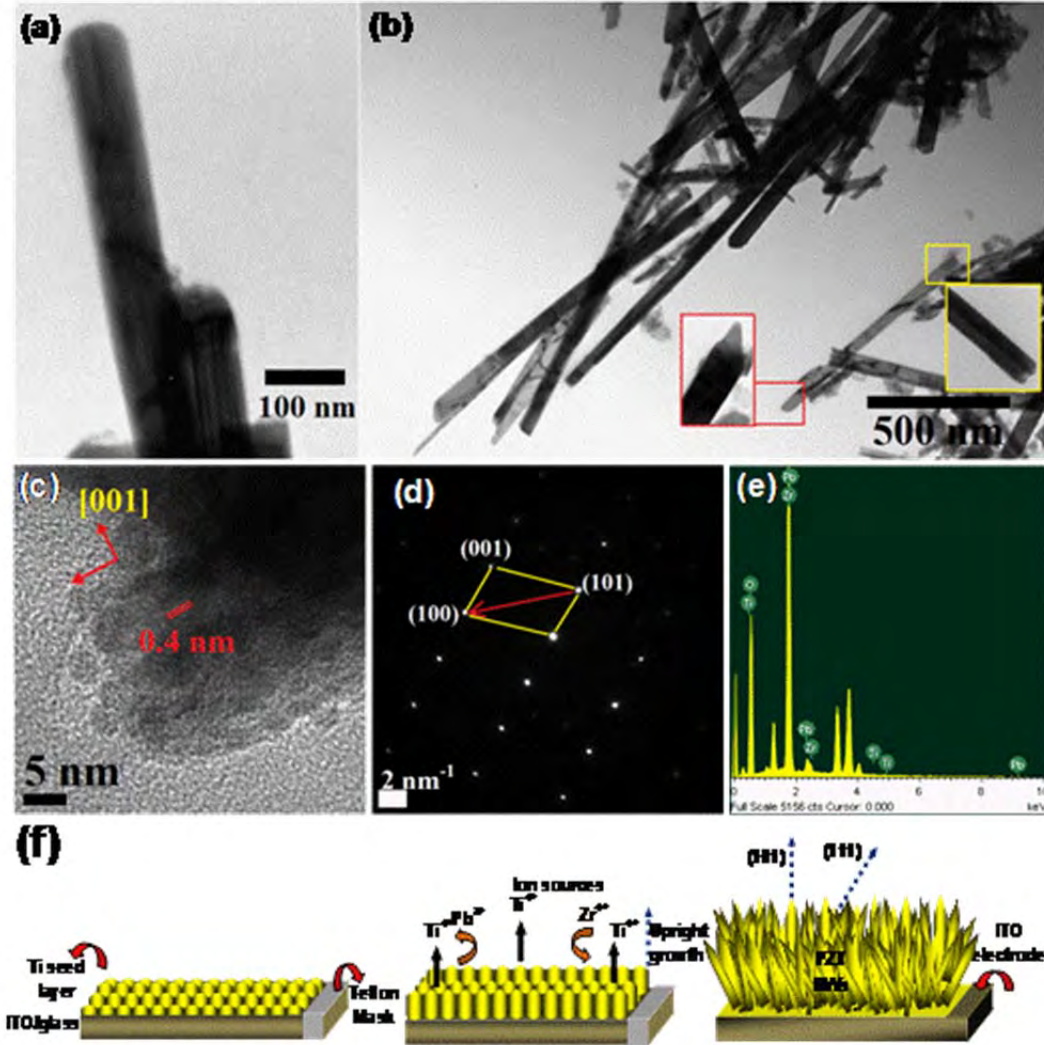


Figure 111: (a,b) TEM images of the PZT NWs. Insets of Figure 111 (a, b) show the morphology of the tip and the base of individual NWs. (c) HRTEM image of a single PZT NW near its tip. (d) SAED pattern collected from an individual PZT NW showing single crystal pattern with marked crystal planes in the tetragonal PZT lattice structure. (e) Representative EDS spectrum collected from different zones of a single PZT NW. (f) Schematic diagram showing the step-by-step growth of PZT NW arrays on Ti coated ITO/glass substrate.

Project 6: Flexible photonic materials for solar-based energy sources

6.1. Synthesis and characterization of PbSe and $\text{PbS}_x\text{Se}_{1-x}$ nanoparticles by microwave plasma:

Quantum dots (QD) of PbSe and PbS have been shown to produce multiple excitons with the absorption of a single uv photon. Efficient dissociation of these excitons in solar cells that are based on QDs has the potential to produce very large currents leading to conversion efficiencies well above the thermodynamic limit. The aim of this project was to investigate the possibility of producing efficient solar devices that are flexible and cost-effective by combining QDs with semiconducting polymers.

The QD-embedded flexible solar device structure developed under this project is shown in Figure 112. Device fabrication included the following main steps;

- (1) Development of a chemical technique to grow crystalline PbSe nanoparticles in the size range of 5-10 nm with a narrow size distribution. As a result of this effort a novel laser-assisted spray deposition technique was developed to produce surfactant-free PbSe QDs on a substrate. Figure 113 shows the experimental set up of the laser-assisted spray deposition process. Transmission Electron Microscopy (TEM) images of PbSe QD coating formed by this technique is shown in Figure 114. The 2-3 nm spacing that exists in surfactant-coated QDs (Figure 3 (a)) is absent in LAS deposited coatings. This enhances charge transport between the QD and the host matrix (polymer).
- (2) Deposition of films of the semiconducting polymer P3HT with optical absorption properties that are similar to bulk.

Clearly, the surfactants have been removed in the LAS process to form intimate contacts between adjacent QDs while the identity of each QD is maintained. Figure 115 shows an optical absorption spectrum comparing the absorption by as-grown surfactant-coated PbSe QDs in a heptane solution to that from a nanoparticle film deposited by LAS. LAS method was also used for the deposition of P3HT polymer films from a solution of P3HT dissolved in heptane. As shown in Figure 116, the absorption spectrum of these films matched that of a film fabricated by spin-coating on a substrate.

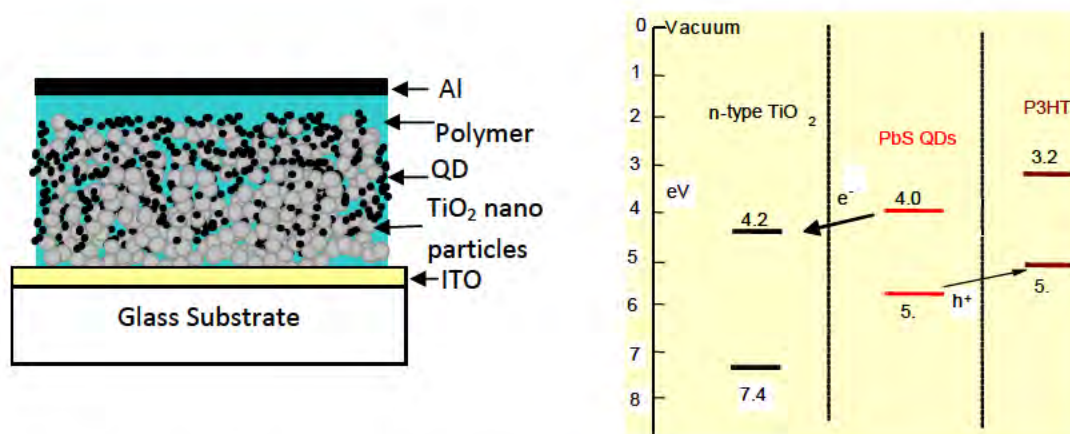


Figure 112: Hybrid structure with nanoporous TiO_2 /QD/P3HT and energy band alignment of the three components

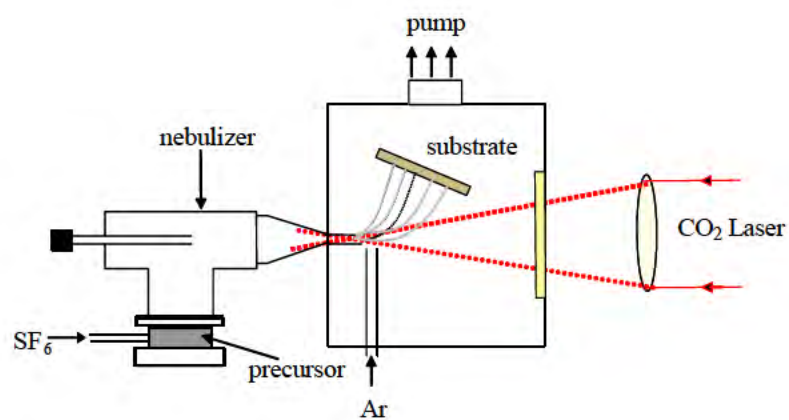


Figure 113: Laser-assisted spray pyrolysis system for nanoparticle growth.

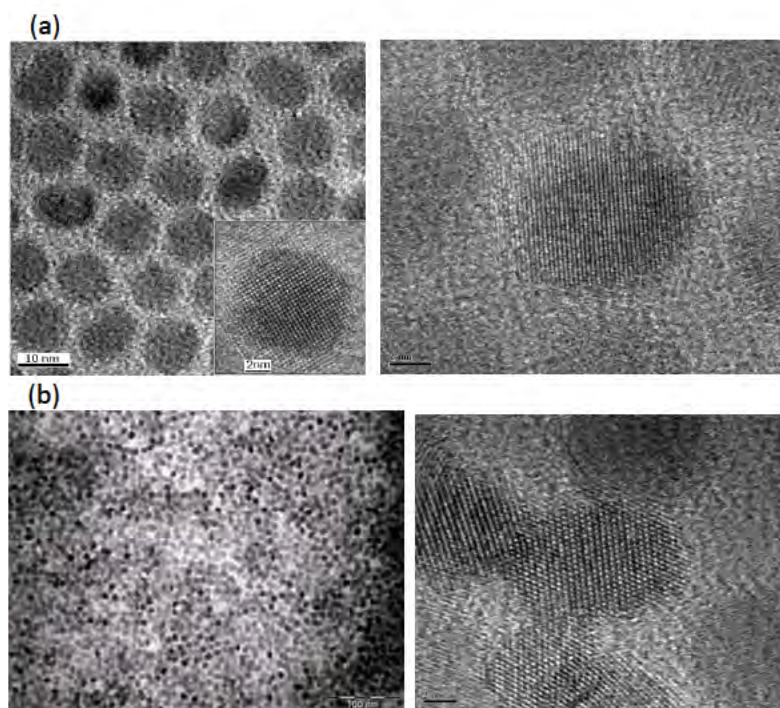


Figure 114: Low and high resolution TEM images of a (a) self-assembled PbSe QDs with surfactants, (b) low and high resolution TEM image of PbSe QD films deposited by LAS.

The overall goal of this project was to fabricate an Al/PEDOT/PbSe/TiO₂/FTO hybrid structure to effectively transport the photo-generated electrons and the holes. We have successfully fabricated TiO₂ nanorods on FTO-coated glass substrates as the electron collection electrode by a solvothermal technique (Figure 117).

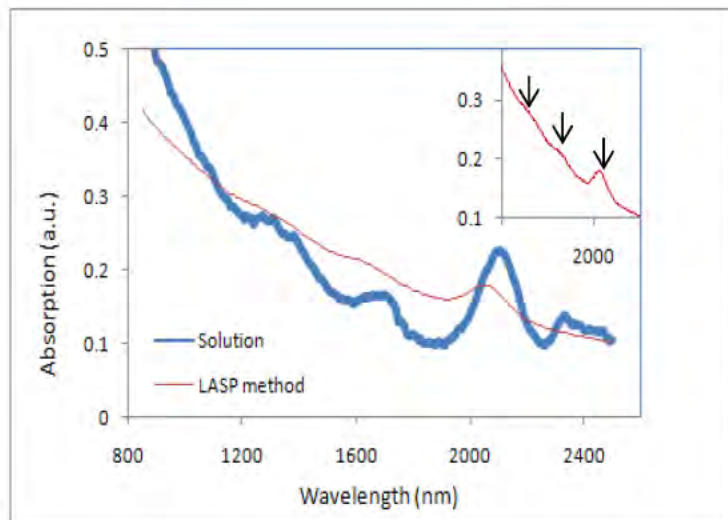


Figure 115: Absorption spectra of 10.9 nm quantum dots in solution and after LASP deposition. Inset: Absorption spectrum of LAS nano-film.

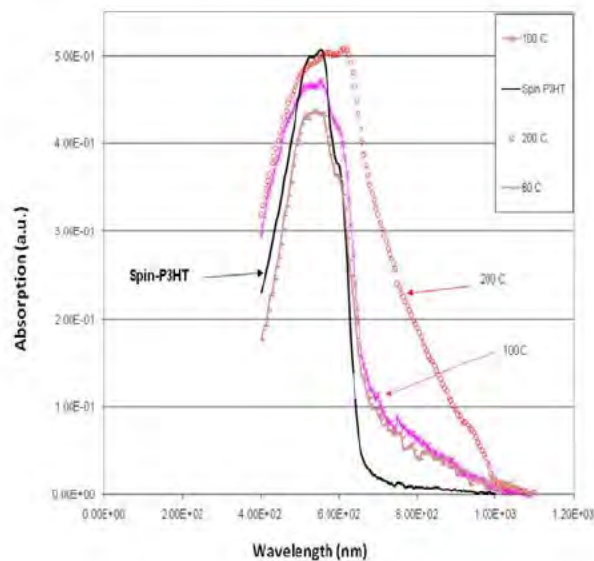


Figure 116: Optical absorption by P3HT polymer films fabricated at different substrate temperatures.

In summary, under this task we have developed a method to fabricate crystalline PbSe quantum dots in a volatile solvent with a narrow particle size distribution. Optical absorption and PL studies confirmed the quantum confinement characteristics of the QDs. We have used a laser-assisted spray process to deposit the PbSe QDs from the solution onto a substrate. QDs form a connected network while maintaining single crystal nature and thus the quantum confinement. This was demonstrated by optical absorption and PL spectroscopy. In addition, we have also produced films of the semiconducting polymer P3HT using the laser-assisted spray process.

These films possessed the desired optical properties. A method for fabricating nanorods of TiO₂ on a transparent conducting electrode has also been developed. QDs of InSb were not developed as QDs of PbSe satisfied the required conditions for efficient multi-exciton generation.

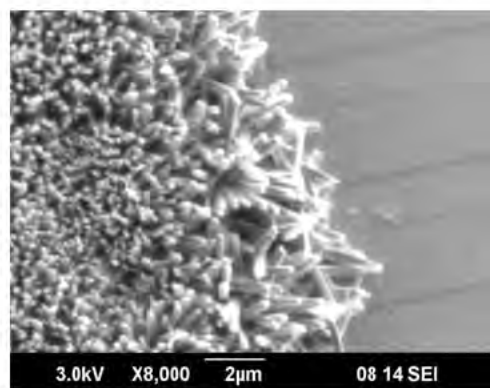


Figure 117: Titanium Dioxide nanorods (TiO₂) deposited on FTO-coated glass substrate

6.2. Integration of nanoparticles with polymer and characterization of optical properties:

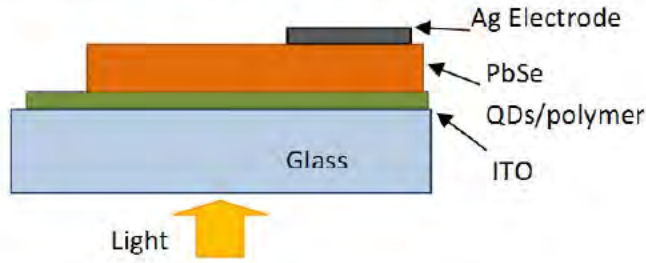


Figure 118: PbSe QD films structure deposited by Laser Assisted Spray (LAS) technique for photocurrent measurements.

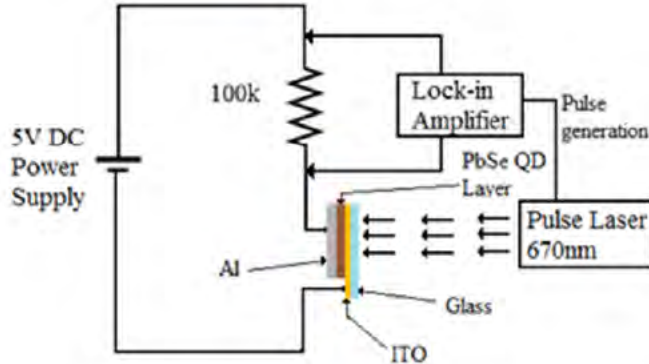


Figure 119: Circuit diagram for detecting photocurrent generated by the diode laser.

LAS process was used to fabricate PbSe QDs/Polymer composite solar cell structure shown in Figure 118.

Diode laser excitation (wavelength of 670 nm) with a sensitive detection technique was used to measure the photocurrent generated by the hybrid structure. The circuitry used for these measurements is shown in Figure 119.

The graph in Figure 120 shows the photo-generated current recorded at various laser powers. The wavelength of the laser at 670 nm has photon energy of 1.85eV which is lower than the band gap of P3HT (1.97eV). Therefore, the measured current mainly

corresponds to the carriers generated by exciton dissociation.

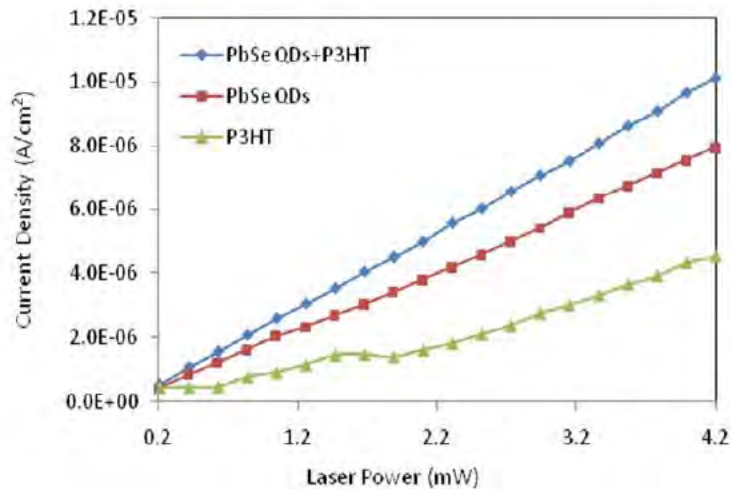


Figure 120: The graph of photo-generated current in the PbSe QDs/P3HT layer sandwich between ITO and Al electrodes at various laser power levels compared to PbSe QDs and P3HT polymer separately.

6.3. Formation of single cell device structures with nanoparticles of different sizes and characterization of the output:

TiO₂ nanorods were deposited on fluorine-doped tin oxide films by a hydrothermal process. Laser-assisted spray (LAS) deposition process was used to deposit PbSe QDs over the vertically aligned TiO₂ nanorods. Subsequently, a layer of the p-type polymer PEDOT was spin-coated over the QD layer to form the composite device structure shown in Figure 121 (a). The photocurrent generated by the composite structure was investigated by exposing the device to different light intensities from a white light source. As shown in the graph in Figure 121 (b) a significant photocurrent was generated by the cell.

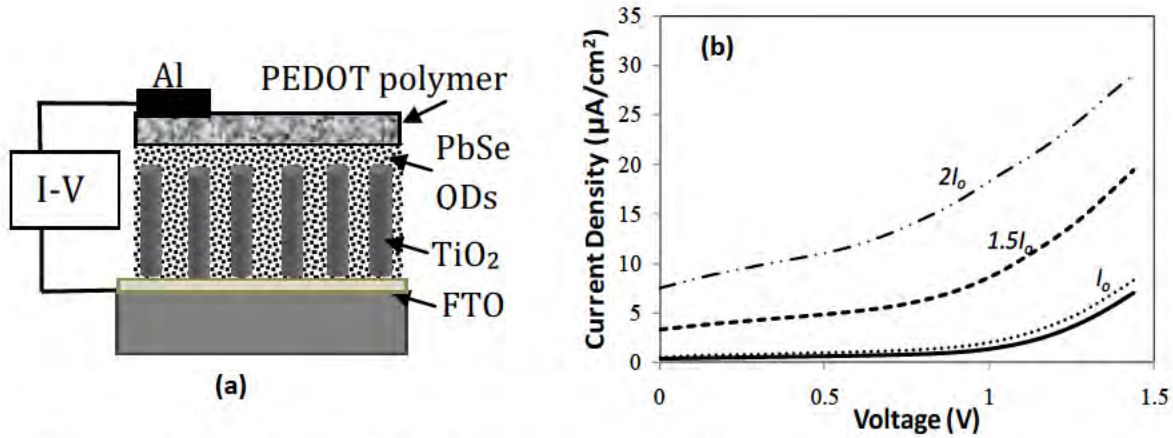


Figure 121: (a) TiO₂-PbSe QD-polymer composite cell structure and, (b) photocurrent at different illumination intensities. $I_0 \sim 0.01 \text{ W/cm}^2$

In summary, laser-assisted spray process was used to deposit PbSe QDs on crystalline TiO₂ nanorods grown by a hydrothermal process. Absence of surfactants enhanced exciton dissociation and charge transport. A significant photocurrent was produced by the composite TiO₂-QD-polymer structures.

Task III: Solid-state materials for power generation and refrigeration

Project 7: High-performance bulk and nanocomposite thermoelectric materials for power generation

The controlled fabrication of nanoscale semiconductors with enhanced physical properties is a current goal of technical as well as fundamental interest. To this end, the influence of semiconductor grain boundaries on carrier transport becomes increasingly important in nanoscale polycrystalline systems, where surface, point defect, dislocation, and interfacial energy barrier scatterings can dominate the transport [172,173]. Recent identification of several higher efficiency thermoelectric (TE) materials can be attributed to nanoscale enhancement [174-181]. These materials demonstrate increased Seebeck coefficient and decreased thermal conductivity due to the phenomenological properties of nanometer length scales, including enhanced interfacial phonon scattering and charge carrier filtering. Nanostructured TE enhancement aims to ‘split’ the interdependence of the electrical and thermal transport, allowing for better optimization of the TE figure of merit, $ZT = S^2T/\rho\kappa$ [182]. This equation defines the effectiveness of a material for TE applications, where S is the Seebeck coefficient, T is the absolute temperature, ρ is the electrical resistivity, and κ is the thermal conductivity. The reduction of κ through the interface scattering of phonons remains the primary mechanism for increased TE performance in nanostructured systems [183,184]. However, to achieve superior TE performance requires enhancement of the power factor (S^2/ρ). Carrier filtering, where the presence of interfacial energy barriers filters low energy charge carriers traversing the interface, has been theoretically predicted [185,186]. This increases $|S|$, as its value depends on the mean carrier energy relative to the Fermi level [182]. An understanding of this phenomenon in bulk materials is of fundamental importance. A small body of work has indicated that TE property improvements for bulk nanocrystalline materials are feasible [187-189]. However, the physical mechanism responsible for S enhancement in these materials has not been developed.

To this end, we started an investigation into the transport properties of doped and undoped nanocomposites, i.e. nanocrystals densified within a macro-scale nanocomposite. In parallel to this experimental investigation, a theoretical study was also undertaken. We aimed to propose a phenomenological model to describe the diffusion transport of carriers through a material composed of nanogranular regions. The material is viewed as containing potential interface barriers due to the grains, and the transport includes quantum transmission and reflection from those barriers. Additional scattering mechanisms, such as carriers/acoustic phonons, carriers/non-polar optical phonons, and carriers/ionized impurities, which are relevant for thermoelectric materials, are also taken into account for theoretical modelling. The model described carrier transport properties of polycrystalline materials in general experimental data or made predictions for other TE materials. The research proceeded according to the scheduled tasks which are described below.

7.1. Bulk nanocomposites: optimize synthesis parameters:

PbTe nanocrystal synthesis with different grain sizes: PbTe nanocrystals were synthesized with different sizes in high-yield employing two different approaches; low temperature reverse microemulsion (ME) with 25-30 nm crystals and direct precipitation (DP) synthesis with 50 nm (DP-small) and 100 nm (DP-

large) crystals [190, 191]. Na-AOT, water and n-hexane, each of high purity grades, were used as the surfactant, water phase, and oil phase, respectively, for the microemulsion process. Pb-acetate, Na-tellurite and Bi-nitrate were used as the Pb, Te and Bi sources, respectively. A tellurium alkaline aqueous solution and lead acetate trihydrate were used for the direct precipitation process. The dark black precipitate in each case was separated out repeatedly with water and ethanol. The carrier concentrations were modified by directly doping the PbTe nanocrystals with Ag (Ag_2Te), Na and Bi (Bi-nitrate) prior to the densification procedure. Nominal doping percentages varied from 1-40 mol % in order to investigate their transport properties as a function of doping. Spark Plasma Sintering (SPS) successfully consolidated these nanoscale grains within a dense polycrystalline matrix.

$\text{Bi}_2\text{Se}_x\text{Te}_{3-x}$ and $\text{Sb}_2\text{Se}_x\text{Te}_{3-x}$ Nanocrystal synthesis: Bismuth telluride and antimony telluride Se-doped nanocrystals were prepared by ethyleneglycol mediated solvothermal process. For the synthesis, Bismuth nitrate ($\text{Bi}(\text{NO}_3)_3 \cdot 5\text{H}_2\text{O}$), antimony(III) chloride (SbCl_3) and selenium dioxide (SeO_2) were chosen as the Bi, Sb and Se sources, respectively. Sodium tellurite (Na_2TeO_3) was the tellurium source for all syntheses. Monohydrate hydrazine hydrate ($\text{N}_2\text{H}_4 \cdot \text{H}_2\text{O}$) was used as a reducing agent and pH regulator to yield the desired nanocrystals. All the chemicals were analytical grade and were used without further purification. Selenium doping was carried out with varying Te:Se atomic ratios (Te:Se = 2.9:0.1, 2.8:0.2 and 2.7:0.3).

Bi-Sb Alloy Nanocrystals synthesis: We prepared Bi and Bi-Sb nanocrystals with different Sb concentrations by a low temperature polyol synthesis process. Bismuth nitrate pentahydrate ($\text{Bi}(\text{NO}_3)_3 \cdot 5\text{H}_2\text{O}$) was used as the Bi source, antimony trichloride (SbCl_3) was used as the antimony source, and Polyvinylpyrrolidone (PVP; Molecular Weight 40000) was used as the complexing and capping agent. Sodium borohydride (NaBH_4) was used as the reducing agent. Initially, 3 mM $\text{Bi}(\text{NO}_3)_3 \cdot 5\text{H}_2\text{O}$ and required SbCl_3 were dissolved along with 1 gm PVP in 100 mL EG until a transparent solution was obtained. A separate solution was prepared by dissolving 0.04M NaBH_4 in 30 mL water. This solution was added slowly to the $\text{Bi}(\text{NO}_3)_3 \cdot 5\text{H}_2\text{O}$ and SbCl_3 solution and refluxed at 140 °C for 2 h under continuous magnetic stirring. When the nanocrystals formed the solution turned black in color. The Bi and Bi-Sb nanocrystals were separated by centrifugation. In order to precipitate the nanocrystals from EG, the reaction mixtures were diluted with ethanol and then placed in a centrifuge at 4500 rpm for ~ 15 min. The centrifugation process was repeated several times until the supernatant liquid was clear. Any residue of PVP, $\text{Bi}(\text{NO}_3)_3 \cdot 5\text{H}_2\text{O}$, and SbCl_3 was removed from the product by continuously washing with ethanol and water. To remove the EG and PVP from the surface of the nanocrystals, and to reduce surface oxidation, ethanol was used for washing. After thorough washing, the nanocrystal specimens were dried at room temperature under vacuum for 6 - 8 h. This process yielded approximately 1.5 gram for each synthesis run. The synthesis process is scalable and economical. This method allowed for the preparation of phase pure, highly crystalline nanocrystals of 30 - 40 nm in diameter in large yield.

CuCoO_2 synthesis: CuCoO_2 has previously been prepared by hydrothermal [192], and solution-based [193] techniques, as well as thermal decomposition of copper-cobalt hydroxysalts [194]. Reactions of CuCl and LiCoO_2 were carried out in alumina crucibles, sealed inside evacuated silica tubes. CuCoO_2 was successfully prepared reproducibly by reaction at 590°C for 2 days. The resulting products were very fine, grayish powders consisting of CuCoO_2 , with only small amounts of impurity phases.

FeSb_2 nanocrystals synthesis: An investigation into nanostructured FeSb_2 has been mainly limited by the lack of a suitable preparative process. Nevertheless, there are a few reports on the synthesis of FeSb_2 nanocrystals by solution-based processes [195, 196]. Recently the synthesis of FeSb_2 nanorods with the

Pnn2 crystal structure using surfactant molecules has been reported [196]. However, to the best of our knowledge, the synthesis of *Pnnm* FeSb₂ nanocrystals has yet to be reported. We have synthesized *Pnnm* FeSb₂ nanocrystals for the first time by using a surfactant and template free ethanol mediated solvothermal process. Analytical grades of iron (II) acetate (Fe(C₂H₃O₂)₂) and antimony (III) acetate (Sb(CH₃COO)₃) were used as the Fe and Sb sources, respectively. An excess molar quantity of Fe(C₂H₃O₂)₂ was always maintained in the solution because of the large difference in the reduction potential between Fe⁺² (Fe⁺² + 2e ↔ Fe, -0.409 V) and Sb⁺³ (Sb⁺³ + 3e ↔ Sb, 0.15 V). In a typical synthesis, 2 mmol of Fe(C₂H₃O₂)₂ and 2 mmol of Sb(CH₃COO)₃ were dissolved in 40 mL (80% volume of the custom made Teflon reactor) anhydrous ethanol. Three mmol sodium borohydride (NaBH₄) was added to the solution as a reducing agent. The entire solution was poured inside a custom made teflon reactor and tightly sealed. The teflon reactor was then inserted in a custom made stainless steel chamber and maintained at 220 °C for 16 h. At the end of the reaction, the chamber was gradually cooled to room temperature. The deep black precipitation (FeSb₂) at the bottom of the Teflon chamber was collected after washing first with 0.1 M HCl solution, then several times with distilled water and ACS grade alcohol. Finally the washed precipitate was dried in vacuum for 6 h and collected for characterization. This process yielded approximately half a gram of FeSb₂ nanocrystals.

Clathrate Nanocomposites: Infrared (IR) detectors are widely used in night vision, thermal imaging and threat detection systems for many military and space applications [197]. While conventional thermoelectric coolers work well down to 150 K, there is a need for cooling further to 80 K and below to improve the efficiency of IR detectors. This underscores the need for considering new materials and strategies for developing efficient solid-state coolers with a broad range in working temperature. While Eu₈Ga₁₆Ge₃₀ clathrates are usually known as excellent thermoelectric refrigerants at high temperature (T > 200 K), our recent discoveries of large, reversible magnetocaloric effects in these materials make them interesting for dual functional thermomagnetic and thermoelectric cooling applications [198, 199]. The goal of our research is to use Eu₈Ga₁₆Ge₃₀ clathrates as the host matrix to make nanocomposites with tunable refrigerant capacity (RC) in the low to intermediate temperature range (10 - 100 K). Polycrystalline Eu₈Ga₁₆Ge₃₀ with the type I crystal structure was synthesized by reacting the high purity elements in stoichiometric ratios inside a boron nitride (BN) crucible which was enclosed in a nitrogen atmosphere, inside a sealed quartz ampoule. The specimen was placed in an induction furnace at 1000 °C for 10 minutes followed by a rapid water quench. To make the clathrate-based composites, the type-I clathrates are combined with EuO in different proportions (80%/20%, 70%/30%, 65%/35%, 60%/40%, 40%/60%).

7.2. Core-shell approach towards optimization:

We successfully prepared PbTe/Ag core/shell crystals and employing SPS crystals in order to prepare nanocomposites. The core and core/shell nanocrystals were characterized by energy dispersive X-ray spectroscopy (EDS, Oxford Instruments INCA X sight), Scanning Electron Microscopy (SEM) and transmission electron microscopy (TEM, FEI Tecnai F20 S-Twin TEM). Figure 122a and 1b are the representative images of 250 core/shell PbTe/Ag nanocrystals before and after SPS, respectively, and Figure 122c and 1d are representative images of EDS spectra of core and core/shell nanocrystals, respectively. After SPS, the PbTe/Ag core/shell nanocomposites were grinded to powder and TEM analysis was performed. TEM images shown in Figure 123a and 123b indicate the formation of Ag shell

around the PbTe nanocrystals. This morphology appears to remain after SPS, i.e. the Ag shell remains attached to the PbTe nanocrystals. In order to understand the effect of Ag shell in the composites room temperature S and ρ were performed. As compared to the ρ value of PbTe core (101 m Ω -cm), the core/shell nanocomposites have 5 times higher resistivity. These results indicate that this approach may not be of interest for improved thermoelectric performance.

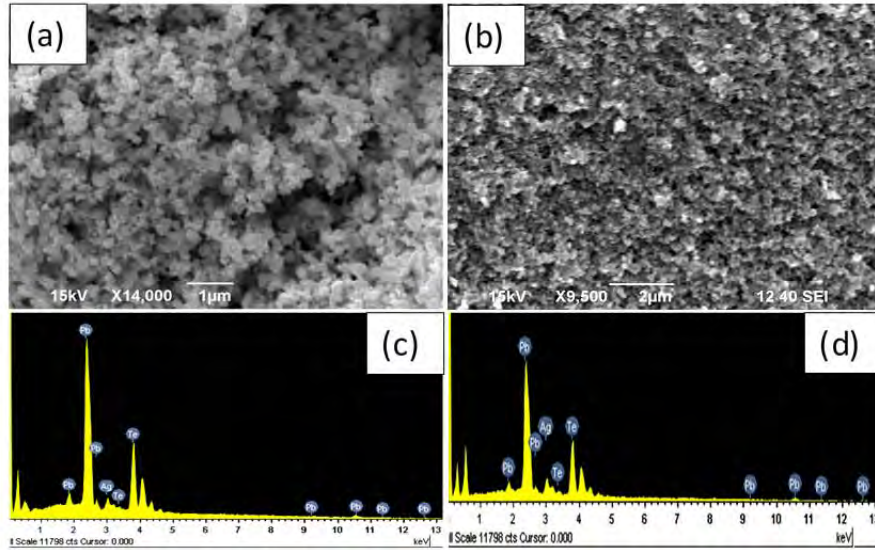


Figure 122: SEM images of PbTe/Ag core/shell crystals (a) before and (b) after the SPS. EDS spectra of (a) PbTe and (b) PbTe/Ag core/shell crystals.

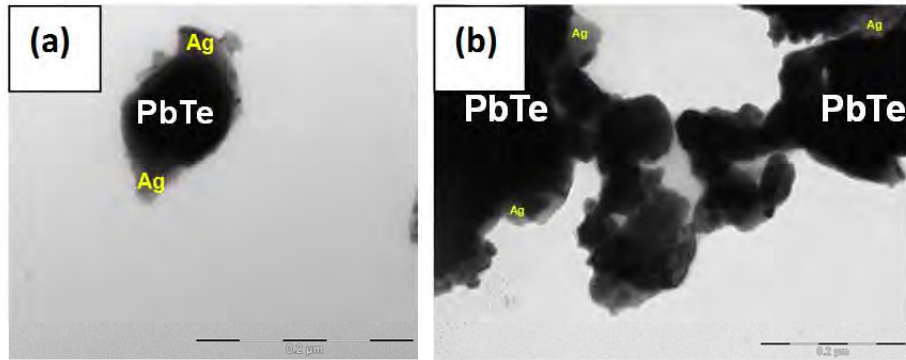


Figure 123: TEM images of (a) PbTe/Ag nanocrystals and (b) ground PbTe/Ag after SPS.

7.3. Structural and calorimetric analysis for thermal stability tests:

Structural Analysis

The synthesized materials were all structurally characterized by X-ray diffraction (XRD, Bruker AXS D8 with Lynx Eye position sensitive detector), EDS, SEM and TEM. Results of the detailed structural analysis are discussed as follows:

Ag-doped PbTe Nanocomposites: Densifying solely the nanocrystals results in the dispersion of non-conglomerated nanostructure within a bulk matrix, with grains ranging from 100 nm to over 1 micron, as

shown in Figure 124. X-ray diffraction following SPS indicated ~ 5 vol. % PbTeO_3 impurity for specimens I and II, and ~ 3 vol. % Te_4O_9 impurity for specimens III and IV.

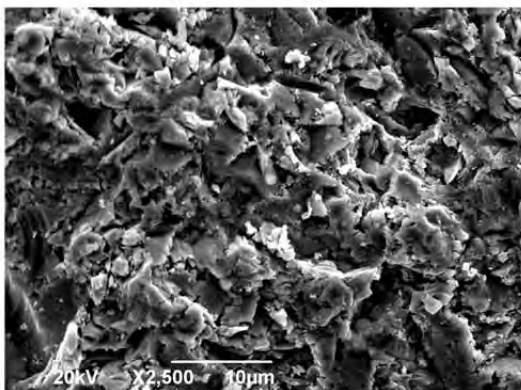


Figure 124: Representative SEM micrograph of a specimen III fracture surface indicating 100 nm to over 1 micron grains distributed within a bulk material.

Bi-doped PbTe Nanocomposites: XRD indicated the PbTe phase only, even for heavily doped PbTe nanoparticles. Impurities did not appear even after SPS. EDS performed on the densified pellets showed the presence of Bi in PbTe. Particle sizes calculated from the XRD spectra by the Debye-scherrer formula were ~30-50nm for nanoparticles synthesized in the microemulsion technique and ~50-100 nm for nanoparticles synthesized by the direct precipitation technique.

Morphological features of the specimens studied by SEM and TEM indicated the relative uniformity in the grain size distribution. These analyses indicated nanostructuring after densification. Figure 125a and 125b show the SEM images of the 15% Bi doped PbTe specimens after SPS. The high resolution SEM images indicate the presence of nanograins (~30-50 nm) within larger grains. The average grain size of the specimens was estimated to be approximately 500 nm after SPS. The grain size of the synthesized specimens calculated from the low resolution TEM was ~25-30 nm before SPS (Figure 125c).

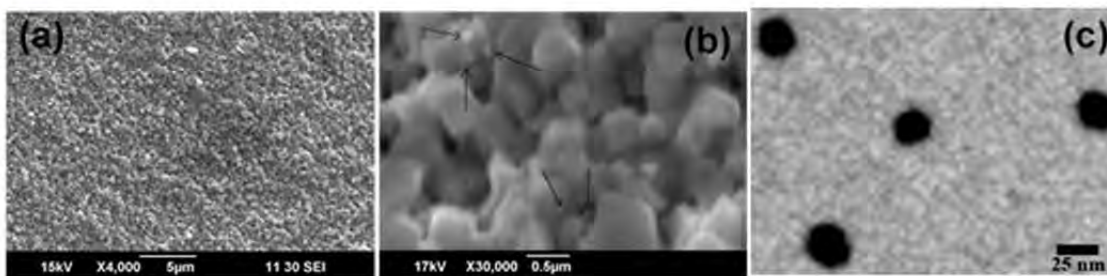


Figure 125: (a) SEM image of a fractured surface of the 15% Bi-doped PbSe specimen after SPS showing the compactness. (b) Higher magnification image showing the presence nanograins within large grains. (c) TEM image of Bi-doped PbTe nanocrystals.

Higher percentages of different sized Bi-doped PbTe nanocrystals did not show Bi-related impurities in the XRD spectra (Figure 126a-c). This along with EDS results suggests successful Se doping. The XRD peaks for the 100 nm Bi-doped PbTe nanocrystals are sharper than that for the 50 nm

and 25 nm sized PbTe nanocrystals, a qualitative corroboration of the differing grain sizes. Nanocrystal sizes were calculated using the Scherrer equation and the results were corroborated by SEM images of the

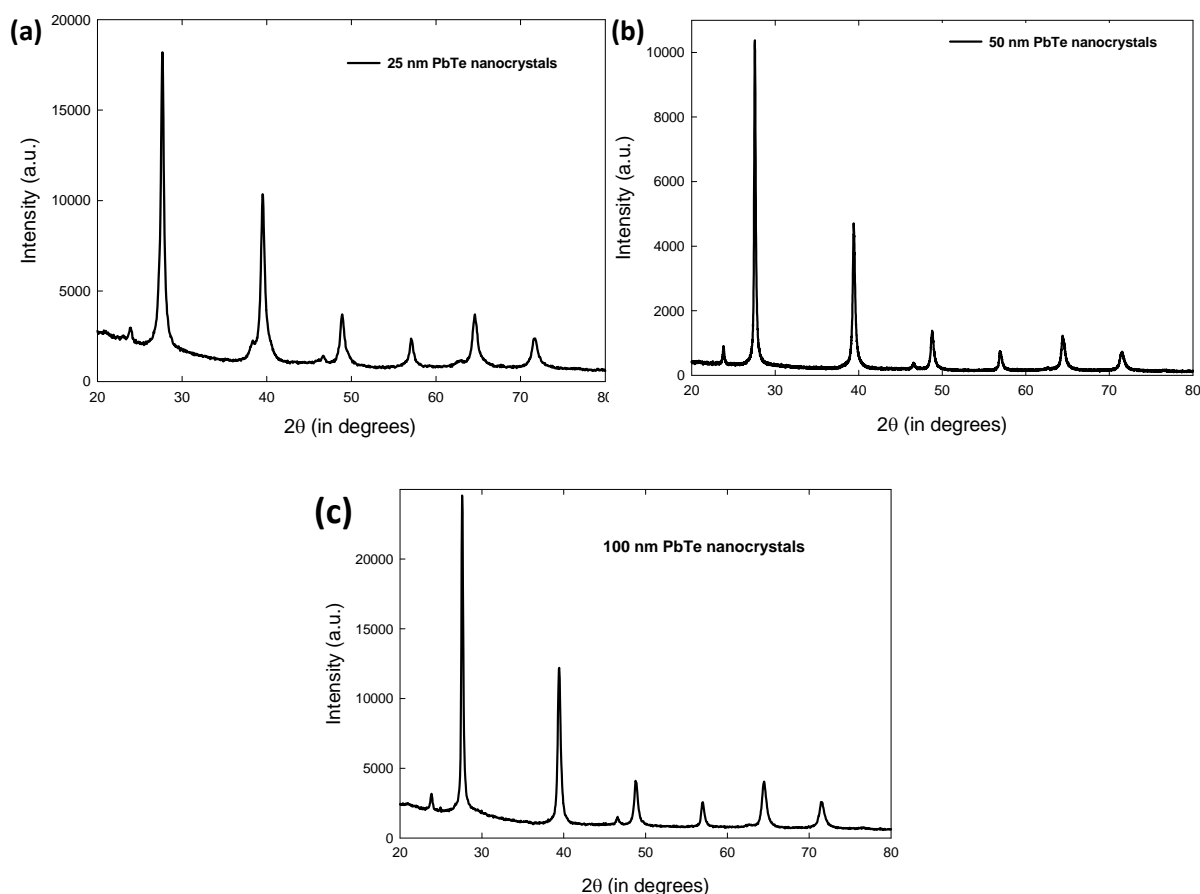


Figure 126: Typical XRD spectra of different grain sized heavily Bi-doped PbTe specimens. The XRD patterns indicate the phase purity of the prepared nanocrystals.

nanocrystals. After densification, the grains ‘grew’ to 30-50 nm for densification of the nanocrystals synthesized by ME, and 50-100 nm for those synthesized by DP-small and 100-300 nm for DP-large.

Composition analysis of the nanocrystal specimens were carried out by EDS. Increasing the nominal Bi concentration increased Bi doping. Bi-doped PbTe nanocomposites did not show any impurities after densification, from XRD results. SEM images indicate the presence of nano-scale grains. SEM images of fractured pellet surfaces indicated densities of 95-98% of that of the theoretical density of PbTe.

Bi_{0.5}Sb_{1.5}Te₃ alloy nanocomposites: Structural studies show successful preparation of Se-doped Bi_{0.5}Sb_{1.5}Te₃ alloy nanocrystals of ~18-25 nm in diameter. Representative XRD spectra of the Se-doped Bi₂Te₃, Bi_{0.5}Sb_{1.5}Te₃ and Sb₂Te₃ nanocrystals are shown in Figure 127a-c. The spectra did not indicate a secondary phase. Nanocrystallite sizes calculated from the Debye-Scherrer formula were ~18-25 nm. Crystal sizes estimated from SEM images corroborate these results. Figure 128 a and b show the representative SEM images of the Se doped Bi_{0.5}Sb_{1.5}Te₃ and Sb₂Te₃ nanocrystals. Both undoped and Se-

doped Bi_2Te_3 and $\text{Bi}_{0.5}\text{Sb}_{1.5}\text{Te}_3$ nanocrystals are particulate in shape whereas undoped and Se doped Sb_2Te_3 nanocrystals are found to be platelets ~ 5 nm thick.

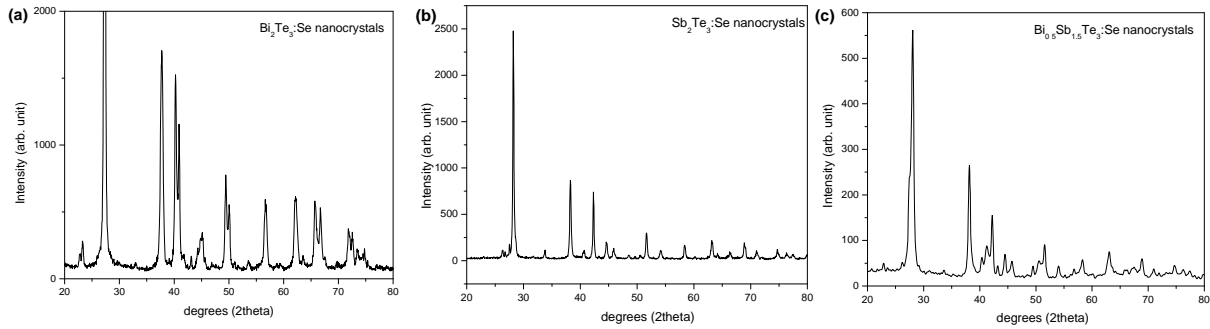


Figure 127: XRD spectra of the representative Bi-Sb-Te-Se specimens (a) $\text{Bi}_2\text{Te}_3\text{:Se}$ (b) $\text{Sb}_2\text{Te}_3\text{:Se}$ and (c) $\text{Bi}_{0.5}\text{Sb}_{1.5}\text{Te}_3\text{:Se}$ nanocrystals .

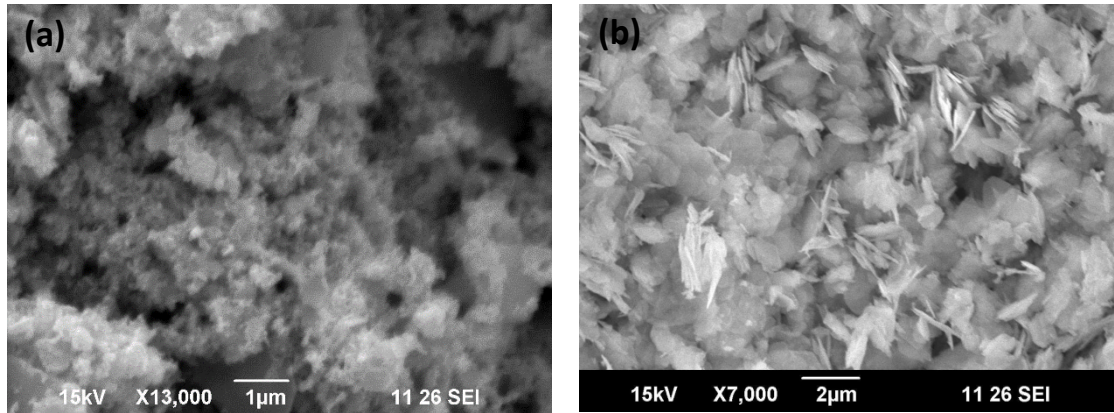


Figure 128 SEM images of the representative Bi-Sb-Te-Se specimens (a) $\text{Bi}_{0.5}\text{Sb}_{1.5}\text{Te}_3\text{:Se}$ nanocrystals and (b) $\text{Sb}_2\text{Te}_3\text{:Se}$ nanocrystals.

Bi & Bi-Sb nanocrystals and nanocomposites: XRD spectra of phase-pure Bi and Bi-Sb nanocrystals are shown in [Figure 129](#). The spectra indicate the formation of Bi-Sb. The nanocrystallites ranged in size from 30 nm to 50 nm. EDS analysis indicated a Bi:Sb ratio of 0.88:0.12 for the Bi-Sb alloy. Both nanocrystals possess a rhombohedral morphology, as shown in TEM images. A representative TEM micrograph of the Bi-Sb nanocrystals is shown in [Figure 130](#).

After phase characterizations we prepared the Bi and Bi-Sb nanocomposites by densifying the as-synthesized nanocrystals by SPS. In the SPS procedure, a pulsed dc current passes through both the graphite die and the specimen under pressure. This heats the specimen internally, providing uniform and rapid thermal ramping while minimizing the sintering time and temperature. At the same time rapid grain growth during a normal sintering process can be minimized using SPS process. However, different temperature and pressure of SPS may result in difference in density of the prepared bulk polycrystalline specimens. All the SPS densification runs were done at 65 MPa under vacuum. Due to the low melting

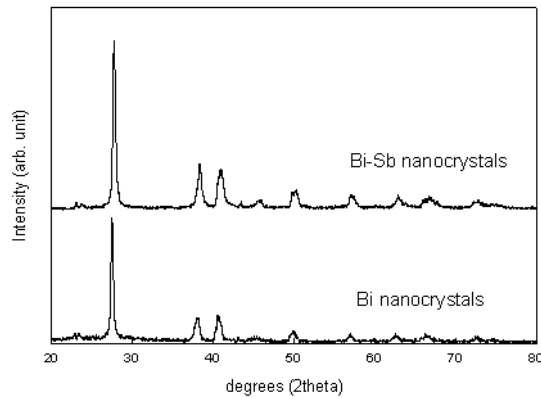


Figure 129: XRD spectra of the pure Bi and $\text{Bi}_{0.88}\text{Sb}_{0.12}$ nanocrystals

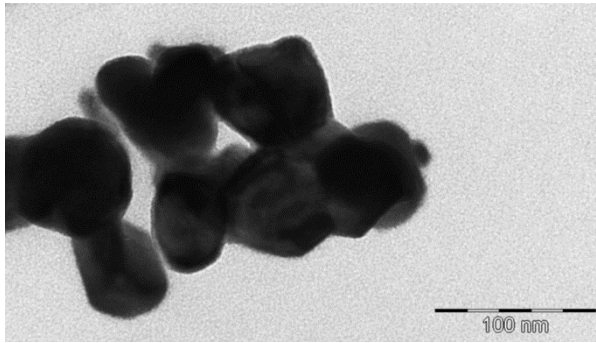


Figure 130: TEM image of the representative $\text{Bi}_{0.88}\text{Sb}_{0.12}$ nanocrystals.

points of the Bi and Bi-Sb nanocrystals (between 260 °C – 275 °C), 250 °C and 265 °C were chosen to densify Bi and Bi-Sb, respectively, with a 5 - 12 min hold time for different compositions.

We densified Bi nanocrystals in three different SPS conditions; (I) 260 °C at 60 MPa with 12 min hold time, (II) 255 °C at 70 MPa with 12 min hold time, and (III) 210 °C at 400 MPa with 5 min hold time, hereby referred as Bi-I, Bi-II and Bi-III, respectively. Due to the low melting points of the Bi nanocrystals, 260 °C was chosen as the maximum SPS temperature. About 78 %, 85 %, and 92 % of the bulk theoretical densities were achieved for specimens Bi-I, Bi-II, and Bi-III, respectively. In case of Bi-Sb nanocomposites a density of only 72 % of the theoretical bulk density was achieved. The low temperature TE properties of single crystal and polycrystalline Bi and Bi-Sb bulk materials were reported to be greatly dependent on the purity of the specimens and orientation of the grains or crystals in case of single crystals. For nanostructured TE materials, densification is an essential processing step in order to make bulk polycrystalline specimen for TE properties measurements and also for practical TE

applications. Electronic and thermal transport properties of TE materials are affected by the porosity in the polycrystalline bulk specimens. However, an investigation of the dependence of density on the transport properties in nanostructured TE materials such as in Bi has not been previously performed.

The XRD analysis of the densified specimens indicated phase purity of the specimens after SPS. Typical XRD spectra of a Bi and $\text{Bi}_{85}\text{Sb}_{15}$ nanocomposites are shown in [Fig. 131a](#). [Figure 131b](#) shows a representative SEM image of the fractured surface of $\text{Bi}_{85}\text{Sb}_{15}$ nanocomposite. The SEM image indicates that after SPS the bulk polycrystalline specimen retains the nanostructural features.

The XRD of the Bi nanocrystals and SPS densified specimens are shown in [Figure 132a](#). The XRD spectra indicated the presence of few percentages of secondary Bi_2O_3 phase in densified specimens as indicated by an asterisk (*) in [Figure 132a](#). The impurity phase increases with higher density and is more prominent in the Bi-III specimen.

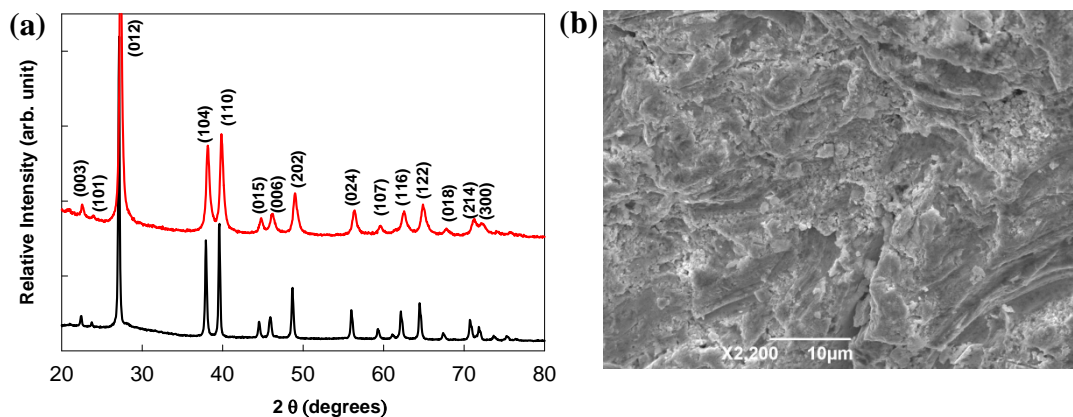


Figure 131: (a) XRD spectra of Bi (in black) and Bi-Sb(85:15) (in red) nanocomposites. (b) A representative SEM image of Bi and Bi-Sb nanocomposites showing the presence of nanostructures after SPS.

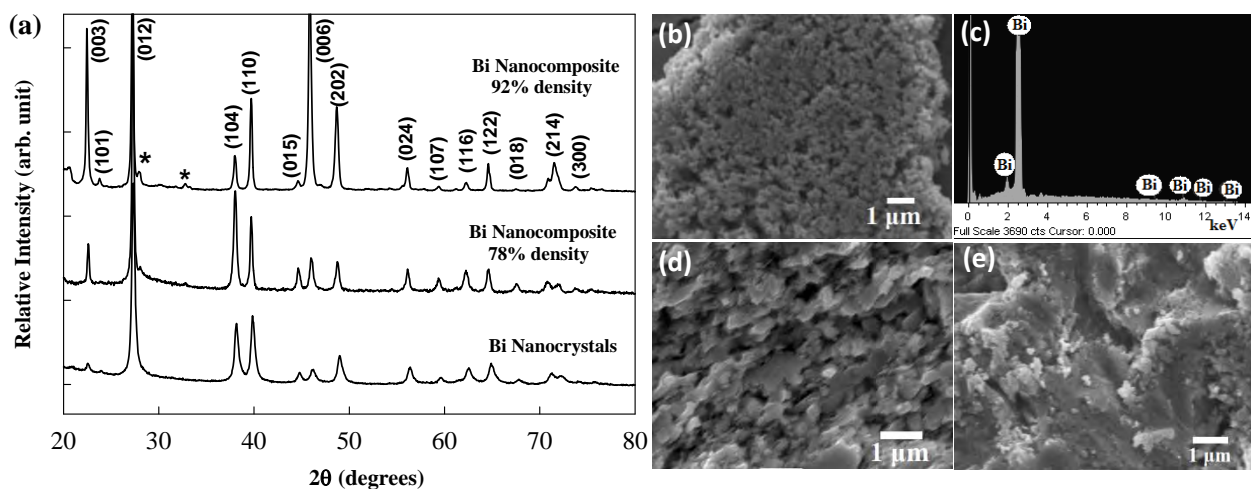


Figure 132 (a) XRD spectra of Bi nanocrystals, polycrystalline bulk Bi nanocomposite of different densities prepared by densifying Bi nanocrystals at different SPS conditions. (*) indicates the presence of Bi_2O_3 phase in nanocomposite specimens. Relatively intense (003) and (0006) planes present in 92 % dense Bi nanocomposite specimen suggests some preferred c-axis orientation. (b) and (c) are SEM image and EDS spectrum of phase pure Bi nanocrystals prepared by polyol synthesis process. (d) and (e) are the SEM images of polycrystalline bulk Bi nanocomposites of 78 % and 92 % densities, respectively.

Some preferred c-axis orientation was also observed in the XRD spectrum of Bi-III specimen. A SEM image of the Bi nanocrystals before SPS is shown in Figure 132b. The composition of the Bi nanocrystals was studied by EDS as shown in Figure 132c. Figure 132d and e show the SEM images of the fractured surfaces of the Bi-I and Bi-III dense polycrystalline bulk specimens, indicating the preservation of nanostructuring after SPS. The higher percentage of porosity in Bi-I specimen compared to the Bi-III specimen are in accordance with the density measured in these specimens. Figure 132e also indicates that at high SPS pressure Bi-III specimens retains the nanostructures more uniformly than in Bi-I specimen where grain growth increased. In case of Bi-Sb nanocomposites a density of only 72 % of the theoretical bulk density was achieved. The low temperature TE properties of single crystal and polycrystalline Bi and

Bi-Sb bulk materials were reported to be greatly dependent on the purity of the specimens and orientation of the grains or crystals in case of single crystals. For nanostructured TE materials, densification is an essential processing step in order to make bulk polycrystalline specimen for TE properties measurements and also for practical TE applications.

CuCoO₂ composites: Denoted by the general chemical formula ABO₂, the crystal structures of these materials (Figure 133) are characterized by layers of distorted, edge-sharing octahedra with oxygen coordinating metal cations (B = typically transition or group 13 elements) separated by planar layers of a transition metal (A = typically Cu, Ag, Pd, or Pt) which are linearly coordinated along the *c*-axis by two oxygen sites. Characterized by a wide range of possible compositions, the delafossite oxides also exhibit a significant richness in properties. Figure 133 shows calculated and experimental p-XRD patterns, confirming the CuCoO₂ 3R-delafossite crystal structure.

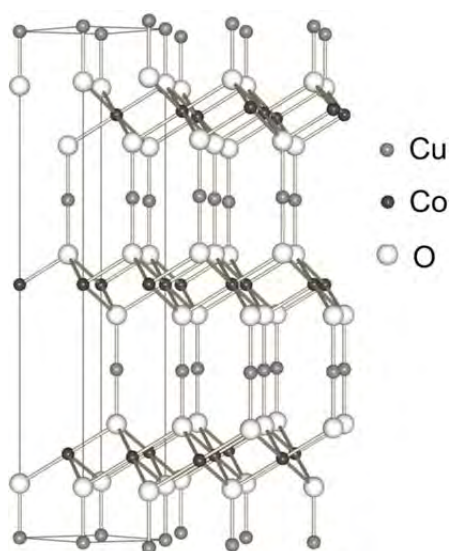


Figure 133: A depiction of the CuCoO₂ 3R delafossite crystal structure. The rhombohedral unit cell is outlined at left.

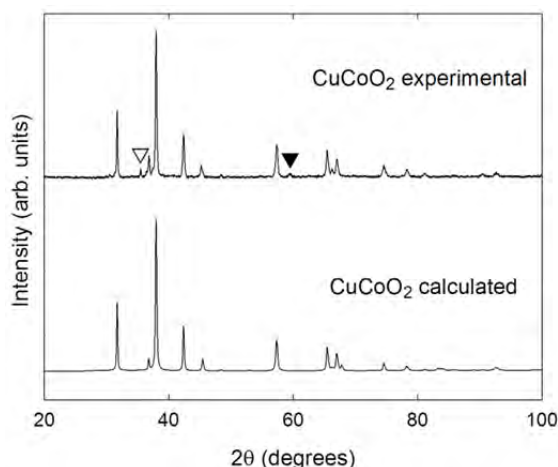


Figure 134: Experimental (top) and calculated (bottom) powder X-ray diffraction patterns for a CuCoO₂ specimen synthesized at 590 °C. Weak reflections due to minor impurity phases of CuO (▽) and LiCoO₂ (▼) are indicated.

Weak reflections due to minor impurity phases CuO and LiCoO₂ are also indicated in Figure 134. As shown, all other peaks are indexed to the CuCoO₂ phase, with the positions and relative intensities in good agreement.

FeSb₂ nanocrystals and nanocomposites: X-ray diffraction analyses confirmed the *Pnnm* FeSb₂ nanocrystals, and we intend to further characterize these materials as well as densify and measure the low temperature properties of dense nanocomposites. Phase pure *Pnnm* FeSb₂ nanocrystals with an average size of 40 nm have been prepared by an ethanol mediated low temperature solvothermal process. No template or capping chemical was used in processing these nanocrystals, allowing the crystals to grow in their inherent orthorhombic symmetry. The *Pnnm* structure of the FeSb₂ nanocrystals was confirmed by

XRD. Figure 135 a shows the indexed XRD pattern of the as prepared FeSb₂ nanocrystals in comparison to the calculated XRD pattern for *Pnnm* FeSb₂.

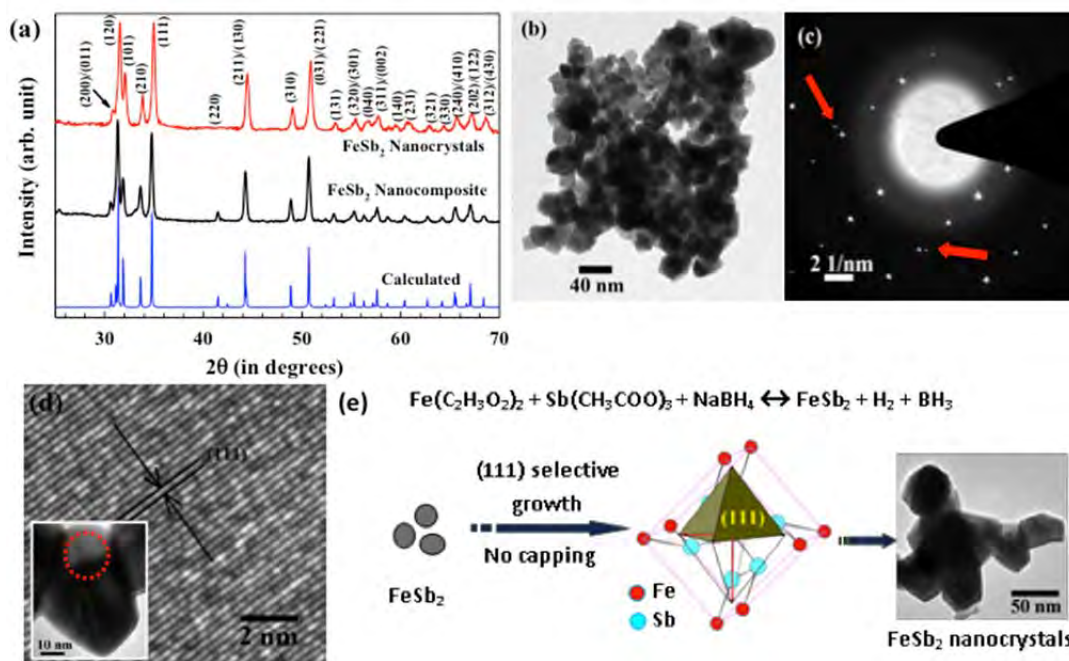


Figure 135 (a) XRD pattern of the as prepared FeSb₂ nanocrystals, (b) TEM image of agglomerated FeSb₂ nanocrystals, (c) Selected Area Electron Diffraction (SAED) patterns, and (d) lattice fringe spacings (d) correspond to (111) planes.

XRD of polycrystalline FeSb₂ after consolidation of the nanocrystals via SPS indicates that the *Pnnm* structure is retained after densification. No other XRD detectable impurity phases were present in the nanocrystals and in the densified specimen. EDS confirmed the formation of stoichiometric FeSb₂. The Fig. 14b also shows a low resolution TEM image of agglomerated FeSb₂ nanocrystals. The nanocrystals were nearly homogeneous in size, at 40 nm, polygonal in shape and resembled bipyramidal forms. Orthorhombic crystal forms were preferred for the FeSb₂ nanocrystals presumably because no surfactant or template molecules were used in the reaction process to control the shape of the nanocrystals. Selected Area Electron Diffraction (SAED) patterns showed linear dot patterns (c), indicating that the FeSb₂ nanocrystal are single crystals. The SAED pattern also confirmed the d-spacings of the major diffraction planes of *Pnnm* FeSb₂ (not shown in the figure). The presence of twin diffraction spots in the SAED pattern (shown by arrows in c) are from lattice planes with the same diffraction angle, also indicated in Figure 135 a. Lattice fringe spacings (d) correspond to (111) planes.

Calorimetric Analysis

CuCoO₂ composites: Differential thermal analysis (DTA, TA Instruments, Q600) and thermogravimetric (TG) data for a CuCoO₂ specimen in the range of 200°C to 1000°C are shown in Figure 136. No thermal events are observed until 680°C, whereupon a prominent endothermic event commences. Two-step decomposition is thereafter observed, with an accompanying loss of weight presumably due to oxygen

loss. Powder XRD revealed the post DTA/TG products consist of a mixture of the binary oxides CoO and Cu₂O, the latter metal-rich oxide being consistent with the observed weight loss.

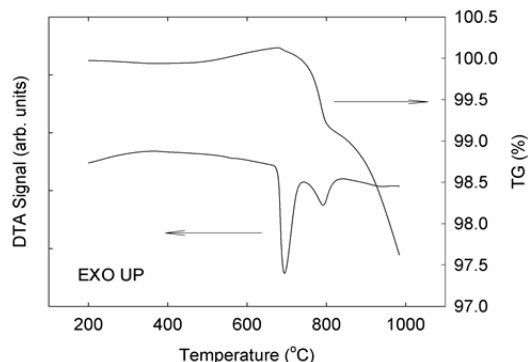


Figure 136: DTA and TG curves for a CuCoO₂ specimen heated at 20 °C/min under flowing N₂.

Bi & Bi-Sb nanocrystals and nanocomposites: In order to understand the thermal stability and melting points of the specimens, we performed DTA. DTA measurements were carried out with ~ 0.05 gm of Bi and Bi-Sb nanocrystals in alumina crucibles in a N₂ environment. The specimens were gradually heated to 350 °C at a heating rate of 5 °C min⁻¹ and a N₂ flow rate of 100 mL/min. Figure 62 shows the DTA spectra of the Bi and Bi-Sb specimens with melting points shown as the dips. The melting point of the Bi nanocrystals is 260 °C, which is 11.4 °C lower than the melting point of bulk Bi (271.4 °C) [200-203]. The lower melting point of Bi nanocrystals can be related to the size of the nanocrystals [200-205]. TEM analysis of our Bi specimens revealed the nanocrystals size of 35-40 nm.

The melting point for our Bi nanocrystals is in agreement with the melting point reported for ~ 30 nm Bi [201]. With increasing Sb concentration in the Bi-Sb alloy, the melting point shifted towards higher

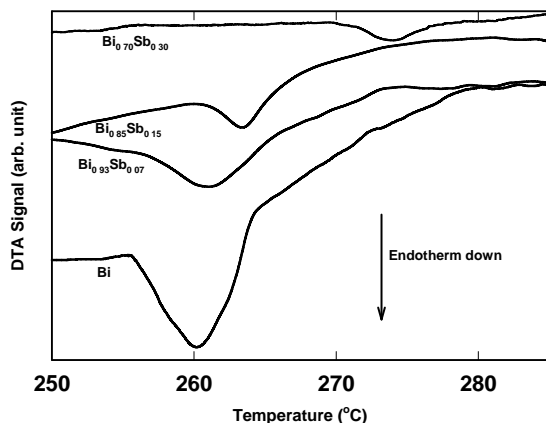


Figure 137: DTA spectra of Bi and different compositions of Bi-Sb alloys.

temperatures (Figure 137). The thermograms for Bi_{1-x}Sb_x were characterized by one endothermic peak with no other observed events. The shift in the melting point towards higher temperatures with increasing Sb concentration was also observed in bulk Bi-Sb semiconducting alloys and were within the range of 284 °C to 301 °C, depending on the alloy composition [204]. Our Bi_{1-x}Sb_x nanocrystals also showed a lowering in melting point compared to these bulk values. For these Bi_{1-x}Sb_x nanocrystal specimens, there was no observed secondary endotherm in the DTA spectra, suggesting these nanocrystals are stoichiometrically homogeneous.

7.4. Measurement of TE properties:

PbTe nanocomposites: The nanocomposites were cut into 2 x 2 x 5 mm³ parallelepipeds for transport property measurements. Four-probe ρ and S were measured from 12 to 300 K in a custom radiation-

shielded vacuum probe with maximum uncertainties of 4 %, and 6 %, respectively, at 300 K [205]. Temperature dependent four-probe Hall measurements were conducted from 5 to 300 K at both positive and negative magnetic fields of up to 5 T to eliminate voltage probe misalignment effects.

For all specimens, a linear and positive magnetic field dependence of the Hall resistance confirms dominant p-type conduction. The carrier concentrations increase upon Ag-doping by more than a factor of 5. Correspondingly, the ρ values, as shown in Figure 138, exhibit a significant reduction in magnitude compared to the undoped specimens. All specimens exhibit relatively large room temperature S values of approximately 325 $\mu\text{V/K}$ for the two undoped specimens and 200 $\mu\text{V/K}$ for the two Ag-doped specimens.

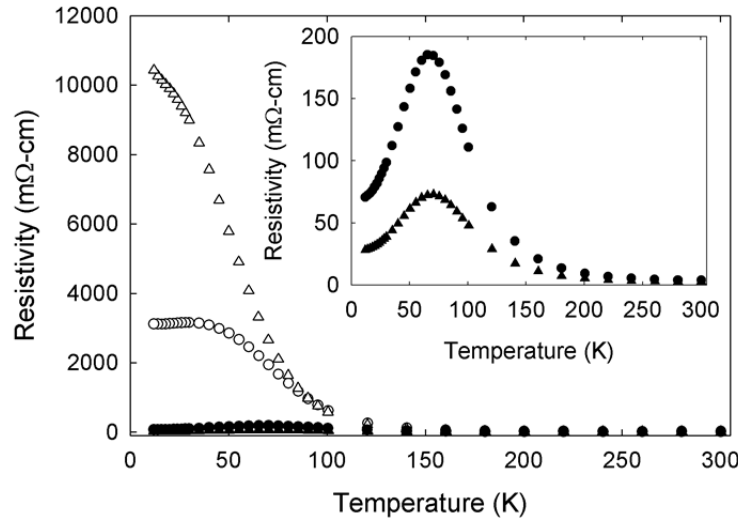


Figure 138: Temperature dependence of the resistivity for specimens I (○), II (△), III (●), and VI (▲).

The low temperature ρ values show activated temperature dependence ($d\rho/dT < 0$) in all specimens, and a nonlinear increase with decreasing temperature but with a sharp peak in ρ near 70 K for the Ag-doped specimens (Figure 138). Below 70 K the ρ values rapidly decrease with decreasing temperature. However, temperature dependent carrier concentration for all specimens indicates only a weak dependence with temperature. Lead chalcogenides exhibit large dielectric permittivity (ϵ) and small effective mass (m^*) that merge impurity levels with the allowed energy bands [206, 207]. The large ϵ results in low temperature impurity ionization, with energy $\propto m^*\epsilon^{-2}$ [208] and consequently, a carrier concentration independent of temperature where there is no degeneracy.

Figure 139 shows the temperature dependence of the mobility, μ , for the two Ag-doped specimens in comparison to the two undoped nanocomposites. While the room temperature mobilities are consistent with those reported in the literature, the temperature dependence differs significantly from single crystal and polycrystalline lead chalcogenides since the nanocomposite mobilities decrease with decreasing temperature, opposite to that of bulk materials reported in the literature [206-210]. In addition, the low temperature μ values for the Ag-doped specimens also show an order of magnitude increase as compared to the undoped specimens and exhibit a dramatic dip in μ (an approximately twenty-fold decrease) near 80 K, as compared to those values at the lowest temperature.

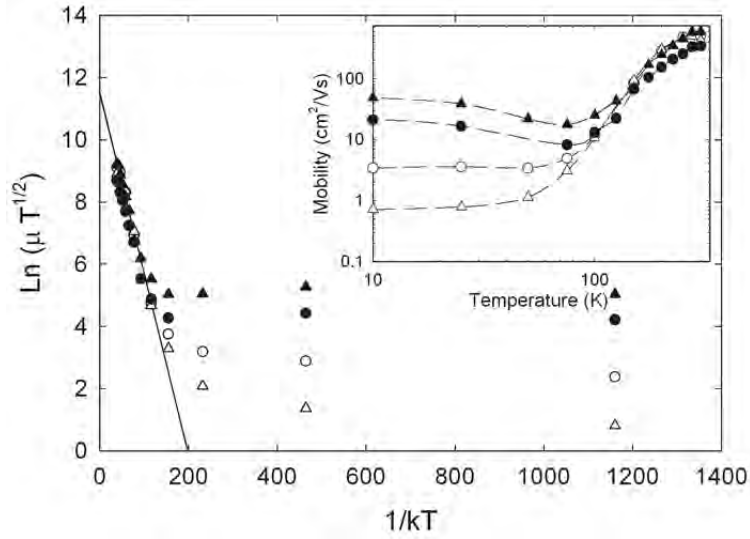


Figure 139: Temperature dependence of the mobility for specimens I (○), II (△), III (●), and VI (▲). Lines are a guide for the eye only. Plotting the logarithm of $\mu_{eff} = \mu_o(1/T)^{1/2} \exp(-E_B/kT)$ and fitting the high temperature data yields an energy barrier of 60 meV for all specimens.

The scattering mechanisms that dominate the transport in bulk lead chalcogenides do not fully describe the unique temperature dependence of μ in these nanocomposites, implying the presence of an additional scattering mechanism. In nondegenerate semiconductors the carriers are scattered by long-wavelength acoustic phonons, $\mu \propto m^{*-5/2} T^{-3/2}$ [206]. Since m^* is inversely proportional to temperature in lead chalcogenides, the mobility therefore varies with $T^{-5/2}$, as experimentally observed in single crystal and polycrystalline lead chalcogenides, with a weaker dependence in degenerate specimens [206,207]. This dependence is opposite of that observed in the PbTe nanocomposites, suggesting phonon scattering is present in combination with an additional mechanism.

Furthermore, the decreasing μ with decreasing temperature in these nanocomposites may suggest large impurity scattering of the carriers, where $\mu \propto T^{3/2}$. However, the high ϵ in PbTe implies suppression of long-range Coulomb potentials, limiting scattering to near the internal point of an impurity due to the large Bohr radius ($\propto m^{*-1}\epsilon$, on the order of the lattice constant) [211] and consequently, a small screening length. This indicates scattering by ionized impurities is not a dominant mechanism in this material, particularly at room temperature where the interaction time (the time required for the carrier to pass the region of one impurity ion) [212] is significantly shorter. Consequently, μ is not proportional to $T^{3/2}$ in these nanocomposites.

The nanocomposite carrier conduction can be effectively described as dominated by grain-boundary potential barrier scattering, in combination with phonon scattering. Similar models have successfully described the electrical properties of silicon, CdTe, and nanostructured metal oxide films [213-216]. Our previous work indicated oxygen adsorption in the PbTe nanocomposites. This surface reactivity is difficult to prevent, considering the aqueous nature of the synthesis technique [217]. The surface oxidation of PbTe is a sequential process, proceeding first through the formation of weak

peroxide-like structures (up to 70 % coverage) then by the chemisorption of oxygen [218]. Density Functional Theory (DFT) calculations of the surface reactivity of PbTe indicate these oxygen complexes form chemical bonds by transferring charge from the tellurium atoms. These chemical shifts were experimentally confirmed through X-ray Photoemission Spectroscopy (XPS). The chemisorption of oxygen essentially forms carrier trapping acceptor states by removing electrons from the grain surface, reducing itinerant carrier density. For nanocrystalline materials, this chemisorption results in increased trapping of carriers at grain boundaries, forming energy barriers that impede the conduction of carriers between grains. Assuming a uniformly distributed concentration of ionized carrier traps, N_t/cm^2 , a grain boundary thickness less than the crystallite size L , whose morphology and size distribution are identical, and ρ within the grains less than through the boundary, the effective mobility is given by [216]:

$$\mu_{\text{eff}} = Lq \left(\frac{1}{2\pi m^* kT} \right)^{1/2} \exp\left(-\frac{E_B}{kT}\right), \quad (7-1)$$

where q is the carrier charge, m^* the effective mass, k the Boltzmann constant, T the temperature, and E_B is the height of the energy barrier in the depletion region. A plot of the logarithm of μ with $1/kT$ for the PbTe nanocomposites indicates activated behavior from conduction through the boundary potential barrier between grains (Figure 139). Fitting the higher temperature data yields an energy barrier $E_B = 60$ meV for all specimens. This suggests the energy barriers form through a similar oxygen chemisorption mechanism in both the undoped and Ag-doped specimens. Conduction through ballistic transport occurs when the average energy of the charge carriers is sufficient to overcome this energy barrier. As the temperature increases, the average energy of the charge carriers increases and therefore the electrical conductivity increases $\propto T^{-1/2} \exp(-E_B/kT)$. This mechanism dominates at higher temperature and for higher carrier densities, where the concentration of carriers with larger average energy is larger. However, an additional conduction mechanism dominates at lower temperature. When the grain boundary energy barrier is sufficiently narrow and high, the charge carriers quantum mechanically tunnel through the barrier (thermionic field emission) [219]. In equilibrium, the dependence of barrier height E_B on the density of trapping states N_t and the carrier concentration p is given by [219]: $E_B = q^2 N_t^2 / 8\epsilon\epsilon_o p$, and the barrier width (space charge region) by: $W = (2\epsilon\epsilon_o E_B / q^2 p)^{1/2}$, where q is the carrier charge, $\epsilon = 414$ for PbTe at 300 K [220], and ϵ_o is the vacuum permittivity. As the carrier concentration increases with doping, the barrier height remains constant, but promotes an increase in trapping state density. Furthermore, as the carrier concentration increases, the barrier width decreases by a factor $\propto p^{-1/2}$. This suggests an increase in tunneling conduction (transmission probability) with doping.

The one-dimensional, time-independent WKB transmission probability τ for the potential barrier is given by [221]:

$$\tau(E) = \exp\left(-2 \int_{x_1}^{x_2} \{2m^* [qV(x) - E]\}^{1/2} dx / \hbar\right), \quad (7-2)$$

where x_1 and x_2 are the classical carrier turning points with energy E , m^* is the effective mass, and $qV(x)$ is the interfacial barrier energy. Therefore, the tunneling probability is a maximum for charge carriers with smaller m^* . The electrical transport in p-type PbTe is dominated by two bands: a lower mobility heavy hole (HH) valence band below the light hole (LH) valence band at low temperature, where $m_{\text{LH}}^* \sim 10 m_{\text{HH}}^*$ [222]. We assume similar m^* and band structure for the nanocomposites, as shown in Figure 140. At low temperature and higher hole densities, the electrical properties are dominated nearly exclusively by the LH carriers. As the temperature increases, the HH band rises, resulting in a decreasing τ and an increase in carrier scattering for the higher carrier density specimens. At higher temperature, when the average energy of the charge carriers is sufficient to overcome the grain boundary energy barrier, conduction is dominated through thermionic emission, $T^{1/2}\exp(-E_B/kT)$, and μ increases with temperature.

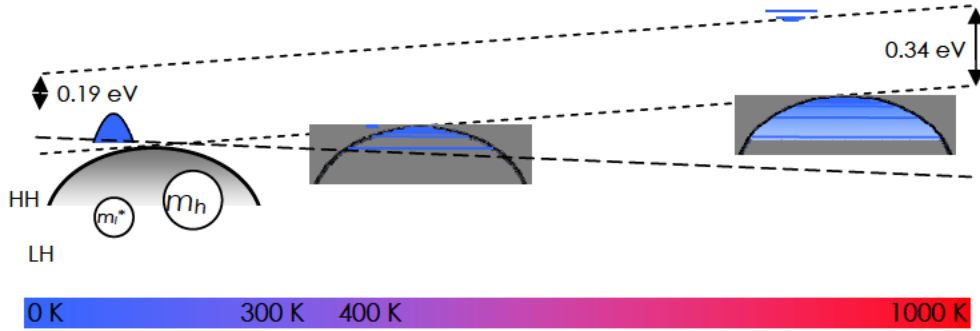


Figure 140: Temperature dependence of the conduction and valence bands of PbTe.

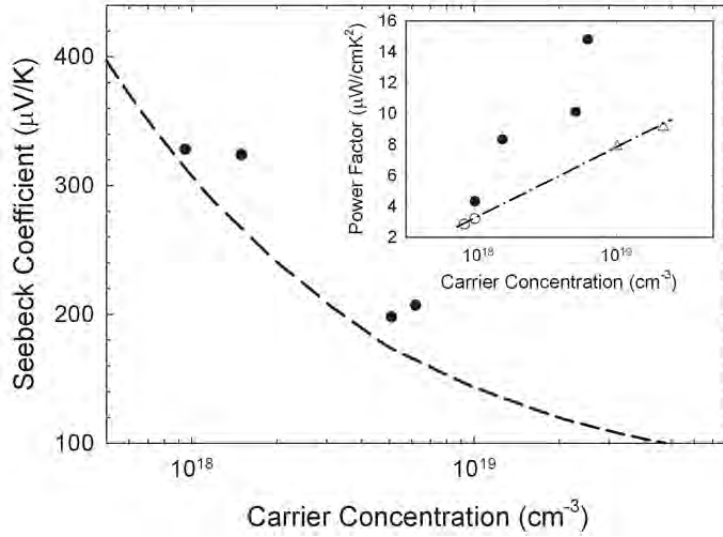
Grain-boundary potential barrier scattering of the carriers, in combination with phonon scattering, gives rise to the unique temperature dependence of the electrical conductivity and the mobility in these nanocomposites.

The effective crystallite size was estimated using Equation 7-1, the energy barriers obtained from fitting the temperature dependence of μ , the μ values calculated from the room temperature carrier concentration, and the HH $m^* = 1.5m_0$. These estimates indicate effective crystallite sizes between 300 and 400 nm and are consistent with the dimensional nanocomposite structure observed in our SEM analyses. This suggests the grain boundary energy barrier scattering is dominated through these nanoscale features. We note that inclusion of LH carriers in the calculation would only slightly lower the effective crystallite size.

Furthermore, conduction through the boundary potential barrier between grains essentially filters lower energy charge carriers, increasing the average carrier energy and consequently, $|S|$. Figure 141 shows the room temperature S for the PbTe nanocomposites in comparison to theoretically calculated

bulk value, indicating an enhancement in S as compared to bulk PbTe at the same carrier concentration. In addition, we compare the room temperature S^2/ρ for the nanocomposites to two of our undoped and two Na-doped bulk PbTe specimens, indicating an enhancement in S^2/ρ over that of bulk PbTe (inset in Figure 141). The larger S^2/ρ in the nanocomposites as compared to bulk polycrystalline materials, in addition to similar thermal conductivities, results in enhanced room temperature ZT as compare to bulk PbTe. This suggests interfacial energy barrier carrier filtering may be an effective method of thermoelectric performance enhancement in these bulk nanocomposites. Similar carrier filtering enhancements to S were observed in InGaAs/InGaAlAs heterostructures [223].

Transport properties measurements of Bi-doped PbTe nanocomposites are shown in Figure 142.



The specimens showed an increasing electrical conductivity with doping. From Figure 142a and b, the temperature dependence of resistivity, ρ , indicates $\Delta\rho/\Delta T > 0$ above 150K, indicating metallic conduction above ~ 150 K, while $\Delta\rho/\Delta T < 0$ below 150K.

Figure 141: Temperature dependent Seebeck coefficient for representative undoped and Bi doped PbTe nanocomposites. The nominal Bi doping concentrations are indicated.

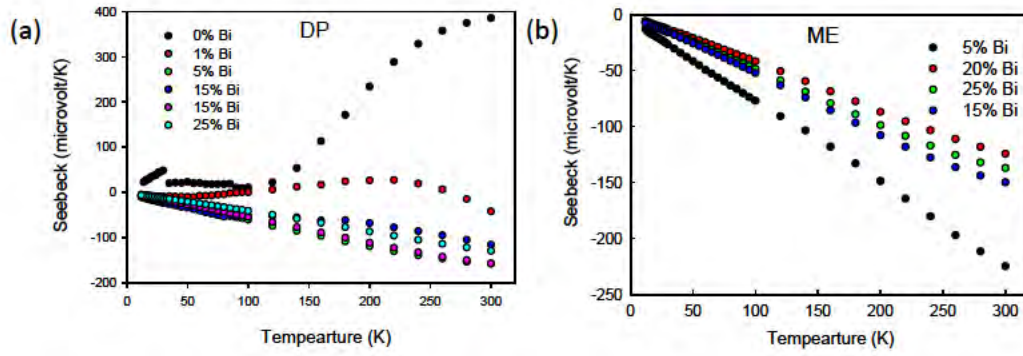


Figure 142: Seebeck coefficient as a function of carrier concentration for the four PbTe nanocomposites (●) and the calculated bulk relationship (dashed line) from Ref. 53. Inset: Power Factor as a function of carrier concentration for the four PbTe nanocomposites in comparison to bulk undoped PbTe (○) and Na-doped PbTe (△). The straight line is a guide for the eye only.

With increasing Bi doping, a systematic decrease in room temperature resistivity values were observed, presumably indicating higher electron concentrations with Bi doping. Figure 143 a and b shows the Seebeck coefficient, S , as a function of temperature for the Bi-doped PbTe specimens. The undoped PbTe nanocomposite shows positive S values, whereas the Bi doped specimens show $S < 0$ suggesting an excess of electron carriers in the doped nanocomposites. For the 1% Bi doped PbTe nanocomposite, conduction from holes and electrons may be present as can be assumed from the change in sign and slope

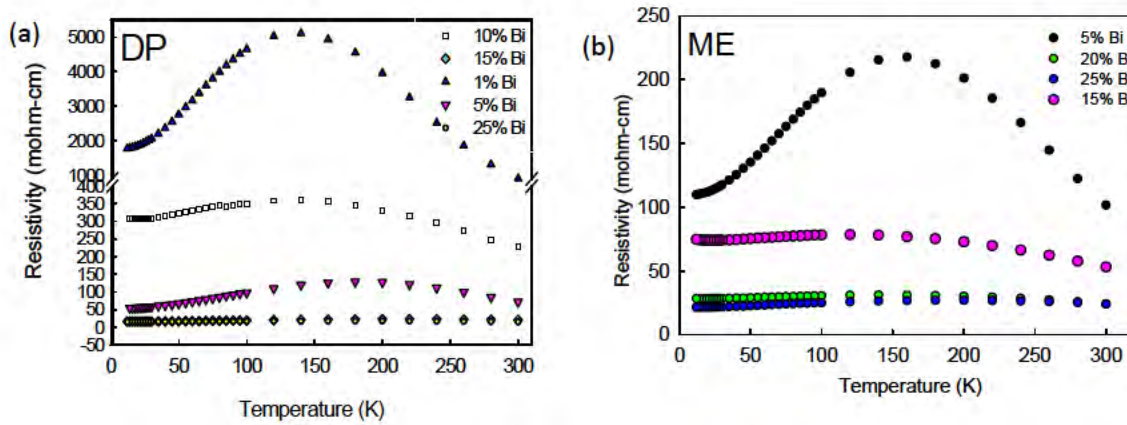


Figure 143: Temperature dependent resistivity for representative undoped and Bi doped PbTe nanocomposites. The nominal Bi doping concentrations are indicated.

of S , in addition to the high ρ values. However, for higher concentrations of Bi, the PbTe nanocomposites show larger absolute S values and lower ρ , indicating an increased electron concentration. Hall measurements will reveal the doping in these specimens [224].

All the Bi-doped PbTe nanocomposites possessed relatively low thermal conductivity, κ , as shown in Figure 144 a and 144b. The temperature dependence of κ for all specimens is similar to that of bulk polycrystalline PbTe with a maxima occurring between 20 K and 30 K.

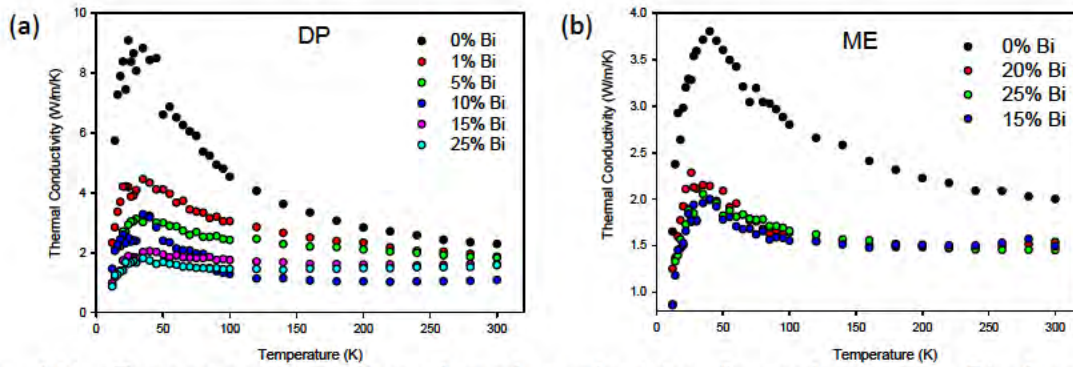


Figure 144: Temperature dependent thermal conductivity for undoped and Bi doped PbTe nanocomposites. The nominal Bi doping concentrations are indicated.

Bi & Bi-Sb nanocomposites: Bulk polycrystalline specimens were cut into 2 mm x 2mm x 5mm parallelepipeds for low temperature transport measurements. Four-probe ρ , steady-state S and κ (gradient sweep method) measurements on 2x2x5 mm³ parallelepipeds from 12 K to 300 K were conducted in a custom radiation-shielded vacuum probe with uncertainties of 4 %, 6 %, and 8 %, respectively. Figure 145 a– c show the low temperature ρ , absolute S ($|S|$), and κ properties, respectively for Bi-I, Bi-II, and Bi-III nanostructured bulk. The results are also compared to the bulk polycrystalline specimens [225], and single crystal data both perpendicular and parallel to the trigonal axis.

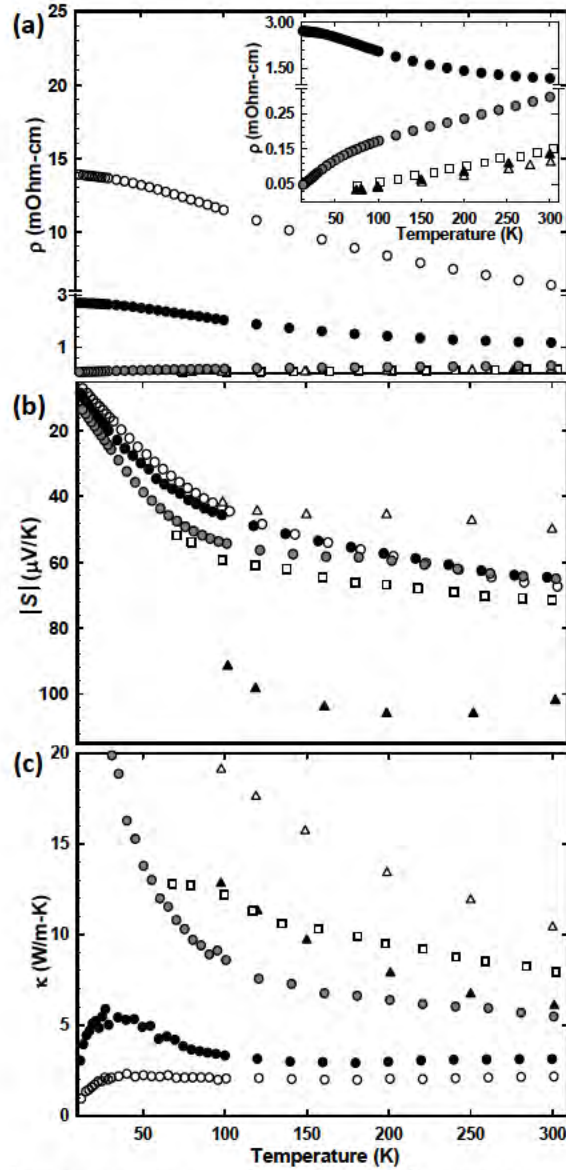


Figure 145: (a)–(c) are the low temperature ρ , S , and κ of Bi nanocomposites with 78 % (\circ), 85% (\bullet) and 92% (\circ) relative theoretical densities. The data is shown in comparison to the low temperature transport properties reported for bulk Bi single crystals (Δ = perpendicular to trigonal axis [226], \blacktriangle = parallel to trigonal axis [226]) and Bi polycrystals (\square) [225].

As Bi is anisotropic in crystal structure (crystallizes in rhombohedral symmetry) distinct orientation dependent low temperature transport properties are observed in Bi single crystals. However, in the Bi nanostructured bulk specimens the orientation of the grains are random and the transport properties may be an average effect of the transport properties in all directions.

The Bi-I and Bi-II specimens show an increase in ρ with decreasing temperature, atypical of metals (Figure 145 a). However, in the case of Bi-III, ρ decreases with decreasing temperature. The inset Figure 145a shows the temperature dependencies of ρ for the Bi-II and Bi-III specimens in comparison to that of bulk specimens. The ρ values for the nanocomposites are several times higher than that in the bulk specimens. However, for the least porous specimen, Bi-III specimen, the ρ values decreased (inset of Figure 145 a). The anomalous temperature dependence in Bi-I and Bi-II specimens may be related to the presence of large percentages of porosity. It may also be related to the presence of Bi_2O_3 impurity phase. Low temperature S values were comparable to that of the bulk (Figure 145). Due to the nanostructuring in the Bi our polycrystalline bulk specimens, the κ values are lower than that of single crystals and bulk specimens. It is clear that the transport properties of Bi the nanocomposite specimens are greatly affected by the presence of porosity in the specimens. Our preliminary study on Bi nanostructured bulk specimens with different densities is a step forward to get a fundamental understanding on the processing dependencies of TE properties in state-of-the-art TE materials. We emphasize that the TE properties may be controlled in some material systems by adjusting the densification parameters, as has been shown here.

$\text{Bi}_2\text{Se}_x\text{Te}_{3-x}$ and $\text{Sb}_2\text{Se}_x\text{Te}_{3-x}$ Nanocomposites: The room temperature carrier concentration, n , for the dense (>95 %) bulk Bi_2Te_3 is relatively high ($n = 4.8 \times 10^{19} \text{ cm}^{-3}$ for Bi_2Te_3 sample 1) and increases with increasing Se doping ($n = 6.6 \times 10^{19} \text{ cm}^{-3}$ for BT-1 and $n = 8.8 \times 10^{19} \text{ cm}^{-3}$ for BT-2 Bi_2Te_3 sample 2). Four-probe resistivity, ρ , steady-state Seebeck Coefficient (gradient sweep method), S , and thermal conductivity, κ , measurements on 2 mm x 2 mm x 5 mm parallelepipeds from 12 K to 300 K were conducted in a custom radiation-shielded vacuum probe,⁴⁴ with uncertainties of 4 %, 6 %, and 8 %, respectively, and are shown in Figure 146 a-c. The room temperature variation of $|S|$ with n is shown in the inset of Figure 146 a. The solid line represents the theoretical bulk relation, assuming a single parabolic band model with ionic impurity scattering⁴⁵ as the dominant scattering mechanism at room temperature and considering the integral density of states effective mass $m_d^* = 0.27m_e$, where m_e is the mass of an electron. This plot indicates an enhancement in $|S|$ for the doped polycrystalline bulk nanocomposites over theoretical predictions [227] and bulk polycrystalline specimens [228, 229]. As shown in Figure 146 a, ρ decreases with increasing Se doping, as expected. The κ measurements show a decrease with Se doping, presumably due to alloy scattering at the Te site (Figure 146 b). The maximum in κ is lower for $\text{Bi}_2\text{Te}_{3-y}\text{Se}_y$ as compared to Bi_2Te_3 and is indicative of such alloy scattering. The above TE properties were independent of the direction (parallel and perpendicular to the SPS pressing direction) of measurement. This is due to the random orientation of the grains within the densified specimens.

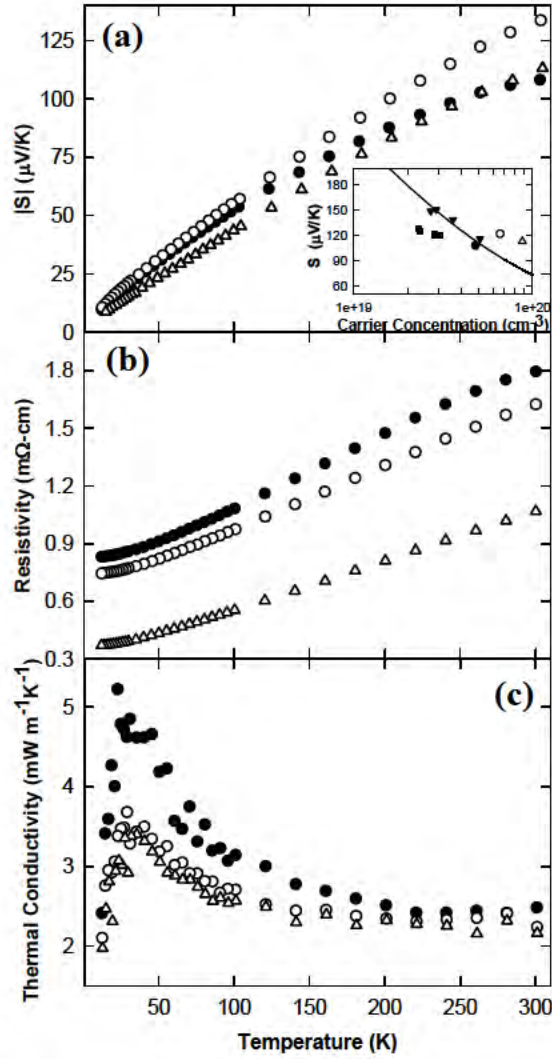


Figure 146. (a) Absolute Seebeck Coefficient, $|S|$, (b) resistivity, ρ , and (c) total thermal conductivity, κ , as a function of temperature for undoped (BT, ●) and Se doped (BT-1, ○; BT-2, △) polycrystalline Bi₂Te₃ nanocomposites. Room temperature $|S|$ versus n for the three specimens in comparison to bulk polycrystalline Bi₂Te₃ (▼ Kim *et al.*⁵⁷; ■ Zhao *et al.*⁵⁸) is shown in the inset of (a). The solid line represents the theoretical bulk relation, as described in the text.

CuCoO₂ composites: Consolidation of CuCoO₂ powders was accomplished at 600°C with an applied pressure of 45 MPa and resulted in a compact that was 72 % of the calculated density from XRD. Electrical resistivity measurements were performed on a parallelepiped specimen cut from the SPS consolidated compact and are shown in Figure 147. The data show an activated temperature dependence with $\rho(300 \text{ K}) \sim 5 \text{ Ohm-m}$. An Arrhenius plot (inset to Figure 147) and corresponding fit indicate a temperature dependence of $\rho(T) \sim \exp(E_a/k_B T)$, where k_B is Boltzmann's constant and E_a is an activation energy for conduction. From the fit, we obtain $E_a = 0.195 \text{ eV}$, which is close to the value 0.2 eV previously reported for conductivity measurements perpendicular to the c -axis on a small single crystal CuCoO₂ platelet. If the data in Figure 147 represent intrinsic conduction (and assuming temperature independent carrier mobility), this would imply a band gap $E_g = 2E_a = 0.39 \text{ eV}$, quite close to the value 0.38 eV predicted [230] from DFT calculations.

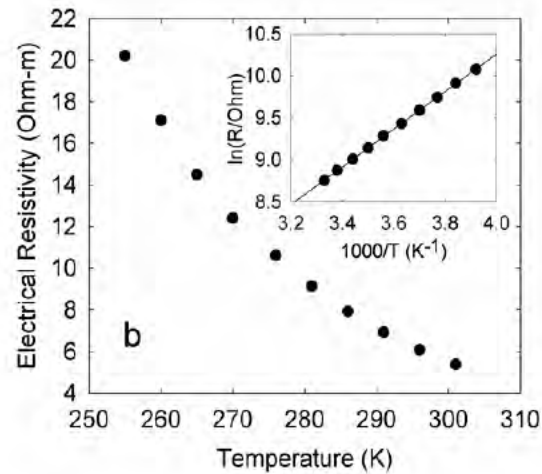


Figure 147: Electrical resistivity data for CuCoO₂ indicating an activated temperature dependence. Inset: Arrhenius plot showing a fit to the data of the form $\rho(T) \sim \exp(E_a/k_B T)$.

FeSb₂ nanocomposites: SPS densification (Thermal Technology LLC, 25-10) of the FeSb₂ nanocrystals was carried out at 100 MPa and 210 °C for 5 min. A density of 88 % of the theoretical density was achieved after densification. After SPS the grain size was in the range of 40 nm – 200 nm. In order to compare the TE properties of the polycrystalline FeSb₂ with nano-scale grains, henceforth referred to as a dimensional nanocomposite, a polycrystalline *Pnnm* FeSb₂ bulk specimen of comparable density was prepared by reacting the elements to form FeSb₂ [231-232] followed by hot pressing at 320 °C and 150 Mpa for 2 h.

Four-probe ρ , and steady-state S (gradient sweep method) and κ measurements between 12 K and 300 K were conducted on 2 mm x2 mm x5 mm parallelepipeds in a custom radiation-shielded vacuum probe, with uncertainties of 4 %, 6 %, and 8 %, respectively at 300 K. Room temperature four-probe Hall measurements were conducted on 0.5 mm x2 mm x5 mm parallelepipeds at multiple positive and negative magnetic fields up to 1 T to eliminate voltage probe misalignment effects using a custom built Hall measurement system with an uncertainty of 4 %. In FeSb₂ the thermoelectric figure of merit (ZT) is degraded due to a large κ that is dominated by κ_L [233-240]. We estimated κ_L by calculating the electronic contribution to the thermal conductivity (κ_e) using the Wiedemann-Franz relation $\kappa_e = L_0 T / \rho$, where $L_0 = 2.44 \times 10^{-8} \text{ V}^2/\text{K}^2$ and ρ was measured as described above, and subtracting it from the measured κ ($\kappa_L = \kappa - \kappa_e$). Figure 148 shows the temperature dependence of κ_L for the two FeSb₂ specimens. The κ_L values for our bulk polycrystalline FeSb₂ are lower than that for single-crystal FeSb₂ due to the relatively small grain size (with a grain size distribution of < 1 μm to 10 μm) as well as the porosity of the specimen, however it exhibits a $1/T$ temperature dependence (Figure 148) typical of crystalline semiconductors dominated by phonon-phonon scattering. The FeSb₂ nanocomposite has smaller κ_L values as compared to the bulk polycrystalline specimen with a very weak temperature dependence above 30 K. The nano-scale grains in the FeSb₂ nanocomposite (inset to Figure 148) results in this reduction in κ_L , with nearly an order-of-magnitude reduction in κ_L at low temperatures. From $\kappa_L = 1/3 C v_s l_p$, where v_s is the sound velocity (3116 ms^{-1}) and C is the specific heat, we estimate the room temperature phonon mean-free path, l_p , in our bulk polycrystalline FeSb₂ to be 0.5 μm . This estimated l_p value is much larger than the average grain size of the FeSb₂ nanocomposite and is an indication of the effect of grain-boundary scattering. This effect is significant at lower temperatures.

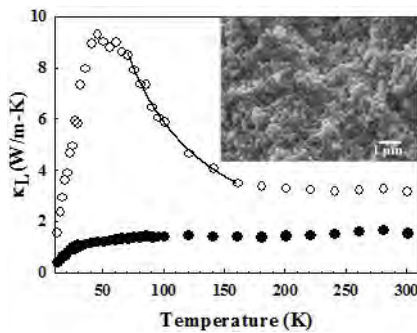


Figure 148: κ_L of the FeSb₂ nanocomposite (solid circle) and bulk FeSb₂ (open circle). The line $1/T$ dependence (solid line) is indicative of phonon-phonon scattering. The inset shows a SEM image of a fractured surface of the FeSb₂ nanocomposite.

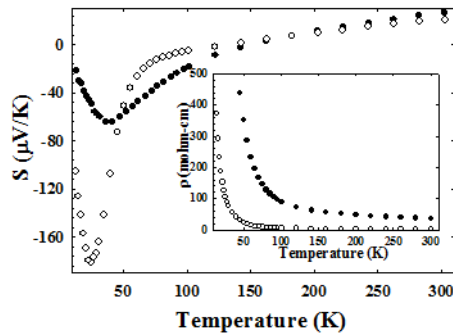


Figure 149: Temperature dependence of S and ρ (inset) for the FeSb₂ nanocomposite (solid circle) and bulk FeSb₂ (open circle).

Figure 149 shows the temperature dependent S for the two specimens. Both have positive S values at room temperature, 26.1 $\mu\text{V/K}$ and 20.6 $\mu\text{V/K}$ for the nanocomposite and bulk FeSb₂, respectively. These values are in general agreement with those previously reported on polycrystalline FeSb₂ specimens. The temperature

dependence of S for both specimens is similar, with a maximum (S_{\max}) of $-64 \mu\text{V/K}$ at 35 K for the nanocomposite and $S_{\max} = -181 \mu\text{V/K}$ at 25 K for our bulk specimen. The shift to higher temperature as well as the smaller absolute S_{\max} value for the nanocomposite may be attributed to the large carrier concentration ($3.2 \times 10^{20} \text{ cm}^{-3}$ at 300 K) and very low mobility ($0.54 \text{ V cm}^2 \text{ V}^{-1} \text{ s}^{-1}$ at 300 K) in the nanocomposite compared to the FeSb_2 single crystals where a mobility as high as $\sim 10^5 \text{ V cm}^2 \text{ V}^{-1} \text{ s}^{-1}$ was observed. [241] Studies on oriented FeSb_2 thin films revealed similar suppression of S_{\max} due to low mobility of charge carriers. It was also observed previously that the position and magnitude of S_{\max} is very sensitive to doping and charge carrier concentration for FeSb_2 single crystals as well as for FeSi . [242]. In addition, charge carrier scattering due to an increased number of grain boundaries in the FeSb_2 nanocomposite may play a role in reducing the potential across the grains, thereby reducing the absolute value of S_{\max} . The temperature dependence of ρ is shown in the inset of Figure 149. In both specimens ρ increases with decreasing temperature, a temperature dependence that is similar to that observed previously. Although porosity will greatly affect ρ , the difference in ρ for the two specimens is also ascribed to the large difference in average grain size between the two specimens.

7.5. Comparative studies and analysis: Synthesis bulk materials for comparison to the nano-scale TE materials:

Comparative studies of specific nanocomposites with bulk materials were carried out according to the proposed plan both experimentally and theoretically. Experimental comparison has been covered in the earlier section under “Measurement of TE properties”. In this task we will discuss the analysis of experimental data by theoretical modelling. Comparison with bulk data is also a part of this study and had been realized in the proposed time-line.

Ag- and Na-doped PbTe nanocomposites:

Theoretical Model

The proposed model for the description of the electronic transport characteristics is based on the well known expressions for σ and S defined as follows [243]:

$$\sigma = \frac{2e^2}{3m^*} \int_0^\infty \tau(E) g(E) E \left(-\frac{\partial f(E)}{\partial E} \right) dE, \quad (7-3)$$

$$S = \frac{1}{eT} \left[\frac{\int_0^\infty \tau(E) g(E) E^2 \left(-\frac{\partial f(E)}{\partial E} \right) dE}{\int_0^\infty \tau(E) g(E) E \left(-\frac{\partial f(E)}{\partial E} \right) dE} - \mu \right] \quad (7-4)$$

where e is the electron charge, m^* is the effective mass, μ is the chemical potential for the specific material, $\tau(E)$ is the momentum relaxation time for the charge carriers, $g(E)$ is the total density of states (DOS) for the material, $f(E) = 1/(e^{(E-E_F)/k_B T} + 1)$ is the Fermi distribution function with E_F being the Fermi level, and k_B is the Boltzmann constant. $\tau(E)$, $g(E)$, and $f(E)$ are energy-dependent functions but they also depend on other physical characteristics as defined for a specific material. Below we consider each of these functions individually and explain the relevant assumptions we make in our model.

Density of states

For PbTe the energy bands responsible for the transport are not parabolic. Their Fermi surfaces are ellipsoids of revolution. Using the two band Kane model, the energy dispersion is given as

$$\frac{\hbar^2 k_l^2}{2m_l^*} + \frac{\hbar^2 k_t^2}{2m_t^*} = E + \alpha E^2 \quad (7-5)$$

where $k_{l,t}$ is the carrier momentum, $m_{l,t}^*$ is the effective mass along the longitudinal and transverse directions at the valence band minimum, respectively, and α is a non-parabolicity factor. For small band gap semiconductors, such as PbTe, $\alpha = 1/E_g$ where E_g is the energy gap. After defining an effective mass for both directions as $m^* = \beta^{2/3}(m_l^* m_t^{*2})^{1/3}$ (where β is the degeneracy of the Fermi surfaces containing more than one pocket), the total Density of States (DOS) for PbTe can be written as

$$g(E) = \frac{\sqrt{2}}{\pi^2} \left(\frac{m^*}{\hbar^2} \right)^{3/2} \sqrt{E(1 + E/E_g)(1 + 2E/E_g)}, \quad (7-6)$$

$$E_g = E_g^0 + \gamma T \quad (7-7)$$

Here the variation of E_g as a function of temperature is also taken into account – $E_g^0 = 0.19\text{eV}$ is the PbTe band gap at $T = 0\text{K}$ and $\gamma \approx 0.0004\text{eV/K}$ is a phenomenological parameter for PbTe [244, 245].

Fermi distribution function

We further consider the Fermi distribution function. Although the expression is known, the Fermi distribution function contains an important parameter, the Fermi level E_F . E_F is specific for each material and is also related to the charge carrier concentration, p , via the expression [246]

$$p = \frac{4}{\sqrt{\pi}} \left(\frac{2\pi m^* k_B T}{h^2} \right)^{3/2} \int_0^\infty E^{1/2} f(E) dE \quad (7-8)$$

where h is the Planck's constant. The self-consistent solution of the above equation allows one to determine the Fermi level E_F for a specific p .

Scattering mechanisms

Finally, we consider the momentum relaxation time, $\tau(E)$, with contributions from different scattering mechanisms. Here it is assumed that each scattering mechanism can be associated with a resistivity. Then the total relaxation time is obtained according to the Mathiessen's rule:

$$\frac{1}{\tau(E)} = \sum_i \frac{1}{\tau_i(E)} \quad (7-9)$$

where $\tau_i(E)$ is the relaxation time for each contributing mechanism. For thermoelectric bulk materials, the carrier scattering may be due to acoustic phonons, non-polar optical phonons, or ionized impurities. For TE composites containing nanostructured grains, an additional scattering mechanism from the grain interfaces is also important.

In this model, the nanocomposite specimen is assumed to have grain regions with the same average characteristics. The grain interfaces in the material are modeled as rectangular potential barriers with an average height E_b , size L , and width w , as shown in [Figure 150](#). The average values of E_b , L , and w can

be inferred from experimental measurements [247,248]. The physical explanation of the role of each boundary is that each grain boundary creates an interface density of traps Q_t [249], which is assumed to be electrically neutral until carriers are trapped, thus creating a potential barrier with height E_b . The barrier height depends on L and p as $E_b = e^2 Q_t^2 / 8\epsilon p$ where ϵ is the dielectric constant of the material. Also, if one considers that the barrier is formed by the complete filling of the traps, $w = Q_t / p$.

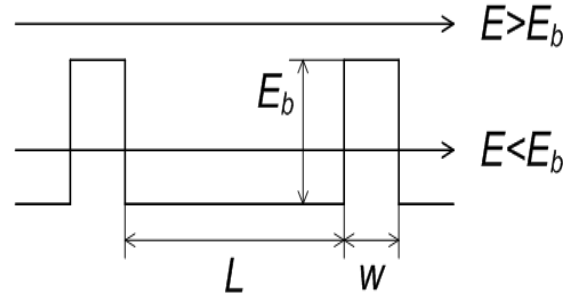


Figure 150: Schematic drawing of a grain region limited by rectangular potential barriers. The height of the barrier is E_b , the width w and the grain size L . The carrier energy is E .

As charge carriers diffuse through the sample, they can be reflected with a reflection coefficient, R , or transmitted with a transmission coefficient, T , quantum mechanically. The relaxation time due to

this mechanism is then determined by the carrier mean free path, λ , and average velocity, v , of the carriers as follows:

$$\tau_b(E) = \frac{\lambda}{v}, \quad (7-10)$$

$$\lambda = \frac{L}{1-T}, \quad v = \sqrt{\frac{2E}{m^*}} \quad (7-11)$$

where λ is assumed to be limited by scatterings from two neighboring barriers according to $\lambda = \frac{L}{1-T}$.

Using the quantum mechanical expression for T [250], the relaxation time is:

$$\tau_b(E) = \begin{cases} L\sqrt{\frac{m^*}{2E}} \left[1 + \frac{4\frac{E}{E_b} \left(1 - \frac{E}{E_b}\right)}{\sinh^2 \left[\sqrt{\frac{2m^*E_b w^2}{\hbar^2} \left(1 - \frac{E}{E_b}\right)} \right]} \right], & E < E_b \\ L\sqrt{\frac{m^*}{2E}} \left[1 + \frac{4\frac{E}{E_b} \left(\frac{E}{E_b} - 1\right)}{\sin^2 \left[\sqrt{\frac{2m^*E_b w^2}{\hbar^2} \left(\frac{E}{E_b} - 1\right)} \right]} \right], & E > E_b \end{cases} \quad (7-12)$$

The relaxation times due to the other mechanisms can be expressed as:

$$\tau(E) = aE^s \quad (7-13)$$

where $s = -\frac{1}{2}, \frac{1}{2}, \frac{3}{4}$ for carrier scattering by acoustic phonons, non-polar optical phonons, and ionized impurities. The parameter a is temperature dependent. We use the expression for a for scattering by phonons. Since the impurity scattering contribution is much less significant for the experiments reported here, we do not consider it further. However, one can readily include this mechanism in the model using the relevant formulas in [251]. Thus

$$a_{a-ph} = \frac{h^4}{8\pi^3} \frac{\rho v_L^2}{k_B T} \frac{1}{(2m^*)^{3/2} D^2},$$

$$a_{o-ph} = \frac{h^2}{2^{1/2} m^{*1/2} e^2 k_B T (\epsilon_\infty^{-1} - \epsilon_0^{-1})} \quad (7-14)$$

where a_{a-ph} and a_{o-ph} are the constants for the acoustic and non-polar optical phonons, respectively, ρ is the mass density, v_L is the longitudinal velocity of sound, D is the deformation potential constant, ϵ_∞ is the high frequency dielectric constant, and ϵ_0 is the static dielectric constant. All of these variables can be taken from the available data in the literature or estimated experimentally for a particular specimen. The value for D is usually adjusted when phenomenological models are used to explain experimental measurements. However, D can also be estimated independently by measuring the changes in the material's E_g as a function of pressure and temperature [252].

Theoretical Results

The model described in the previous section provides all the necessary tools to calculate and explain the experimental data for σ and S for any small band gap TE material containing granular interfaces. The physical parameters and constants can be taken from available experimental data for a specific material or they can be measured independently for a particular specimen. The model can also be used to make predictions by varying one or several parameters characterizing the grain inclusions. Experiments involving such manipulations can be time consuming and expensive, thus this model can be used to steer and complement the experiments. Furthermore, it can be easily adapted to include additional features in the DOS (for example, a three band Kane model), additional scattering mechanisms, and two or one-dimensional transport.

Here we demonstrate that our model can be used to effectively describe experimental data for PbTe nanocomposite material. The model is tested by comparing to low temperature transport measurements for Ag-doped PbTe nanocomposites, synthesized and characterized as described above.

The experimental results for the carrier conductivity for two Ag-doped specimens with carrier concentration $p = 6.1 \times 10^{18} \text{ cm}^{-3}$ and $p = 5.9 \times 10^{18} \text{ cm}^{-3}$ are shown in Figure 151 a. In Figure 151 b, the experimental data S are also given. In addition, σ and S are calculated and shown in Fig. 151a and 151b, respectively. In our calculations, we used the barrier parameters estimated from the reported experimental data described above, $E_b = 60 \text{ meV}$, $w = 50 \text{ nm}$, and $L = 300 \text{ nm}$. The rest of the parameters are taken as follows. The other parameters used are $m^* = 0.16m_0$, where m_0 is the electron mass, $\rho = 8160 \text{ kg/m}^3$, $v_L = 1730 \text{ m/s}$, and $\epsilon_\infty^{-1} - \epsilon_0^{-1} = 0.0072 \times E_g$ [252]. The value for D is varied in the range 5 – 15 eV range, as is usually done when phenomenological models are used to compare with experimental data. As shown in Figure 151, there is excellent agreement between the experimental results for the PbTe specimens and the model calculations in all temperature regions.

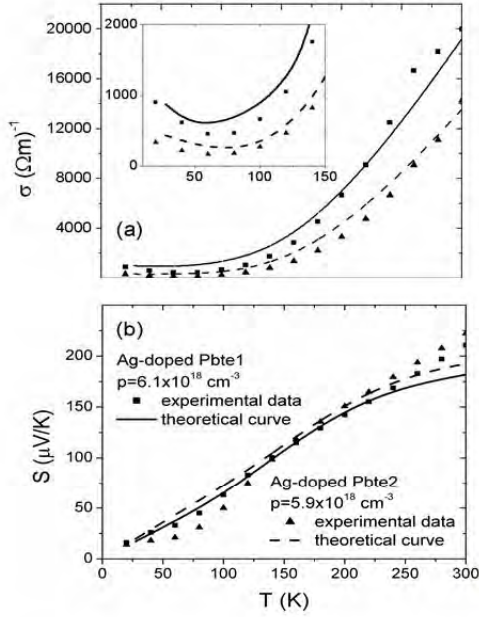


Figure 151: Calculated and experimentally measured (a) electrical conductivity σ , and (b) Seebeck coefficient S as a function of the absolute temperature T for two values of the carrier concentrations.

Another feature that one finds using this model is that the location of the σ minimum shifts toward larger T as p increases. We explain this by noting that at higher concentrations and temperatures, more carriers are excited above the barrier height, and the transmission probability through the barrier also increases. Thus σ increases for larger temperatures. At lower temperatures, the majority of the charge carriers have energies less than the barrier height; therefore the conductivity can increase as there are more carriers available for tunneling. As a result of the interplay between these two relevant scattering mechanisms, σ exhibits a minimum at an intermediate temperature.

The model is further used to understand the importance of the different material characteristics that affect the transport properties. We investigate the role of carrier concentration on σ and S by changing p , and keeping all other parameters the same. The potential boundary characteristics are taken to be $E_b = 0.1 \text{ eV}$, $w = 50 \text{ nm}$, and $L = 300 \text{ nm}$, and the calculated results are shown in Figure 152 a and b. The figures show that σ and S increase as a function of temperature. However, σ is larger for p due to the increased number of carriers, while S is larger for smaller p due to the higher mean energy per carrier.

The low temperature behavior of σ is similar to that of the experimental specimens, as shown in the inset in Figure 151. As shown in Figure 151 a, σ shows a minimum at $T \sim 70 \text{ K}$ for higher carrier concentrations.

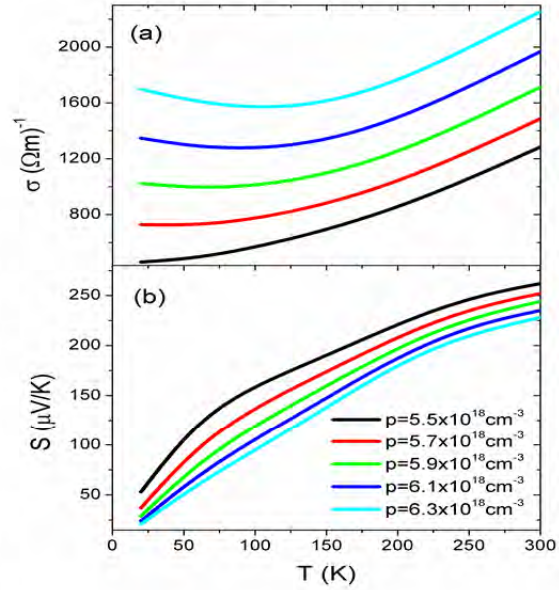


Figure 152: (a) Electrical conductivity, σ , and (b) Seebeck coefficient, S , as a function of the absolute temperature T for different values of the carrier concentrations.

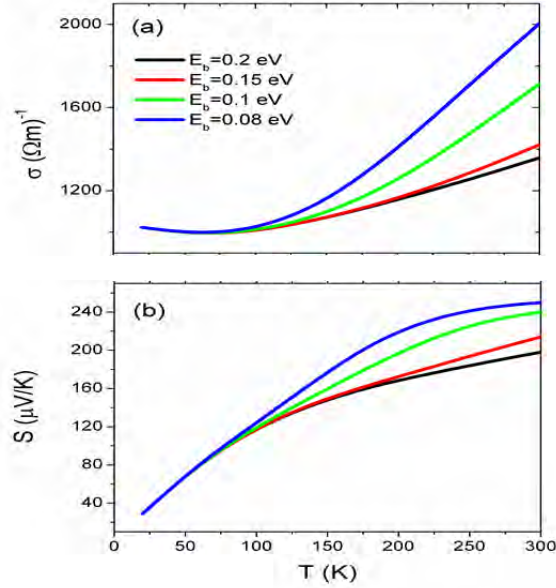


Figure 153: (a) Electrical conductivity, σ , and (b) Seebeck coefficient, S , as a function of the absolute temperature T for different values of the potential barrier height.

The model can also be used to determine how other parameters, related to the grain boundary specifications, affect the transport characteristics. One can calculate σ and S as a function of temperature for various barrier heights, barrier widths, and distances between the barriers. In Figure 153, we show the calculated results for σ and S as a function of temperature for several values of the barrier height, while fixing the other barrier parameters to $w = 50nm$ and $L = 300nm$. The results from the model allows one to conclude that as E_b increases less carriers contribute to the transport in the specimen, thus leading to smaller σ , and larger S due to the larger mean energy per carrier.

We can achieve the same physical behavior by manipulating w or L . For example, increasing w results in a decrease in σ and an increase in S due to the smaller quantum

mechanical transmission probability of the carriers through the barrier. Furthermore, decreasing L results in a decrease in σ and an increase in S due to more frequent carrier scattering from the barriers. The dependence of σ and S for various w and L show similar behavior as that described above.

In our phenomenological model several parameters characterizing the potential grain barriers can be adjusted in order to achieve a certain trend in the functional dependence of the carrier transport characteristics as a function of temperature. For thermoelectric applications, however, one is interested in increasing $S^2\sigma$. Thus the optimal E_b , w , and/or L are needed to optimize σ and S in order to achieve the highest performing TE materials. We therefore calculated $S^2\sigma$ in order to show how $S^2\sigma$ varies as a function of E_b , w , and L at a specific temperature. Our results are shown in Figure 154. All parameter dependences show a maximum in $S^2\sigma$ vs. T , indicating the optimal parameters necessary in achieving the highest ZT values. It appears the highest $S^2\sigma$ for PbTe nanocomposites for the studied concentrations (shown in Figure 154) can be achieved with $w \sim 50 nm$, $L \sim 300 nm$ and $E_b \sim 0.05 eV$. We note that the existence of a maximum in $S^2\sigma$ is a consequence of the interplay between tunneling, reflectance, scattering from the barriers, and phonon scattering. In addition, the model described here, together with Figure 154 a-c indicate that the carrier transport characteristics of a nano-polycrystalline material are not entirely independent. The mean energy per carrier can be affected by varying different grain characteristics. This will also have competing effects on S and σ . The reason for this is unambiguously related to the expressions for $\tau_i(E)$, DOS, and p . Our calculations show that it is possible to find a regime for which S increases but σ does not decrease substantially thus resulting in an overall increase in $S^2\sigma$. In fact, our model is one approach that directly shows how E_b , w , and L can be adjusted in such a way as to achieve the best TE performance for a given polycrystalline thermoelectric material.

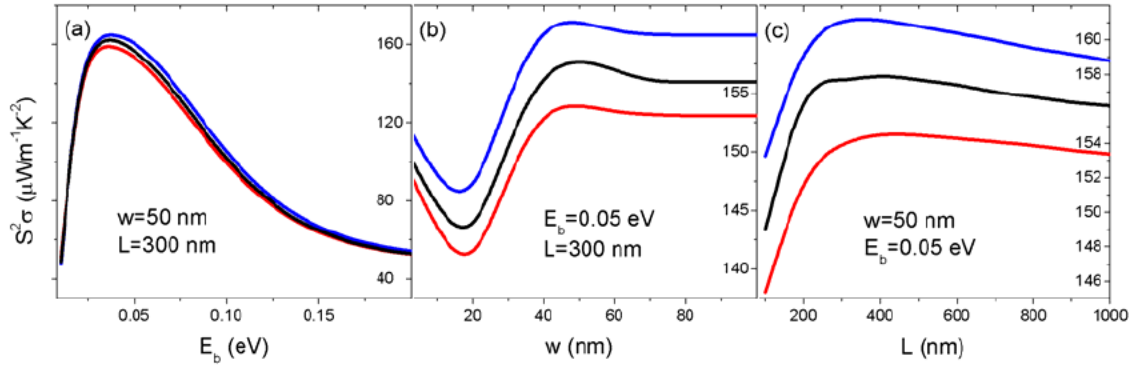


Figure 154: Power factor as a function of (a) barrier height, (b) barrier width, and (c) grain size, at $T=300$ K. The carriers concentrations are $p=5.7 \times 10^{18} \text{ cm}^{-3}$ (red line), $p=5.9 \times 10^{18} \text{ cm}^{-3}$ (black line), and $p=6.1 \times 10^{18} \text{ cm}^{-3}$ (blue line).

A phenomenological model for describing the transport properties in nanocomposite materials was proposed and successfully applied to explain relevant experimental data. We model the TE material as consisting of nano-scaled granular regions with interfaces modeled as rectangular barriers. The transport through the material includes carrier quantum transmission and scattering from the barriers and carrier/phonon scattering within the grains. The theoretically calculated σ and S can reproduce the experimental observations obtained for Ag-doped PbTe and undoped PbTe nanocomposite specimens. We have shown that the interplay between the different scattering mechanisms, as well as the carrier concentration and the physical parameters for the barriers, is important in finding an optimal regime for optimizing a material's TE parameters. Specifically, our model reveals that by manipulating the barrier size and height, the mean energy per carrier can be increased leading to an increase in S without substantial degradation of σ . More importantly, this model can be adapted for other material systems by incorporating the relevant electronic structure parameters in the total density of states and scattering mechanisms.

Bi-doped PbTe nanocomposites:

To understand the underlying mechanisms limiting the characteristics in these studied materials, we present theoretical modeling of the transport. Our goal is to apply a reliable model that will allow one to investigate the influence of the scattering mechanisms and PbTe band structure properties simultaneously. Of particular importance here is the increased number of grain boundaries in the specimens containing nano-scale domains. Our goal is to explain the role of grain boundary scattering since this mechanism is characteristic of composites with small nano-scale grains. For this purpose, we employ a model that was previously developed, and was successfully applied, for p-type Ag doped PbTe granular composites [253]. Since this model led to excellent agreement with previous experimental results, it is of interest to apply it to the current material system, n-type PbTe. The model relies on the solution of the Boltzmann transport equation within the relaxation time approximation for isotropic transport:

$$\rho^{-1} = e^2 \int dE \left(-\frac{\partial f_0}{\partial E} \right) \Sigma(E) \quad (7-15)$$

$$S = \frac{e}{\sigma T} \int dE \left(-\frac{\partial f_0}{\partial E} \right) \Sigma(E)(E - \mu) \quad (7-16)$$

$$\kappa_e = \frac{1}{T} \int dE \left(-\frac{\partial f_0}{\partial E} \right) \Sigma(E)(E - \mu)^2 - T\sigma S^2 \quad (7-17)$$

$$\Sigma(E) = \int \frac{2d^3k}{(2\pi)^3} v_e^2(\mathbf{k}) \tau_e(\mathbf{k}) \delta[E - E(\mathbf{k})] \quad (7-18)$$

where e is the carrier charge, μ is the chemical potential for the specific material, and $f_0(E)$ is the Fermi distribution function. The transport distribution function $\Sigma(E)$ includes the electronic group velocity $\mathbf{v}_e(\mathbf{k}) = (1/\hbar)\nabla E(\mathbf{k})$ and the total electronic relaxation time τ_e . Since PbTe is a small band gap semiconductor with ellipsoidal Fermi surfaces, the non-parabolic two-band Kane model is an adequate description for the energy band structure [34], with $\gamma(E) = \hbar^2 k^2 / 2m_d^*$ where m_d^* is the band-edge density of states effective mass and $\gamma(E) = E(1 + E/E_g)$ with E_g being the band gap. This also enables one to determine the carrier group velocity $v_e = (2/m_d^*)^{1/2} (\gamma(E))^{1/2} (\gamma'(E))^{-1}$.

The total relaxation time is obtained using Mathiessens's rule, which assumes that each scattering mechanism is independent of the others. For PbTe, τ_e depends on the wave vector \mathbf{k} only through the electron energy E , i.e. $\tau_e(\mathbf{k}) = \tau_e(E)$. Thus the relaxation time is obtained from $\tau(E)^{-1} = \sum_i \tau_i(E)^{-1}$,

where $\tau_i(E)$ corresponds to each contributing mechanism. The most relevant $\tau_i(E)$ for these PbTe composites are due to phonons, ionized impurities and granular interface scatterings. Expanded expressions for the scattering relaxation times relevant for this material are given in the Appendix. The effect of screening is included for the carrier/polar optical phonon scattering, while the effect of non-parabolicity on the transition matrix element energy dependence is included for the electrons scattered by acoustic phonons through the deformation potential approximation.

The granular interfaces in the PbTe composites are described as an infinite series of potential barriers with average height E_b , size of the barrier region w , and size of the grains L . τ_{gr} can be calculated by determining the transmission probability through each barrier, and the expression is given in the Appendix. The characteristics of the granular barriers can be taken as input or adjustable parameters for modeling purposes. In a previous study [253], the role of the granular barrier on the transport properties was investigated and revealed the dependence of carrier scattering due to grain boundaries and other mechanisms typical for bulk in the transport. Here, we take $E_b=0.06$ eV and $w=10$ nm, and L is estimated from the experimental data, about 40 nm and 75 nm for the S1 and S2 specimens, respectively.

The lattice thermal conductivity is calculated using the Holland-Callaway model [254-256]

$$\kappa_L = \frac{k_B}{2\pi^2 v_{ph}} \left(\frac{k_B T}{\hbar} \right)^3 \int_0^{\theta_D/T} \tau_{ph}(x) \frac{x^4 e^x}{(e^x - 1)^2} dx \quad (7-19)$$

where $v_{ph}=1771.67$ m/s is the average phonon group velocity, $\theta_D=136$ K is the Debye temperature, and $x = \hbar\omega/k_B T$ is dimensionless. τ_{ph} is the total phonon relaxation time, and it is given by $\tau_{ph}^{-1} = \sum_i \tau_{ph,i}^{-1}$ within the Mathiessen's rule, where each $\tau_{ph,i}$ corresponds to a phonon scattering mechanism. In the case of the doped PbTe composites,

$$\tau_{ph}^{-1} = \tau_{ph,U}^{-1} + \tau_{ph,d}^{-1} + \tau_{ph,e}^{-1} + \tau_{ph,b}^{-1} \quad (7-20)$$

where the terms represent Umklapp scattering, point defect scattering, electron-phonon scattering and grain boundary scattering, respectively.

Using this model (Eqs. (7-15 to 7-20)), we can calculate the transport properties of the PbTe composites. The biggest difference occurs in the low temperature regions, although the calculated results are within the experimental uncertainty for each measurement. A possible source of this discrepancy can be the existence of porosity within the nanocomposites. Thus the presence of macrodefects, besides granular boundaries, may influence the transport properties. However, since the density in all specimens was estimated to be relatively high ($\geq 92\%$) we believe grain boundary scattering is more important, and the effects of macrodefect scatterings are not considered.

The experimental and theoretical results show that ρ is larger for the smaller grain size composites. This is directly related to the importance of the carrier scattering from the grain interfaces accounted for by the relaxation time τ_{gr} . As the grains become smaller, the carrier scattering becomes more frequent resulting in increase in ρ . The electron/grain scattering is also found to be responsible for the values of κ , with *power factor* ~ 1.5 W/mK at room temperature. This value is lower by $\sim 25\%$ as compared to that of the bulk.

S is also sensitive to the presence of granular interfaces and carrier concentration, particularly at higher temperatures. The enhancement of $|S|$ is higher for nanocomposites with higher carrier concentrations. This was also observed for p-type PbTe and Bi₂Te₃ [253-257], and may be due to the combined effect of carrier/grain scattering and ionized impurity scattering more so than the grain size differences.

The formed granular interfaces due to the synthesis process, i.e. dense small grain polycrystalline materials, result in potential barriers between the grains that affect the electrical and heat transport. Simply stated, the carries with energy smaller than E_B scatter from the interfaces, however, those with energy larger than E_B traverse through the specimen determining the transport. Grain interfaces with larger barriers will result in scattering of electrons with a relative large energy distribution, while wider barriers and smaller grains will contribute to more frequent scattering events and a larger number of electrons being scattered. Because of the electron/grain scattering, ρ is larger, as expected in granular materials as compared to that of micron-sized grain polycrystalline bulk materials. An increase in ρ is usually accompanied by enhancement in S , since a smaller number of carriers contributes to the transport.

Furthermore, grain scattering also reduces κ . It is interesting to note that $\kappa_e > \kappa_L$ for bulk PbTe. For example, at T=300 K, $\kappa_e = 4.2$ W/mK while $\kappa_L = 2$ W/mK, and confirmed by our model here. Our

model also shows that phonon/interface scattering is less effective for the reduction of κ_L at higher temperatures. It is a decrease in κ_e that leads to an overall decrease in κ at higher temperatures. Nevertheless, despite the beneficial changes due to reductions in κ and increase in $|S|$, the increase in ρ results in a small ZT for Bi-doped n-type PbTe. We note that the role of the carrier and phonon scattering from the granular interfaces is critical in understanding and describing the transport properties of n-type PbTe composites. If granular interface scattering is not taken into account, the transport properties cannot be described in a satisfactory manner.

Theoretical study of CoSb₃

The theoretical model we have developed and applied to PbTe nanocomposites can be used to understand the transport properties in nanocomposites of different chemical composition providing the assumptions made initially are valid. The applicability of this phenomenological model is limited by diffusive carrier transport, relaxation time approximation, same electronic structure for the grains as bulk, and two-band Kane model for the bandstructure.

We suggest that carrier conductivity, σ , and S of granular composites made of skutterudite CoSb₃ can also be described by our theoretical model. For granular regions larger than the carrier mean free path, the electronic structure is similar to the electronic structure of bulk CoSb₃. Also, the bandstructure can be approximated by the two-band Kane model [258].

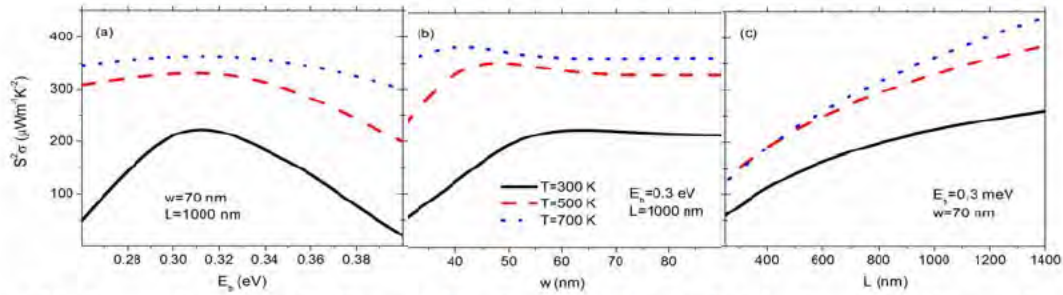


Figure 155: Power factor for CoSb₃ as a function of (a) barrier height E_b ; (b) barrier width w ; and (c) distance between the barriers L for different temperatures and $p=6.2 \times 10^{18} \text{ cm}^{-3}$.

From Ref. [253], we can calculate the dependence of S and σ on the carrier concentration and various characteristics of the grains using the physical parameters for CoSb₃. For CoSb₃ we find similar dependences as for the case of PbTe nanocomposites. For example, for longer grains, shorter barrier heights, and thinner barriers, σ is larger, but the S is smaller. For thermoelectric applications, however, we are interested in a large power factor, $PF = S^2\sigma$. Thus one must choose an optimal set of granular characteristics to achieve the highest PF . In Figure 155, we show the power factor at different temperatures as a function of E_b , w , and L for the skutterudites. All scattering mechanisms are included and the concentration is $N_i=15\%$.

Figure 155 shows that PF has similar behavior as that for PbTe. In particular, PF exhibits maxima for certain E_b and w . The maxima for PF vs. E_b is more pronounced for lower temperatures,

while the maxima for PF vs. w is more pronounced at higher temperature. When L is changed, however, PF increases towards that for the bulk. Thus our model shows that for CoSb_3 it is possible to obtain an optimum set of parameters for improved thermoelectric performance due to the interplay between the grain interface scattering mechanism and the other scattering mechanisms, such as carrier-phonon and carrier-ionized impurity scattering mechanisms.

So far our focus was to model the carrier transport properties, such as σ and S . κ , however, is also of interest since it is explicitly found in ZT . κ has an electronic and lattice component, $\kappa = \kappa_e + \kappa_l$, respectively. κ_e will be calculated using similar expressions as that used for σ and S [259], while κ_l will be calculated using the Callaway model derived from the phonon Boltzmann equation of motion within the relaxation time approximation for various phonon scattering mechanisms [260].

Based on this work it will be possible to include the phonon scattering due to the grain boundaries explicitly in the future. This will permit comprehensive modeling of all transport parameters entering the ZT . Thus our study answers questions directly related to the possibility of using nanocomposite materials with granular formations for higher ZT applications.

7.6. Optimization employing the developed materials:

The synthesis of different thermoelectric materials in nanocrystalline form has been optimized. Synthetic approaches have achieved nanocrystal formation in high yield allowing for nanocomposite processing and TE properties investigations. Optimization employing the developed materials, in addition to an investigation of bulk oxide TE materials was successfully completed. Theoretical investigations corroborated our experimental data and provided impetus for future directions. To our knowledge, many of the studies represented the first characterization of TE nanocomposites densified within a macro-scale matrix. Furthermore, the enhanced TE properties in optimized nanocomposites suggested interfacial energy barrier carrier scattering which proved to be an effective method of thermoelectric performance enhancement in bulk nanocomposites. A systematic investigation of the morphology and thermoelectric properties at elevated temperatures as well as core-shell morphologies were also investigated.

Apart from the optimization for TE properties we also looked into the optimization of Clathrate Nanocomposites for dual functional thermoelectric and thermomagnetic cooling applications. Magnetocaloric properties were studied using PPMS. Magnetic measurements were conducted using a Physical Property Measurement System from Quantum Design. In our study, the magnetic entropy change (ΔS_M) of the samples was calculated from a family of the M-H isotherms using the Maxwell relation, $\Delta S_M = \mu_0 \int (\partial M / \partial T)_H dH$, where M is the magnetization, H is the magnetic field and T is the temperature. The refrigerant capacity (RC) was calculated as $RC = [-\Delta S_M]_{\max} \times \delta T_{\text{FWHM}}$, where δT_{FWHM} is the full width at half maximum of the $\Delta S_M(T)$ curve.

Figure 156 a-b shows the temperature dependence of $-\Delta S_M$ for different applied field changes up to 6 T for the type I clathrate-EuO (40%-60%) composite and for the same field change of $\mu_0\Delta H = 6$ T for

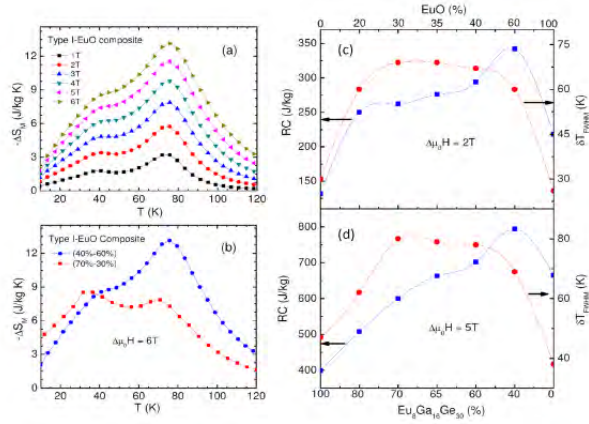


Figure 156 (a) The temperature dependence of $-\Delta S_M$ (a) for different field changes up to 6 T for the Type I clathrate-EuO (40%-60%) composite and (b) for a field change of 6 T for the Type I clathrate-EuO (40%-60%) and (70%-30%) composites; (b) The refrigerant capacity (RC) and the temperature interval (δT_{FWHM}) vary with the clathrate/EuO ratio.

the type I clathrate-EuO (40%-60%) and (70%-30%) composites. It is interesting to note that the large ΔS_M has been achieved over a wide temperature range in these composites. This is very beneficial for enhancing the cooling efficiency. More interestingly, the combination of the type I clathrates with EuO at appropriate portions can produce novel composites with enhanced RC for active magnetic refrigeration (AMR) around 70 K. Figure 156 c-d shows the variation in RC and FWHM with the portion of EuO and $\text{Eu}_8\text{Ga}_{16}\text{Ge}_{30}$ for the field change of 2 T and 5 T. We have achieved a very large RC of 794 J/kg at 5 T over a temperature interval of 70 K in the clathrate type I – EuO (40%-60%) composite, which is the largest value ever achieved among the existing materials for magnetic refrigeration around 70 K. This composite is particularly attractive for AMR for nitrogen liquefaction.

Overall, we have demonstrated the possibility of combining type I clathrates with other magnetocaloric materials such as EuO at appropriate portions to produce nanocomposites with enhanced and tunable refrigerant capacity for active magnetic refrigeration applications [261].

7.7 & 7.8 *Device design development; Measurement, optimization and re-development of prototype TE devices*

Our optimized transport data on different TE nanocomposites indicate that they may be of interest through improved performance of materials for thermoelectric power generation and refrigeration. The effort on specific device development and optimization was re-directed to subtasks related to the synthesis of artificial blood platelets and magnetic nanosystems for hyperthermia experiments as more directly relevant to the medical needs of the soldier in the field. Remaining funds will be expended in these research efforts as per the plan for the no-cost extension and detailed in the conclusion of this final report.

7.9 *Theoretical modeling of conductance and thermopower of core-shell nanocomposites*

This task was merged with sub-task 7.5 and the results related to the theoretical modeling of the PbTe nanocomposite system are presented in 7.5.

7.10 *Fabrication of $\text{Ca}_3\text{Co}_4\text{O}_9$ nanoparticle coatings by a microwave plasma process and investigation of thermoelectric properties:*

Layered cobaltates have been shown to have excellent thermoelectric properties and are promising candidate as a high temperature thermoelectric (TE) material. $\text{Ca}_3\text{Co}_4\text{O}_9$ has been grown in

many forms including bulk, polycrystalline, and thin-film. Interfaces are expected to increase phonon scattering, so thin-films with good material properties could result in a higher ZT values. Furthermore, the additional incorporation of nanoparticles in a thin-film is expected to increase phonon scattering even further. In this study, a microwave plasma process has been used to fabricate nanoparticle coating of $\text{Ca}_3\text{Co}_4\text{O}_9$. Electrical conductivity and Seebeck measurements were performed to characterize the deposited films.

Quality of TE materials is measured by the Seebeck coefficient, which related to performance of a TE device, given by ZT. Specifically, the Figure of merit is given as in equation (7-21):

$$ZT = S^2T/(\rho\kappa) \quad (7-21)$$

where S, T, ρ and κ are Seebeck coefficient, temperature, electrical resistivity, and thermal conductivity, respectively. Bulk cobaltates have reported S values as high as $\sim 130 \mu\text{V/K}$. It is well known that increased boundaries can lower thermal conductivity. Thin films and nanoparticles are expected to have a higher resistivity due to interfaces, and at the same time a lower thermal conductivity. This implies that exploiting these effects could result in maximizing ZT, the figure of merit. Our study investigated the effect of reduced particle size on film morphology and electrical properties.

Nanoparticle Film Growth:

A microwave plasma-assisted spray (MPAS) deposition process was used to form nanoparticle films of the thermoelectric material $\text{Ca}_3\text{Co}_4\text{O}_9$. By varying the concentration of the precursor used for forming the particles, different-sized nanoparticulates were grown. The resistivity, Seebeck coefficient, and thus power factor, of a set of films grown by MPAS with varying concentrations of calcium and cobalt salts were investigated. The resistivity and Seebeck coefficients of these films were measured from 300 – 700 K. The films with larger embedded nanoparticles showed a trend toward higher power factors than those with smaller nanoparticles. The best films grown by this process were shown to have good electrical conductivities, and subsequently high power factors. Films grown by this technique had room temperature power factors as high as $220 \mu\text{W/mK}^2$.

In this microwave-assisted spray process radiation transferred through a waveguide was coupled into a gas through a quartz flow tube as shown in [Figure 157](#). Oxygen was used as the carrier gas for the droplet transport. The microwave was resonantly absorbed by O_2 and water molecules, heating the gas and the droplets.

Initially, molar solutions were prepared by dissolving stoichiometric amounts of nitrates. A nebulizer was operated at a frequency of 2.4 MHz to generate uniformly distributed droplets of a precursor with an average diameter of 1.5 microns. The aerosol was injected into the energy flow tube by flowing a carrier gas through a nozzle as seen in [Figure 157](#).

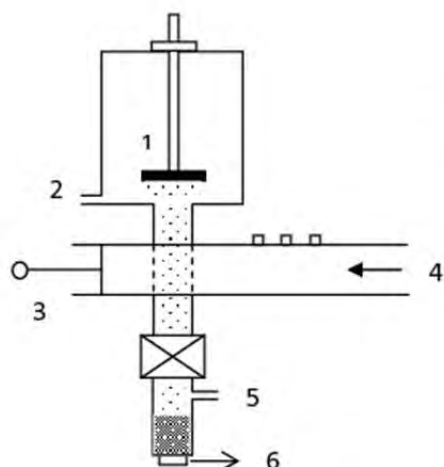


Figure 157: Schematic of a microwave assisted spray (MPAS) system. 1. Substrate. 2. Outlet for vacuum. 3. Microwave waveguide with three tuners and a handle which can slide back and forth to adjust the length of the guide. 4. Microwave input. 5. Inlet for gas flow. 6. Nebulizer below the cylinder which contains the precursor solution.

The created droplets pass through the microwave plasma into the deposition chamber. The aerosol droplets reduce in size and react due to the plasma and are finally deposited onto a heated substrate ($\sim 300^{\circ}\text{C}$ – 400°C). Note that this temperature is well below the $>800^{\circ}\text{C}$ melting point of $\text{Ca}_3\text{Co}_4\text{O}_9$. The temperature of the gas entering the deposition chamber was measured using a thermocouple. The temperature within the plasma region was determined by an optical emission spectroscopy technique. The morphology and crystallinity of as-grown films were investigated by SEM and XRD while electrical properties were investigated by a 4-point probe.

Film Morphology:

Top surface film images show formations of individual platelet-like particles of fairly uniform sizes (Figure 158). Note that this is a surface picture and crystals of different sizes may form under the surface. This size can be estimated from XRD data. The nanoparticle nature of the films was additionally verified by AFM and XRD scans of nanoparticle films as seen in Figure 159.

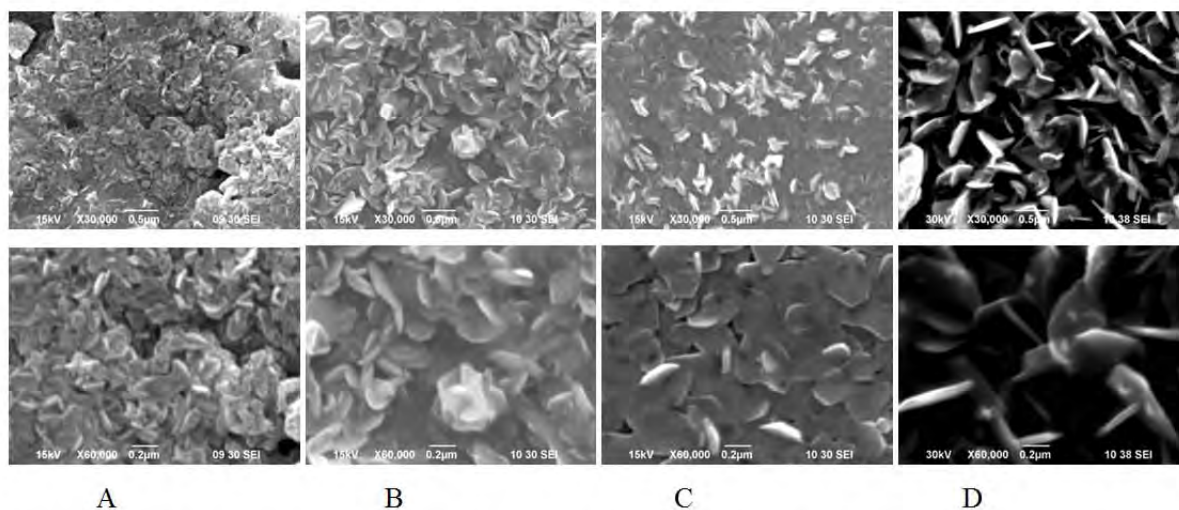


Figure 158: SEM's of prepared films varying in surface size from between 100nm to 500nm. Scan magnification is 30kX (top), and 60kX (bottom).

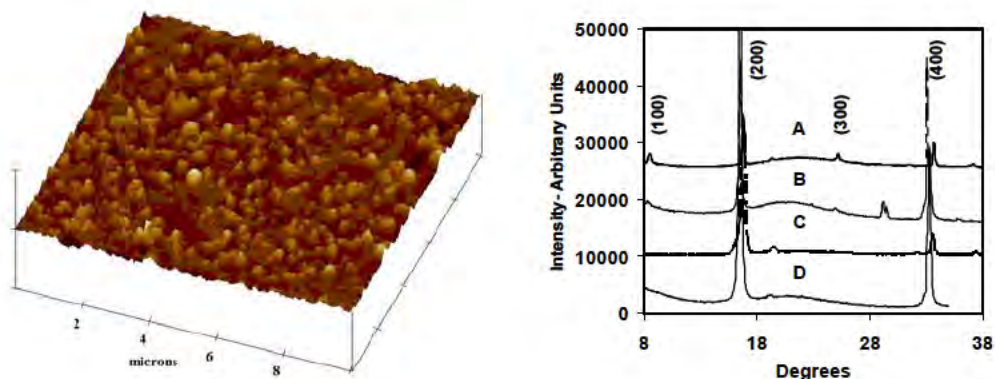


Figure 159: (a) AFM 10 μm scan of film C. (b) XRD of films A – D respectively.

Signature peaks of $\text{Ca}_3\text{Co}_4\text{O}_9$ in crystalline phase are shown. The average particle size of two thin films was calculated from data due to peak broadening caused by the small crystals. The diameter of the crystals was calculated using data from the [200] peak and the full width half maximum (FWHM).

Crystal sizes of films were estimated to be in the range of 20-70 nm from XRD data. As expected, the resistance measurements of the films showed semiconductor behavior and higher resistivity values for smaller particle size (Figure 160).

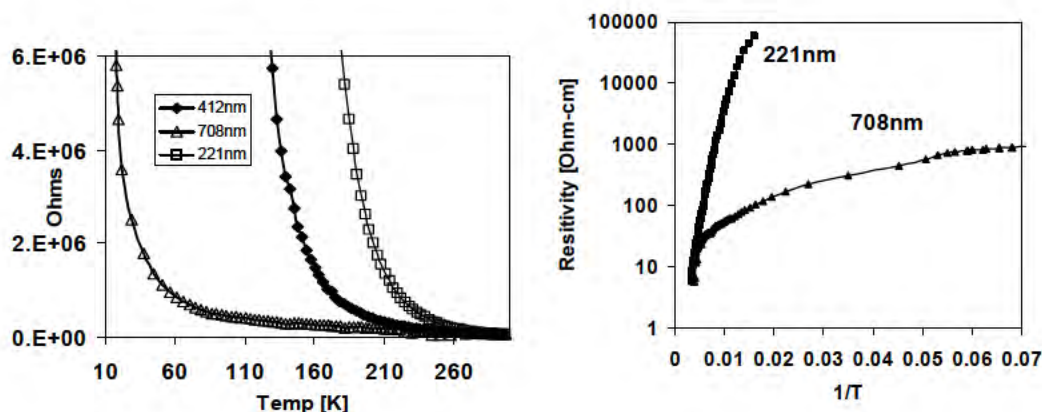


Figure 160: Normalized resistance (a) and resistivity measurements (b) on films containing different sized particles.

The film with the smallest particles shows what appears to be a different type of activated conduction mechanism than that of the largest particles as seen from the graph of ρ vs. $1/T$ shown in Figure 160 (b). The large particles exhibit the primarily thermally-activated conduction typically seen in bulk materials. The smaller-particle film shows a deviation from the larger particles just below room temperature, and the resistivity quickly increases exponentially. This suggests that the smaller particle

film exhibits an additional conduction mechanism, such as carrier hopping. This effect is attributed to the larger number of interfaces and defects due to the smaller particle size.

Seebeck Measurements:

A system capable of measuring the Seebeck coefficient in the region near room temperature was constructed. It is desired to get high temperature Seebeck measurements of this material due to its prospective use at high temperatures. Measurements are done by heating one side of the substrate, allowing temperature to reach a steady state, and measuring the values of voltage and temperatures at steady state.

A typical Seebeck measurement on one of the $\text{Ca}_3\text{Co}_4\text{O}_9$ films is shown in Figure 161. The value of the slope shows the Seebeck value as $158 \mu\text{V/K}$, which is near or slightly better than typical values ($\sim 130 \mu\text{V/K}$) given for bulk material (Figure 161).

In summary, the growth of $\text{Ca}_3\text{Co}_4\text{O}_9$ nanocrystalline thin films using a microwave-assisted spray technique has been demonstrated. Thin films containing nanocrystals of different sizes were grown and the dominant mechanism of current transport was shown to be carrier hopping. Seebeck measurements showed the coefficients to be in the same range as bulk material.

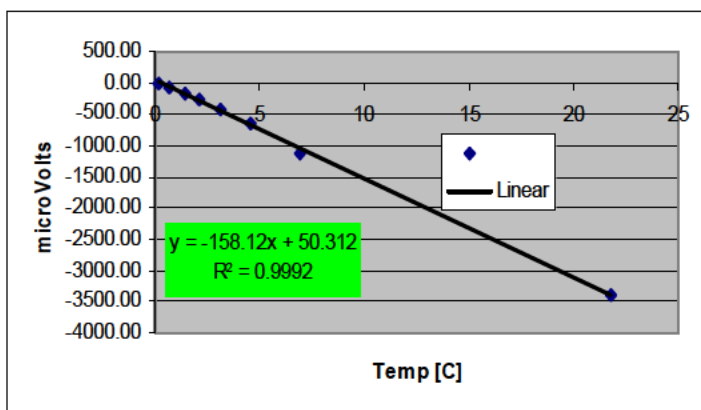


Figure 161: Sample Seebeck measurement on a film grown with the microwave system.

7.11. Synthesis of bulk thermoelectrics:

Projects involving synthesis of bulk thermoelectric materials are distributed through tasks 7.1 to 7.6. Results are reported under those tasks.

III. Key Research Accomplishments

The following bulleted items describe the significant research accomplishments for each of the seven projects undertaken:

PROJECT 1

- A novel chemical method for the synthesis and characterization of monodisperse ferrite nanoparticles of Fe_3O_4 , CoFe_2O_4 , NiFe_2O_4 , and MnFe_2O_4 with controlled size and shape was developed. The size of particles can be tuned from 5 nm to 20 nm, while their shape can be altered from spherical to cubic and octopus. These nanoparticles are excellent candidate materials for biomedical applications, including MRI, hyperthermia, and biodetection.
- A chemical technique for the synthesis of core/shell Fe_3O_4 -Au nanoparticles with controlled thickness of the Au coating layer was successfully advanced. The Au coating renders the magnetic nanoparticles with plasmonic properties, making this core/shell nanostructure extremely interesting for magnetic, optical, and biomedical applications. We have demonstrated that the synthesized Fe_3O_4 -Au nanoparticles are useful for biodetection of kidney cells.
- The mechanism for growth of dumbbell-like Pt- $\gamma\text{Fe}_2\text{O}_3$ nanoparticles with controlled size and shape was found for the first time. The hybrid nanostructures of Pt and $\gamma\text{Fe}_2\text{O}_3$ can be used as an extra degree of freedom to control magnetic properties for potential applications in memory storage devices and biomedicine, and their unique morphology can serve as both magnetic and optical probes for radiation therapy and diagnosis.
- A novel method for the synthesis of core/shell $\text{FeO}/\text{Fe}_3\text{O}_4$ nanoparticles with controlled size and shape was developed. This provides an efficient way for fabrication of different isotropic and anisotropically grown iron-oxide nanoparticles for a wide variety of technological applications.
- A thermal decomposition technique for the synthesis of $\text{Fe}/\gamma\text{-Fe}_2\text{O}_3$ nanoparticle systems with uniform and tunable particle sizes was successfully developed. It was demonstrated that these nanoparticles are useful for biomedical applications in MRI, hyperthermia, and biodetection. A systematic study of the magnetic properties of size-variant particles yielded new insights into the collective contributions of interface and surface spins to the EB in core-shell nanoparticle systems, knowledge of which is the key to manipulating EB in magnetic nanostructures for spintronics and biomedical applications.
- The first comparative study of ferrofluids, with particle blocking and carrier fluid freezing temperatures being close or far apart from each other was performed, yielding evidence for distinctly different behaviors seen in the magnetic response in the liquid, frozen and mixed states. It was demonstrated that the physical origins of relaxation peaks in the complex susceptibility or the spin-glass-like cusps in the ZFC magnetization are associated with the particle blocking and carrier liquid freezing effects. These findings are crucial in tailoring the magnetic properties of nanoparticles suspended in a liquid solution for actual biomedical applications.

- Cube-shaped FeCo nanoparticles with tunable sizes and magnetic properties were successfully synthesized and functionalized for the first time. These nanoparticles possess higher magnetic moments compared to iron oxide particles and have great potential in MRI and hyperthermia applications.
- It was demonstrated that the core/shell Fe/ γ -Fe₂O₃ nanoparticles with surface functionalization are excellent candidate materials for MRI applications. The tunability of the Fe core not only allows enhancing contrast images, but improves the inductive heating efficiency and detection capacity of these core/shell nanostructures.
- A new class of hollow γ -Fe₂O₃ nanoparticles was developed. The size of particles can be tuned from 5 to 20 nm, while remaining the same thickness of the shell of 2 nm. The possibility of tuning the exchange bias (EB) effect in this system by tuning particle size was also demonstrated. This finding is of practical importance as such nanostructures can be ideal for use in applications where their anisotropic magnetic properties can be controlled using the so-called “exchange bias” mechanism. These nanoparticles also have potential applications in memristors, hyperthermia agent in nanomedicine, and targeted drug delivery.
- The important impact of particle shape on the inductive heating capacity in Fe₃O₄ nanoparticles with cubic, spherical, and octopod shapes was demonstrated. The octopod-shaped Fe₃O₄ nanoparticles exhibit a higher magnetic heating efficiency as compared to their spherical and cubic particle counterparts. These particles can also provide more magnetic labeling options that are currently restricted to spherical magnetic nanoparticles below 15 nm in size.

PROJECT 2

- It was demonstrated that the presence of the Co coating layer enhances both the GMI effect and field sensitivity in the Co-coated ribbons. The largest values of the GMI effect and field sensitivity are achieved in the sample coated with Co on the free ribbon surface having the smaller surface roughness as compared to that coated with Co on the wheel-side ribbon surface with the larger surface roughness. Our findings are therefore of practical importance, demonstrating a new way to tailor the GMI effect and field sensitivity in surface-modified ferromagnetic ribbons for use in highly sensitive magnetic sensors.
- It was demonstrated that the GMI response of a Co-based amorphous ribbon can be tuned by tuning the surface anisotropy of the ribbon by capping it with an antiferromagnetic material FeMn in the presence of a small magnetic field applied in the longitudinal or transverse directions. We find that the orientation of the deposition field greatly impacts the GMI of the bilayer structures. Our studies provide further guidance for tailoring GMI in surface modified soft ferromagnetic ribbons as well as optimizing specific frequency ranges for particular sensors.
- A new method of using a pulsed laser deposition (PLD) technique for the controlled growth of a thin magnetic oxide (CoFe₂O₄) layer on the surface of Co-based amorphous ribbons to improve the GMI response was developed. Our study indicates that both the surface roughness of the ribbon and closure of magnetic flux paths due to the presence of the additional magnetic layer play important roles in tailoring the GMI effect and field sensitivity.

- The possibility of tuning magnetic anisotropy and hence the GMI effect and its field sensitivity in nanocomposite $(\text{Co}_{1-x}\text{Fe}_x)_{89}\text{Zr}_7\text{B}_4$ ribbons with $x = 0, 0.025, 0.05$, and 0.10 was demonstrated. The variations of the GMI ratio and the field-induced magnetic anisotropy field upon Fe doping are correlated with the microstructural changes in the nanocrystalline samples. These ribbons can be ideally used in magnetic and stress sensors.
- A systematic study has been performed of the GMI effect in soft ferromagnetic amorphous $\text{Co}_{65}\text{Fe}_4\text{Ni}_2\text{Si}_{15}\text{B}_{14}$ ribbons with width varying from 4 mm down to 300 μm . It was demonstrated that the GMI response is greatly improved in ribbons when the width is reduced to the microscale. Our studies provide important insights into the correlation between the GMI effect and ribbon dimensions towards the GMI optimization and demonstrate the usefulness of soft ferromagnetic microribbons for high frequency sensor applications.
- Through a comprehensive study of the influence of sample length ($L = 2, 5, 8$, and 10 mm) on the GMI effect and magnetic sensitivity parameter (η) in $\text{Co}_{69}\text{Fe}_{4.5}\text{Ni}_{1.5}\text{Si}_{10}\text{B}_{15}$ amorphous ribbons over a frequency range of $0.1 - 10$ MHz, it was demonstrated that there exists a critical length ($L_0 \cong 8$ mm) in the amorphous ribbon, for which the largest GMI and η are achieved. These findings point to the importance of the geometrical dimensions of samples and provide some insights for optimizing the GMI effect in highly sensitive GMI-based magnetic sensors.
- The giant magnetoimpedance (GMI) effect and its field sensitivity (η) have been studied in $\text{Co}_{69}\text{Fe}_{4.5}\text{X}_{1.5}\text{Si}_{10}\text{B}_{15}$ ($X = \text{Ni}, \text{Al}, \text{Cr}$) amorphous ribbons. Magnetization and atomic force microscopy (AFM) experiments revealed that the largest values of the low-frequency GMI effect and η for the Al-containing sample result from the largest value of magnetic permeability, while the largest values of the high-frequency GMI effect and η for the Ni-containing sample are attributed to the smallest surface roughness of this sample. These results point to the importance of the sample surface in determining high-frequency GMI behavior. A correlation between the sample surface and high-frequency GMI was established in the investigated ribbons.
- A systematic study of the magneto-resistance (MR), magneto-reactance (MX), and magneto-impedance (MI) effects in single and multiple glass-coated amorphous magnetic microwires revealed that the MR, MX, and MI ratios and their corresponding field sensitivities strongly depend on the number of microwires in an array and on the distance between them. The highest field sensitivity of MX has been achieved, revealing the possibility of developing ultrahigh sensitivity magnetic field sensors based on the principle of the MX effect.
- A new class of a fiber Bragg grating-based microwave energy sensor was developed. The sensor relies on a soft ferromagnetic glass-coated microwire that is bonded to the cladding of the grating. The microwire absorbs microwave energy and heats up thus raising the temperature of the fiber Bragg grating. Compared to a similar sensor that uses gold to absorb electromagnetic radiation, the microwire yields a sensor with greater sensitivity (~ 10 times at $f = 3.25$ GHz) relative to the perturbation of the microwave field. With this sensor, the best sensitivity to electromagnetic radiation corresponded to ac electric fields that have RMS amplitude of approximately 36 V/m.

PROJECT 3

- A chemical vapor deposition technique for fabrication of carbon nanotubes with controlled diameter and length was successfully advanced. These carbon nanotubes are desirable for a wide range of technological applications.
- A novel method for filling carbon nanotubes completely with monodisperse superparamagnetic nanoparticles of different compositions (Fe_3O_4 , CoFe_2O_4 , NiFe_2O_4) for spintronics, sensors and microwave device applications was developed. High saturation magnetization and shape anisotropy achieved in these magnetic nanotubes indicate their usefulness not only for microwave and sensor device applications, but also for others such as cantilever tips in magnetic force microscopes, CNT-based biomedical agents, and as interconnects in hybrid CMOS spintronic devices.
- A new approach for carbon nanotubes based gas and chemical sensing using the radio-frequency magnetoimpedance technology was developed. This gas sensor had a much higher field sensitivity compared with current state-of-the-art sensors based on the dc resistance change.
- It was demonstrated that the carbon nanotubes filled with superparamagnetic nanoparticles are promising candidate materials for applications in spintronics and microwave devices, as well as excellent magnetic biomarkers in biological systems for biomedical applications.
- A new method of combining the ac magnetoresistance (MR), magnetoreactance (MX), and magnetoimpedance (MI) effects to produce an integrated magnetic biosensor with tunable and enhanced sensitivity was demonstrated. The MX-based approach showed the most sensitive detection of superparamagnetic nanoparticles at low concentrations, demonstrating a sensitivity level comparable to that of a SQUID-based biosensor. Unlike a SQUID, however, the proposed MX technique is cryogen-free and operates at room temperature, providing a promising avenue to the development of low-cost highly sensitive biosensors.
- A new approach to improving the detection sensitivity of a magnetic ribbon-based GMI biosensor by patterning nanoscale holes on the ribbon surface was demonstrated. This sensor showed a much higher detection sensitivity compared to a conventional GMI biosensor.
- A novel biosensor based on the MX effect of a soft ferromagnetic ribbon with a nanohole-patterned surface was developed for the detection and quantification of anticancer drugs (e.g. Curcumin) tagged to superparamagnetic (e.g. Fe_3O_4) nanoparticles. Since these magnetic nanoparticles are widely used as magnetic resonance imaging (MRI) contrast agents, our biosensing technique can also be used as a new, low-cost, fast and easy pre-detection method before MRI.
- A new type of magnetic biosensor based on a tunnel diode oscillator (TDO)-based radio-frequency (RF) transverse susceptibility technique for detection of Au- Fe_3O_4 nanoparticles taken up by human embryonic kidney (HEK) cells was developed. Since this resonant method can detect small changes in the magnetic signal of even small amounts of nanoparticles taken up by cells, it is a very promising tool for biosensing applications.

- A new type of coil-based magnetic biosensor for biodetection was developed. This sensor allows detailed investigation of the dynamic magnetic properties of various ferrofluids, which is essential in manipulating functionalized magnetic nanoparticles for biomedical applications.
- The integrated ferroelectric-ferromagnetic high aspect ratio nanostructures with CoFe_2O_4 core and $\text{Pb}(\text{Zr}_{0.52}\text{Ti}_{0.48})\text{O}_3$ shell using an alumina template were synthesized for the first time. This novel nanostructure is attractive for a wide range of applications in spintronics and sensors.

PROJECT 4

- Highly water dispersible iron oxide nanoparticles were prepared. Optical microscopy images and ECIS data clearly demonstrated uptake of the particles by the 3T3 cells. ECIS data further showed that the cells containing the Fe_3O_4 nanoparticles can survive for 24h without cell death.
- Mechanical stimulation in PLL/PLGA multilayer films was achieved by changing film thickness and stiffness. It was shown that the mechanochemical properties of the multilayer film system could be employed in the diagnosis of disease, perhaps in cancer research.

PROJECT 5

- A new way of making novel magnetic polymer nanocomposites, including PVDF- Fe_3O_4 and Rogers- CoFe_2O_4 nanocomposite systems was successfully developed.
- The tunability of the magnetic and microwave responses of the PVDF- Fe_3O_4 and Rogers- CoFe_2O_4 nanocomposites by varying concentrations of the particle loading was demonstrated, indicating that these nanocomposites are excellent candidate materials for applications in biomedical sensing and microwave communication devices.
- Nanocolumnar thin films of the magnetic CFO were successfully grown using oblique-angle PLD and nanowire arrays of the ferroelectric PZT were successfully grown using a combinatorial physical/chemical route.
- Ferroelectric/ferromagnetic (PZT/CFO) heterostructures were successfully grown using PLD and showed evidence of interfacial strain-mediated magneto-electric coupling.
- In an attempt to incorporate nano-inclusions in piezoelectric films, PZT thin films doped with varying concentrations of La were successfully grown using PLD. La-PZT films showed enhanced polarization in comparison to undoped PZT thin films grown under the same conditions.
- ZnO:V and ZnO:Mn thin films and ZnO:V/ZnO:Mn heterostructures were fabricated using PLD and showed evidence of multiferroic coupling within these structures.

- PZT nano-wire arrays were grown over a large surface area on ITO/glass substrate. Thermally-evaporated Ti seed layers and laser-deposited thin PZT films were shown to facilitate the upright growth of PZT nano-wires.

PROJECT 6

- Single crystal PbSe quantum dots with band gaps in the range of 0.6-0.8 eV were grown by solvothermal techniques. Optical absorption and electrical measurements have shown the QDs to be quantum confined while the presence of surfactants was shown to give rise to poor charge transport in a film.
- A laser-assisted spray process was developed to deposit surfactant-free QD film where charge transport was enhanced by few orders of magnitude.
- Techniques were developed to uniformly embed surfactant-free PbSe quantum dots (QDs) in semiconducting polymers for enhanced charge transport between QDs and the polymer.
- Chemically-grown TiO₂ nano-rods, PbSe QDs, and transparent conducting polymers were integrated to form solar cell structures. Photocurrent generation in these cells was demonstrated.

PROJECT 7

- State-of-the-art and novel thermoelectric (TE) materials were successfully synthesized by various low-cost chemical processes. The synthesis processes have been optimized in order to prepare high yield of nanocrystals through batch fabrication.
- Novel core-shell nanocrystals of important TE materials were synthesized through optimization of two-step chemical synthesis process.
- The core-shell nanocrystals were successfully densified by SPS to prepare core-shell nanocomposites preserving the core-shell structure even after high pressure and temperature densification. Calorimetric analysis of the prepared TE nanocrystals and nanocomposites revealed stability of these materials at high temperature regime. Phase purity of the prepared TE nanocrystals and nanocomposites was understood from X-ray diffraction studies, while other structural characterization indicated the high quality of the prepared materials for further property studies.
- Doped PbTe, Bi₂Te₃ nanocomposites exhibited improved Seebeck coefficient and reduced thermal conductivity properties as compared to the bulk indicating their potential in TE applications.
- Electrical resistivity data for CuCoO₂ indicated an activated temperature dependence.

- *Pnnm* FeSb₂ nanocomposites showed reduction in thermal conductivity by nearly an order of magnitude.
- Interfacial energy barrier carrier scattering is an effective method of thermoelectric performance enhancement in bulk nanocomposites. Specifically by manipulating the barrier size and height, the mean energy per carrier can be increased leading to an increase in S without substantial degradation of σ . Grain scattering also reduces κ in the nanocomposites. A phenomenological model for describing the transport properties in nanocomposite materials was proposed and successfully applied to explain relevant experimental data.
- Nanocomposite materials of PbTe, Bi₂Te₃, Bi, Bi_xSb_{1-x} and FeSb₂ were optimized for density and grain size tuning in order to achieve improved thermoelectric properties. In all cases, κ showed reduction by orders of magnitude.
- Optimized clathrate composite showed enhanced magnetocaloric effect and hence potential to tune refrigerant capacity for active magnetic refrigeration applications.
- Microwave plasma-assisted spray process for the growth of Ca₃Co₄O₉ nanoparticle coatings was developed in which the size of the nano-particles was controlled by the initial solution concentration. Thermoelectric coatings fabricated by this method have shown high power factors.

IV. Reportable Outcomes

The following sections list book chapters, publications, presentations, patent-related activity, professional activities, students graduated, student awards/scholarships and impact of grant-funded research acknowledging support from CIFM through grant USAMRMC W81XWH-07-1-0708 and/or continuation grant USAMRMC W81XWH1020101/3349 (participating CIFM faculty and postdoctoral contributors are shown in bold, while CIFM student contributors are italicized):

Book chapters:

1. *K. Stojak*, **H. Srikanth**, **P. Mukherjee**, **M.H. Phan** and N.T.K. Thanh, Size- and Shape-Variant Magnetic Nanoparticles: Synthesis and Characterisation for Biomedical Applications, in **Metal Nanoparticles of Complex Morphologies, Bottom up Synthesis to Applications**, (2012) Ed. Tapan K. Sau and Andrey L. Rogach, Wiley, Chapter 6.

Journal Publications:

1. *J. Devkota*, T.T.T. Mai, *K. Stojak*, P.T. Ha, H.N. Pham, X.P. Nguyen, **P. Mukherjee**, **H. Srikanth**, and **M.H. Phan**, “Synthesis, inductive heating, and magnetoimpedance-based detection of multifunctional Fe₃O₄ nanoconjugates”, *Sensors and Actuators B: Chemical* 190, 715 (2014)
2. **H. Khurshid**, *S. Chandra*, W. Li, G. C. Hadjipanayis, **P. Mukherjee**, **M.H. Phan**, and **H. Srikanth**, “Mechanism and Controlled Growth of Shape and Size Variant Core/Shell FeO/Fe₃O₄ Nanoparticles”, *Nanoscale* 5, 7942 (2013)
3. **H. Khurshid**, *S. Chandra*, **P. Mukherjee**, and **H. Srikanth**, “Synthesis and Magnetic Properties of Hybrid Nanostructures of Pt-Fe_xO_y”, *Journal of Materials Chemistry C* 1, 6553 (2013)
4. *N. A. Frey-Huls*, **M. H. Phan**, A. Kumar, S. Mohapatra, S. S. Mohapatra, **P. Mukherjee** and **H. Srikanth**, “Transverse susceptibility as a biosensor for detection of nanoparticle-embedded human embryonic kidney cells”, *Sensors* 13, 8490 (2013)
5. *J. Devkota*, *A. Ruiz*, **P. Mukherjee**, **H. Srikanth**, and **M.H. Phan**, “Magneto-resistance, magneto-reactance, magneto-impedance effects in single and multi-wire systems”, *Journal of Alloys and Compounds* 549, 295 (2013)
6. *J. Devkota*, *A. Ruiz*, C. Wang, S. Mohapatra, **P. Mukherjee**, **H. Srikanth**, and **M.H. Phan**, “Detection of low-concentration superparamagnetic nanoparticles using an integrated radio frequency magnetic biosensor,” *Journal of Applied Physics* 113, 104701 (2013)
7. *A. Ruiz*, **D. Mukherjee**, *J. Devkota*, *M. Hordagoda*, **S. Witanachchi**, **P. Mukherjee**, **H. Srikanth**, and **M.H. Phan**, “Enhanced GMI effect in soft ferromagnetic amorphous ribbons with pulsed laser deposition of cobalt ferrite”, *Journal of Applied Physics* 113, 17A323 (2013)
8. **H. Khurshid**, *S. Chandra*, W. Li, G. C. Hadjipanayis, **P. Mukherjee**, **M. H. Phan**, and **H. Srikanth**, “Synthesis and magnetic properties of core/shell FeO/Fe₃O₄ nano-octopods”, *Journal of Applied Physics* 113, 17B508 (2013)

9. J. Devkota, A. Ruiz, P. Mukherjee, H. Srikanth, and M.H. Phan, "Magneto-impedance biosensor with enhanced sensitivity for highly sensitive detection of Nanomag-D beads", *IEEE Transactions on Magnetics* **49**, 4060 (2013)
10. J. Devkota, A. Ruiz, J. Wingo, F.X. Qin, P. Mukherjee, H. Srikanth, M.H. Phan, "Soft ferromagnetic microribbons with enhanced GMI properties for high frequency sensor applications," *Physics Express* **4**, 10 (2013)
11. N.H. Hong, A.T. Raghavender, O. Ciftja, M.-H. Phan, K. Stojak, H. Srikanth, Y.H. Zhang, "Ferrite nanoparticles for future heart diagnostics", *Applied Physics A: Materials Science and Processing* **112**, 323 (2013).
12. S. Datta, S. Chandra, S. Samanta, K. Das, H. Srikanth, B. Ghosh, "Growth and physical property study of single nanowire (diameter 45 nm) of half doped manganite " - *Journal of Nanomaterials* **2013**, 162315 (2013)
13. D. Mukherjee, M. Hordagoda, R. Hyde, N. Bingham, H. Srikanth, S. Witanachchi, and P. Mukherjee, "Nano-columnar Interfaces and Enhanced Magnetic Coercivity in Preferentially-oriented Cobalt ferrite Thin Films grown using Oblique-angle Pulsed Laser Deposition", *ACS Applied Materials and Interfaces*, **5**(15), 7450 (2013)
14. A. Datta, D. Mukherjee, M. Hordagoda, S. Witanachchi, and P. Mukherjee, "Controlled Ti Seed Layer Assisted Growth and Field Emission Properties of $\text{Pb}(\text{Zr}_{0.52}\text{Ti}_{0.48})\text{O}_3$ Nanowire Arrays", *ACS Applied Materials and Interfaces*, **5**(13), 6261 (2013)
15. A. Ruiz, D. Mukherjee, J. Devkota, M. Hordagoda, S. Witanachchi, P. Mukherjee, H. Srikanth, and M.H. Phan, "Enhanced GMI effect in soft ferromagnetic amorphous ribbons with pulsed laser deposition of cobalt ferrite", *Journal of Applied Physics*, **113**, 17A323 (2013)
16. A. Datta, D. Mukherjee, S. Witanachchi, and P. Mukherjee, "Low temperature synthesis, optical and photoconductance properties of nearly monodisperse thin In_2S_3 nanoplatelets", *RSC Advances* **3**, 141 (2013)
17. A. Datta and G.S. Nolas, "Nanostructuring and Porosity in Anisotropic Thermoelectric Materials Prepared by Bottom-Up Processing" in *Thermoelectric Nanomaterials*, eds. K. Koumoto and T. Mori, Springer-Verlag, Berlin, 2013
18. H. Khurshid, W. Li, M.H. Phan, P. Mukherjee, H. Srikanth, and G.C. Hadjipanayis, "Surface spin disorder and exchange-bias in hollow maghemite nanoparticles", *Applied Physics Letters* **101**, 022403 (2012)
19. S. Chandra, H. Khurshid, W. Li, G. C. Hadjipanayis, M. H. Phan, and H. Srikanth, "Spin dynamics and criteria for onset of exchange bias in superspin glass $\text{Fe}/\gamma\text{-Fe}_2\text{O}_3$ core-shell nanoparticles", *Physical Review B* **86**, 014426 (2012)
20. - A. Chaturvedi, K. Stojak, N. Laurita, P. Mukherjee, H. Srikanth and M. H. Phan, "Enhanced magnetoimpedance effect in Co-based amorphous ribbons coated with carbon nanotubes", *Journal of Applied Physics* **111**, 07E507 (2012)

21. S. Chandra, A. I. Figueroa, Barnali Ghosh, A. K. Raychaudhuri, **M. H. Phan, P. Mukherjee and H. Srikanth**, “Fabrication and magnetic response probed by RF transverse susceptibility in $\text{La}_{0.67}\text{Ca}_{0.33}\text{MnO}_3$ nanowires”, *Physica B: Condensed Matter* **407**, 175 (2012)
22. S. Chandra, **H. Khurshid, M.H. Phan, and H. Srikanth**, “Asymmetric hysteresis and its dependence on magnetic anisotropy in exchange biased Co/CoO core-shell nanoparticles”, *Applied Physics Letters* **101**, 232405 (2012)
23. **D. Mukherjee, N. Bingham, M. Hordagoda, M. H. Phan, H. Srikanth, S. Witanachchi, and P. Mukherjee**, “Influence of microstructure and interfacial strain on the magnetic properties of epitaxial $\text{Mn}_3\text{O}_4/\text{La}_{0.7}\text{Sr}_{0.3}\text{MnO}_3$ layered-composite thin films”, *Journal of Applied Physics* **112**, 083910 (2012)
24. **D. Mukherjee, M. Hordagoda, N. Bingham, H. Srikanth, P. Mukherjee and S. Witanachchi**, “Challenges in the polycrystalline and epitaxial growth of stoichiometric $\text{PbZr}_{0.52}\text{Ti}_{0.48}\text{O}_3/\text{La}_{0.7}\text{Sr}_{0.3}\text{MnO}_3$ multiferroic heterostructures using pulsed laser ablation”, *Journal of Applied Physics* **112**, 064101 (2012)
25. **D. Mukherjee, S. Witanachchi, R. Hyde, and P. Mukherjee**, “Advantages of Dual-laser Ablation in the Growth of Multicomponent Thin Films”, *American Institute of Physics Conference Proceedings* **1464**, 325 (2012)
26. **D. Mukherjee, R. Hyde, P. Mukherjee, H. Srikanth, and S. Witanachchi**, “Role of dual-laser ablation in controlling the Pb depletion in epitaxial growth of $\text{Pb}(\text{Zr}_{0.52}\text{Ti}_{0.48})\text{O}_3$ thin films with enhanced surface quality and ferroelectric properties”, *Journal of Applied Physics* **111**, 064102 (2012)
27. **D. Mukherjee, P. Mukherjee, H. Srikanth, and S. Witanachchi**, “Carrier-mediated Interaction of Magnetic Moments in Oxygen Vacancy Controlled Epitaxial Mn doped ZnO Thin Films.”, *Journal of Applied Physics* **111**, 07C318 (2012)
28. **D. Mukherjee, N. Bingham, M. H. Phan, H. Srikanth, P. Mukherjee, and S. Witanachchi**, “Ziz-zag interface and strain-influenced ferromagnetism in epitaxial $\text{Mn}_3\text{O}_4/\text{La}_{0.7}\text{Sr}_{0.3}\text{MnO}_3$ thin films grown on SrTiO_3 (100) substrates”, *Journal of Applied Physics* **111**, 07D730 (2012)
29. N.H. Hong, C.-K. Park, A. T. Raghavender, O. Ciftja, N.S. Bingham, **M.H. Phan, and H. Srikanth**, “Room temperature ferromagnetism in monoclinic Mn-doped ZrO_2 thin films”, *Journal of Applied Physics* **111**, 07C302 (2012)
30. N.S. Bingham, P. Lampen, T.L. Phan, **M.H. Phan, S.C. Yu, and H. Srikanth**, “Magnetocaloric effect and refrigerant capacity in $\text{Sm}_{1-x}\text{Sr}_x\text{MnO}_3$ ($x=0.42, 0.44, 0.46$) manganites”, *Journal of Applied Physics* **111**, 07D705 (2012)
31. P. Lampen, A. Puri, **M.H. Phan, and H. Srikanth**, “Structure, magnetic, and magnetocaloric properties of amorphous and crystalline $\text{La}_{0.4}\text{Ca}_{0.6}\text{MnO}_{3+\delta}$ nanoparticles”, *Journal of Alloys and Compounds* **94**, 512 (2012)

32. **A. Datta**, *A. Popescu*, **L. Woods**, and **G.S. Nolas**, “The Bottom-Up Approach To Bulk Thermoelectric Materials with Nano-Scale Domains”, Ch. 14, CRC Handbook: Thermoelectrics and its Energy Harvesting, edited by D.M. Rowe, CRC Press, Boca Raton, 2012
33. **A. Datta** and **G.S. Nolas**, “Solution-Based Synthesis & Low-Temperature Transport properties of CsBi_4Te_6 ”, *Applied Materials & Interfaces*. **4**, 772 (2012)
34. **A. Datta** and **G.S. Nolas**, “Synthesis and Characterization of Nanocrystalline FeSb_2 for Thermoelectric Applications”, *Eur. J. Inorg. Chem.* **55** (2012)
35. *K. Stojak*, **S. Pal**, **H. Srikanth**, C. Morales, J. Dewdney, J. Wang, T. Weller, “Polymer nanocomposites exhibiting magnetically tunable microwave properties”, *Nanotechnology* **22**, 135602 (2011)
36. C. Morales, J. Dewdney, **S. Pal**, *K. Stojak*, **H. Srikanth**, J. Wang and T. Weller, “Magnetically tunable nanocomposites for microwave applications”, *IEEE Transactions of Microwave Theory and Techniques* **59**, 302 (2011)
37. *N. Laurita*, *A. Chaturvedi*, C. Bauer, P. Jayathilaka, Alex Leary, C. Miller, **M.H. Phan**, M.E. McHenry and **H. Srikanth**, “Enhanced GMI effect and field sensitivity in Co-coated soft ferromagnetic amorphous ribbons”, *Journal of Applied Physics* **109**, 07C706 (2011)
38. *A. Chaturvedi*, *N. Laurita*, A. Leary, **M.H. Phan**, M.E. McHenry and **H. Srikanth**, “Giant magnetoimpedance and field sensitivity in amorphous and nanocrystalline $(\text{Co}_{1-x}\text{Fe}_x)_{89}\text{Zr}_7\text{B}_4$ ($x = 0, 0.025, 0.05, 0.1$) ribbons”, *Journal of Applied Physics* **109**, 07B508 (2011)
39. A.I. Figueroa, *S. Chandra*, **M.H. Phan**, **H. Srikanth**, C. M. Bonilla, L.M. García, F. Bartolomé, J. Bartolomé, and J. Herrero-Albillos, “Magnetic switching and magnetic transitions in ErCo_2 probed by radio frequency transverse susceptibility”, *Journal of Applied Physics* **109**, 07E118 (2011)
40. *M.B. Morales*, **S. Pal**, *N.A. Frey*, **M.H. Phan**, **P. Mukherjee**, and **H. Srikanth**, “Origin of Magnetic Anomalies in the Liquid, Mixed and Frozen States of Ferrofluids” *Physics Express* 2011;1:247 (5 pages)
41. **D. Mukherjee**, **T. Dhakal**, **M. H. Phan**, **H. Srikanth**, **P. Mukherjee**, and **S. Witanachchi**, “Role of crystal orientation on the magnetic properties of CoFe_2O_4 thin films grown on Si (100) and Al_2O_3 (0001) substrates using pulsed laser deposition”, *Physica B: Condensed Matter* **406**, 2663 (2011)
42. *T. Wangenstein*, **T. Dhakal**, *M. Merlak*, **M .H. Phan**, **P. Mukherjee**, and **S. Witanachchi**, “Growth of uniform ZnO nanoparticles by a microwave plasma process”, *Journal of Alloys and Compounds*, **509** Issue: 24 Pages: 6C859-6863 (2011)
43. *A. Chaturvedi*, *S. Stefanoski*, **M.H. Phan**, **George S. Nolas**, and **H. Srikanth**, “Table-like magnetocaloric effect and enhanced refrigerant capacity in $\text{Eu}_8\text{Ga}_{16}\text{Ge}_{30}$ -EuO composite materials”, *Applied Physics Letters* **99**, 162513 (2011)

44. **M.H. Phan**, V. Franco, A. Chaturvedi, S. Stefanoski, **G.S. Nolas**, and H. **Srikanth**, “Origin of the magnetic anomaly and tunneling effect of europium on the ferromagnetic ordering in $\text{Eu}_8\text{Ga}_{16}\text{Ge}_{30}$ type-I clathrates”, *Physics Review B*, 84, 054436 (2011)
45. A. Popescu, **A. Datta**, **G. S. Nolas**, and **L. M. Woods**, “Thermoelectric properties of Bi-doped PbTe composites”, *J. Appl. Phys.* 109, 103709 (2011)
46. **A. Datta**, and **G. S. Nolas**, “Composition controlled synthesis of Bi rich $\text{Bi}_{1-x}\text{Sb}_x$ alloy nanocrystals by a low temperature polyol process”, *Cryst. Eng. Comm.* 13, 2753 (2011).
47. A. Chaturvedi, **T. Dhakal**, A.-T. Le, **S. Witanachchi**, **M.H. Phan** and **H. Srikanth**, “Critical length and giant magnetoimpedance in Co-Fe-Ni-Si-B amorphous ribbons”, *Materials Science and Engineering B* 172, 146 (2010)
48. A. Chaturvedi, **T. Dhakal**, A.-T. Le, **S. Witanachchi**, **M.H. Phan** and **H. Srikanth**, “Correlation between magnetic softness, sample surface and magneto-impedance in $\text{Co}_{69}\text{Fe}_{4.5}\text{X}_{1.5}\text{Si}_{10}\text{B}_{15}$ (X = Ni, Al, Cr) amorphous ribbons”, *Physica B: Condensed Matter* 405, 2836 (2010)
49. A. T. Le, N. Q. Hoa, D. G. Park, **M. H. Phan**, **H. Srikanth** and S. C. Yu, “Enhancement of the giant magnetoimpedance effect and its magnetic response in ion-irradiated amorphous ribbons”, *Materials Science and Engineering B* 166, 89 (2010)
50. V. Franco, A. Conde, D. Sidhaye, B. L. V. Prasad, P. Poddar, S. Srinath, **M. H. Phan** and **H. Srikanth**, “Field dependence of the magnetocaloric effect in core-shell nanoparticles”, *Journal of Applied Physics* 107, 09A910 (2010)
51. D. Mukherjee, **T. Dhakal**, R. Hyde, **P. Mukherjee**, **H. Srikanth**, and **S. Witanachchi**, “Role of Epitaxy in Controlling the Magnetic and Magnetostrictive Properties of Cobalt Ferrite-PZT Bilayers”, *Journal of Physics D: Applied Physics* 43, 485001 (2010)
52. D. Mukherjee, **T. Dhakal**, **H. Srikanth**, **P. Mukherjee**, and **S. Witanachchi**, “Evidence of Carrier-Mediated Magnetism in Mn-Doped ZnO Thin Films”, *Physical Review B* 81, 205202 (2010)
53. **T. Dhakal**, D. Mukherjee, R. Hyde, **P. Mukherjee**, **M. H. Phan**, **H. Srikanth**, and **S. Witanachchi**, “Magnetic anisotropy and field-switching in cobalt ferrite thin films deposited by pulsed laser ablation”, *Journal of Applied Physics* 107, 053914 (2010)
54. H. Verma, D. Mukherjee, **S. Witanachchi**, **P. Mukherjee**, and **M. Batzill**, “Comparative Study of ZnO Thin Film and Nano-Pillar Growth on YSZ(111) and Sapphire (0001) Substrates by Pulsed Laser Deposition”, *Journal of Crystal Growth* 312, 2012 (2010)
55. Khadka, Dhan B.; **Haynie, Donald T.**, “Insoluble Synthetic Polypeptide Mats from Aqueous Solution by Electrospinning”, *ACS APPLIED MATERIALS & INTERFACES* Volume: 2 Issue: 10 Pages: 2728-2732 (2010)

56. **A. Datta**, *J. Paul*, A. Kar, A. Patra, Z. Sun, L. Chen, J. Martin and **G.S. Nolas**, 'Facile chemical synthesis of nanocrystalline thermoelectric alloys based on Bi-Sb-Te-Se', *Crystal Growth and Design*. 10, 3983 (2010)
57. **S. Pal**, *S. Chandra*, **M. H. Phan**, **P. Mukherjee** and **H. Srikanth**, "Carbon Nanostraws: Nanotubes filled with superparamagnetic particles", *Nanotechnology* 20, 485604 (2009)
58. V. Alexandrakis, G. Basina, D. Niarchos, G. Hadjipanayis, **S. Pal**, **H. Srikanth**, I. Panagiotopoulos, V. Tzitzios, "Chemical synthesis and magnetic properties of cubic CoO nanocrystals and 3D nanostructures", *Crystal Growth and Design* 9, 3353 (2009)
59. **M. H. Phan**, *M. B. Morales*, C. N. Chinnasamy, V. G. Harris and **H. Srikanth**, "Magnetism and magnetocaloric effect in gadolinium-iron garnet nanostructures", *Journal of Physics D: Applied Physics* 42, 115007 (2009)
60. **S. Pal**, *M. B. Morales*, **P. Mukherjee**, **H. Srikanth**, "Synthesis and magnetic properties of gold-coated iron oxide nanoparticles", *Journal of Applied Physics* 105, 07B504 (2009)
61. *M. B. Morales*, **M. H. Phan**, **S. Pal**, *N. A. Frey* and **H. Srikanth**, "Particle blocking and carrier fluid freezing effects on magnetic properties of Fe₃O₄-based ferrofluids", *Journal of Applied Physics* 105, 07B511 (2009)
62. *N. A. Frey*, *M. H. Phan*, **H. Srikanth**, *S. Srinath*, C. Wang, S. Sun, "Inter-particle interactions in coupled Au-Fe₃O₄ nanoparticles", *Journal of Applied Physics* 105, 07B502 (2009)
63. *D. Mukherjee*, *R. Hyde*, **T. Dhakal**, **H. Srikanth**, **P. Mukherjee**, and **S. Witanachchi**. "Investigation of the Pb Depletion in Single and Dual Pulsed Laser Deposited Epitaxial PZT Thin Films and Their Structural Characterization", in *Multiferroic and Ferroelectric Materials* (A. Gruverman, C.J. Fennie, I. Kunishima, B. Noheda, T.W. Noh, eds.) *Materials Research Society Symposium Proceedings*, 1199, 1199-F03-37 (2009)
64. **T. Dhakal**, *D. Mukherjee*, *R. Hyde*, **H. Srikanth**, **P. Mukherjee**, and **S. Witanachchi** "Enhancement in Ferroelectricity in V-Doped ZnO Thin Film Grown Using Laser Ablation", in *Multiferroic and Ferroelectric Materials* (A. Gruverman, C.J. Fennie, I. Kunishima, B. Noheda, T.W. Noh, eds.) *Materials Research Society Symposium Proceedings*, 1199, 1199-F03-44 (2009)
65. *D. Mukherjee*, **T. Dhakal**, **H. Srikanth**, **P. Mukherjee**, and **S. Witanachchi**, "Growth of Epitaxial ZnO:Mn/ZnO:V Heterostructures and Ferroelectric-Ferromagnetic Characterization", *Materials Research Society Symposium Proceedings*, 1161, 1161-I02-02, 2009
66. *H. Kirby*, J. Martin, **A. Datta**, L. Chen, **G.S. Nolas**, "Enhanced thermoelectric properties in PbTe nanocomposites", *Materials Research Society Symposium Proceedings*, 1166, 1166-NO3-27 (2009)
67. P. Poddar, *M. B. Morales*, *N. A. Frey*, S. A. Morrison, E. E. Carpenter and **H. Srikanth**, "Transverse susceptibility study of the effect of varying dipolar interactions on anisotropy peaks in a 3D assembly of soft ferrite nanoparticles", *Journal of Applied Physics* 104, 063901 (2008)

68. S. Srinath, P. Poddar, D. S. Sidhaye, B. L. V. Prasad, J. Gass and **H. Srikanth**, “Static and dynamic magnetic properties of Co nanoparticles”, **Journal of Nanoscience and Nanotechnology** **8**, 4086 (2008)
69. **G.S. Nolas**, M. Beekman, J. Martin, D. Wang and **X.S. Lin**, “Bulk materials research for thermoelectric power generation applications”, **Materials Research Society Symposium Proceedings**, Vol. 1044, 1044-U05-01 (2007)
70. J. Martin, S. Stefanoski, L. Wang, L. Chen and **G.S. Nolas**, “Synthesis and thermoelectric properties of lead chalcogenide nanocomposites”, **Materials Research Society Symposium Proceedings**, Vol. 1044, 1044-U01-05 (2007)

Journal Publications (under review / in preparation to be submitted):

71. S. Chandra, **N. A. Frey-Huls**, **M. H. Phan**, S. Srinath, **H. Srikanth**, M. A. Garcia, Y. Lee, C. Wang, S. Sun and O. Iglesias, “Exchange Bias in Au-Fe₃O₄ Composite Nanoparticles” *Nanotechnology* (under review)
72. P. Colostro, A. Chen, J. Devkota, **H. Srikanth**, **M.H. Phan**, “Sensing RF and microwave energy with fiber Bragg grating heating via soft ferromagnetic glass-coated microwires,” *Sensors and Actuators A: Physical* 2013 (under review)
73. H. Khurshid, Z. N. Porshokouh, **P. Mukherjee**, **M. H. Phan**, and **H. Srikanth**, “Impacts of surface spins and inter-particle interactions on the magnetism of hollow γ -Fe₂O₃,” *Journal of Applied Physics* 2013 (under review)
74. J. Devkota, J. Wingo, T. T. T. Mai, X. P. Nguyen, N. T. Huong, **P. Mukherjee**, **H. Srikanth**, and **M. H. Phan**, “A highly sensitive magnetic biosensor for detection and quantification of anticancer drugs tagged to superparamagnetic nanoparticles” *Journal of Applied Physics* 2013 (under review)
75. J. Devkota, P. Colosimo, A. Chen, V.S. Lari, **H. Srikanth**, and **M.H. Phan**, “Tailoring magnetic and microwave absorption properties of glass-coated soft ferromagnetic amorphous microwires for microwave energy sensing”, *Journal of Applied Physics* 2013 (under review)
76. **A. Datta**, **D. Mukherjee**, **S. Witanachchi** and **P. Mukherjee**, "Hierarchically-Ordered Nano-Heterostructured PZT Thin Films with Enhanced Ferroelectric Properties", (under review *Advanced Functional Materials*).
77. **D. Mukherjee**, M. Hordagoda, P. Lampen, **M. H. Phan**, **H. Srikanth**, **S. Witanachchi**, and **P. Mukherjee**, "Enhanced magnetism and ferroelectricity in epitaxial Pb(Zr_{0.52}Ti_{0.48})O₃ / CoFe₂O₄ / La_{0.7}Sr_{0.3}MnO₃ multiferroic heterostructures grown using dual-laser ablation technique", (under review *Journal of Applied Physics*)
78. **A. Datta**, **D. Mukherjee**, **S. Witanachchi** and **P. Mukherjee**, "On-the-surface photoconductive response of pelletized thin In₂S₃ nanosheets", (under review *Materials Research Bulletin*).
79. A. Ruiz, A. Chaturvedi, K. Stojak, **P. Mukherjee**, **H. Srikanth** and **M. H. Phan**, “Magneto-

impedance as Chemical and Biosensing Probes”, *Sensors* – 2012 (Invited paper, in preparation).

80. **J. Devkota, D. Mukherjee, A. Ruiz, S. Witanachchi, P. Mukherjee, H. Srikanth, and M.H. Phan**, “Impact of coating amorphous and crystalline cobalt ferrite films on the magneto-impedance response of a soft ferromagnetic amorphous ribbon” *Applied Surface Science* 2013 (to be submitted)
81. **B. Duong, H. Khurshid, P. Gangopadhyay, J. Devkota, K. Stojak, H. Srikanth, L. Tetard, R. Norwood, N. Peyghambarian, M.H. Phan, and J. Thomas**, “Enhanced Magnetism of Highly Ordered Magnetite Nanoparticle-filled Nanohole Arrays” *ACS Nano* 2013 (to be submitted)
82. **H. Khurshid, P. Mukherjee, M. H. Phan, and H. Srikanth**, “Tuning Exchange Bias in Fe/ α -Fe₂O₃ Core-Shell Nanoparticles: Impacts of Interfacial Frozen and Surface Spins”, *Applied Physics Letters* 2013 (to be submitted)

Conference Presentations (contributed):

1. **D. Mukherjee, M. Hordagoda, H. Srikanth, S. Witanachchi, and P. Mukherjee**, "Enhanced surface-quality, magnetic and ferroelectric properties in epitaxial PZT/LSMO multiferroic heterostructures grown using dual-laser ablation", American Ceramic Society, 38th International Conference and Exposition on Advanced Ceramics and Composites, Daytona, FL (Jan. 26th-31st, 2014) (accepted)
2. **D. Mukherjee, M. Hordagoda, M. H. Phan, H. Srikanth, S. Witanachchi, and P. Mukherjee**, "Enhanced magnetism and ferroelectricity in high-quality epitaxial PbZr_{0.52}Ti_{0.48}O₃/CoFe₂O₄/La_{0.7}Sr_{0.3}MnO₃ multiferroic heterostructures grown using the dual-laser ablation technique" Magnetism and Magnetic Materials, 58th Annual Conference on MMM, Denver, CO (Nov. 4th - 8th, 2013) (accepted)
3. **D. Mukherjee, M. Hordagoda, M. H. Phan, H. Srikanth, S. Witanachchi, and P. Mukherjee**, " Strain modification of magnetization using the structural transitions of the ferroelectric BaTiO₃ sandwich-layer in high-quality epitaxial CoFe₂O₄/BaTiO₃/La_{0.7}Sr_{0.3}MnO₃ multiferroic heterostructures grown using the dual-laser ablation technique", Magnetism and Magnetic Materials, 58th Annual Conference on MMM, Denver, CO (Nov. 4th - 8th, 2013) (accepted)
4. **M. Hordagoda, D. Mukherjee, H. Srikanth, S. Witanachchi, and P. Mukherjee**, " Role of dilute La-doping in enhancing the polarization in epitaxial Pb_{1-x}La_xZr_{0.52}Ti_{0.48}O₃ thin films", American Ceramic Society, 38th International Conference and Exposition on Advanced Ceramics and Composites, Daytona, FL (Jan. 26th-31st, 2014) (accepted)
5. **H. Khurshid; S. Chandra; M.H. Phan; P. Mukherjee; H. Srikanth**, “Static and dynamic magnetic properties of hollow spherical γ -Fe₂O₃ nanoparticles”, The 58th Annual Magnetism and Magnetic Materials (MMM) Conference, November 4-8, 2013, Denver, Colorado, USA
6. **H. Khurshid; M.H. Phan; P. Mukherjee; H. Srikanth**, “Tuning Exchange Bias in Core/Shell Fe/ γ -Fe₂O₃ Nanoparticles: Role of Frozen Interfacial and Surface Spins”, The 58th Annual

Magnetism and Magnetic Materials (MMM) Conference, November 4-8, 2013, Denver, Colorado, USA

7. *S. Chandra*, A. Biswas; **M.H. Phan**; **H. Srikanth**, “Magnetic properties of polycrystalline and nanocrystalline NdMnO₃”, The 58th Annual Magnetism and Magnetic Materials (MMM) Conference, November 4-8, 2013, Denver, Colorado, USA
8. *J. Devkota*; *K. Stojak*; J. Wingo; T.T. Mai T; P.T. Ha; H.N. Pham; X.P. Nguyen; **P. Mukherjee**; **H. Srikanth**; **M.H. Phan**, “Synthesis, inductive heating, and magnetoimpedance-based detection of multifunctional Fe₃O₄ nanoconjugates”, The 58th Annual Magnetism and Magnetic Materials (MMM) Conference, November 4-8, 2013, Denver, Colorado, USA
9. *S. Chandra*; A. Biswas; **H. Khurshid**; W. Li; G.C. Hadjipanayis; **H. Srikanth**, “Spin freezing and inverse magnetocaloric effect in core/shell and hollow nanostructures”, The 58th Annual Magnetism and Magnetic Materials (MMM) Conference, November 4-8, 2013, Denver, Colorado, USA
10. *J. Devkota*; P. Colosimo; J. Wingo; A. Chen; **H. Srikanth**; **M.H. Phan**, “Tailoring magnetic and microwave absorption properties of glass-coated soft ferromagnetic microwires for microwave energy sensing applications”, The 58th Annual Magnetism and Magnetic Materials (MMM) Conference, November 4-8, 2013, Denver, Colorado, USA
11. *A. Ruiz*, **D. Mukherjee**, *J. Devkota*, *M. Hordagoda*, **S. Witanachchi**, **P. Mukherjee**, **H. Srikanth**, **M.H. Phan**, “Enhanced GMI effect in soft ferromagnetic amorphous ribbons with pulsed laser deposition of cobalt ferrite,” 12th Joint MMM/Intermag Conference, Jan 14 – 18, 2013, Chicago, IL, USA
12. *J. Devkota*, *A. Ruiz*, **P. Mukherjee**, **H. Srikanth**, **M.H. Phan**, W. Wang, S. Mohapatra, “Magneto-impedance biosensor with enhanced sensitivity for highly sensitive detection of superparamagnetic nanoparticles,” 12th Joint MMM/Intermag Conference, Jan 14 – 18, 2013, Chicago, IL, USA
13. *P. Lampen*, **H. Khurshid**, *S. Chandra*, **M.H. Phan**, **H. Srikanth**, J. Borchers, K. Krycka, B. Kirby, M. Wasbrough, S. Watson and W. Chen, “Surface pinning and exchange bias phenomena in core/shell structured Fe/γ-Fe₂O₃ nanoparticles”, 12th Joint MMM/Intermag Conference, Jan 14 – 18, 2013, Chicago, IL, USA
14. *S. Chandra*, **H. Khurshid**, **M.H. Phan**, and **H. Srikanth**, “Asymmetric hysteresis and its dependence on magnetic anisotropy in exchange biased Co/CoO core-shell nanoparticles”, 12th Joint MMM/Intermag Conference, Jan 14 – 18, 2013, Chicago, IL, USA
15. *H. Khurshid*, W. Li, *S. Chandra*, **M.H. Phan**, G. Hadjipanayis, **P. Mukherjee**, and **H. Srikanth**, “Shape controlled synthesis and magnetic properties of core/shell structured FeO/Fe₃O₄ nanoparticles”, 12th Joint MMM/Intermag Conference, Jan 14 – 18, 2013, Chicago, IL, USA

16. **K. Stojak, S. Chandra, H. Khurshid, M.H. Phan, H. Srikanth**, “Enhanced Magnetic Properties in Nanoparticle-Filled CNTs,” American Physical Society March Meeting 2013, March 18-22, 2013, Baltimore, MD, USA
17. **J. Devkota, A. Ruiz, P. Mukherjee, H. Srikanth, M.H. Phan, W. Wang, and S. Mohapatra**, “Detection of low-concentration superparamagnetic nanoparticles using a functional biosensor based on magneto-impedance technology,” APS March Meeting, March 18 – 22, 2013, Baltimore, MD, USA
18. **M.H. Phan, J. Devkota, H. Srikanth, P. Colostro, and A. Chen**, “Sensing RF and microwave energy with fiber Bragg grating heating via soft ferromagnetic glass-coated microwires,” APS March Meeting, March 18 – 22, 2013, Baltimore, MD, USA
19. **A. Ruiz, J. Devkota, P. Mukherjee, H. Srikanth, and M.H. Phan**, “Giant magnetoimpedance effect of Co-based magnetic ribbon as a chemical sensing probe,” APS March Meeting, March 18 – 22, 2013, Baltimore, MD, USA
20. **M. Hordagoda, D. Mukherjee, R. Hyde, D. Ghosh, J. L. Jones, P. Mukherjee, and S. Witanachchi**, "Ferroelectric properties of La doped PZT thin films deposited using dual laser ablation", *American Chemical Society (Florida Section), 2013 Florida Annual Meeting and Exposition (FAME)*, Tampa, FL (May 10th, 2013)
21. **A. Datta, D. Mukherjee, S. Witanachchi and P. Mukherjee**, "Growth of low-dimensional $\text{Pb}(\text{Zr}_x\text{Ti}_{1-x})\text{O}_3$ nanostructures by combined physical and wet-chemical synthesis approaches with enhanced electronic properties", *Materials Research Society, 2013 MRS Spring Meeting & Exhibit*, San Francisco, CA (April 1st - 5th, 2013)
22. **D. Mukherjee, M. Hordagoda, N. Bingham, H. Srikanth, S. Witanachchi, and P. Mukherjee**, "Challenges and solutions to the stoichiometric growth of high quality epitaxial $\text{PbZr}_{0.52}\text{Ti}_{0.48}\text{O}_3/\text{La}_{0.7}\text{Sr}_{0.3}\text{MnO}_3$ multiferroic heterostructures using single and dual laser ablation processes", *Materials Research Society, 2013 MRS Spring Meeting & Exhibit*, San Francisco, CA (April 1st - 5th, 2013)
23. **D. Mukherjee, R. Hyde, M. Hordagoda, N. Bingham, M. H. Phan, H. Srikanth, S. Witanachchi, and P. Mukherjee**, "Growth and characterization of high quality epitaxial $\text{La}_{0.7}\text{Sr}_{0.3}\text{MnO}_3$ thin films using dual-laser ablation technique", *Magnetism and Magnetic Materials, 12th Joint MMM/INTERMAG Conference*, Chicago, IL (Jan. 14th - 18th, 2013)
24. **M. Hordagoda, D. Mukherjee, N. Bingham, D. Ghosh, J. L. Jones, H. Srikanth, P. Mukherjee, and S. Witanachchi**, "Effect of La doping in PZT on the magnetic and ferroelectric properties of epitaxial PZT/LSMO multiferroic heterostructures", *Magnetism and Magnetic Materials, 12th Joint MMM/INTERMAG Conference*, Chicago, IL (Jan. 14th - 18th, 2013)
25. **D. Mukherjee, R. Hyde, M. Hordagoda, N. Bingham, H. Srikanth, P. Mukherjee, and S. Witanachchi**, "Magnetic properties of preferentially-oriented nanostructured cobalt ferrite thin films grown using oblique-angle pulsed laser deposition", *Magnetism and Magnetic Materials, 12th Joint MMM/INTERMAG Conference*, Chicago, IL (Jan. 14th - 18th, 2013)

26. **D. Mukherjee, M. Hordagoda, R. Hyde, D. S. Hromalik, N. Bingham, H. Srikanth, S. Witanachchi, and P. Mukherjee**, "Magnetic polaron percolation in epitaxial Mn doped ZnO thin films grown at higher doping concentrations using dual-laser ablation technique", *Magnetism and Magnetic Materials, 12th Joint MMM/INTERMAG Conference*, Chicago, IL (Jan. 14th - 18th, 2013)
27. **A. Ruiz, D. Mukherjee, J. Devkota, M. Hordagoda, P. Mukherjee, S. Witanachchi, H. Srikanth, M. H. Phan**, "Enhanced GMI effect in soft ferromagnetic amorphous ribbons with pulsed laser deposition of cobalt ferrite", *Magnetism and Magnetic Materials, 12th Joint MMM/INTERMAG Conference*, Chicago, IL (Jan. 14th - 18th, 2013)
28. **A. Ruiz, D. Mukherjee, J. Devkota, M. Hordagoda, S. Witanachchi, P. Mukherjee, H. Srikanth, M.H. Phan**, "Enhanced GMI effect in soft ferromagnetic amorphous ribbons with pulsed laser deposition of cobalt ferrite," 12th Joint MMM/Intermag Conference, Jan 14 – 18, 2013, Chicago, IL, USA
29. **J. Devkota, A. Ruiz, P. Mukherjee, H. Srikanth, M.H. Phan, W. Wang, S. Mohapatra**, "Magneto-impedance biosensor with enhanced sensitivity for highly sensitive detection of superparamagnetic nanoparticles," 12th Joint MMM/Intermag Conference, Jan 14 – 18, 2013, Chicago, IL, USA
30. **P. Lampen, H. Khurshid, S. Chandra, M.H. Phan, H. Srikanth, J. Borchers, K. Krycka, B. Kirby, M. Wasbrough, S. Watson and W. Chen**, "Surface pinning and exchange bias phenomena in core/shell structured Fe/ γ -Fe₂O₃ nanoparticles", 12th Joint MMM/Intermag Conference, Jan 14 – 18, 2013, Chicago, IL, USA
31. **S. Chandra, H. Khurshid, M.H. Phan, and H. Srikanth**, "Asymmetric hysteresis and its dependence on magnetic anisotropy in exchange biased Co/CoO core-shell nanoparticles", 12th Joint MMM/Intermag Conference, Jan 14 – 18, 2013, Chicago, IL, USA
32. **H. Khurshid, W. Li, S. Chandra, M.H. Phan, G. Hadjipanayis, P. Mukherjee, and H. Srikanth**, "Shape controlled synthesis and magnetic properties of core/shell structured FeO/Fe₃O₄ nanoparticles", 12th Joint MMM/Intermag Conference, Jan 14 – 18, 2013, Chicago, IL, USA
33. **S. Chandra, H. Khurshid, W. Li, G.C. Hadjipanayis, M.H. Phan, and H. Srikanth**, "Spin dynamics and criteria for onset of exchange bias in superspin glass Fe/ γ -Fe₂O₃ core-shell nanoparticles", 12th Joint MMM/Intermag Conference, Jan 14 – 18, 2013, Chicago, IL, USA
34. "Recent Advances and Future Research Directions in Giant Magneto-impedance Materials" Invited Talk by **M.H. Phan**, in the Special Session: "Tunable metamaterials, Giant Magnetoimpedance and GMI-related Applications" at Advanced Electromagnetics Symposium, April 16-19, 2012, Paris, France
35. **M. Hordagoda, D. Mukherjee, D. Ghosh, J. L. Jones, P. Mukherjee, S. Witanachchi**, "Growth and characterization of La doped lead zirconium titanate epitaxial thin films", Materials Research Society, 2012 MRS Fall Meeting & Exhibit, Boston, MA (Nov. 25th - 30th, 2012)

36. **D. Mukherjee, M. Hordagoda, R. H. Hyde, N. Bingham, H. Srikanth, P. Mukherjee, and S. Witanachchi**, "Epitaxial Growth of Multiferroic Heterostructures of Magnetic and Ferroelectric Oxides using the Dual-laser Ablation Technique", American Vacuum Society, 59th International AVS Symposium and Exhibition, Tampa, FL (Oct. 28th - Nov. 2nd, 2012)
37. **D. Mukherjee, M. Hordagoda, R. H. Hyde, N. Bingham, H. Srikanth, P. Mukherjee, and S. Witanachchi**, "Role of Dual-laser Ablation in Controlling Mn Oxide Precipitation during the Epitaxial Growth of Mn Doped ZnO Thin Films with Higher Doping Concentrations", American Vacuum Society, 59th International AVS Symposium and Exhibition, Tampa, FL (Oct. 28th - Nov. 2nd, 2012)
38. **C. Hettiarachchi, D. M. Feliciano, D. Mukherjee, P. Mukherjee, and S. Witanachchi**, "Improvement of Carrier Transport in PbSe Quantum Dot-Embedded Polymeric Solar Cells Fabricated by a Laser Assisted Spray Process", American Vacuum Society, 59th International AVS Symposium and Exhibition, Tampa, FL (Oct. 28th - Nov. 2nd, 2012)
39. **D. Mukherjee, S. Witanachchi, R. Hyde, and P. Mukherjee**, "Advantages of Dual-laser Ablation in the Growth of Multicomponent Thin Films", 2012 HPLA International High-Power Laser Ablation Conference, Santa Fe, NM (April 30th - May 3rd, 2012)
40. **D. Mukherjee, M. Hordagoda, R. Hyde, P. Mukherjee, H. Srikanth, and S. Witanachchi**, "Dual Laser Ablation: A Novel Technique for the In-situ Growth of Epitaxial Multiferroic Heterostructures of Ultra-thin Films", NANOSMAT-USA-2012 Conference, Tampa, FL (March 27th - 30th, 2012)
41. **C.L. Hettiarachchi, D. Ferizovic, D. Mukherjee, R. Hyde, S. Witanachchi, and P. Mukherjee**, "Structural and Optical Properties of Surfactant-free Coatings of PbSe Quantum Dots deposited by a Laser Assisted Spray Process", NANOSMAT-USA-2012, Tampa, FL, (March 27th - 30th, 2012)
42. **M. Hordagoda, D. Mukherjee, R. Hyde, P. Mukherjee, and S. Witanachchi**, "Growth and Characterization of Epitaxial Pb(Zr_{0.52}Ti_{0.48})O₃ Ultra-thin Films using a Novel Dual Laser Deposition Technique", NANOSMAT-USA-2012, Tampa, FL, (March 27th - 30th, 2012)
43. **A. Datta, M. Hordagoda, D. Mukherjee, S. Witanachchi, and P. Mukherjee**, "Growth of one-dimensional Pb(ZrxTi1-x)O₃ nanostructures by combined physical and wet-chemical synthesis approaches for enhanced ferroelectric properties", NANOSMAT-USA-2012, Tampa, FL, (March 27th - 30th, 2012)
44. **J. Devkota, A. Ruiz, H. Khurshid, A. Chaturvedi, A. Puri, P. Mukherjee, H. Srikanth, M.H. Phan**, "Detection of Functional Magnetic Nanoparticles using Ferromagnetic Microwires-based Giant Magneto-impedance Sensors", Nano-Bio Collaborative International Conference, March 22-24, 2012, Tampa, Florida, USA
45. **A. Ruiz, J. Devkota, A. Chaturvedi, K. Stojak, P. Mukherjee, H. Srikanth, M.H. Phan**, "GMI sensors with superparamagnetic nanoparticles for highly sensitive detection of cancer cells and

biomolecules”, Nano-Bio Collaborative International Conference, March 22-24, 2012, Tampa, Florida, USA

46. **K. Stojak, P. Mukherjee, H. Srikanth, M.H. Phan**, “Synthesis of carbon nanotubes filled with magnetic nanoparticles for biomedical applications”, Nano-Bio Collaborative International Conference, March 22-24, 2012, Tampa, Florida, USA
47. **K. Stojak, S. Chandra, A. Ruiz, M.H. Phan, P. Mukherjee, and H. Srikanth**, “Filled Carbon Nanotubes with Novel Magnetic Properties for Biomedical Applications”, NanoFlorida Conference, September 28-29, 2012 Tampa, Florida, USA
48. **J. Devkota, A. Ruiz, P. Mukherjee, H. Srikanth, M.H. Phan, C. Wang and S. Mohapatra**, “Amorphous Ribbon-based Magnetic Biosensor with Enhanced Sensitivity for Highly Sensitive Detection of Nanomag-D Beads”, NanoFlorida Conference, September 28-29, 2012 Tampa, Florida, USA
49. **A. Popescu, A. Datta, G.S. Nolas and L. Woods**, ‘Tailoring Thermoelectric Properties of Bismuth: Theoretical Investigations’, American Institute of Physics Conference Proceedings 1449, 9th European Conference on Thermoelectrics, pp. 45 – 48, 2012.
50. **A. Ruiz, J. Devkota, P. Mukherjee, H. Srikanth, M.H. Phan**, “Improving the magnetic response of giant magneto-impedance in single and multi-wire systems”, NanoFlorida Conference, September 28-29, 2012 Tampa, Florida, USA
51. **A. Chaturvedi, N. Laurita, K. Stojak, M.H. Phan, P. Mukherjee, and H. Srikanth**, “Carbon nanotube-based gas sensors using the magnetoimpedance effect”, 56th Annual MMM Conference on Magnetism and Magnetic Materials, October 30 to November 3, 2011, Scottsdale, Arizona, USA
52. **N. Laurita, A. Chaturvedi, P. Jayathilaka, M.H. Phan, H. Srikanth, and C. W. Miller**, “Impact of field-induced exchange anisotropy on the magnetoimpedance effect in FeMn/Metglas ribbons bilayer structures”, 56th Annual MMM Conference on Magnetism and Magnetic Materials, October 30 to November 3, 2011, Scottsdale, Arizona, USA
53. **K. Stojak, S. Pal, H. Srikanth, C.Morales, J. Dewdney, J.Wang and T.Weller**, “Magnetic Polymer Nanocomposites with Tunable Microwave and RF Properties”, 56th Annual MMM Conference on Magnetism and Magnetic Materials, October 30 to November 3, 2011, Scottsdale, Arizona, USA
54. **D. Mukherjee, R. Hyde, M. H. Phan, N. Bingham, H. Srikanth, P. Mukherjee and S. Witanachchi**, “Enhanced ferroelectricity and ferromagnetism in epitaxial $\text{PbZr}_{0.52}\text{Ti}_{0.48}\text{O}_3/\text{La}_{0.7}\text{Sr}_{0.3}\text{MnO}_3$ thin films with a CoFe_2O_4 sandwich layer” *Materials Research Society, 2011 MRS Fall Meeting & Exhibit*, Boston, MA (Nov. 28th - Dec 2nd, 2011)
55. **D. Mukherjee, R. Hyde, M. H. Phan, N. Bingham, H. Srikanth, P. Mukherjee and S. Witanachchi**, “Hetero-epitaxial Growth of Ferromagnetic Mn doped ZnO Thin Films on Al_2O_3

- (0001) Substrates with Higher Doping Concentrations using Dual-laser Deposition”, *Materials Research Society, 2011 MRS Fall Meeting & Exhibit*, Boston, MA (Nov. 28th - Dec. 2nd, 2011)
56. **D. Mukherjee, R. Hyde, P. Mukherjee and S. Witanachchi**, “Dual-laser Ablation for the Growth of Epitaxial $\text{Pb}(\text{Zr}_{0.52}\text{Ti}_{0.48})\text{O}_3$ Ultrathin Films”, *Materials Research Society, 2011 MRS Fall Meeting & Exhibit*, Boston, MA (Nov. 28th - Dec. 2nd, 2011)
 57. **D. Mukherjee, R. Hyde, N. Bingham, M. H. Phan, H. Srikanth, P. Mukherjee and S. Witanachchi**, “Ziz-zag Interface and Strain-influenced Ferromagnetism in Epitaxial $\text{Mn}_3\text{O}_4/\text{La}_{0.7}\text{Sr}_{0.3}\text{MnO}_3$ Thin Films grown on MgO (100) and SrTiO_3 (100) substrates”, *Magnetism and Magnetic Materials, 56th Annual MMM Conference*, Scottsdale, AZ (Oct. 30th – Nov. 3rd 2011)
 58. **D. Mukherjee, P. Mukherjee, H. Srikanth, and S. Witanachchi**, “Carrier-mediated Interaction of Magnetic Moments in Oxygen Vacancy Controlled Epitaxial Mn doped ZnO Thin Films”, *Magnetism and Magnetic Materials, 56th Annual MMM Conference*, Scottsdale, AZ (Oct. 30th – Nov. 3rd 2011)
 59. **D. Mukherjee, R. Hyde, N. Bingham, M. H. Phan, H. Srikanth, P. Mukherjee, and S. Witanachchi**, “Interfacial magnetoelectric coupling in epitaxial LSMO and Mn doped PZT heterostructures”, *Materials Research Society, 2011 MRS Spring Meeting & Exhibit*, San Francisco, CA (April 25th - 29th, 2011)
 60. *L. Nicholas, A. Chaturvedi, K. Stojak, S. Chandra, M. H. Phan, H. Srikanth*, “Giant magnetoimpedance in magnetic nanoparticles patterned Co-based amorphous ribbons for biosensing applications”, the APS March Meeting, March 21 - 25, 2011, Dallas, Texas
 61. *A. Chaturvedi, T. Dhakal, S. Witanachchi, M.H. Phan, H. Srikanth*, and A.T. Le, “Correlation between magnetic softness, sample surface and magnetoimpedance in $\text{Co}_{69}\text{Fe}_{45}\text{X}_{15}\text{Si}_{10}\text{B}_{15}$ (X = Ni, Al, Cr) amorphous ribbons”, the APS March Meeting, March 21 - 25, 2011, Dallas, Texas
 62. “Synthesis and characterization of graphene patterned with Fe_3O_4 nanoparticles” - *S. Chandra, K. Stojak, D. Ferizovic, M. Munoz, M. H. Phan and H. Srikanth*, the APS March Meeting, March 21 - 25, 2011, Dallas, Texas
 63. *N. Laurita, A. Chaturvedi, A. Leary, P. Jayathilaka, C. Bauer, Casey W. Miller, M.H. Phan, M.E. McHenry, H. Srikanth*, “Enhanced magnetoimpedance effect in $\text{Co}_{89}\text{Zr}_7\text{B}_4$ ribbon/ $\text{Fe}_{80}\text{Ni}_{20}$ bilayer structures”, the Symposium on Magnetic Materials for Energy Applications, February 27 to March 3, 2011, San Diego, California, USA
 64. **D. Mukherjee, T. Dhakal, H. Srikanth, P. Mukherjee, and S. Witanachchi**, “Complementary Ferromagnetic Mechanisms in Mn doped ZnO Thin films deposited using Pulsed Laser Ablation”, *American Physical Society, APS March Meeting 2011*, Dallas, TX (March 21st - 25th, 2011).
 65. **D. Mukherjee, T. Dhakal, R. Hyde, P. Mukherjee, H. Srikanth, and S. Witanachchi**, “Effect of substrate induced strains on the magnetic and ferroelectric properties of epitaxial bilayer thin

films of lead zirconate titanate and cobalt ferrite”, *American Physical Society, APS March Meeting 2011*, Dallas, TX (March 21st - 25th, 2011).

66. J. Duscha, R. Hyde, **D. Mukherjee**, **S. Witanachchi**, “Growth and characterization of $\text{Ba}_8\text{Ga}_{16}\text{Ge}_{30}$ Type I clathrate thin films grown by pulsed laser deposition”, *American Physical Society, APS March Meeting 2011*, Dallas, TX (March 21st - 25th, 2011).
67. **A. Datta**, K. Wei, A. Popescu, **L. Woods** and **G.S. Nolas**, ‘Processing Dependence on the Thermoelectric Properties of Nanostructured Thermoelectric Materials’, Materials Research Society Conference, November 29, Boston, Massachusetts, 2011.
68. **A. Datta**, ‘Bottom-Up Strategy For Thermoelectric Nanocomposites’, American Physical Society Annual Meeting, Dallas, Texas, March 22, 2011.
69. **George S. Nolas**, **Anuja Datta**, Jagannath Paul, Adrian Popescu, and Lilia Woods "Bottom-Up Approach for the Synthesis of Thermoelectric Materials with Nano-Scale Domains" 35th International Conference and Exposition on Advanced Cermics and Composites, Daytona Beach, Florida, January 27, 2011.
70. A. Chaturvedi, S. Stefanoski, **M. H. Phan**, **G. Nolas** and **H. Srikanth**, “Magnetocaloric effect and refrigeration capacity in $\text{Eu}_8\text{Ga}_{16}\text{Ge}_{30}$ – EuO composites”, 54th annual Magnetism and Magnetic Materials (MMM) conference, Nov. 14-18, 2010, Atlanta GA
71. S. Chandra, A. Figueroa, **M. H. Phan**, **H. Srikanth**, B. Ghosh and A. K. Raychaudhuri, “Phase coexistence and magnetic anisotropy in polycrystalline and nanocrystalline LaMnO_{3+d} ”, 54th annual Magnetism and Magnetic Materials (MMM) conference, Nov. 14-18, 2010, Atlanta GA
72. A. Chaturvedi, A. Leary, N. Laurita, **M. H. Phan**, M. E. McHenry and **H. Srikanth**, “Giant magnetoimpedance and field sensitivity in amorphous and nanocomposite $(\text{Co}_{1-x}\text{Fe}_x)_{89}\text{Zr}_7\text{B}_4$ ribbons”, 54th annual Magnetism and Magnetic Materials (MMM) conference, Nov. 14-18, 2010, Atlanta GA
73. K. Stojak, **S. Pal**, **H. Srikanth**, S. Skidmore, C. Morales, J. Dewdney, J. Wang and T. Weller, “Magnetic polymer composites with tunable microwave properties”, APS March meeting, Portland OR (March 15 – 19, 2010)
74. S. Chandra, N. A. Frey, **M. H. Phan**, **H. Srikanth**, C. Wang and S. Sun, “Probing magnetic anisotropy and exchange bias in coupled $\text{Au-Fe}_3\text{O}_4$ nanoclusters”, APS March meeting, Portland OR (March 15 – 19, 2010)
75. **S. Pal**, K. Stojak, S. Chandra, **M. H. Phan**, **P. Mukherjee** and **H. Srikanth**; “Fabrication and magnetic properties of CNT filled with Fe_3O_4 nanoparticles”, APS March meeting, Portland OR (March 15 – 19, 2010)
76. **M. H. Phan**, A. Chaturvedi, S. Stefanoski, H. Kirby. **G. S. Nolas** and **H. Srikanth**; “Ferromagnetism and large MCE in EuGaGe clathrates”, APS March meeting, Portland OR (March 15 – 19, 2010)

77. *D. Mukherjee, R. Hyde, T. Dhakal, H. Srikanth, P. Mukherjee, and S. Witanachchi*, “Dual-Laser Deposition of Stoichiometric PZT/CoFe₂O₄ Epitaxial Heterostructures”, *Materials Research Society, 2010 MRS Spring Meeting & Exhibit*, San Francisco, CA (April 5th - 9th, 2010)
78. *A. Chaturvedi, M. H. Phan, H. Srikanth, A. Leary and M. McHenry*; “Optimization of GMI in amorphous CoFeZrB ribbons”, APS March meeting, Portland OR (March 15 – 19, 2010)
79. *S. Pal, K. Stojak, S. Chandra, M. H. Phan, P. Mukherjee and H. Srikanth*, “High-aspect ratio magnetic nanotubes, ”11th joint MMM-INTERMAG conference, Washington DC (Jan 18-22, 2010)
80. *D. Mukherjee, R. Hyde, T. Dhakal, S. Hariharan, P. Mukherjee, and S. Witanachchi*, “Enhanced Ferroelectric Properties in Highly Epitaxial and Fatigue-Resistant PZT Thin Films Deposited Using Dual-laser Ablation”, *Materials Research Society, 2010 MRS Fall Meeting & Exhibit*, Boston, MA (Nov. 29th - Dec. 3rd, 2010)
81. *A. Datta, J. Paul, A. Popescu, L. Woods, G.S. Nolas*, “Synthesis and Transport properties of Dimensional Nanocomposite Chalcogenides”, *The American Physical Society Annual Meeting*, March 15-19, 2010, Portland, Oregon.
82. *A. Datta, J. Paul and G.S. Nolas*, “Solution Phase Synthesis Routes In Preparing Chalcogenide Nanocomposites With Enhanced Thermoelectric Properties”, *The 86th American Chemical Society Florida Annual Meeting and Exposition*, May 13-15, 2010.
83. *H. Kirby, J. Martin, L. Chen, G.S. Nolas*, “Synthesis and Characterization of Doped and Undoped PbTe Nanocomposites”, *The 86th American Chemical Society Florida Annual Meeting and Exposition*, May 13-15, 2010.
84. *D. Mukherjee, R. Hyde, T. Dhakal, S. Hariharan, P. Mukherjee, and S. Witanachchi*, “Investigation of the Pb Depletion in Single and Dual Pulsed Laser Deposited Epitaxial PZT Thin Films and Their Structural Characterization”, *Materials Research Society, 2009 MRS Fall Meeting & Exhibit*, Boston, MA (Nov. 3rd - Dec. 4th, 2009)
85. *T. Dhakal, D. Mukherjee, R. Hyde, H. Srikanth, P. Mukherjee, and S. Witanachchi*, “Enhancement in Ferroelectricity in V-Doped ZnO Thin Film Grown Using Laser Ablation”, *Materials Research Society, 2009 MRS Fall Meeting & Exhibit*, Boston, MA (Nov. 3rd - Dec. 4th, 2009)
86. *D. Mukherjee, T. Dhakal, R. Hyde, P. Mukherjee, S. Hariharan, and S. Witanachchi*, “Growth of Epitaxial ZnO:Mn/ZnO:V Heterostructures and Ferroelectric-Ferromagnetic Characterization”, *Materials Research Society, 2009 MRS Spring Meeting & Exhibit*, San Francisco, CA (April 13th - 17th, 2009)
87. *M. Morales, M.H. Phan, S. Pal and H. Srikanth*, “Origin of glass-like relaxation in Fe₃O₄ ferrofluids”, 2009 INTERMAG Conference, Sacramento CA (May 4-8, 2009)

88. **M. H. Phan**, *M. B. Morales*, C. N. Chinnasamy, B. Latha, V. G. Harris and **H. Srikanth**, “Magnetic frustration and particle size effects in nanostructured gadolinium iron garnets”, 2009 INTERMAG Conference, Sacramento CA (May 4-8, 2009)
89. *M. B. Morales*, **M. H. Phan**, *N. A. Frey*, **S. Pal** and **H. Srikanth**, “Origin of magnetic anomalies and relaxation mechanisms in ferrofluids”, APS March Meeting, Pittsburgh, PA (March 16-20, 2009)
90. **M. H. Phan**, *M. B. Morales*, **H. Srikanth**, C. N. Chinnasamy and V. G. Harris, “Competing effects of blocking and spin frustration in nanostructured gadolinium iron garnets”, APS March Meeting, Pittsburgh, PA (March 16-20, 2009)
91. *K. Stojak*, **S. Pal**, M. J. Miner, **H. Srikanth**, S. Skidmore, J. Wang and T. Weller, “Functional nanocomposite polymer films with uniform nanoparticle dispersions”, APS March Meeting, Pittsburgh, PA (March 16-20, 2009)
92. *A. Chaturvedi*, *S. Stefanoski*, **M. H. Phan**, G. T. Woods, **G. Nolas** and **H. Srikanth**, “Magnetic transitions and giant magnetocaloric effect in EuGaGe clathrates”, 2009 APS March Meeting, Pittsburgh, PA (March 16-20, 2009)
93. *H. Kirby*, J. Martin, **A. Datta**, L. Chen, **G.S. Nolas**, ‘Enhanced thermoelectric properties in PbTe nanocomposites’, *Mater. Rec. Soc.*, Boston, 2009.
94. Joshua Martin, **Anuja Datta**, Hillary Kirby, Adrian Popescu, Lilia Woods, Nathan Crane and **George S Nolas** “Enhanced Power Factor in Nanocomposite Chalcogenides”. DOE Thermoelectric Applications Workshop, San Diego, October 1, 2009.
95. **M. B. Morales**, *N. A. Frey*, **M. H. Phan** and **H. Srikanth**, “Magnetic properties of Fe₃O₄ and CoFe₂O₄ based ferrofluids” 52nd annual Magnetism and Magnetic Materials (MMM) conference, Tampa, FL (November 7 – 11, 2008)
96. *M. B. Morales*, *N. A. Frey*, P. Poddar and **H. Srikanth**, “Transverse susceptibility probe of magnetic anisotropy and dipolar interactions in ferrite nanoparticles” 2008 APS March meeting (New Orleans, LA)
97. **H. Srikanth**, *M. B. Morales*, *N. A. Frey*, P. Poddar, **M. H. Phan**, “Radio frequency transverse susceptibility in magnetic nanoparticles”, INTERMAG conference, May 4 – 8, 2008 (Madrid, Spain)
98. “Magnetism and magnetocaloric effect in ferrite and garnet nanoparticles” –**Invited talk by H. Srikanth** at the workshop on “Research trends in novel magnets for electromagnetic applications” –Santorini, Greece (Sep 2-5, 2008)
99. **M. H. Phan**, *M. B. Morales*, *N. A. Frey* and **H. Srikanth** , “Origin of magnetic anomalies in the liquid, frozen and mixed states of ferrofluids” the 53rd annual MMM conference, Nov. 2008 (Austin, TX)

100. **S. Pal, M. B. Morales, M. H. Phan, P. Mukherjee and H. Srikanth**, “Synthesis and magnetic properties of gold-coated core-shell Au@Fe₃O₄ nanoparticles”, the 53rd annual MMM conference, Nov. 2008 (Austin, TX)
101. **N. A. Frey, M. H. Phan, S. Srinath, C. Wang, S. Sun and H. Srikanth**, “Anomalous magnetism and exchange bias in coupled Au-Fe₃O₄ nanoparticles”, 2008 MRS Fall meeting, Dec. 1-5, 2008 (Boston, MA)
102. **M. H. Phan, M. B. Morales, S. Pal, N. A. Frey and H. Srikanth**, “Origin of magnetic anomalies in the liquid, frozen and mixed states of ferrofluids”, 53rd annual MMM conference, Nov. 10-14, 2008 (Austin, TX)
103. **M.H. Phan, M. B. Morales, H. Srikanth, C. N. Chinnasamy and V. G. Harris**, “Magnetization dynamics and magnetocaloric effect in nanostructured Gd₃Fe₅O₁₂ garnets” , –53rd annual MMM conference, Nov. 10-14, 2008 (Austin, TX)
104. **S. Pal, M. B. Morales, M. H. Phan, P. Mukherjee and H. Srikanth**, “Synthesis and magnetic properties of gold-coated core-shell Au@Fe₃O₄ nanoparticles”, 53rd annual MMM conference, Nov. 10-14, 2008 (Austin, TX)
105. **M. J. Miner, S. Pal, K. Stojak, H. Srikanth, S. Skidmore, J. Wang and T. Weller**, “Synthesis of surface functionalized magnetic nanoparticles and their polymer composites”, 53rd annual MMM conference, Nov. 10-14, 2008 (Austin, TX).
106. **D. Mukherjee, T. Dhakal, R. Hyde, P. Mukherjee, S. Hariharan, and S. Witanachchi**, “Growth of Epitaxial CoFe₂O₄/PZT Heterostructures and Ferroelectric-Ferromagnetic Characterization”, *Materials Research Society, 2008 MRS Fall Meeting*, Boston, MA (Dec. 1st - 5th, 2008).
107. **J. Martin, L. Wang, L. Chen and G.S. Nolas**, “Enhanced thermoelectric properties of PbTe nanocomposites”, presented at the 27th International Thermoelectrics Conference, Corvallis, OR, August 7, 2008.
108. **G.S. Nolas, J. Martin, S. Stefanoski, L. Wang and L. Chen**, “Transport Properties of Lead Chalcogenide Nanocomposites”, presented at the American Physical Society March Meeting, New Orleans, LA, March 13, 2008.

Invited presentations:

1. **M.H. Phan**, "Magneto-impedance based detection of magnetic biomarkers: Opportunities and Challenges" Invited Talk at the Energy Materials Nanotechnology (EMN) Fall Meeting, December 7 – 10, 2013 Orlando, Florida, USA
2. **G. S. Nolas**, “Structure-property Relationships in Skutterudites, Clathrates and Other Open-structured Materials”, Plenary Presentation, 27th International Conference on Thermoelectrics, Corvallis, OR, August 4, 2007.

3. **G. S. Nolas**, “Enhanced Power Factor in Nanocomposite Chalcogenides”, 2009 Department of Energy Thermoelectric Applications Workshop, October 1, 2009, San Diego, California.
4. **G. S. Nolas**, “Enhanced Power Factor in Nanocomposite Materials and Magnetocaloric Materials”, Invited, 8th Pacific Rim Conference on Ceramic and Glass Technology (PacRim8), Vancouver, Canada, May 31 – June 5, 2009.
5. **G. S. Nolas**, “Thermoelectric Nanocomposite Chalcogenides”, 451st WE-Heraeus-Seminar: Nanostructured Thermoelectric Materials, February 23, 2010, Bad Honnef, Germany.
6. **G.S. Nolas**, “Bottom-up Approach for Enhanced Thermoelectric Properties in Materials with Nano-scale Domains”, Colloquium at the Department of Physics, Central Michigan University, September 2nd, 2010, Mount Pleasant, Michigan.
7. **G. S. Nolas**, “New Synthesis Techniques and Strategies for Materials Research towards Solid-state Power Conversion and Refrigeration Applications”, Seminar for Inorganic Chemistry, Max-Planck Institute for Chemical Physics of Solids, Dresden, Germany, March 18, 2011.
8. **G.S. Nolas**, “A Bottom-up Approach for Nanostructured Thermoelectrics”, Invited, 9th European Conference on Thermoelectrics, September 30, Thessaloniki, Greece, 2011.
9. **G.S. Nolas**, “New Crystal Growth Techniques in Investigating Single-crystal Inorganic Clathrates”, Invited, to be presented at the Collaborative Conference on Crystal Growth, Orlando, Florida, December 11-14, 2012.
10. **G.S. Nolas**, ‘Synthesis and Characterization of Nanostructured Thermoelectric Materials Prepared by a Two-step Bottom-up Synthetic Process’, European Materials Research Society Conference, May 15, Strasbourg, France, 2012.
11. **H. Srikanth**, Invited speaker, Defense Sciences Research Council (DSRC –a division of DARPA) sponsored ‘Advanced Materials for Enhanced Passive Components’ Workshop, Oct. 30-31, 2008
12. **H. Srikanth**, Condensed Matter Seminar, Department of Physics, University of Delaware, Newark, DE (October 14, 2008)
13. **H. Srikanth**, Center for Integrated Electronics Seminar, Department of ECE, Rensselaer Polytechnic Institute, Troy, NY (October 1, 2008)
14. **H. Srikanth**, Invited Speaker, Novel Trends in Magnetic Materials for Electromagnetic Applications Workshop, Santorini, Greece (September 3 – 5, 2008)
15. **H. Srikanth**, Invited talk, “Surface and Interface magnetism in nanostructures and heterostructures”, at the 2008 APS March meeting (New Orleans, LA)
16. **H. Srikanth**, Invited talk, “Interface magnetism in magnetic oxide nanostructures”, at the 2008 MRS Spring meeting (San Francisco, CA)

17. **H.Srikanth**, Invited Speaker, International Conference on Materials for Advanced Technologies (ICMAT 2009), Singapore (June 2009)
18. **H. Srikanth**, Invited Speaker, US-Indo Technology Forum on “New Directions and Novel Applications in Magnetism”, Mumbai, India (March 1 – 4, 2009)
19. **H. Srikanth**, Invited Speaker, “Functional magnetic nanostructures”, Workshop on Magnetic Nanomaterials, S. N. Bose Center for Basic Sciences, Kolkata, India (January 26-28, 2009)
20. **H. Srikanth**, Condensed Matter Seminar, Department of Physics, University of Florida, Gainesville FL (November 16 2009)
21. **H. Srikanth**, Colloquium, Advanced Materials Research Institute, University of New Orleans, October 6, 2009
22. **H. Srikanth**, Invited Speaker, Conference on Strongly Correlated Materials (iConQuest 2010), New Delhi, INDIA (December 20-23, 2010)
23. **H. Srikanth**, Seminar, Northwestern University, Department of Physics, Evanston, IL (Oct. 14, 2010)
24. **H. Srikanth**, Invited Speaker, Symposium on Magnetic and Transport Properties of Oxides, CIMTEC 2010, Montecatini Terme, ITALY (June 6-11, 2010)
25. **H. Srikanth**, Seminar, “Functional magnetic nanostructures”, CNR-ISMN, Bologna, ITALY (June 11, 2010)
26. **H. Srikanth**, Seminar, “Functional magnetic nanostructures”, University of Uppsala, Uppsala, SWEDEN (June 4, 2010)
27. **H. Srikanth**, Seminar, “Functional magnetic nanostructures”, KTH –Royal Institute of Technology, Stockholm, SWEDEN (June 3, 2010)
28. **H. Srikanth**, Seminar, “Functional magnetic nanostructures”, IFW-Dresden, Dresden, GERMANY (May 31, 2010)
29. **H. Srikanth**, Invited Speaker, Focus Topic on “Bulk properties of oxides”, APS March Meeting, Portland, OR (March 15-19, 2010); Title “Magnetism in complex oxides probed by transverse susceptibility and magnetocaloric effect”
30. **H. Srikanth**, Invited Speaker, “Magnetocaloric effect in oxide nanostructures” - H. Srikanth and M. H. Phan, the Symposium on Magnetic Materials for Energy Applications, February 27 to March 3, 2011, San Diego, California, USA (Invited Talk)
31. **H. Srikanth**, Invited Speaker, Multifunctional Materials-6 Workshop organized by DoD agencies, Kodiak, Alaska (July 31-Aug03, 2011)
32. **H. Srikanth**, Seminar on magnetic nanostructures, CSIC, University of Autonoma – Madrid, Spain (May 30, 2011)

33. **H. Srikanth**, Seminar, Cavendish Lab, Cambridge University, UK (June 6, 2011)
34. **H. Srikanth**, Seminar, Physics Department, Imperial College, London UK (June 7, 2011)
35. **H. Srikanth**, Invited Speaker, Soft Magnetic Materials (SMM 20) Conference, Kos Island, Greece (September 2011)
36. **H. Srikanth**, Invited talk, “Tunable Microwave Properties in Magnetic Polymer Nanocomposites”, 12th Joint MMM/Intermag Conference, Jan 14 – 18, 2013, Chicago, IL, USA

Patent-related activity:

1. **G.S. Nolas**, "Bulk Dimensional Nanocomposites for Thermoelectrics Applications", Patent Pending, US Provisional Patent Application # 12/104,016, filed April 2, 2009.

Other noteworthy professional activities by CIFM researchers:

- George Nolas was elected Fellow of the American Association for the Advancement of Science (AAAS) in 2012.
- Hari Srikanth was nominated as a Member of the IEEE Magnetics Society Administrative Committee. Election results due in October 2008.
- FML researcher Dr. Natalie Frey was selected with partial financial support from NSF to present her CIFM-affiliated research at the Gordon Research Conference on Magnetic Nanostructures (Aussois, France, Aug 31-Sept 8, 2008)
- Hari Srikanth is a member of the Program Committee and a Publication Editor for the 53rd Magnetism and Magnetic Materials (MMM) conference held in Austin, TX (Nov. 2008)
- Hari Srikanth, Scientific Committee Member, Symposium E: Magnetic materials at the nanoscale, 11th International Conference on Advanced Materials (ICAM 2009), Rio de Janeiro, Brazil (Sept 2009)
- Hari Srikanth co-organized the symposium on ‘Functional oxide nanostructures and heterostructures’ at the 2010 MRS Spring Meeting in April 2010 in San Francisco
- Hari Srikanth served as a Program Committee member and Publication Editor for the annual Magnetism and Magnetic Materials (MMM) conference held in Austin, TX in Nov. 2008. He continues to serve as a publication editor for the 2010 joint MMM/Intermag conference in January 2010 in Washington DC
- Hari Srikanth was an Invited Speaker, “Functional Magnetic Nanostructures” –Evening with a Scholar lecture to the Tampa Bay community leaders/entrepreneurs, November 6, 2009
- Hari Srikanth, Publication Chair and Steering Committee Member, 2011 MMM Conference, Scottsdale, AZ (November 2011)

- Hari Srikanth, Session Chair, Session AT: Magnetocaloric Materials I, joint MMM/INTERMAG conference, January 2010, Washington DC
- Hari Srikanth, Co-organizer of MRS 2010 Spring Meeting Symposium N, “Functional oxide nanostructures and heterostructures”, April 2010, San Francisco, CA
- Hari Srikanth, Publications Editor of 11th Joint INTERMAG/MMM conference, Washington DC, January 2010

Students graduated:

12 CIFM students (11 of whom were funded from the grant) received graduate degrees including 9 Ph.D. degrees in Applied Physics and 3 Master’s degrees in Physics. They are:

- Mr. Joshua Martin graduated with a Ph.D. degree in 2008
- Ms. Marienette Morales graduated with a M.S. degree in 2009
- Mr. Devajyoti Mukherjee graduated with a Ph. D. degree in 2010
- Mr. Gayan Dedigamuwa graduated with a Ph.D. degree in 2010
- Mr. Robert Hyde graduated with a Ph.D. degree in 2011
- Mr. Anurag Chaturvedi graduated with a Ph.D. degree in 2011
- Mr. Ted Wangenstein graduated with a Ph.D. degree in 2012
- Mr. Dino Ferizovic graduated with a Ph. D. degree in 2012
- Mr. Nicholas Bingham graduated with a Ph.D. degree in 2013.
- Ms. Kristen Stojak graduated with an M.S. degree in 2013
- Mr. Jason Rejman graduated with an M.S. degree in 2013
- Mr. Sayan Chandra graduated with a Ph.D. degree in 2013.

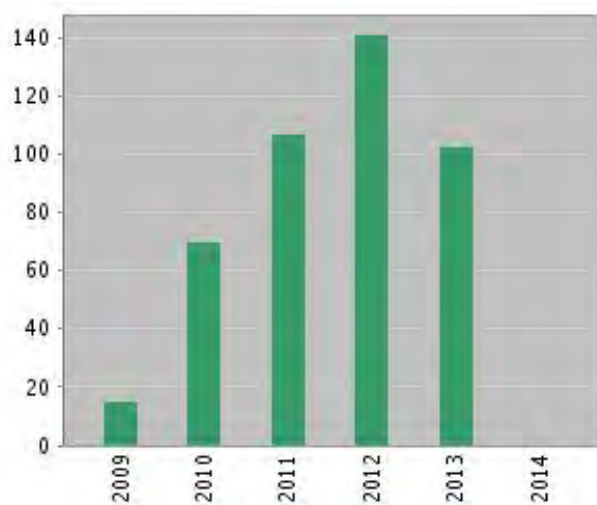
CIFM students’ awards/scholarships:

- Ph.D. student Jagannath Devkota received the GMAG-APS Student Travel Award to attend the American Physical Society Meeting, Baltimore, Maryland, March 18-22, 2013
- Undergraduate research student Alex Ruiz received the presidential graduate research fellowships for Ph.D. in Applied Physics from the University of California – Berkeley, Yale University, and Penn State University, 2013
- M.S. student Kristen Stojak and undergraduate student Alex Ruiz won the Best Poster Presentation Award at NanoFlorida conference, USF, Sept. 2012
- Ph.D. student Nicholas Bingham received the Travel Grant Award to attend the 1st Centennial of Superconductivity: Trends on Nanoscale Superconductivity and Magnetism International Workshop (June 28-July 1st, 2011), Cali, Colombia, USA; the Travel Grant Award to attend the 2nd Annual IEEE Magnetics Society Summer School (September 20-25, 2009), China
- Ph.D. student Paula Lampen received the NSF Travel Grant Award to attend the IEEE Magnetics Society Summer School (May 22-28, 2011), New Orleans, LA, USA

- Undergraduate research student Nicholas Laurita received the Ph.D. fellowship from Johns Hopkins University, 2011
- M.S. student Marienette Morales received financial support to attend the IEEE Magnetics Society summer school at UCCS, Colorado Springs in August 2008.
- M.S. student Marienette Morales completed an Industrial Practicum in Summer 2008 at SINMAT, Inc. in Gainesville, FL where she worked on ceramic nanoparticle slurries for tribological applications.

Impact of grant-funded research:

According to the Web of Science, the number of publications from this grant is higher than that from any other single grant in the history of the Physics Department at the University of South Florida. We expect many more scholarly publications during the ensuing 24-month, no-cost extension period. As of November 1, 2013 these publications have garnered 436 citations with a trajectory of increasing annual citations. The annual history of citations for publications from this grant at USF according to the Web of Science is indicated below:



V. Conclusion

Update on Milestones and their Status:

1. Chemical synthesis of magnetic nanoparticles and ferrofluids, Structural analysis, DC and AC magnetization studies.
Completed in year 1
2. Functionalization of ferrofluids with biocompatible surfactant coatings of the nanoparticles. Chemical and Physical properties characterization of the functionalized ferrofluids.
Completed in year 2
3. Studies of magnetic and hydrodynamic properties of bio-functionalized ferrofluids under flow conditions.
Completed in year 3
4. Synthesis of PEG, Dextran coated nanoparticles and clusters for hyperthermia experiments and their structural and magnetic characterization.
Initiated in year 4, will continue on no-cost extension
5. Measurements and comparative analysis of specific absorption rates and AC power losses of ferrofluids for magnetic hyperthermia applications.
Initiated in year 4, will continue on no-cost extension
6. Bifunctional metal-oxide coupled and core-shell nanostructures
Initiated in year 4, completed in year 5
7. Synthesis and characterization of Au templates with variable spacing and formation of In nano-pore structures.
Completed in year 1
8. Growth of nano-wires of inorganic compounds with variable diameters.
Completed in year 3
9. Formation of polymer nano-templates.
Completed in year 3
10. Manipulation of molecules using electrical stimulation
Completed in year 3
11. Molecular dynamics simulations of structural and mechanical properties of oxide nanostructures and density functional theory studies of electronic properties of nano-wires and nano-ribbons.
Completed in year 3
12. Development and testing of amorphous magnetic ribbons for MI-based sensing.
Completed in year 5
13. Improving the field sensitivity and figure of merit of giant magnetoimpedance (GMI) materials.
Initiated in year 4; completed in year 6
14. CVD and cluster deposition of carbon nanotube networks.
Completed in year 1
15. Structural, electrical, and capacitive measurements on nanotube networks.
Completed in year 2
16. Biosensor fabrication using carbon nanotube arrays and evaluating the potential to sense different chemicals adsorbed to the surface.
Completed in year 5

17. Theoretical modeling and simulation of toxic absorption, external fields and mechanics on carbon nanotubes.
This milestone was dropped as the emphasis was shifted to experimental investigation of carbon nanotubes for biological and environmental sensor applications. (2011 annual report)
18. Magnetoimpedance measurements and sensing of biomolecules.
Initiated in year 4, will continue on no-cost extension
19. Integrated ferroelectric-ferromagnetic high-aspect ratio nanostructures
Completed in year 6
20. Magnetic nanoparticle attachment to cell membranes.
Completed in year 1
21. Design and fabrication of lithographically patterned metallic micro wires.
Completed in year 2
22. Design and fabrication of substrates with controlled nanotopography.
Discontinued as initial results were not promising.
23. Study of cell migration, cell-substrate adhesion, and cell growth.
Merged with the project to develop an artificial Matrigel.
24. Stimuli-response studies using ECIS of magnetic nanoparticle loaded cells.
Merged with the project to develop an artificial Matrigel.
25. An integrated functional materials approach to the development of an artificial Matrigel.
Completed in year 4
26. Formation and delivery of functionalized artificial platelets for rapid cessation of internal bleeding.
Initiated in year 4, will continue on no-cost extension
27. Chemical synthesis of ferrite nanoparticles and fabrication of polymer nanocomposite films, analysis of structural, electrical and magnetic properties.
Completed in year 3
28. PLD growth of ferroelectric/ferrite heterostructures with controlled interface strain, RF and microwave measurements of polymer composites and oxide films.
Completed in year 3
29. Materials growth efforts continued with piezoelectric films containing nanoparticle inclusions, experiments to study the magneto-electric and multiferroic coupled response in materials and prototype device structures.
Completed in year 6
30. Fabricate and characterize ZnO:V, ZnO:Mn and ZnO:V/ZnO:Mn heterostructures. Investigate the multiferroic coupling in these structures.
Completed in year 4
31. Synthesis of ferroelectric-ferromagnetic nanopillar-nanoparticle structure and exploration of magnetoelectric coupling.
Completed in year 6
32. Synthesis and characterization of PbSe and PbS_xSe_{1-x} nanoparticles by microwave plasma.
Completed in year 2
33. Integration of nanoparticles with polymer and characterization of optical properties.
Completed in year 4

34. Formation of single cell device structures with nanoparticles of different sizes and characterization of the output.
Completed in year 4
35. Fabrication and evaluation of tandem structures.
Composite device structure demonstrated in year 4
36. Synthesis and characterization of InSb nanoparticles.
Discontinued since synthesis of InSb quantum dots was not successful; PbSe quantum dots are still the most efficient material for solar absorption to generate excitons.
37. Fabricate InSb-polymer hybrid solar cell structures and compare the performance with PbSe based devices
In view of above, this comparison was not needed.
38. Bulk nanocomposites: optimize synthesis parameters.
Completed in year 2
39. Core-shell approach towards optimization.
Completed in year 2
40. Structural and calorimetric analysis for thermal stability tests.
Completed in year 3
41. Measurement of TE properties.
Completed in year 5
42. Comparative studies and analysis: Synthesis bulk materials for comparison to the nano-scale TE materials.
Completed in year 4
43. Optimization employing the developed materials.
Completed in year 5
44. Device design development.
Effort redirected to focus on medically relevant research in no-cost extension
45. Measurement, optimization and re-development of prototype TE devices.
Effort redirected to focus on medically relevant research in no-cost extension
46. Theoretical modeling of conductance and thermopower of core-shell nanocomposites.
Completed in year 3
47. Fabrication of CaCoO nanoparticle coatings by a microwave plasma process and investigation of thermoelectric properties.
Completed in year 4
48. Synthesis of bulk thermoelectric.
Completed in year 5

Ongoing Milestones through No-cost Extension of Continuation:

1. Synthesis of PEG, Dextran coated nanoparticles and clusters for hyperthermia experiments and their structural and magnetic characterization.
2. Measurements and comparative analysis of specific absorption rates and AC power losses of ferrofluids for magnetic hyperthermia applications.
3. Magnetoimpedance measurements and sensing of biomolecules.
4. Formation and delivery of functionalized artificial platelets for rapid cessation of internal bleeding.

All of the milestones for the grant have been completed as described above, except for the sub-tasks that will be continued and completed during the approved 24-month no-cost continuation of the Contract No. W81XWH-1020101/3349 through September 19, 2015. These sub-tasks will permit us to continue interdisciplinary work on research for the development of artificial platelets for delivery to promote coagulation at wound sites. This work will rely on advances already made in designed magnetic nanoparticles and physical techniques for the fabrication of polymeric micro- and nano-structures. Supporting work on related magnetic nanostructures will also continue as indicated above. Any further advances during the no-cost extension period in areas of research that have already accomplished program goals will also be reported.

In addition to the key research accomplishments outlined in Section III and the outcomes reported in Section IV, a major accomplishment of the grant has been to establish a multi-investigator Center for Integrated Functional Materials (CIFM) in the Physics Department at the University of South Florida (USF). CIFM is physically located in multiple laboratories on the fifth floor of the seven-story Interdisciplinary Sciences building at USF and provides an ongoing resource for the synthesis of novel materials using physical and chemical processes, and their characterization and development for multifunctional applications and devices. It is anticipated that this Center and associated researchers will continue to address the development of technologically significant materials for military and commercial applications well beyond the continuation and conclusion of this particular grant.

VI. References

1. A. G. Roca, R. Costo, A. F. Rebolledo, S Veintemillas-Verdaguer, P. Tartaj, T. González-Carreno, M. P. Morales and C. J. Serna, *Journal of Physics D: Applied Physics* **2009**, *42*, 224002.
2. D. Ung, L.D. Tung, G. Caruntu, D. Delapostas, Y. Alexandrous, I. Prior and N.T.K. Thanh, *CrystEngComm*. **2009**, *11*, 1309.
3. G. Gao, X. Liu, R. Shi, K. Zhou, Y. Shi, R. Ma, E. T. Muromachi and G. Qiu, *Crystal Growth & Design* **2010**, *10*, 2889.
4. R. Hao, R. Xing, Z. Xu, Y. Hou, S. Gao and S.H. Sun, *Advanced Materials* **2010**, *22*, 2729.
5. Dave S.-R., Gao X.-H., *Nanobiotech.* 2009, *1*, 583.
6. S. Pal, M. B. Morales, P. Mukherjee, H. Srikanth, *Journal of Applied Physics* **105**, 07B504 (2009)
7. A. Y. Louie *Chem. Rev.* **110**, 3146 (2010).
8. H. Khurshid, S. Chandra, P. Mukherjee, and H. Srikanth *J. Mater. Chem. C* **1**, 6553 (2013)
9. H. Khurshid, V. Tzitzios, W. F. Li, C. G. Hadjipanayis, and G. C. Hadjipanayis, *J. Appl. Phys.* **107**, (2010).
10. C. Srivastava, J. Balasubramanian, C. H. Turner, J. M. Wiest, H. G. Bagaria, and G. B. Thompson, *J. Appl. Phys.* **102**, 104310 (2007).
11. Levent Colak and George C. Hadjipanayis, *Nanotechnology* **20**, 485602 (2009).
12. B. Li and J. G. Liu, *J. Nonl. Sci.* **14**, 429 (2004).
13. N. A. Frey, M. H. Phan, H. Srikanth, S. Srinath, C. Wang, and S. Sun, *J. Appl. Phys.* **105**, 07B502 (2009).
14. M. Bellusci, S. Canepari, G. Ennas, A. La Barbera, F. Padella, A. Santini, A. Scano, L. Seralessandri, and F. Varsano, *J. Am. Cera. Soc.* **90**, 3977 (2007).
15. M. Gheisari, M. Mozaffari, M. Acet, and J. Amighian, *J. Magn. Magn. Mater.* **320**, 2618 (2008).
16. H. Khurshid, S. Chandra, W. Li, G. C. Hadjipnayis, P. Mukherjee, M. H. Phan, and H. Srikanth, *Nanoscale* **5**, 7942 (2013)
17. Goya, G. F.; Berquo, T. S.; Fonseca, F. C.; Morales, M. P., Static and dynamic magnetic properties of spherical magnetite nanoparticles. *J. Appl. Phys.* **2003**, *94*, 3520-3528.
18. Chandra, S.; Khurshid, H.; Li, W.; Hadjipnayis, G. C.; Phan, M. H.; Mukherjee, P.; Srikanth, H., Spin dynamics and criteria for onset of exchange bias in superspin glass Fe/ γ -Fe₂O₃ core-shell nanoparticles *Phys. Rev. B* **2012**, *86*, 014426-014433.
19. Ong, Q. K.; Lin, X. M.; Wei, A., Role of Frozen Spins in the Exchange Anisotropy of Core-Shell Fe@Fe₃O₄ Nanoparticles. *J. Phys. Chem C* **2011**, *115*, 2665-2672.
20. S. Odenbach, *J. Phys.: Condens. Matter* **16**, R1135 (2004).
21. M. B. Morales, M.H. Phan, N. A. Frey, and H. Srikanth, *Journal of Applied Physics* 2009; **105**, 07B511
22. M.B. Morales, S. Pal, N.A. Frey, M.H. Phan, P. Mukherjee, and H. Srikanth, *Physics Express* 2011; **1**:247

23. H. Khurshid, V. Tzitzios, F. Li, and G. C. Hadjipanayis, *Nanotech.* **22**, 265605 (2011).
24. M.H. Phan and H. X. Peng, *Prog. Mater. Sci* **53**, 323 (2008).
25. N. Laurita, A. Chaturvedi, C. Bauer, P. Jayathilaka, A. Leary, C. Miller, M.H. Phan, M.C. McHenry, H. Srikanth, *J. Appl. Phys.* **109**, 07C706 (2011).
26. Lahiri, J., Lin, Y., Bozkurt, P., Oleynik, I. I., & Batzill, M. (2010). An extended defect in graphene as a metallic wire. *Nature nanotechnology*, 5(5), 326–9. doi:10.1038/nnano.2010.53
27. A. Ruiz, D. Mukherjee, J. Devkota, M. Hordagoda, S. Witanachchi, P. Mukherjee, H. Srikanth, and M.H. Phan, *Journal of Applied Physics* 2013;113:17A323
28. A. A. Taysioglu, Y. Kaya, A. Peksoz, S.K. Akay, N. Derebasi, G. Irez, G. Kaynak, *IEEE Trans. Magn.* 46, 405 (2010).
29. C. Garcia, V. Zhukova, A. Zhukov, N. Usov, M. Ipatov, J. Gonzalez and J. M. blanco, *Sensors Letters* 5, 1 (2007).
30. H. Chiriac, D.D. Herea, S. Corodeanu, *J. Magn. Mater.* 311, 425 (2007).
31. V.S. Larin, A.V. Torcunov, A. Zhukov, J. Gonzalez, M. Vazquez, L. Panina, *J. Magn. Mater.* 249, 39 (2002).
32. A. D. Kersey, M. A. Davis, H. J. Patrick, M. LeBlanc, K. P. Koo, C. G. Askins, M. A. Putnam and E. J. Friebele, *J. Lightwave Technology* 15, 1442 (1997).
33. Rinkiö M, Johansson A, Paraoanu G S and Törmä P 2009 *Nano Lett.* 9 643-47
34. Kim C, Kim Y A, Kim J H, Kataoka M and Endo M 2008 *Nanotechnology* 19 145602 (1-5).
35. Kornev K G, Halverson D, Korneva G, Gogotsi Y and Friedman G 2008 *Appl. Phys. Lett.* 92 233117(1-3).
35. Gupta A K and Gupta M 2005 *Biomaterials* 26 3995-4021.
36. Lu F, Gu L, Mezziani M J, Wang X, Luo P G, Veca L M, Cao L and Sun Y-P 2009 *Adv. Mater.* 21 139-52.
37. Korneva G, Ye H, Gogotsi Y, Halverson D, Friedman G, Bradley J-C and Kornev K. G 2005 *Nano Lett.* 5 879-84.
38. S. Pal, S. Chandra, M. –H. Phan, P. Mukherjee and H. Srikanth, *Nanotechnology* 2009; 20, 485604
39. A. Chaturvedi, K. Stojak, N. Laurita, P. Mukherjee, H. Srikanth, and M.H. Phan Carbon nanotube-based gas sensors using the magnetoimpedance effect *Journal of Applied Physics* 2012;111: 07E507
40. C. Morales, J. Dewdney, S. Susmita, S. Skidmore, K. Stojak, H. Srikanth, T. Weller and J. Wang, *IEEE Trans. Magn.* 1, 1340 (2010).
41. K. Stojak, S. Pal, H. Srikanth, C. Morales, J. Dewdney, J. Wang, T. Weller, *Nanotech.* 22, 135602 (2011).
42. Y. Wang and John T. W. Yeow, *J. Sens.* 1, 1 (2009).
43. J. Richardson, A. Hill, R. Luxton, and P. Hawkins, *Biosens. Bioelectron.* 16, 1127 (2001).
44. D.L. Graham, H. Ferreira, J. Bernardo, P.P. Freitas, and J.M.S. Cabral, *J. Appl. Phys.* 91, 7786 (2002).

45. J. Devkota, A. Ruiz, C. Wang, S. Mohapatra, P. Mukherjee, H. Srikanth, and M.H. Phan *Journal of Applied Physics* **113**, 104701 (2013)
46. J. Devkota, A. Ruiz, P. Mukherjee, H. Srikanth, and M.H. Phan, *IEEE Transactions on Magnetics* **49**, 9464 (2013)
47. J. Devkota, M.T. Trang, K. Stojak, P.T. Ha, H.N. Pham, T. L. Ngo, N.X. Phuc, P. Mukherjee, H. Srikanth, and M.H. Phan, *Sensors and Actuators B: Chemical* **190**, 715 (2014)
48. G. Kurlyandaya, J. Magn. Mater. 321, 659 (2009).
49. N. A. Frey Huls, M. H. Phan, A. Kumar, S. Mohapatra, S. S. Mohapatra, P. Mukherjee, and H. Srikanth, *Sensors* 2013;13:8490
50. C.A.F. Vaz, J. Phys.: Condens. Matter 24, 333201 (2012).
51. F. Qin and C. Brosseau, J. Appl. Phys. 111, 061301 (2012)
52. C. Morales, J. Dewdney, S. Susmita, S. Skidmore, K. Stojak, H. Srikanth, T. Weller and J. Wang, Microwave Theory and Techniques IEEE Trans. Magn. 59, 302 (2011).
53. K. Stojak, S. Pal, H. Srikanth, C. Morales, J. Dewdney, J. Wang, T. Weller, Nanotech. 22, 135602 (2011).
54. S. Sun, H. Zeng *J. Am. Chem. Soc.* 2002, 124, 8204.
55. M. Liu, X. Li, J.Lou, S. Zheng, K.Du, N. X. Sun. *J. Appl. Phys.* 2007, 102, 083911.
56. J. Xie, C. J. Xu, Z. C. Xu, Y. L. Hou, K. L. Young, S. X. Wang, N. Pourmand, S. H. Sun, *Chem. Mater.* **2006**, 18, 5401.
57. Sun S and Zeng H (2002), *J. Am. Chem. Soc.* 124 8204-5.
58. P. R. Wallace (1947). *Physical Review* **71**: 622.
59. C. Lee *et al.* (2008). *Science* **321**: 385.
60. Nair, R. R.; Blake, P.; Grigorenko, A. N.; Novoselov, K. S.; Booth, T. J.; Stauber, T.; Peres, N. M. R.; Geim, A. K. (2008). *Science* **320**: 1308.
61. Qingkai *et al.* (2008). *Applied Physics Letters* **93**, 113103
62. Gelehrter, T.D. and R. Sznycer-Laszuk, Thrombin induction of plasminogen activator-inhibitor in cultured human endothelial cells. *J Clin Invest*, 1986. 77(1): p. 165-169.
63. Moore, K.L., et al., Endotoxin enhances tissue factor and suppresses thrombomodulin expression of human vascular endothelium in vitro. *J Clin Invest*, 1987. 79(1): p. 124-130.
64. Weiss, T., et al., Serial subculture and relative transport of human endothelial cells in serum-free, defined conditions. *In Vitro Cellular & Developmental Biology - Plant*, 1990. 26(8): p. 759-768.
65. Maciag, T., et al., Organizational behavior of human umbilical vein endothelial cells. *J Cell Biol*, 1982. 94(3): p. 511-520.
66. Kubota, Y., et al., Role of laminin and basement membrane in the morphological differentiation of human endothelial cells into capillary-like structures. *J Cell Biol*, 1988. 107(4): p. 1589-1598.
67. Grant, D.S., et al., Two different laminin domains mediate the differentiation of human endothelial cells into capillary-like structures in vitro. *Cell*, 1989. 58(5): p. 933-943.

68. Folkman, J., Angiogenesis in cancer, vascular, rheumatoid and other disease. *Nat Med*, 1995. 1(1): p. 27-31.
69. Bergers, G. and L.E. Benjamin, Tumorigenesis and the angiogenic switch. *Nat Rev Cancer*, 2003. 3(6): p. 401-410.
70. Yonemura, S., et al., Cell-to-cell adherens junction formation and actin filament organization: similarities and differences between non-polarized fibroblasts and polarized epithelial cells. *J Cell Sci*, 1995. 108 (Pt 1): p. 127-142.
71. Pelham, R.J., Jr. and Y. Wang, Cell locomotion and focal adhesions are regulated by substrate flexibility. *Proc Natl Acad Sci U S A*, 1997. 94(25): p. 13661-13665.
72. Discher, D.E., P. Janmey, and Y.L. Wang, Tissue cells feel and respond to the stiffness of their substrate. *Science*, 2005. 310(5751): p. 1139-1143.
73. Georges, P.C. and P.A. Janmey, Cell type-specific response to growth on soft materials. *J Appl Physiol*, 2005. 98(4): p. 1547-1553.
74. Califano, J.P. and C.A. Reinhart-King, Substrate Stiffness and Cell Area Predict Cellular Traction Stresses in Single Cells and Cells in Contact. *Cellular and Molecular Bioengineering*, 2010. 3(1): p. 68-75.
75. Picart, C., Polyelectrolyte multilayer films: from physico-chemical properties to the control of cellular processes. *Curr Med Chem*, 2008. 15(7): p. 685-697.
76. Richert, L., et al., Improvement of stability and cell adhesion properties of polyelectrolyte multilayer films by chemical cross-linking. *Biomacromolecules*, 2004. 5(2): p. 284-294.
77. Richert, L., et al., Elasticity of native and cross-linked polyelectrolyte multilayer films. *Biomacromolecules*, 2004. 5(5): p. 1908-1916.
78. Schneider, A., et al., Elasticity, biodegradability and cell adhesive properties of chitosan/hyaluronan multilayer films. *Biomed Mater*, 2007. 2(1): p. S45-S51.
79. Lavalle, P., et al., Comparison of the Structure of Polyelectrolyte Multilayer Films Exhibiting a Linear and an Exponential Growth Regime: An in Situ Atomic Force Microscopy Study. *Macromolecules*, 2002. 35(11): p. 4458-4465.
80. Picart, C., et al., Molecular basis for the explanation of the exponential growth of polyelectrolyte multilayers. *Proc Natl Acad Sci U S A*, 2002. 99(20): p. 12531-12535.
81. Lavalle, P., et al., Modeling the Buildup of Polyelectrolyte Multilayer Films Having Exponential Growth, *The Journal of Physical Chemistry B*, 2003. 108(2): p. 635-648.
82. Haynie, D.T., et al., Quantal self-assembly of polymer layers in polypeptide multilayer nanofilms. *Biomacromolecules*, 2006. 7(8): p. 2264-2268.
83. Zhang, L., et al., Context dependence of the assembly, structure, and stability of polypeptide multilayer nanofilms. *ACS Nano*, 2007. 1(5): p. 476-486.
84. Vautier, D., et al., Polyelectrolyte multilayer films modulate cytoskeletal organization in chondrosarcoma cells. *J Biomater Sci Polym Ed*, 2002. 13(6): p. 713-732.
85. Boura, C., et al., Endothelial cells grown on thin polyelectrolyte multilayered films: an evaluation of a new versatile surface modification. *Biomaterials*, 2003. 24(20): p. 3521-3530.

86. Picart, C., et al., Primary Cell Adhesion on RGD-Functionalized and Covalently Crosslinked Thin Polyelectrolyte Multilayer Films. *Advanced Functional Materials*, 2005. 15(1): p. 83-94.
87. Schneider, A., et al., Polyelectrolyte multilayers with a tunable Young's modulus: influence of film stiffness on cell adhesion. *Langmuir*, 2006. 22(3): p. 1193-1200.
88. Werner, S., et al., The effect of microstructured surfaces and laminin-derived peptide coatings on soft tissue interactions with titanium dental implants. *Biomaterials*, 2009. 30(12): p. 2291-2301.
89. Kim, S., A.E. English, and K.D. Kihm, Surface elasticity and charge concentration-dependent endothelial cell attachment to copolymer polyelectrolyte hydrogel. *Acta Biomater*, 2009. 5(1): p. 144-151.
90. Zhu, Y. and Y. Sun, The influence of polyelectrolyte charges of polyurethane membrane surface on the growth of human endothelial cells. *Colloids and Surfaces B: Biointerfaces*, 2004. 36(1): p. 49-55.
91. Knight, C.G., et al., The collagen-binding A-domains of integrins $\alpha(1)\beta(1)$ and $\alpha(2)\beta(1)$ recognize the same specific amino acid sequence, GFOGER, in native (triple-helical) collagens. *J Biol Chem*, 2000. 275(1): p. 35-40.
92. Reyes, C.D., et al., Biomolecular surface coating to enhance orthopaedic tissue healing and integration. *Biomaterials*, 2007. 28(21): p. 3228-3235.
93. Wojtowicz, A.M., et al., Coating of biomaterial scaffolds with the collagen-mimetic peptide GFOGER for bone defect repair. *Biomaterials*, 2010. 31(9): p. 2574-2582.
94. Saunders, R. and D. Hammer, Assembly of Human Umbilical Vein Endothelial Cells on Compliant Hydrogels. *Cellular and Molecular Bioengineering*, 2010. 3(1): p. 60-67.
95. Li, C., A. Hill, and M. Imran, In vitro and in vivo studies of ePTFE vascular grafts treated with P15 peptide. *J Biomater Sci Polym Ed*, 2005. 16(7): p. 875-891.
96. Hersel, U., C. Dahmen, and H. Kessler, RGD modified polymers: biomaterials for stimulated cell adhesion and beyond. *Biomaterials*, 2003. 24(24): p. 4385-4415.
97. Massia, S.P. and J.A. Hubbell, An RGD spacing of 440 nm is sufficient for integrin $\alpha V\beta 3$ -mediated fibroblast spreading and 140 nm for focal contact and stress fiber formation. *J Cell Biol*, 1991. 114(5): p. 1089-1100.
98. Beer, J.H., K.T. Springer, and B.S. Collier, Immobilized Arg-Gly-Asp (RGD) peptides of varying lengths as structural probes of the platelet glycoprotein IIb/IIIa receptor. *Blood*, 1992. 79(1): p. 117-128.
99. Haynie, D.T., et al., Polypeptide multilayer films: role of molecular structure and charge. *Langmuir*, 2004. 20(11): p. 4540-4547.
100. Leung, D.W., et al., Vascular endothelial growth factor is a secreted angiogenic mitogen. *Science*, 1989. 246(4935): p. 1306-1309.
101. Neufeld, G., et al., Vascular endothelial growth factor (VEGF) and its receptors. *FASEB J*, 1999. 13(1): p. 9-22.

102. Byrne, A.M., D.J. Bouchier-Hayes, and J.H. Harmey, Angiogenic and cell survival functions of vascular endothelial growth factor (VEGF). *J Cell Mol Med*, 2005. 9(4): p. 777-794.
104. Sieminski, A.L. and K.J. Gooch, Biomaterial-microvasculature interactions. *Biomaterials*, 2000. 21(22): p. 2232-2241. F. Qin and C. Brosseau, *J. Appl. Phys.* 111, 061301 (2012)
105. C. Morales, J. Dewdney, S. Susmita, S. Skidmore, K. Stojak, H. Srikanth, T. Weller and J. Wang, *Microwave Theory and Techniques IEEE Trans. Magn.* 59, 302 (2011).
106. K. Stojak, S. Pal, H. Srikanth, C. Morales, J. Dewdney, J. Wang, T. Weller, *Nanotech.* 22, 135602 (2011).
107. Ramesh R and Spaldin N A 2007 *Nature Materials* 6 21-9
108. N. A. Spaldin, and M. Fiebig, *Science* **309**, 391 (2005)
109. W. Eerenstein, N. D. Mathur and J. F. Scott, *Nature*, 442, 759 (2006).
110. J. P. Zhou, Z. C. Qiu, and P. Liu, *Mater. Res. Bull.* **43**, 3514 (2008)
111. M. Vopsaroiu, J. Blackburn, and M. G. Cain, *J. Phys. D: Appl. Phys.* **40**, 5027 (2007)
112. Alex Goldman, *Modern Ferrite Technology*, 2nd Edition, Springer, New York (2006).
113. J. Schwarzkopf, and R. Foranari, *Progress in Crystal Growth and Characterization of Materials* 52, 159 (2006).
114. N. Izyumskaya, Y. I. Alivov, S. J. Cho, H. Morkoç, H. Lee, and Y. S. Kang, *Crit. Rev. Solid State Mater. Sci.* 32, 111 (2007).] [J. F. Scott, *Science* 315, 954 (2007).
115. T. J. Zhu, L. Lu, and M. O. Lai, *Appl. Phys. A* **81**, 701 (2005).
116. S. Witanachchi, K. Ahmed, P. Sakthivel, P. Mukherjee, *Appl. Phys. Lett.* 66, 1469 (1995).
117. P. Mukherjee, J. Cuff, S. Witanachchi, *Appl. Surface Science* 127-129 (1998) 620-625.
118. S. Witanachchi and P. Mukherjee, *J. Vacuum Sci. Technol. A* 13, 1171-1174, 1995.
119. P. Mukherjee, S. Chen and S. Witanachchi, *Appl. Phys. Lett.*, 74, 1546-1548, 1999.
120. P. Mukherjee, J. B. Cuff, and S. Witanachchi, *Rev. Sci. Instrum.* 72, 2380 (2001)
121. Feng Chen, Q. Z. Liu, H. F. Wang, F. H. Zhang, and Wenbin Wu, *Appl. Phys. Lett.* 90, 192907 (2007)
122. W. Wu, K. H. Wong, C. L. Choy, and Y. H. Zhang, *Appl. Phys. Lett.* 77, 3441 (2000).
123. S. Dussan, A. Kumar, J. F. Scott, and R. S. Katiyar, *Appl. Phys. Lett.* 96, 072904 (2010).
124. J. J. Lee, C. L. Thio, and S. B. Desu, *J. Appl. Phys.* 78, 5073 (1995).
125. F. Chen, Q. Z. Liu, H. F. Wang, F. H. Zhang, and W. Wu, *Appl. Phys. Lett.* 90, 192907 (2007).
126. Z. Li, Y. Wang, Y. Lin, and C. Nan, *Phys. Rev. B* **79**, 180406(R) (2009).
127. C. H. Sim, Z. Z. Pan, and J. Wang, *J. Appl. Phys.* **105**, 084113 (2009).
128. H. He, J. Ma, Y. Lin, and C. W. Nan, *J. Appl. Phys.* **104**, 114114 (2008).
129. H. C. He, J. Wang, J. P. Zhou, and C. W. Nan, *Adv. Funct. Mater.* **17**, 1333 (2007). [24] J. P. Zhou, H. C. He, Y. Zhang, C. Y. Deng, Z. Shi, and C. W. Nan, *Appl. Phys. A* **89**, 553 (2007).
130. J. P. Zhou, H. He, Z. Shi, and C. W. Nan, *Appl. Phys. Lett.* **88**, 013111 (2006).
131. N. Ortega, A. Kumar, R. S. Katiyar, and C. Rinaldi, *J. Mater. Sci.* **44**, 5127 (2009)

132. Y. Zhang, Z. Li, C. Deng, J. Ma, Y. Lin, and C. W. Nan, *Appl. Phys. Lett.* **92**, 152510 (2008).
133. J. X. Zhang, J. Y. Dai, and H. L. W. Chan, *J. Appl. Phys.* **107**, 104105 (2010).
134. C. Nan, M. I. Bichurin, S. Dong, D. Viehland, and G. Srinivasan, *J. Appl. Phys.* **103**, 031101 (2008).
135. M. Narayanan, S. Tong, S. Liu, B. Ma, and U. Balachandran, *Appl. Phys. Lett.* **102**, 062906 (2013).
136. Wanlin Zhu, Ichiro Fujii, Wei Ren, and Susan Trolier-McKinstry, *J. Am. Ceram. Soc.*, **95** [9] 2906–2913 (2012).
137. Q. Tan, Z. Xu, and D. Viehland, *Philosophical Magazine B*, **80**, 1585-1597 (2000).
138. R. Gerson, *J. Appl. Phys.*, **31** [1] 188–94 (1960).
139. A. Pramanick, D. Damjanovic, J. E. Daniels, J. C. Nino, and Jacob L. Jones, *J. Amer. Ceram. Soc.* **94** [2], 293 (2011).
140. Kyoung Bo Han, Chang Hoon Jeon, Hee Sauk Jhon, Sang Yeol Lee, *Thin Solid Films* **437** (2003) 285–289.
141. Young-Hoon Son, Kyoung-Tae Kim, and Chang-Il Kim, *J. Vac. Sci. Technol. A* **22**, 1743 (2004).
142. I. Stolichnov, A. Tagantsev, N. Setter, J. S. Cross, and M. Tsukada, *Appl. Phys. Lett.* **74**, 3552 (1999).
143. D. Mukherjee, N. Bingham, M. Hordagoda, M. H. Phan, H. Srikanth, S. Witanachchi, and P. Mukherjee, *J. Appl. Phys.* **112**, 083910 (2012).
144. D. Mukherjee, M. Hordagoda, N. Bingham, H. Srikanth, P. Mukherjee and S. Witanachchi, *J. Appl. Phys.* **112**, 064101 (2012).
145. B. Ma, S. Liu, S. Tong, M. Narayanan, and U. Balachandran, *J. Appl. Phys.* **112**, 114117 (2012).
146. J. F. Scott, *Ferroelectr. Rev.* **1** (1), 1 (1998).
147. M. Prabu, I.B. Shameem Banu, S. Gobalakrishnan, Murthy Chavali, *J. Alloys Compds.* **551** (2013) 200–207.
148. J. Schwarzkopf, and R. Foranari, *Prog. Cryst. Growth Character. Mater.* **52**, 159 (2006).
149. W. Wu, K. H. Wong, C. L. Choy, and Y. H. Zhang, *Appl. Phys. Lett.* **77**, 3441 (2000).
150. K.-S. Liu, Y.-J. Chen, G. Jamn, I.-N. Lin, *Appl. Phys. Lett.* **75** (1999) 2647.
151. E.C.F. Souza, A.Z. Simões, M. Cilense, E. Longo, J.A. Varela, *Mater. Chem. Phys.* **88** (2004) 155–159.
152. G. H. Haertling, *Ferroelectrics*, **75**, 25-55, 1987.
153. Q. M. Zhang, J. Zhao, K. Uchino, and J. Zheng, *J. Mater. Res.*, **12** [1] 226–34 (1997).
154. F. Pan, C. Song, X.J. Liu, Y.C. Yang, F. Zeng, *Mater. Sci. Engineering R* **62**, 1 (2008).
155. Z. W. Liu et al., *Mater. Lett.* **62**, 1255 (2008).
156. M. J. Calderon and S. Das Sharma, *Annals of Physics*, **322**, 2618 (2007).
157. T. Dietl, H. Ohno, F. Matsukura, J. Cibert, and D. Ferrand, *Science* **287**, p. 1019 (2000).

158. P. Sharma, A. Gupta, K.V. Rao, F. J. Owens, R. Sharma, R. Ahuja, J. M. Osorio Guillen, B. Johansson, and G. A. Gehring, *Nature Mat.* **2**, p. 673 (2003).
159. Y. C. Yang et al., *Appl. Phys. Lett.* **92**, 012907 (2008)
160. Y. C. Yang et al., *Appl. Phys. Lett.* **90**, 242903, (2007)
161. J. T. Drotar, Y.-P. Zhao, T.-M. Lu, and G.-C. Wang, *Phys. Rev. B* **62**, 2118 (2000).
162. Y. Shim and J. G. Amar, *Phys. Rev. Lett.* **98**, 046103 (2007).
163. S. G. Mayr and K. Samwer, *J. Appl. Phys.* **91**, 2779 (2002).
164. K. Robbie, G. Beydaghyan, T. Brown, C. Dean, J. Adams, and C. Buzea, *Rev. Sci. Instruments* **75**, 1089 (2004).
165. K. Robbie and M. J. Brett, *J. Vac. Sci. Technol. A* **15**, 1460 (1997).
166. T. Karabacak, A. Mallikarjunan, J. P. Singh, D. Ye, G. C. Wang, and T. M. Lu, *Appl. Phys. Lett.* **83**, 3096 (2003).
167. D.-X. Ye, Y-P. Zhao, G-R. Yang, Y-G. Zhao, G-C. Wang and T-M. Lu, *Nanotechnology* **13**, 615 (2002).
168. F. Tang, D. L. Liu, D. X. Ye, Y. P. Zhao, T. M. Lu, G. C. Wang and A. Vijayaraghavan, *J. Appl. Phys.* **93**, 4194-4200 (2003).
169. D. Mukherjee, T. Dhakal, M. Phan, H. Srikanth, P. Mukherjee, and S. Witanachchi, *Physica B: Condensed Matter* **406**, 2663 (2011).
170. T. Dhakal, D. Mukherjee, P. Mukherjee, R. Hyde, M. H. Phan, H. Srikanth, and S. Witanachchi, *J. Appl. Phys.* **107**, 053914 (2010).
171. A. Lisfi and C. M. Williams, *J. Appl. Phys.* **93**, 8143 (2003).
172. A. Lisfi and C. M. Williams, *J. Appl. Phys.* **93**, 8143 (2003). G. Blatter and F. Greuter, *Phys. Rev. B* **34**, 8555 (1986).
173. C. H. Seager, *J. Appl. Phys.* **52**, 3960 (1981).
174. M. S. Dresselhaus, G. Chen, M. Y. Tang, R. Yang, H. Lee, D. Wang, Z. Ren, J. P. Fleurial, and P. Gogna, *Adv. Mater.* **19**, 1043 (2007).
175. L. D. Hicks, M. S. Dresselhaus, *Phys. Rev. B* **47**, 16631 (1993).
176. R. Venkatasubramanian, E. Siivola, T. Colpitts, B. O'Quinn, *Nature* **413**, 597 (2001).
177. T. C. Harman, P. J. Taylor, M. P. Walsh, and B. E. LaForge, *Science* **297**, 2229 (2002).
178. T. Kong, S. B. Cronin, M. S. Dresselhaus, *Applied Physics Letters* **77**, 1490 (2000).
179. J. P. Heremans, C. M. Thrush and D. T. Morelli, *J. Appl. Phys.* **98**, 063703 (2005).
180. K. F. Hsu, S. Loo, F. Guo, W. Chen, J. S. Dyck, C. Uher, T. Hogan, E. K. Polychroniadis and M. G. Kanatzidis, *Science* **303**, 5659, 818-821 (2004).
181. M. S. Dresselhaus, G. Chen, M. Y. Tang, R. G. Yang, H. Lee, D. Z. Wang, Z. F. Ren, J. P. Fleurial and P. Gogna, *Proc. Mater. Res. Soc.* **886** 3 (2006).
182. G. S. Nolas, J. Sharp, and H. J. Goldsmid, *Thermoelectrics: Basic Principles and New Materials Developments* (Springer, New York, NY, 2001).
183. R. D. Schaller and V. I. Kilmov, "High efficiency multiplication in PbSe nanocrystals: Implications for solar energy conversion, *Phys. Rev. Lett.* **92**, 186601 (2004).
184. H. Marom, M. Ritterband, M. Eizenberg, *Thin Solid Films* **510**, 62 (2006).

185. Y. I. Ravich, In *CRC Handbook of Thermoelectrics*, edited by D. M. Rowe, pages 67-73, CRC Press, New York, (1995).
186. B. Moyzhes and V. Nemchinsky, *Appl. Phys. Lett.* 73, 1895 (1998).
187. K. Kishimoto and T. Koyanagi, *J. Appl. Phys.* 92, 2544 (2002).
188. J. P. Heremans, C. M. Thrush, and D. T. Morelli, *Physical Review B* 70, 115334 (2004).
189. J. Martin, G. S. Nolas, W. Zhang, and L. Chen, *Appl. Phys. Lett.* 99, 222112 (2007).
190. W. Zhang, L. Zhang, Y. Cheng, Z. Hui, X. Zhang, Y. Xie, and Y. Qian, *Materials Research Bulletin* 35, 2009 (2000).
191. M. Fanun, *Microemulsions: Properties and Applications*, CRC Press (2008).
192. R.D. Shannon, D.B. Rogers, C.T. Prewitt, *Inorg. Chem.* 10, 713 (1971).
193. H.H. Emons, E. Beger, *Z. Chem.* 7, 200 (1967).
194. P. Porta, R. Dragone, G. Fierro, M. Inversi, M. L. Jacono, G. Moretti, *J. Chem. Soc. Faraday Trans.* 88, 311 (1992).
195. J. Xie, X. B. Zhao, J. L. Mi, J. Tu, H. Y. Qin, G. S. Cao, J. P. Tu, *Electrochem. Solid-State Lett.* 2006, 9, A336.
196. L. Kumari, W. Li, J. Y. Huang, P. P. Provencio, *J. Phys. Chem. C* 2010, 114, 9573.
197. R. Radebaugh, *Infrared Technology and Applications, Proceedings of SPIE* 4130, 363 (2000).
198. Phan et al., *Appl. Phys. Lett.* 93, 252505 (2008).
199. Phan et al. *J. Appl. Phys.* 107, 09A910 (2010).
200. S. J. Peppiatt, *Proc. R. Soc. London, Ser. A*, 345, 401 (1975).
201. G. L. Allen, R. A. Bayles, W. W. Gile and W. A. Jesser, *Thin Solid Films*, 144, 297 (1986).
202. P. Pawlow, *Z. Phys. Chem., Stoechiom. Verwandtschaftsl.*, 65, 545 (1909).
203. E. A. Olson, M. Y. Efremov, M. Zhang, Z. Zhang and L. H. Allen, *J. Appl. Phys.*, 97, 034304 (2005).
204. R. Martin-Lopez, B. Lenoir, X. Devaux, A. Dauscher and H. Scherrer, *Mater. Sci. Engin. A*, 248, 147 (1998).
205. J. Martin, G.S. Nolas, H. Wang, and J.J. Yang, *J. Appl. Phys.* 102, 103719 (2007).
206. Yu. I. Ravich, B. A. Efimova, and I. A. Smirnov, *Semiconducting Lead Chalcogenides*, Plenum, New York, p. 91 (1970) and references therein.
207. W. Scanlon, in *Solid State Physics* 9, Academic Press, NY (1959).
208. C. Kittel, *Introduction to Solid State Physics*, Second Edition, John Wiley & Sons, Inc., New York, p. 356 (1956).
209. Z. H. Dughaish, *Physica B*, 322, 205 (2002).
210. E. H. Putley, *Proc. Phys. Soc. B* 65, 388 (1952).
211. E. H. Putley, *Proc. Phys. Soc. B* 65, 736 (1952).
212. N. A. Poklonski, S. A. Vyrko, V. I. Yatskevich, and A. A. Kocherzhenko, *J. Appl. Phys.* 93, 9749 (2003).
213. C. H. Seager, *J. Appl. Phys.* 52, 3960 (1981).
214. J. Y. W. Seto, *J. Appl. Phys.* 46, 5247 (1975).

215. O. Vigil-Galan, Lídice Vaillant, R. Mendoza-Perez, G. Contreras-Puente, J. Vidal-Larramendi, and A. Morales-Acevedo, *J. Appl. Phys.* 90, 3427 (2001).
216. G. Kiriakidis, M. Suche, S. Christoulakis, and N. Katsarakis, *Rev. Adv. Mater. Sci.* 10, 215 (2005).
217. W. Zhang, L. Zhang, Y. Cheng, Z. Hui, X. Zhang, Y. Xie, and Y. Qian, *Materials Research Bulletin* 35, 2009 (2000).
218. T. S. Zyubina, V. S. Neudachina, L. V. Yashina, V. I. Shtanov, *Surface Science* 574, 52 (2005).
219. O. Vigil-Galan, Lídice Vaillant, R. Mendoza-Perez, G. Contreras-Puente, J. Vidal-Larramendi, and A. Morales-Acevedo, *J. Appl. Phys.* 90, 3427 (2001).
220. R. Clasen, G. Harbeke, A. Krost, F. Levy, O. Madelung, K. Maschke, G. Nimtz, B. Schlicht, F. J. Schmitte, and J. Treusch, *Landolt-Bornstein: Numerical Data and Functional Relationships in Science and Technology*, Volume 17 Semiconductors, Subvolume f, Ed. by K. H. Hellwege and O. Madelung, (Springer, New York, pg. 170, 1983).
221. V. V. Miten, *Phys. Rev. B* 31, 2584 (1985).
222. L. M. Rogers, *Brit. J. Appl. Phys.* 1, 1067 (1968).
223. J. M. O. Zide, D. Vashaee, Z. X. Bian, G. Zeng, J. E. Bowers, A. Shakouri, and A. C. Gossard, *Phys. Rev. B* 74, 205335 (2006).
224. A. J. Crocker and L. M. Rogers, *Brit. J. Appl. Phys.* 18, 563 (1967).
225. J. P. Heremans, and C.M. Jaworski, *Appl. Phys. Lett.* 93, 122107 (2008).
226. C.F. Gallo, B.S. Chandrashekhar, and P.H. Sutter, *J. Appl. Phys.* 1963, 34, 144.
227. A. F. Ioffe, *Physics of Semiconductors*; Academic: New York, 1960.
228. D. H. Kim, T. J. Mitani, *Alloys Compd.* 399, 14 (2005).
229. L. D. Zhao, B.-P. Zhang, W. S. Liu, H. L. Zhang, J.-F. Li, *J. Alloys Compd.* 467, 91 (2009).
230. D.J. Singh, *Phys. Rev. B* 76 (2007) 085110.
231. A stoichiometric mixture of high-purity Fe and Sb inside a BN crucible was melted by an induction furnace in a nitrogen atmosphere at 630 °C for 10 min before water quenching. The resulting product was then annealed at 600 °C for a week.
232. A. Bentien, S. Johnsen, G. K. H. Madsen, B. B. Iversen, F. Steglich, *Eur. Phys. Lett.* 2007, 80, 17008.
233. A. Bentien, G. K. H. Madsen, S. Johnsen, B. B. Iversen, *Phys. Rev. B* 74, 205105 (2006).
234. P. Sun, M. Søndergaard, Y. Sun, S. Johnsen, B. B. Iversen, F. Steglich, *Appl. Phys. Lett.* 98, 072105 (2011).
235. A. Herzog, M. Marutzky, J. Sichelschmidt, F. Steglich, S. Kimura, S. Johnsen, B. B. Iversen, *Phys. Rev. B* 82, 245205 (2010).
236. A.-M. Racu, D. Menzel, J. Schoenes, M. Marutzky, S. Johnsen, B. B. Iversen, *J. Appl. Phys.* 103, 07C912 (2008).
237. Y. Zhang, M. S. Dresselhaus, Y. Shi, Z. F. Ren, G. Chen, *Nano Lett.* 11, 1166 (2011).

238. I. A. Zaliznyak, A. T. Savici, V. O. Garlea, R. Hu, C. Petrovic, *Phys. Rev. B* 83, 184414 (2011).
239. T. M. Tritt, *J. Mater. Res.* DOI:10.1557/jmr.2011.86.
240. P. Sun, N. Oeschler, S. Johnsen, B. B. Iversen, F. Steglich, *Phys. Rev. B* 79, 153308 (2009).
241. R. Hu, V. F. Mitrovic, C. Petrovic, *Appl. Phys. Lett.* 92, 182108 (2008).
242. B. Buschinger, C. Geibel, F. Steglich, D. Mandrus, D. Young, J. L. Sarrao, Z. Fisk, *Phys. B* **1997**, 784, 230, and references cited therein.
243. L. Horng, G. Chern, M. C. Chen, P. C. Kang, D. S. Lee, *J. Magn. Magn. Mater.* 207, 389 (2004).
244. E. A. Albanesi, C. M. I. Okoye, C. O. Rodriguez, E. L. Peltzer y Blanca, and A. G. Petukhov, *Phys. Rev. B* 61, 16589 (2000).
245. Z. Dashevsky, R. Kreizman, and M. P. Dariel, *J. Appl. Phys.* 98, 094309 (2005).
246. A. K. Sreedhar and S. C. Gupta, *Phys. Rev. B* 5, 3160 (1972)
247. K. Kishimoto and T. Koyanagi, *J. Appl. Phys.* 92, 2544 (2002)
248. K. Kishimoto, K. Yamamoto, and T. Koyanagi, *Jpn. J. Appl. Phys.* 42, 501 (2003)
249. R. E. Jones, Jr. and S. P. Wesolowski, *J. Appl. Phys.* 56, 1701 (1984)
250. N. Zettili, *Quantum Mechanics: Concepts and Applications* (John-Wiley, Chichester, 2001)
251. W. Scanlon, in *Solid State Physics* 9, Academic Press, NY (1959).
252. C. M. Bhandari and D. M. Rowe, *Thermal Conduction in Semiconductors* (Wiley, New York, 1988)
253. A. Popescu, L. M. Woods, J. Martin, and G. S. Nolas, *Phys. Rev. B* 79, 205302 (2009).
254. J. Callaway, *Phys. Rev.* 113, 1046 (1959).
255. M. G. Holland, *Phys. Rev.* 132, 2461 (1963).
256. J. He, S. N. Girard, M. G. Kanatzidis, and V. P. Dravid, *Adv. Funct. Mater.* 20, 764 (2010).
257. S. V. Faleev and F. Leonard, *Phys. Rev. B* 77, 214304 (2008).
258. Sofo, J. O., and Mahan, J. D., *Phys. Rev. B*, 58, 15620 (1998).
259. Vafayi, K., Calandra, M., and Gunnarsson, O., *Phys. Rev. B*, 74, 235116 (2006).
260. Srivastava, G. P., *The Physics of Phonons* (Adam Hilger, Bristol), 1990.
261. A. Chaturvedi, S. Stefanoski, M-H. Phan, G. S. Nolas, and H. Srikanth, *Appl. Phys. Lett.* 99, 162513 (2011).